DESIGN AND DEVELOPMENT OF AN OPTIMIZED FLUXGATE MAGNETOMETER FOR IMPROVED EARTH'S MAGNETIC FIELD STUDIES

BY

WAHEED OLUJIDE OLUYOMBO

DEPARTMENT OF ELECTRICAL AND COMPUTER ENGINEERING
FACULTY OF ENGINEERING AHMADU BELLO UNIVERSITY,

ZARIA, NIGERIA

DECEMBER, 2016.

DESIGN AND DEVELOPMENT OF AN OPTIMIZED FLUXGATE MAGNETOMETER FOR IMPROVED EARTH'S MAGNETIC FIELD STUDIES

BY

Waheed Olujide OLUYOMBO
B. Eng. (FUTA) 2002; M. Eng. (FUTA) 2011
(PhD/ENG/15427/2011-2012)
oluyomboow2008@yahoo.com

A THESIS SUBMITTED TO THE SCHOOL OF POSTGRADUATE STUDIES, AHMADU BELLO UNIVERSITY, ZARIA IN PARTIAL FULFILLMENT OF THE REQUIREMENTS FOR THE AWARD OF DOCTOR OF PHILOSOPHY (PhD) DEGREE IN ELECTRONICS ENGINEERING.

DEPARTMENT OFELECTRICAL AND COMPUTER ENGINEERING
FACULTY OF ENGINEERING
AHMADU BELLO UNIVERSITY, ZARIA, NIGERIA.

DECEMBER, 2016

DECLARATION

Ideclare that the work in thisThesis entitled **"Design and Development of an Optimized Fluxgate Magnetometer for Improved Earth's Magnetic Field Studies"**has been carried out by me in the Department of Electrical and Computer Engineering. The information derived from the literaturehas been duly acknowledged in the text and a list of references provided. No part of this thesis was previously presented for another degree or diploma at this or any other Institution.

Waheed Olujide OLUYOMBO _____ _____

Name of StudentSignature Date

CERTIFICATION

This thesisentitled **"DESIGN AND DEVELOPMENT OF AN OPTIMIZED FLUXGATE MAGNETOMETER FOR IMPROVED EARTH'S MAGNETIC FIELD STUDIES"** by **Waheed Olujide OLUYOMBO** meets the regulations governing the award of the degree of Doctor of Philosophy (PhD)of theAhmadu Bello University, and is approved for its contribution to knowledge and literary presentation.

_____ _____

Chairman, Supervisory Committee Signature Date
(Dr. S. M. Sani)

_____ _____

Member, Supervisory Committee Signature Date
(Dr. A. M. S. Tekanyi)

_____ _____

Member, Supervisory Committee Signature Date
(Prof. B. Jimoh)

_____ _____

Head of Department Signature Date
(Dr. Y. Jibril)

_____ _____

Dean, School of Postgraduate Studies Signature Date
(Prof. K. Bala)

DEDICATION

This thesis is dedicated to Almighty Allah, the Unseen, the Sovereignty of Heaven and the Earth, the Owner of the day of judgment for His endless mercy and protection throughout the period of this research work.

ACKNOWLEDGEMENTS

I am grateful to Almighty Allah for the fulfillment of my desire for the completion of this thesis. Completing a PhD is truly a marathon event and I would not have been able to complete this journey without the aid and support of countless people over the past four years.

I would like to start by thanking my mom and dad,as well as my parents-in-law for all their trust, support, and solicitude on me. They have a huge part in every accomplishment I have made and they will always have a great place in my life.

My very special thanks goes to my supervisory team Chairman, Dr. S.M. Sani, who was always there when I needed help, got stuck, or had an idea and looking for someone to discuss it with. I am very grateful to him both for the many joyful moments we shared and for the moments when he converted burden into fun. I would never forget how he smoothly, efficiently, and valuably conducted meetings on this work, as well as the significant contributions he made in all discussions of this thesis. Indeed, I owe him a lot of appreciation for the work well done.

I owe a big thank you to the members of my supervisory team, Prof. B. Jimoh and Dr. A.M. S. Tekanyi fortheir intensive knowledge on their subject areas. Prof. B. Jimoh for been helpful anytime I needed either an opinion or a material and Dr. A.M.S. Tekanyifor the many fruitful discussions we had on this work. They created stress-free collaboration environment and their optimism had always encourage me during these years.

Numerous people deserve recognition for their contributions large and small, which made it possible for me to complete this thesis. I really appreciate Prof. M.B. Mu'azu for his constructive criticisms which not only better this research work, but also improved my theoretical knowledge on the subject. I also would like to extend my thanks to Prof. B. G. Bajoga, Dr. J. Yusuf, Dr. K. A. Abu-Bilal, Dr. A. D. Usman, and Dr. T. H. Sikiru who had generously given their time and expertise to better my work. I thank them for their contributions and valuable support. They created a conducive environment that made me realizedthat the University is the onlysuitable placefor operational research to discover new things and Ahmadu Bello University, Zaria is a better place to study due to their unforgettable contributions.

I am indebted to the Nigerian Government through the National Space Research and Development Agency (NASRDA) for providing me the study leave with pay in order to achieve this wonderful dream. The Director General, Prof. S. O. Mohammed,who has givenme the challenge to pursue this program.I am also grateful for the support of the Management and staff of NASRDA, particularly the Director of Engineering and Space Systems (ESS) Department, Dr.

O. A. Agboola, who introduced and guided me on Fluxgate Magnetometer subject which basically shaped my research interest. He also gave me the consideration to pursue this course and approved my application letter for study leave.The same sentiment goes tothe Advanced Computation Laboratory and Magnetometer Research Group, who shared their memories and experiences, especially, Prof. B. Rabiu, Dr. F. Ale,Dr. O. Shoyinka,and Engr. E.A. Daodu for their endless help.

I wish to express my deepest gratitude to Mrs. Patricia Olubunmi FolukeEtteh for her unfailing love and unforgettable support.

The support, technical experience, and goodwill of the Departmentaltechnical staff have minimized the hard times of the long equipment setup hours during this study. I would like to thank especially Engr. F.O. Sadiku, Engr. M.A. Ogbole, Engr. S.M. Aminu, Mr. A. Kabiru, Mr. A. Buhari,Mr.M. Suleiman, Mr. A.A. Sadiq, Mr. T. Abdullahi and Mrs. M. A. Prudencefor being very helpful anytime I needed either an opinion or material in the Telecommunications, ETAP, Computer, and Power Laboratories. They created a favourable environment for research and discussions to discover many new things, not only on this subject area but even personal issues.

I would also like to thank Mrs. M. A. Aiyejumo, Mr.L. Durojaiye, Engr. T. Ajayi, Engr. B. O. Sadiq, and Mr. A. Olaniyanfor their friendship and support as well asDr. K. Bello for his unending help and valuable friendship, Dr. A. Oyetunji for his motivation and advice, Mr. O.M. Adegboyega and Mr. S. Ogunjinmi for their prayers throughout these years.

I would also like to sincerely thank all the members of my wonderful family, particularlyDr. R. Oluyombo, Mr. and Mrs. Hammed, Dotun, Barrister S. Oluyombo, Banke, Iyabo, Tolulope and Bolaji Oluyombo for their endless support and love throughout my education. Your thoughtfulness, friendship, and love had made it possible again.

I am eternally grateful for the patience, understanding, and encouragement of mybrothers-in-law and sisters-in-law,Adebayo Babatunde, Sadiat, Saheed, Muri and Hammedfor their love and support. I apologize to those whose names are not included here; this only means that you are closer to my heart than you are to my mind.

I really appreciate my lovely wife, Sherifat and children, Maryam, Khadijat, and Zainab who deserve the biggest hugs for their patience and support, which always gave me the confidence I needed during very difficult times. Without them, this course of research would have been much more difficult to achieve. You remain a fundamental pillar to our success and progress and only God will reward you abundantly.

ABSTRACT

This research work was centered on optimizing the Fluxgate Magnetometer Sensor (FMS)at reduced noise level and enhanced sensitivity. The FMS was developed using Manganese Zinc (MnZn) ferrite alloy different from the usual permalloy and amorphous alloy materials. The developed FMS using MnZn ferrite achieved reduced sensor dimensions with high sensitivity and reduced noise level, thus meeting the necessary requirements for the earth's magnetic field studies. However, the sensor was realized using MnZn ferrite ring core material, excitation and pick-up coils, and the interface electronic circuits.The performance of this designed and developed FMS was optimized using the modified Firefly Optimization Algorithm (FOA). The characteristics of the developed fluxgate sensors were modeled using the modified FOA and the matching between the excitation and detection circuits was then considered. Analysis was then carried out to determine the values of relevant parameters using modified FOA written in MATLAB program. The model yielded an accurate prediction of the sensitivity and noise level compared to the commonly used conventional Part-by-Part Optimization (PPO) and analytical optimization techniques.Three ring core FMS with different diameters (14 mm and 10 mm) were constructed based on the PPO technique while 12 mm ring core was constructed based on the FOA technique. Experiments were employed to validate the PPO and the FOA techniques. The sensitivity and noise of the 12 mm ring core external diameter FOA sensor were 64.04mV/μT and 4.94pT/√Hz at 1 Hz in the range of ±75μT, while the sensitivity and noise level of PPO sensor A with 14 mm ring core external diameter and PPO sensor B with 10 mm ring core external diameter were 34.31 mV/μT and 19.50 mV/μT with 12.34 pT/√Hz at 1 Hz and 72.22 pT/√Hz at 1 Hz, respectively in the range of ±75μT. The modified FOA-based sensor, therefore achieved the overall objectives of this research.

TABLE OF CONTENTS

CHAPTER THREE: MATERIALS AND METHODS

CHAPTER FOUR: RESULTS AND DISCUSSIONS

CHAPTER FIVE: CONCLUSION AND RECOMMENDATIONS

LIST OF FIGURES

LIST OF PLATES

LIST OF TABLES

LIST OF SYMBOLS

Acronym	Definition
A	Cross-sectional area
α	Step size factor
B	Magnetic flux density
β	Attractiveness of firefly
β_0	Maximum attractiveness
D	Demagnetizing factor
f	Frequency
γ	Absorption coefficient of light intensity
Φ	Magnetic flux
H	Magnetic field strength
I	Electrical current
I_0	Maximum brightness of firefly
k_B	Boltzmann constant
M	Magnetization
M_{sat}	Saturation magnetization
μ_0	Permeability of free space
μ_r	Relative permeability
μ_a	Apparent permeability
μ_{abs}	Absolute permeability
N	Number of turns in a coil
n	numbers of fireflies
S	Sensitivity
V	Voltage
ω	Angular velocity
χ	Susceptibility

CHAPTER ONE

INTRODUCTION

1.1 Background

There have been increasing demands for integration of a magnetic field sensor which can detect the magnitude and direction of the earth's magnetic field in complex electronic systems (Lv and Liu, 2014). Such a magnetic field sensing system will find application in low power mobile devices such as in terrestrial and space navigation systems including military detection, craft navigation, medical recognition, modern digital navigation, and non-destructive inspection (David *et al.,* 2010; Hsieh *et al.,* 2013). The aim of this research is to design and develop an optimized Fluxgate Magnetometer Sensor (FMS), which has a small size, high sensitivity, low noise, low power consumption and capable of detecting the magnitude and direction of the earth's magnetic field.

In order to optimize the performance of magnetometers, different optimization techniques for their structures and core materials had been developed. For example, the conventional approach was based on Part-by-Part Optimization (PPO) technique, which includes designing the sensor core first, then select the dimension of pick-up coil, and finally develop a low noise detection circuit. However, PPO technique is too slow, time consuming, and expensive (Grosz and Paperno, 2012). Another optimization technique for the magnetometer parameters proposed by Chen *et al.,* (2011) and Grosz *et al.,* (2011) was based on an analytical model, which was numerically solved to obtain improved large set of parameters such as volume and weight of pick-up coil, power consumption, and the noise of the signal conditioning circuit. However, the analytical optimization technique becomes unnecessarily complex when performing large number of numerical calculations to optimize the magnetometer, hence, introducing difficulty in interpreting the results obtained (Grosz and Paperno, 2012). Recently, optimization of Fluxgate Magnetometer Sensors (FMS) had been based on Finite

Element Method (FEM) by using simulation software such as ANSYS, FEMM, Flux 2D, and others. On the other hand, most of these tools could not offer the users the ability to fully express their optimization purposes by formulating the objective functions (Kim *et al.,* 2013).

Hence, the design of fluxgate magnetometers is typically a nonlinear multi-objective optimization problem. Different objectives often conflict with each other, and sometimes optimal magnetometer performance is not achieved. Metaheuristic algorithms are very powerful in dealing with non-linear multi-objective optimization problem (Yang, 2013). The multi-objective Firefly Optimization Algorithm (FOA) is one of the nature-inspired metaheuristic algorithms, which is capable of handling the design problems in electromagnetics with a large number of design variables and multiple objectives under complex nonlinear constraints (Yang, 2013). For instance, sensitivity and noise of a fluxgate magnetometer can be improved while the sensor core, pick-up coil, and detection circuit are minimized. The combined multi-objective FOA and systematic optimization approach is suggested to improve FMS's design in this work by simultaneously finding the dimensions and geometry of the sensor core, pick-up coil, and detection circuit in order to reduce its noise and increase its sensitivity.

FMS are commonly used magnetic field sensors for measuring DC or low frequency magnetic field vectors (Lu and Huang, 2015). FMS have very high sensitivity spans a wide range from 100 pT to 100 μT (Lv and Liu, 2013), low noise, small size, small power requirements, and high temperature stability (Frydrych *et al.,* 2014). Moreover, the advancements in magnetic materials which form the heart of FMS and characterize their sensitivity, noise level, and linearity range responsible for their popularity among other competitive magnetic field sensors (Can and Topal, 2015). These make them one of the magnetic field sensors that still attract the attention of many researchers because of their wide applications (Todaro *et al.,* 2012) in space research and navigation systems (Indrasari *et al.,*

2012), particularly in Earth's magnetic field exploration surveys (Kim *et al.*, 2013; Lv and Liu, 2014).

Magnetic field sensors for low field strength (less than 1mT) and low frequency (less than 1 kHz) magnetic field (typically for Earth's magnetic field studies) include Anisotropic-Magneto-Resistance (AMR), fluxgate, Giant Magneto-Impedance (GMI), and Giant Magneto-Resistance (GMR) sensors (Coillot *et al.*, 2013; He and Shiwa, 2014; Tseng *et al.*, 2014; Lu and Huang, 2015). Traditional FMS consist of ferromagnetic core, wire-wound excitation and pick-up coils (Tseng *et al.*, 2014). They possess low noise, high sensitivity, and good sensing accuracy. However, when compared to other competitive magnetic sensors such as MI sensors and MR sensors, including AMR and GMR, traditional FMS experience bulky volume due to wire-wound coils, higher power consumption and lower integration capability (Leepattarapongpan *et al.*, 2014; Tseng *et al.*, 2014; Lu and Huang, 2015). As a result of the evolution of system miniaturization, the recent progress in miniature FMS using PCB and magnetic on Silicon fluxgate (coils replaced with metallic layers and layers interconnections) has been promising (Lu and Huang, 2015). However, they have limitations on the availability of space, total number of metallic layers, and total number of coil turns which result in higher noise level and lower sensitivity level of the sensors. FMS are employed in military detection, craft navigation, medical recognition, modern digital navigation, and non-destructive inspection (David *et al.*, 2010).

The sensitivity and noise level of FMS depend on the number of sensor windings, core size and the relative permeability of the core material (Jeng *et al.*, 2012; Lv and Liu, 2013). The use of core material causes demagnetization that influences the magnitude of the sensor voltage (Kirchhoff and Buttgenbach, 2010; Coillot *et al.*, 2013). Generally, core material is a material that can magnetize with very high permeability ($\mu_r \sim 10^5$) (Li and Ren, 2014), low coercivity, and saturation magnetic induction at 550 mT (Tumanski, 2013). Because of low

power losses of the ferrite alloy, early fluxgate magnetometers were assembled with Ferrite as magnetic core material (Musmann and Afanassiev, 2010). However, ferrite-based fluxgate sensors exhibit poor sensor performance because of its low permeability (Tumanski, 2013). Due to high permeability of the NiFe Permalloy, most of the prior literature focused on Permalloy as the magnetic core (He and Shiwa, 2014). Still, the high saturation magnetic flux density and low resistance (Kirchhoff and Buttgenbach, 2010; Lu *et al.*, 2014) of iron-nickel causes the emergence of Co-based amorphous alloy. The Co-based amorphous alloy soft magnetic material becomes an ideal substitute for Permalloy due to its high permeability, low coercivity, good temperature, and aging stability (Frydrych *et al.*, 2014). Therefore, it is widely used in the production of the fluxgate sensors (Tumanski, 2011; Matandirontya *et al.*, 2013).

The general electronics requirements for the fluxgate sensor include the drive electronics and the sense electronics (Can and Topal, 2015). Good results for driving the fluxgate sensor core can be obtained with a square wave and this is easier to generate than a sine wave, so it commonly used for fluxgate sensor excitation. Generation of square wave excitation together with a second harmonic (2f) reference frequency can be accomplished by means of a few discrete logic devices or microcontroller as an alternative. The sense electronics is usually called the sensor signal conditioning. After the information about the external magnetic field is measured by a sensor, it must be changed to a form appropriate for input into the Analog to Digital Converter (ADC) or data acquisition system. In most applications this means changing the sensors input to a voltage, modifying the sensors dynamic range to maximize the accuracy of the ADC or data acquisition system, removing unwanted signals, and limiting the sensor's spectrum.

The objectives of the research are to analyze the proposed FMS by analytical model equations and computer simulations, fabricate prototype FMS using traditional wire-wound

excitation and pick-up coils, and characterize the FMS by series of experiments. In addition, comprehensive characterizations such as sensitivity investigation, field noise spectra density, and Direct Current (DC) or low frequency magnetic field measurement, will also be verified.

1.2 Motivation

Recently, optimization of fluxgate magnetometer performance is based on Part-by-Part Optimization (PPO) and analytical optimization techniques. However, PPO technique is difficult, slow, time consuming, expensive, and does not produce optimal magnetometer performance while the complexity of analytical optimization technique when performing large number of numerical calculations introduces difficulty in interpreting the results obtained.

Hence, a multi-objective FOA and systematic optimization approach for improving the design of FMS in this research by simultaneously optimizing the sensitivity and noise of a FMS while the sensor core, pick-up coil, and detection circuit are minimized is suggested in this research.

1.3 Problem Statement

The design of fluxgate magnetometers is typically a nonlinear multi-objective optimization problem. Different objectives often conflict with each other (Can and Topal, 2015), and sometimes an optimal magnetometer performance is difficult to achieve (Grosz and Paperno, 2012). The sensitivity of the sensor decreases with an increase of noise level while trying to reduce the sensor dimension (Can and Topal, 2015).

Different optimization techniques had been developed for the structures and core materials of FMS. For instance, the conventional approach was based on Part-by-Part Optimization (PPO) technique. However, PPO technique is difficult, slow, time consuming, expensive, and does not produce optimal magnetometer performance (Grosz and Paperno, 2012). Another, optimization technique for the magnetometer parameters was based on an analytical model,

which was numerically solved to obtain an improved large set of parameters such as volume and weight of pick-up coil, power consumption, and the noise of the detection circuit. However, the analytical optimization technique becomes unnecessarily complex when performing large number of numerical calculations to optimize the magnetometer, hence introducing difficulty in interpreting the results obtained (Grosz and Paperno, 2012).

Hence, there is need for a systematic optimization approach for FMS design to find its optimum performance. The combined modified multi-objective FOA and systematic optimization approach is suggested to improve FMS's design in this research by simultaneously optimizing the sensitivity and noise of a FMS while the sensor core, pick-up coil, and detection circuit are minimized. Such a multi-objective optimization algorithm is powerful in dealing with design problems in electro-magnetics with a large number of design variables and multiple objectives under complex nonlinear constraints. Therefore, this research proposes such an algorithm as a tool for optimizing the design of a ring core parallel-type FMS.

1.4 Significant Contributions of the Research

Significant contributions achieved from this research work are as follows:

1. The developed model allowed improved sensitivity of 86.65%, reduction of noise level by 59.97% while still keeping the sensor size small by 14.29%, when compared to the conventional PPO sensors.
2. In addition to the simplicity of FMS fabrication utilizing a traditional wire-wound technology, the modified FOA model yielded a relatively more accurate prediction of the sensitivity and noise level, compared to the commonly used PPO and analytical optimization techniques by other researchers, the improved sensitivity of a factor of 5.6, reduced noise level of 50.6%, and reduced sensor size of 40% had been achieved.

3. The availability of materials for the modified FOA sensor was very easy while the manufacturing process follow smooth patterns. This fact allows the adoption of simplified 10-step processes only, rather than 20-step processes during the fabrication process, which improved the overall manufacturing efforts of the FMS by 50%.

1.5 Research Aim and Objectives

The aim of this research is to develop an optimized fluxgate magnetometer to achieve improved earth's magnetic field studies. In order to achieve the proposed aim of the research, the following objectives were performed:

i. Optimize the design of the proposed FMS that requires reduced noise and enhanced sensitivity, and protected Helmholtz coil needed for characterizing the developed FMS using analytical model equations and computer simulations.
ii. Fabricate different FMS using Manganese Zinc (MnZn) ferrite alloy as the magnetic core material and the Helmholtz coils based on traditional technology with wire-wound excitation and pick-up coils.
iii. Develop interface electronics circuits which can reduce the noise and increase the sensitivity of the entire fluxgate sensor system.
iv. Characterize the developed fluxgate magnetometer sensors using magnetic fields.
v. Compare the performance of the developed optimized fluxgate magnetometer.

1.6 Methodology

In order to achieve the objectives of this research, the following methodology was adopted in carrying out the research:

1. Determination of the appropriate commercial-off-the-shelf MnZn ferrite ring core by considering critical parameters such as high initial magnetic permeability, lower saturation flux density, and high excitation frequency of the magnetic material.
2. Analyze the magnetic field distribution and excitation current needed to saturate the ferromagnetic core material by using three dimensional (3D) ANSYS electromagnetic software tool.
3. Designing the FMS based on traditional technology with wire-wound excitation and pick-up coils to achieve low noise and high sensitivity, as well as use the Helmholtz coils to generate uniform magnetic field by employing analytical model equations.
4. Optimizing the design of a fluxgate sensor and Helmholtz coils using FOA in a Matlab environment to simultaneously find the dimensions and geometry of the sensor core, pick-up coil, and detection circuit elements.
5. Fabrication of two sensors (A and B) with different dimensions based on the PPO analytical model equations results and one FOA fluxgate sensor and Helmholtz coils based on the FOA design results for their performance comparison.
6. Implementation of the ferro-resonance excitation circuit and the detection circuit based on the parametric amplification mode (the process of transferring maximum energy between the excitation and the detection circuit) as well as the characterization of the Helmholtz coils to verify the optimization design results and research aim.
7. Evaluation of the performance responses of the sensors pick-up coil without detection circuit by moving a magnetic object around the sensor and also by imposing the magnetic field generated from the developed Helmholtz coils and in conjunction with the calibrated magnetometer.
8. Measurement of sensitivity and noise effects of fabricated sensors using the magnetic field of the Helmholtz coils and detection circuit, as well as measurement of magnetic

field at different locations to obtain the total earth's magnetic field intensity for each location for comparison with the IGRF standard values.

1.7 Organization of the Thesis

In Chapter One of this thesis, the general introduction has been presented. The statement of the research problem followed by the limitations of research, significant of the study as well as the aim and objectives together with the methodology used to achieve the set aim and objectives are also given in detail. The rests of the thesis are organized as follows: Chapter Two is on the pertinent fundamental concepts of FMS and detailed review of the relevant literature is presented. Chapter Three describes the materials used and the methodology adopted in achieving the set objectives. The results obtained were analyzed and discussed in Chapter Four. Chapter Five includes the conclusion and the recommendations for further works. At the end of the thesis, the references and Appendices were also provided.

CHAPTER TWO

LITERATURE REVIEW

2.1 Introduction

In this chapter, magnetic field sensors are reviewed with respect to the sensitivity, noise, power consumption, and physical size. This chapter is divided into two sections. The

fundamental concepts relevant to the thesis are discussed in the first section while similar works reviewed are presented in the second section.

2.2 Review of Fundamental Concepts

In this section, the fundamental concepts surrounding this research work are presented, which include the definition of pertinent terms and other relevant information related to the magnetic field sensors.

2.2.1 Overview of Earth's Magnetic Field and Magnetic Storm

The earth has a varying magnetic field which comprised of an intense radiation and plasma zones, primarily due to the action of the charged particles of the solar rays impinging on the field (Waheed and Rehman, 2011; Mann *et al.,* 2011). The maximum magnetic field that the magnetic field sensor can experience in space is about ±60000nT (Lu and Huang, 2015). Figure 2.1 shows the magnetic field model with respect to latitude and longitude of the earth.

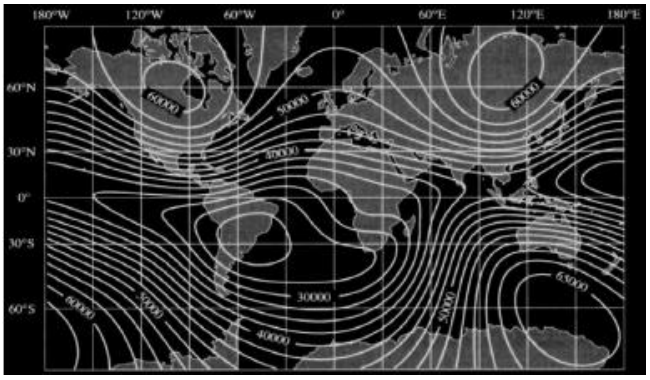

Figure 2.1: The Variations of the Magnetic Field of the Earth (Waheed and Rehman, 2011).

Earth's magnetic field monitoring is essential in order to predict the occurrence of the major disturbances on the solar terrestrial environment (Yousif, 2011). The major disturbances on the solar terrestrial system include the geomagnetic storms, geomagnetic sub-storms, sudden commencement, and geomagnetic pulsations (Miles *et al.,* 2013; Matsuoka *et al.,* 2013). These disturbances reach the earth from the solar terrestrial system through the magnetosphere (Miles *et al.,* 2013).

The earth magnetosphere is formed as a result of the magnetic field mapping together with the close intense of plasma (plasmasphere and other plasma regions) and interplanetary magnetic field (the nearby solar terrestrial environment) (Yousif, 2011; Trishchenko and Garand, 2012; Matsuoka *et al.*, 2013).

Magnetic storm (also called geomagnetic storm) is a worldwide disturbance of geomagnetic field (earth's magnetic field). Magnetic storms can cause significant damage across the world with a single event (Baumjohann *et al.*, 2010). Severe geomagnetic storms can disrupt the operation of electricity power transmission systems and critical space-based infrastructures. A geomagnetic storm that damages the electric power grid would not only affect the energy sector but also the transportation, communications, banking, and finance sectors of a region affected by the geomagnetic storm.

Magnetometer is used to monitor and record the earth's magnetic field data at the geomagnetic observatory. It is also used to measure the three components of the field such as the horizontal component (H), the declination component (D), and the downward component (Z). Earth's magnetic field data from ground-based magnetometer observatories are important for studies related to geomagnetic storm. The absence of earth's magnetic field data observatories results in a complex mysterious phenomena of the geomagnetic storm and remains as unexplained one. Fluxgate magnetometer is contributing to the ongoing extensive research work dedicated to explanation of some of the complex phenomena related to the geomagnetic storm and solar terrestrial system (Benkhoff *et al.*, 2010).

2.2.2 Overview of Fluxgate Magnetometers

Fluxgate magnetometers are commonly used for measuring Direct Current (DC) (Lv and Liu, 2013) or low frequency Alternating Current (AC) magnetic fields (He and Shiwa, 2014; Can and Topal, 2015). Typically, fluxgate sensors work on the second harmonic principle (Lv and Liu, 2013) and close-loop configuration (Matsuoka *et al.*, 2013). When the excitation current,

I_{exc} is applied to the excitation coil, a lock-in amplifier (phase sensitive detector and amplifier) is used to obtain the second harmonic of the induced voltage, E_{sec} in the output of the pick-up coil, (measuring coil) of the fluxgate (Miles *et al.*, 2013; Lv and Liu, 2014). The amplitude of the induced second harmonic signal in the pick-up coil is proportional to the magnetic field (H or H_{ext}) to be measured (Lv and Liu, 2013; Lu and Huang, 2015). In the conventional fluxgates sensor design, the output of the lock-in is low pass filtered to avoid high frequency noise and the output is used as feedback (Matsuoka *et al.*, 2013). This feedback improves the linearity of the response and increases the measurement range (Lu and Huang, 2015). The magnetic field range of fluxgate magnetometer is suitable for measuring earth's magnetic field and a resolution on the order of about 10 pT (Korepanov and Marusenkov, 2012; Tumanski, 2013).

The earliest investigation of outer space environment (Korepanov and Marusenkov, 2012) revealed the importance of research of magnetic fields in the solar system (Matsuoka *et al.*, 2013). Earth's magnetic field was found to be important for terrestrial life because it forms a protective bubble with distinct regions, called magnetosphere and detects charged particle from the sun and other extraterrestrial sources (Matandirotya *et al.*, 2013). Traditionally, FMS has been used for geophysical measurements, space research (Indrasari *et al.*, 2012), identification, location and compasses, measurements of electric current and non-destructive measurements (Korepanov and Marusenkov, 2012; Lu and Huang, 2015).

Fluxgate magnetic sensors configurations are classified according to the direction of the excitation field (H_{exc}) with respect to the external magnetic field (H) to be measured (Lv and Liu, 2013). Two main configurations known are the orthogonal type configuration and parallel type configuration (Zorlu *et al.*, 2010). Figure 2.2 shows the basic orthogonal and parallel fluxgate configurations. The orthogonal fluxgate sensor (Figure 2.2(a)) has the

excitation magnetic field and external magnetic field perpendicular to each other (Weiss and Paperno, 2011).

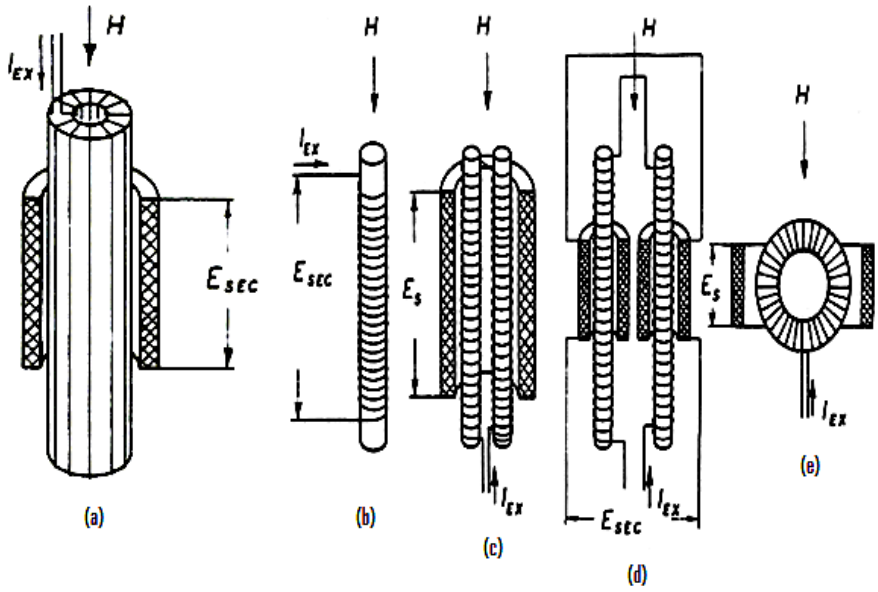

Figure 2.2: Orthogonal and Parallel Fluxgate Configurations (Ripka, 2001)

The orthogonal fluxgate configuration is similar to the ring core parallel type, with a tubular core and the excitation coil wound circumferentially around the core (Butta, 2012). Orthogonal fluxgate configuration is sensitive to the magnetic field along the length of the ferromagnetic core, and pick-up coil also wound diametrically around the core is used to detect the external magnetic field (Weiss and Paperno, 2011).

The most common type of fluxgate magnetometer is the parallel type configuration (Solorzano, 2013). In parallel type fluxgate magnetometer configuration (Figure 2.2(b-e)), the external magnetic field and the excitation magnetic field are in the same direction (Zorlu *et al.*, 2010). FMS parallel type configuration are also divided into broadly three categories, those employing rod cores geometry, ring cores geometry, and the combination of the rod and ring core geometries popularly called racetrack core geometry (Butta, 2012; Tumanski, 2013). The rod cores were the first to be developed from about 1930 onwards (Matsuoka *et al.*, 2013). The rod core type is the simplest of the parallel fluxgate configuration, which

contains a ferromagnetic rod core (Figure 2.2(b)) and two coils wound around the core (Ripka, 2010). One of the coils acts as the excitation coil which produces the excitation magnetic field to periodically saturate the core when certain magnitude and frequency of excitation current is applied through it, while the other coil acts as the pick-up coil to detect changes in the flux through the core. However, the excitation signal has large odd harmonics components at the pick-up coil output due to transformer effect between the excitation and pick-up coils, which makes it rarely used. (Eyal and Eugene, 2011).

In order to get rid of this odd harmonics at the output of pick-up coil, the double-rod core geometry (shown in Figures (2.2(c) and (d)) is employed (Ripka, 2001). The two cores are both magnetized in opposite direction in order to cancel the mutual inductance between the excitation and pick-up coils. The main advantages of the double-rod sensors are the high sensitivity and resistance to orthogonal fields (Ripka, 2001). However, the double rod cores sensors suffer from noise, temperature and aging stability than the closed cores sensors. In addition, difficulty in core saturation which results in increased power consumption and susceptibility to perming effect errors (Ripka, 2001). The double-rod core geometry is also split into two types; the Vaquier (Figure 2.2(c)) and Forster (Figure 2.2(d)) based (Suitella and Windarto, 2011). This fluxgate sensor type has two rod core elements with separate excitation coils, producing excitation field in opposite directions. The most commonly used of this type is in the case when both rod cores share a single pick-up coil (Figure 2.2(c)), for which the flux generated by the excitation coils is subtracted (Ripka, 2010). Saturation of the double-rod cores type fluxgate sensor is easier than the single-rod core fluxgate because the second core provides a high permeability return path for the excitation magnetic field (Ripka, 2010; Butta, 2012). However, the magnetic circuit for the excitation is still not completely closed (Ripka, 2001). A completely closed magnetic circuit provides closed magnetic path for

the excitation field, which allows much deeper saturation of the sensor core, which reduces the perming effect, hysteresis and sensor noise.

The ring core geometry shown in Figure 2.2(e) produces closed magnetic path for the excitation field (Ripka, 2010). The ring core geometry which appeared in the 1930s was not really developed until 1962 onward when it was rapidly accepted (Narod, 2014) and became a serious competitor to the rod core geometries (Matsuoka *et al.*, 2013; Can and Topal, 2015). In ring core fluxgate type, the excitation coil is wound circumferentially around a ring core. The pick-up coil is wound diametrically on the bobbin and is used to detect the magnetic field parallel to its plane. The ring core sensor has low sensitivity due to higher demagnetization factor. However, they are found to have low noise because of the balance of the core symmetry and the pick-up coil, uniform distribution of possible mechanical stress in the core, and the absence of the open ends which is often accompanied by regions of increased noise (Ripka, 2001).

Racetrack sensors can be regarded as hybrid core with a combination of rod and ring cores. A typical racetrack core is shown in Figure 2.3.

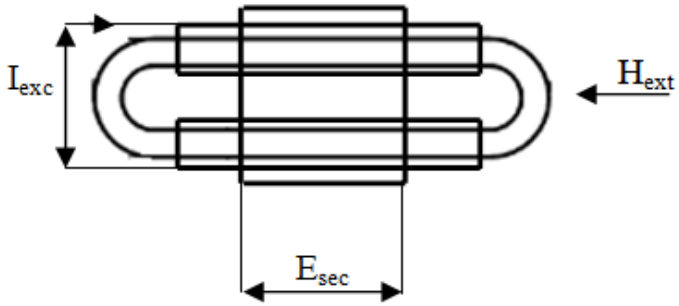

Figure 2.3: Racetrack Core Geometry.

Racetrack core based fluxgate sensors has lower demagnetization factor than the ring core, which results in increased sensitivity and high resistance to orthogonal fields (Butta, 2012). However, racetrack core sensor is susceptible to noise due to imbalance between the core symmetry and the pick-up coil (Ripka, 2010).

2.2.3 Principle of Operation of Fluxgate Magnetometers

The operation principle of FMS is based on the periodic saturation of a ferromagnetic core material (Zhang *et al.*, 2010; Solorzano, 2013). The permeability of the ferromagnetic material is modulated based on the *B-H* curve of the magnetic material (Suitella *et al.*, 2011), between the permeability of air μ_0 and the absolute permeability $\mu_0\mu_r$ of the magnetic material with a periodic excitation field at certain frequency (Ripka *et al.*, 2010; Bae *et al.*, 2013). Figure 2.4 shows the operation principle of parallel type configuration fluxgate magnetometer in ring and rod core geometries. A winding through which the excitation current is applied is placed around the core (Weiss *et al*, 2011; Bae *et al.*, 2013). The coils are wound so that the induced excitation fields are in opposite directions (Ripka, 2010). The excitation current must be large enough to drive the cores into saturation, typically, with currents larger in magnitude than theoretically necessary (Tumanski, 2013; Indrasari *et al*, 2012). The output signal is obtained from the pick-up coil winding that encircles the magnetic core.

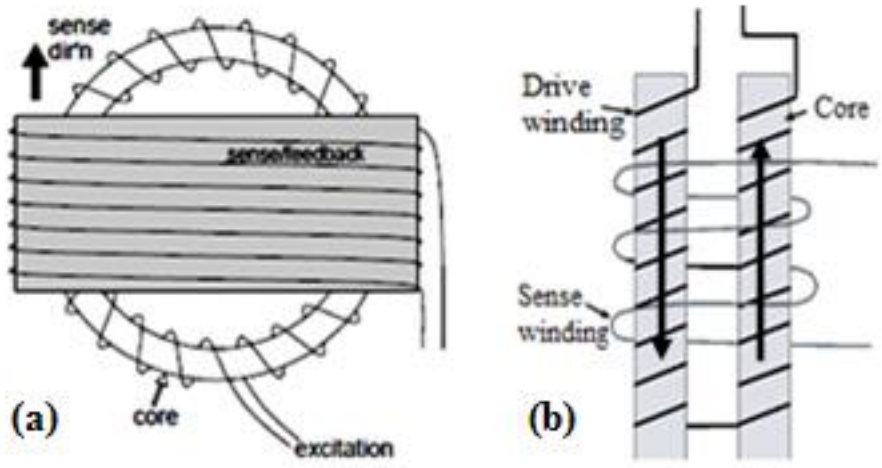

Figure 2.4: Fluxgate Sensor Architecture (Evans, 2006).

The name fluxgate is clearly derived from the action of the core gating flux 'in and out' of the pick-up coil (Butta, 2012). When the core is not saturated (the excitation current $I_{exc} = 0$), the core's relative permeability, μ_r, is maximum (Ripka, 2010). This concentrates the ambient field within the core (as shown in Figure 2.5(a)) and produces a magnetic flux, Φ, that is μ_r

times larger than the field in a vacuum, μ_0 (Tumanski, 2013). During the first half cycle, when the excitation current I_{exc} is fed into the excitation winding ($I_{exc} \neq 0$), it creates magnetic field, H_{exc} that is strong enough to saturate the core (Solorzano, 2013), the permeability becomes close to that of a vacuum, μ_0 and the field within the core collapses (Ripka, 2001) as shown in Figure 2.5(b).

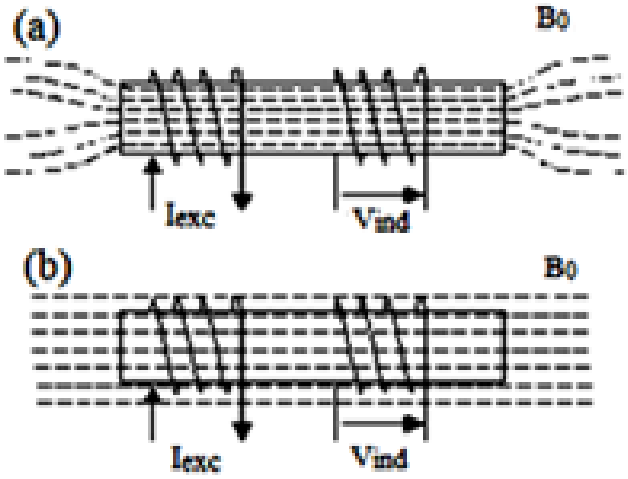

Figure 2.5: Fluxgate Sensor Principle, (a) Flux Recovery (b) Flux Collapse (Evans, 2006).

Figure 2.6 shows the excitation stages of fluxgate principle. The sensor core recovers during the second half cycle of the core excitation (excitation voltage shown in Figure 2.6(a) with resonance voltage in Figure 2.6(b)), only to collapse again when the core saturates (Evans, 2006). The pick-up coil, detects these flux changes, which occur at twice the frequency of the excitation signal, since there are two flux collapses during each cycle as shown in Figure 2.6(c) (Weiss *et al*, 2010). It can clearly be seen that the sense voltage is twice the frequency of the excitation signal.

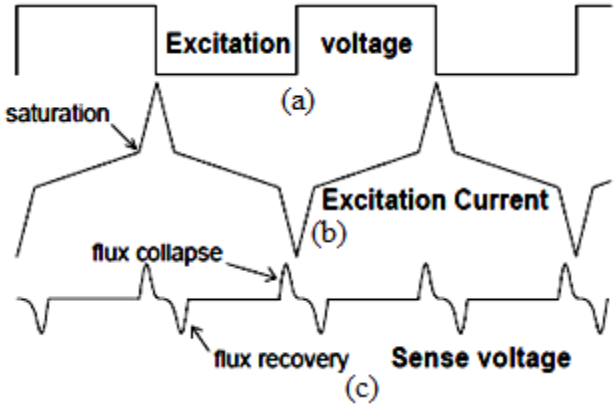

Figure 2.6: Fluxgate Sensor Waveform, (a) Excitation Voltage, (b) Excitation Current, and (c) Sense Voltage (Evans, 2006).

When a ferromagnetic core of cross-sectional area, A_c is caused to experience magnetic field *H(t)*, the induced magnetic flux ϕ_c in the core cross section is expressed as (Todaro *et al.*, 2012; Tumanski, 2013):

$$\phi_c(t) = \mu_0 \times \mu_r(t) \times H(t) \times A_c \tag{2.1}$$

The derivative of the induced magnetic flux ϕ_c with respect to time is given as (Todaro *et al.*, 2012):

$$\frac{d\phi_c(t)}{dt} = \mu_0 A_c \left[\mu_r(t) \times \frac{dH(t)}{dt} + \frac{d\mu_r(t)}{dt} \times H(t)\right] \tag{2.2}$$

The magnetic flux changes (equation 2.2) in the ferromagnetic core can be calculated by using the magnetic field *H(t)*, which is composed of the excitation magnetic field $H_{exc}(t)$ and the external magnetic field $H_{ext}(t)$ being measured.

In parallel fluxgate configuration, excitation field, $H_{exc}(t)$ and external field, $H_{ext}(t)$ are usually in the same direction (see Figure 2.2), hence *H(t)* is the scalar sum of the excitation magnetic field and external magnetic field (Tumanski, 2013; Todaro *et al.*, 2012; Ripka and Janosek, 2010). However, in orthogonal fluxgate configuration, scalar sum is not possible, because of the perpendicular nature of excitation and external magnetic fields (Todaro *et al.*, 2012). The total magnetic field *H(t)* inside the ferromagnetic core for parallel gating

mechanism can be expressed (Ripka, 2001; Zorlu, 2008; Todaro *et al.*, 2012; Solorzano, 2013) as:

$$H(t) = H_{exc}(t) + H_{ext} \tag{2.3}$$

Induced magnetic flux density inside the ferromagnetic core is expressed (Ripka, 2001) as:

$$\mu_r(H(t)) = \mu_r(H_{exc}(t) + H_{ext}) \tag{2.4}$$

Substituting Equation (2.3) and Equation (2.4) into Equation (2.2) we obtain (Ripka, 2001):

$$\frac{d\phi_c(t)}{dt} = \mu_0 A_c \left[\mu_r(t) \times \frac{dH_{exc}(t)}{dt} + \frac{d\mu_r(t)}{dt} \times (H_{exc}(t) + H_{ext})\right] \tag{2.5}$$

As a result of the magnetic flux change in the ferromagnetic core, a time varying induced voltage $V_{ind}(t)$ is obtained at the output of the pick-up coil having N turns of coil wound diametrically around the ferromagnetic core. The induced voltage $V_{ind}(t)$ across the pick-up coil is expressed as (Todaro *et al.*, 2012; Solorzano, 2013; Lu *et al.*, 2014; Lu and Huang, 2015) as:

$$V_{ind}(t) = -N\frac{d\phi_c(t)}{dt} \tag{2.6}$$

Therefore, the induced voltage across the pick-up coil by substituting equation (2.5) into equation (2.6) gives (Ripka, 2001; Zorlu, 2008):

$$V_{ind}(t) = -N\mu_0 A_c \left[\mu_r(t) \times \frac{dH_{exc}(t)}{dt} + \frac{d\mu_r(t)}{dt} \times (H_{exc}(t) + H_{ext})\right] \tag{2.7}$$

Equation (2.6) is usually the basic equation for any kind of fluxgate sensor operation. The ferromagnetic core is periodically driven deep in and out of saturation through the excitation coil. The strong nonlinear coupling due to core saturation results in harmonics of the excitation frequency in the pick-up coil. The amplitude of the even harmonics is proportional to the external magnetic field component parallel with the excitation magnetic field induced in the ferromagnetic core (Todaro *et al.*, 2012; Solorzano, 2013; Lu and Huang, 2015).

2.2.4 Classification of Magnetic Sensors and their Technologies

Magnetic field sensor is a transducer that converts magnetic field into electrical signal. Each sensor has specific characteristics that make it suitable for a given range of applications. There are different categories of magnetic field sensors with their approximate sensitivity ranges (Baschirotto *et al.,* 2010). In addition to the sensitivity, it is necessary to take into account the range of temperature, the sensor physical size, and its on-chip manufacturability (Lu *et al.,* 2011). Table 2.1 shows the classification of the various magnetic field sensors.

Table 2.1: Classification of Magnetic Field Sensors (Baschirotto *et al.,* 2010).

Magnetic sensor Technology	**Detectable Field Range (Tesla)**	
	From	**To**
Search Coil Magnetometer	10^{-12}	10^{1}
Optically Pumped Magnetometer	10^{-12}	10^{-4}
Nuclear Precision Magnetometer	10^{-11}	10^{-2}
SQUID Magnetometer	10^{-14}	10^{-8}
Hall Effect Magnetometer	10^{-4}	10^{2}
Fluxgate Magnetometer	10^{-11}	10^{-2}
Magneto-resistive Magnetometer	10^{-10}	10^{-2}
Magneto-diode	10^{-4}	10^{0}
Magneto-transistor	10^{-5}	10^{0}
Fibre Optic Magnetometer	10^{-11}	10^{-3}
Magneto-impedance Magnetometer	10^{-10}	10^{-4}

Magnetic fields less than 100 pT are very low and well below the earth's magnetic field (Baschirotto *et al.,* 2010; Huang and Lu, 2010). Sensors with a range of 10 μT to few micro-Tesla are considered earth's magnetic field sensors and sensors with sensitivity above 1 mT can be considered bias magnet field (high field) sensors (Baschirotto *et al.,* 2010).

For measuring the earth's magnetic field with sensors that are suitable for portable applications, the search coil, Hall-effect, SQUID, and magneto-resistance (MR) are available as well as the fluxgate magnetometer sensors. The sensitivity range for each technology depends on the detection circuits along with frequency response, physical size, and power applied to the sensors (Baschirotto *et al.,* 2010).

Search-coil or induction sensors are high sensitive and low power sensors, but their sensitivity reduces as the cross section area reduces, making miniaturization counterproductive. Because search-coils can detect AC magnetic field, it cannot detect a static magnetic field such as the Earth's magnetic field (Tumanski, 2013).

Semiconductor-based magnetic sensors, such as Hall-Effect sensors, magneto-transistors, and magneto-diodes, are very compact in size (Ripka and Janosek, 2010). The Hall-Effect sensor is widely used due to its low manufacturing cost and CMOS compatible (Ripka and Janosek, 2010; Rovati and Cattini, 2012). However, Hall-effect sensor usually suffer from large offset, temperature dependence and some sort of offset reduction or compensation method are often used (Ripka and Janosek, 2010; Rovati and Cattini, 2012).

The Superconducting Quantum Interference Device (SQUID) is the most sensitive low-field sensor (Tumanski, 2013). It is based on Brian J. Josephson's work on the point-contact junction designed to measure extremely low currents (Ripka, 2001). The SQUID sensor has three superconducting components: the SQUID ring itself, the radio-frequency coil, and the large antenna loop. All three must be cooled to a superconducting state (Ripka, 2001). The SQUID itself can be very small, but the need for liquid-helium coolant makes the complete instrument bulky and heavy (Han *et al.*, 2012).

Magneto-resistive sensors (MR) are high sensitivity (Ali *et al.*, 2012), low-cost manufacturing, and compact size sensors (Rovati and Cattini, 2012; Sun and Kosel, 2013). However, they have poor noise performance and linearity, combined with the narrow dynamic range which makes them unattractive and unsuitable for many applications requiring low noise (Rovati and Cattini, 2012; Sun and Kosel, 2013). Furthermore, their sensitivity is degraded as the power consumption is reduced (David *et al.*, 2010).

Fluxgate magnetometer is preferred with respect to other magnetic field sensors for many applications, because of their ruggedness and ability to survive in thermal, magnetic, and mechanical shocks environment (Rovati and Cattini, 2012). Moreover, fluxgate sensors perform better among the magnetic field sensors operating at room temperature, and in applications requiring low cost, high resolution, and low temperature (Rovati and Cattini, 2012).

The developments of FMS started in the 20th century (Velasco *et al.,* 2011) and were rapidly used for a number of applications during the Second World War such as in airborne magnetic surveys, submarine and UneXploded Ordinance (UXO) detection (Rovati and Cattini, 2012). Since then, numerous configurations and technologies have been developed, and several analytical models have been suggested (Marshall, 1967; Primdahl, 1970; Gordon and Brown, 1972).

In recent times, miniature FMS using PCB and CMOS-MEMS technologies were developed (Huang and Lu, 2010; Zorlu *et al.,* 2010; Lei *et al.,* 2012a; Lu *et al.,* 2011; Lu *et al.,* 2014). The PCB technology based FMS consist of a lithographically structured amorphous ferromagnetic core laminated between thin planar coil windings on epoxy boards gluing together using standard PCB techniques have been reported (Kirchhoff and Buttgenbach, 2010). However, in order to obtain the intrinsic properties of the amorphous material, a complicated process including mechanical polishing, wet chemical thinning, and thermal annealing are required (Lu *et al.,* 2012). CMOS-MEMS technology based FMS using spiral coils surrounding a ferromagnetic thin film that acts as a sensing core have been promising and were reported (Lu *et al.,* 2011; Lu *et al.,* 2012; Wu *et al.,* 2012; Lv and Liu, 2014). On the other hand, weak excitation fields generated by the planar coils and complicated MEMS manufacturing processes put MEMS sensors at disadvantages (Jeng *et al.,* 2012; Rovati and

Cattini, 2012). This is due to the limitations on the space, number of magnetic layers, and number of excitation and pick-up coils (Rovati and Cattini, 2012; Lv and Liu, 2014).

The traditional coils of fluxgate sensors, commonly wire-wound are usually characterized as high sensitivity and low noise; but, they are too bulky to meet the dimensional requirements of a miniature product (Huang *et al.,* 2010; Lu *et al.,* 2011; Lu and Huang, 2015). Generally, the miniaturization of the coils and integration of the ferromagnetic core are two major problems to overcome in the miniaturization of fluxgate sensors (David *et al.,* 2010; Zorlu *et al.,* 2010; Rovati and Cattini, 2012; Lu and Huang, 2015).

2.2.5 Fluxgate Sensor Electronics

Driving the excitation coil and detecting the pick-up coil signal require careful design of the excitation and detection electronics circuits (Baschirotto *et al.,* 2010; Velasco *et al.,* 2011). In most literatures, the excitation circuits for fluxgate sensors are typically based on a sinusoidal (Zorlu *et al.,* 2010), triangular (Baschirotto *et al.,* 2010) or pulsed excitation (Waheed and Rehman, 2011). The pulsed excitation is easier to generate than sinusoidal or triangular excitation (Ripka, 2001) and represents a trade-off between the sensitivity and power consumption (Cui, 2013). A pulsed excitation reduces power consumption at the expense of low sensitivity (Baschirotto *et al.,* 2010; Cui, 2013).

The block diagram of the entire fluxgate magnetometer is shown in Figure 2.7. To periodically saturate the ferromagnetic material, the excitation signal is fed into the excitation coil of the fluxgate sensor with a square excitation current waveform with excitation frequency *f*. The pick-up coil of the FMS detects the signal by the rising and falling edges of core magnetizing current (see Figure 2.6(c)). The pick-up coil is fed into a pre-amp with mild tuning to the second harmonic (*2f*) of the excitation frequency because the second harmonic fluxgate magnetometers produce the highest sensitivity and the lowest noise (Lu and Huang, 2015). Therefore, it is possible to extract the information on the external magnetic field by a

synchronous demodulation (Miles *et al.*, 2013). Demodulation is usually accomplished with a phase sensitive detector, typically, a CMOS analogue switch following the pre-amp (Tumanski, 2013).

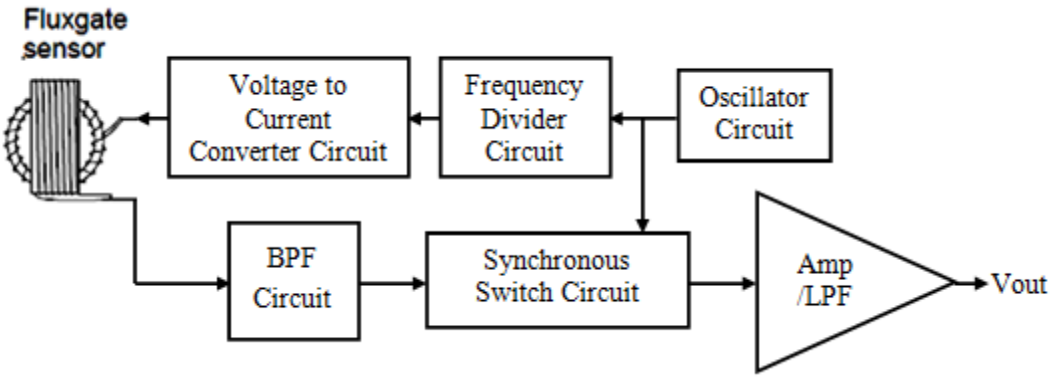

Figure 2.7: Typical Second Harmonic Demodulator Scheme

2.2.5.1 Square Wave Current Generator

Sinusoidal, triangular or square wave excitation signal can be used to energize the excitation coil of fluxgate sensors. To obtain the shape features of the hysteresis loop (magnetization curve), a triangular current is sufficient. Using a triangular wave also has the advantage that the output waveform should be relatively square (Karthik, 2013). However, the current waveform of a triangular excitation signal wanders, causing the magnetization field to wanders and the output is distorted and less useful. Sinusoidal excitation provides low noise signals, but consumes much power and is not easier to implement compared to square wave excitation circuit. Hence, square wave excitation is most suited for fluxgate sensors due to its lower power consumption and simplicity in implementation (Ripka, 2001).

Frequency generators circuits can be designed using different electronics components such as operational amplifier, transistors, hex inverters, and so on. The IC 4069 is a CMOS logic chip having six independent inverters. Connecting two hex inverters in series can make a non-inverting buffer. One of the advantages of the hex inverter is that the input-signal high level (V_{IH}) can exceed the V_{CC} supply voltage when these devices are used for logic-level

conversions. Hex inverters are intended for use as CMOS (Complementary Metal-Oxide Semiconductor) to Diode Transistor Logic/Transistor Transistor Logic (DTL/TTL) converters and can directly drive two DTL/TTL loads (Fairchild, 2002). The Maximum power supply must not exceed 18V (Fairchild, 2002). It is used for interfacing and to make simple square wave generators as shown in Figure 2.8.

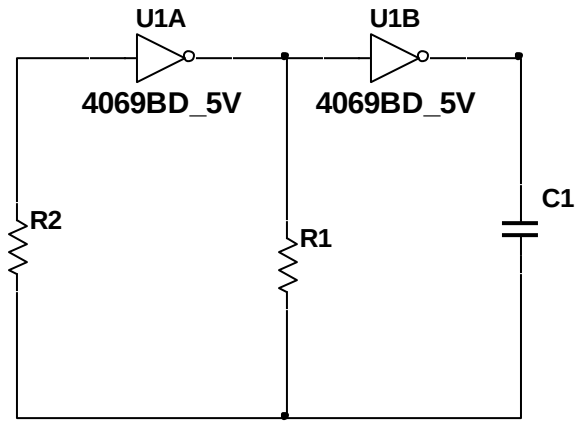

Figure 2.8: Schematic Diagram of a Square Wave Generator

The pulse generators can also produce a 50% duty cycle square wave. A duty cycle different from 50% could compromise the demodulation of the signals produced by the pick-up coil (Baschirotto *et al.,* 2005). The frequency determined by R_1 and C_1 (Fairchild, 2002) is:

$$F = \frac{1}{1.39 \times R_1 \times C_1} \tag{2.8}$$

Where F is the frequency in Hz, R_1 is the timing resistor in ohms and C_1 is the timing capacitor in Farad.

As shown in Figure 2.8, the hex inverter CMOS digital IC is IC 4069 Hex Inverting Buffer IC can be used to design a Square wave oscillator generator circuit diagram or Simple Pulse Generator circuits. The circuit uses a few components such as two resistors with R_1 used as timing resistor and a capacitor C_1 and consumes less power. A capacitor is a circuit element that stores charge. The total charge is proportional to voltage. The output frequency produced by the square wave oscillator depends on two components R1 and C1. Changing the values of

the resistor R1 and capacitor C1 will result in change of output frequency. The output frequency is relatively constant while the rate of change in frequency of the power supply voltage is less.

2.2.5.2 Frequency Divider

The circuit shown in Figure 2.9 is a frequency divider which is capable of dividing the input clock frequency by means of a certain factor. The Frequency divider circuit uses IC 4013, a dual D-type flip-flop which divides the incoming pulse frequency from the incoming square wave of Figure 2.8. The hex inverter IC (shown in Figure 2.8) is wired as a square wave oscillator and this forms the source of the clock pulse.

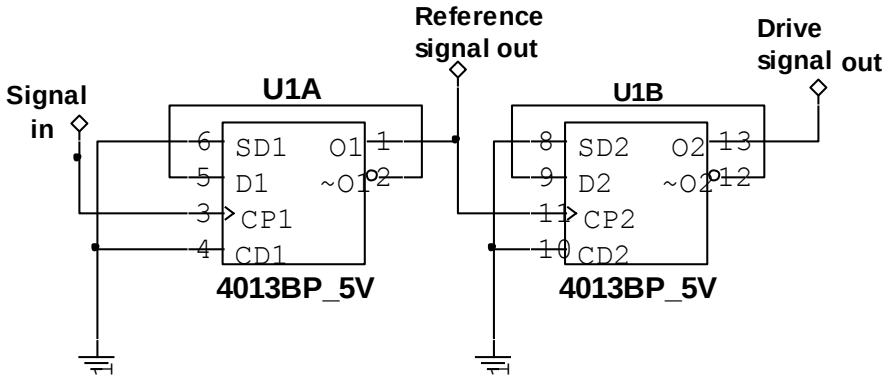

Figure 2.9: Schematic Diagram of Frequency Divider

IC 4013 is a dual D-type flip-flop consists of two flip flops which can be used in an independent manner (Fairchild, 2002). As shown in Figure 2.9, in a D Flip-Flop, D1 & D2 pins are meant for data input which can be either logic 1 or 0. CP1 and CP2 are the pins where the clock input for Flip Flop 1 & 2 are fed (Fairchild, 2002). This is of edge triggered type so that it switches output states to sudden changes in voltage levels. The SD1 and CD1 as well as SD2 and CD2 are Set and Reset pins of the respective Flip Flops (Fairchild, 2002). To wire IC 4013 as a Frequency divider, the complement pin (~Q) to the data input D1 of the flip flops. The feedback signal of the complement (~Q) pin to the data input divides the clock signal frequency by half. Connecting the next Flip flop in such a way gives a signal of F/4 of

the original frequency of the pulse obtained from the square wave oscillator. Thus we can obtain F/8, F/16 signals by connecting the Flips Flops in continuous sequence.

2.2.5.3 Voltage to Current Converter

The frequency divider output produce analog output voltage but the currents are weak and cannot be directly used to drive the magnetic core to saturation. The oscillator and the frequency divider can only produce a few tens of milli-amperes at most, while the sensor core requires many amperes. Hence, there is need for current amplification by using power transistors. Therefore, a complementary emitter-follower is commonly used for efficient bipolar current amplification. Figure 2.10 shows a low-noise class-AB power amplifier using NPN and PNP transistors Q1 and Q2 respectively. The two transistors Q1 and Q2 were configured as a complementary emitter-follower. There are many amplifier circuits suitable for voltage to current conversion in fluxgate design, but the class-AB amplifier provides sufficient current required for sensor core saturation (Karthik, 2013).

Class AB amplifier shown in Figure 2.10 is very similar to class B amplifiers, but their performance is improved by the addition of two diodes that eliminate the crossover region and allows both transistors to be turned on at the same time. The efficiency (around 50%) is not as high as class B because both transistors are turned on simultaneously, but accuracy is improved. It is the most commonly used voltage to current converter amplifier.

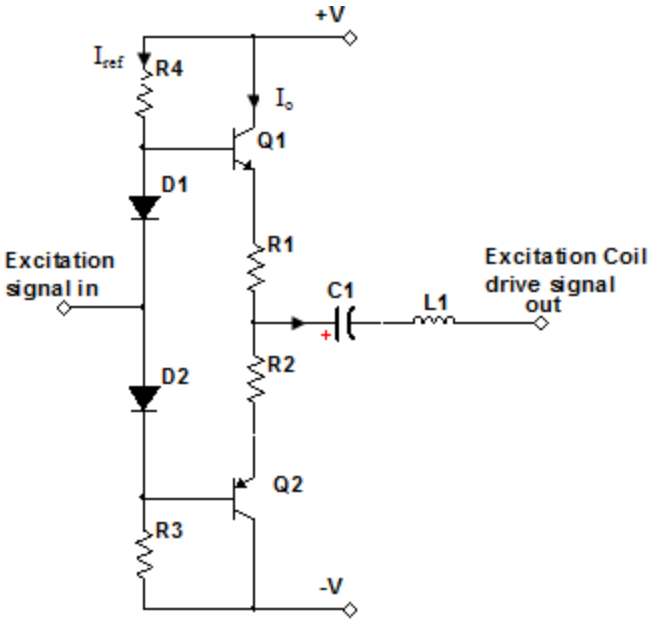

Figure 2.10: Schematic Diagram of a Voltage to Current Converter

As shown in Figure 2.10, resistor R4 and diode D1 biased the NPN transistor Q1 while D2 and R3 biased the transistor Q2. The values of the biasing resistors R3 and R4 are calculated as:

$$R_4 = \frac{V_{cc} - V_{be}}{I_{ref}} \tag{2.9}$$

Where R4 is a bias resistor and R3 is equal to R4. V_{cc} is the supplied voltage, V_{be} is the emitter-base voltage and I_{ref} is the transistor base bias current.

Resistors R1 and R2 are equal in values and set the operating current for the output of the transistors. The values of the emitter biasing resistors R1 and R2 are calculated as:

$$R_1 = \frac{V}{I_o} ln\left(\frac{I_{ref}}{I_o}\right) \tag{2.10}$$

Where R1 is an emitter bias resistor and R1 is equal to R2. V is the supplied voltage, I_o is the output current, and I_{ref} is the transistor base bias current.

The two diodes serve to bias the transistors and reduce the cross-over distortion that occurs when the input waveform crosses zero. Without the diodes, the oscillator output would have to swing 1.4V to turn one transistor on and then bring the other transistor off.

Connecting the excitation circuit to the excitation coil requires coupling capacitor that serves to isolate the AC signal from any DC bias voltages. In order for a coupling capacitor to operate effectively, it must have the right size. Capacitor C1 served to block the DC component of the current source from reaching the excitation resonant circuit. The equation to calculate the value of the coupling capacitor C_1 is:

$$C_1 = \frac{1}{3.2 f_{exc} R_{coil}} \tag{2.11}$$

Where C is the capacitance in Farads, and f_{exc} is the excitation signal frequency in Hertz. R_{coil} is the impedance on the load side of the capacitor which in this case is the excitation coil resistance.

As shown in Figure 2.10, when transistor Q1 is turned on, capacitor C3 is charged smoothly as the charging current is limited by inductor L1. The main function of the inductor L1 is to limit the current drawn from the source for the fluxgate excitation current. This was achieved by the use of a high impedance (larger than the fluxgate sensor) inductor, which operates in the non-saturated mode over part of the excitation period. In the non-saturated state, the high impedance of the inductor limits the current flowing from the source to the excitation circuit.

2.2.5.4 Detection Electronics

The pick-up coil of the fluxgate sensor detects the signal induced by the flux collapse (saturation) and flux recovery (de-saturation) of the core magnetizing current (Evans, 2006). This small induced voltage output signal of the pick-up coil was detected and it is compensated by amplifying and filtering the signal. The second harmonic component of the induced voltage across the pick-up coil is conditioned by using the electronics circuit shown in Figure 2.11.

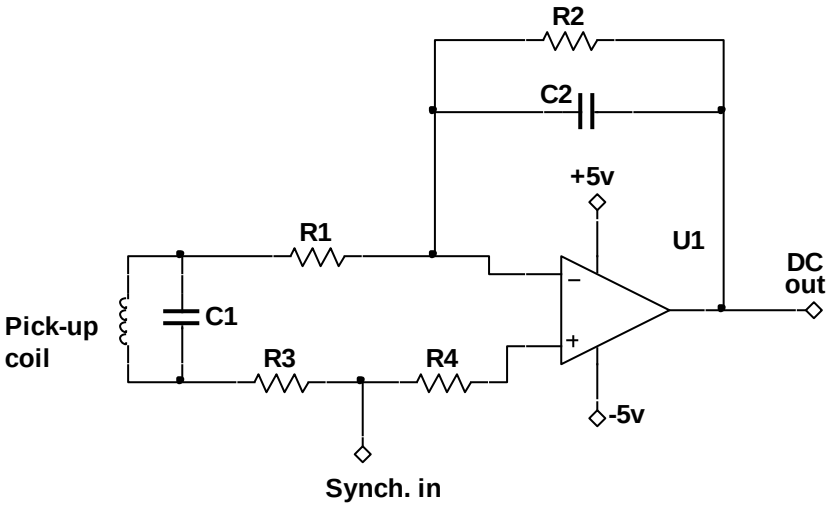

Figure 2.11: Schematic Diagram of Detection Electronic

The output voltage from the pick-up coil is usually small compared to the reference voltage of the Analog to Digital Converter (ADC). A low noise operational amplifier is needed to amplify the output voltage of the pick-up coil. As shown in Figure 2.11, at very low frequencies (within the cut-off frequency or frequency response of the amplifier), the capacitor C2 was an open circuit and the gain of the signal conditioning circuit was high, which made it acted as an amplifier. Likewise low frequency occurs when no current goes through the capacitor C2, so the voltage across the resistor R1 was near zero. The Low Pass transfer functions A(s) is (Kugelstadt, 2001):

$$H(s) = \frac{-\frac{R_2}{R_1}}{1 + \omega_c R_2 C_2 s} \tag{2.12}$$

Where *H*(s) is the amplifier transfer function, R_1 and R_2 are resistors, C_2 is the capacitor, *s* is the complex frequency variable, and ω_c is the -3dB frequency.

The negative sign indicates that the inverting amplifier generates a 180^o phase shift from the filter input to the output. The amplifier Direct Current (dc) gain A_o is calculated as (Kugelstadt, 2001):

$$A_o = -\frac{R_2}{R_1} \tag{2.13}$$

Where A_o is the dc pass band gain.

$$a_1 = \omega_c R_2 C_2 \tag{2.14}$$

Where a_1 is the filter coefficient. The filter coefficient a_1 is taken from the coefficient tables.

To dimension the circuit, the corner frequency (f_c), the dc gain (A_o), and capacitor C_2 are specified. Then resistors R_1 and R_2 are calculated as (Kugelstadt, 2001):

$$R_2 = \frac{a_1}{2\pi f_c C_2} \tag{2.15}$$

$$R_1 = -\frac{R_2}{A_o} \tag{2.16}$$

In order to evaluate the performance of FMS associated with the detection circuit, the frequency response of FMS detection amplifier is computed as (Han *et al.*, 2012; Chen *et al.*, 2015):

$$V_o = \frac{R_2}{R_1} \cdot \frac{V_{pick-up\ coil}}{1 + \left(\frac{L_w + R_2 C_2}{R_1}\right) j\omega - \frac{R_2}{(R_1)} . L_w C_2 \omega^2} \tag{2.17}$$

Where, $R_z = R_w + R_g$, R_w is the pick-up coil winding resistance, L_w is the pick-up coil inductance, C_f is the amplifier feedback capacitor, R_f is the amplifier feedback resistor.

2.2.5.5 Synchronization Switch

Figure 2.12 shows the main section of the synchronization switch which uses a PNP transistor and CD4066 quad analog switch low off-set. There are several other methods of fluxgate signal synchronization (such as lock-in amplifier method) but the complexity and cost of the circuit put them at disadvantage.

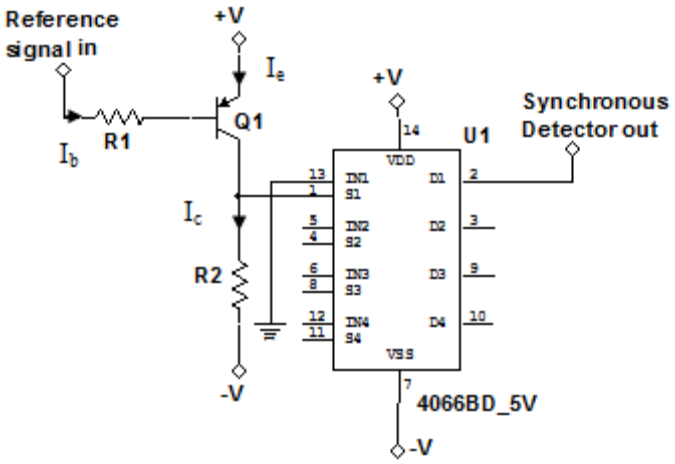

Figure 2.12: Synchronization Switch Circuit Diagram

The CD4066 could be used as a switch due to its low charge injection which makes it avoid further offset problems. To cause the base current to flow in a PNP transistor, the base needs to be more negative than the emitter (current must leave the base) by approx 0.7 volts for a silicon device or 0.3 volts for a germanium device with the formulas used to calculate the base current, base resistor, and the load resistor for a given transistor is given as:

Transistor base current is

$$I_b = \frac{I_c}{\beta} \tag{2.18}$$

The value of the input resistor is

$$R_1 = \frac{V_{ref} - V_{be}}{I_b} \tag{2.19}$$

The value of load resistor is

$$R_2 = \frac{+V}{I_c} ln\left(\frac{I_b}{I_c}\right) \tag{2.20}$$

Where I_b is the transistor base current, I_c is the transistor collector current, β is the transistor dc gain, R_1 is the base resistor, R_2 is the load resistor, V_{ref} is reference signal input voltage, V_{be} is the emitter-base voltage, +V is the supplied voltage.

The output of the transistor is being fed to the control pin (pin 1) of the analog switch. This switch will be turned on and off at the rate of the reference frequency being used in fluxgate sensor design.

2.2.5.6 Ferro-resonance Excitation Drive and Parametric Amplification

The sensitivity and stability of fluxgate sensor could be achieved by employing the effective combination of ferro-resonance mode of excitation and parametric amplification (Cao *et al.*, 2011). Ferro-resonance excitation mode involves connecting a shunt capacitance in parallel with excitation coil (tuned excitation coil) of fluxgate sensor to achieve a non-linear oscillator and pick-up coil (tuned pick-up coil) of the fluxgate sensor to achieve high sensor sensitivity (Musmann & Afanassiev, 2010). Figure 2.13 shows a typical schematic of ferro-resonance drive mode and parametric amplification of fluxgate sensor.

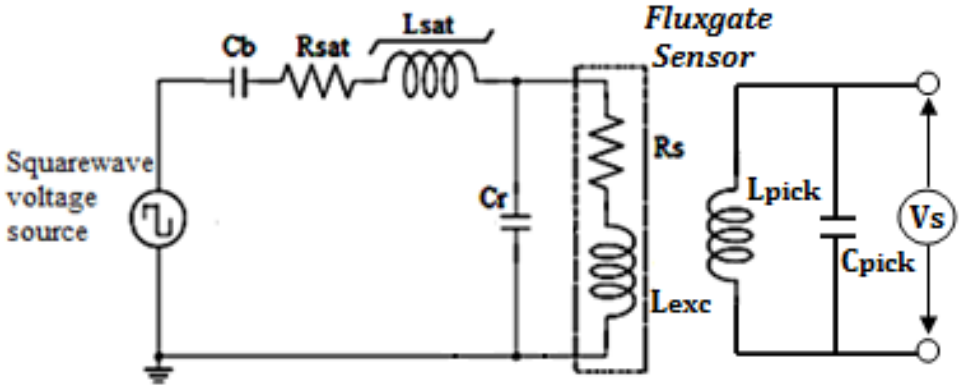

Figure 2.13: Parallel Resonant Excitation Circuit (Musmann and Afanassiev, 2010).

In ferro-resonance excitation circuit, a resistor R_{sat}, which plays the role of nonlinear inductance, is connected in series with the parallel connection of excitation coil, L_{exc} and resonance capacitor, C_r. As seen in Figure 2.13, when the core is not saturated, the excitation coil inductance is high, and the excitation current passes through the resistor R_{sat} while the capacitor charges. When the core is saturated, excitation coil inductance drops suddenly and the inductance is close to the value of excitation coil inductance in the absence of ferromagnetic core material (Musmann and Afanassiev, 2010). The induced charge on the

excitation parallel capacitor during negative magnetization produces a discharge current within a small time interval. After core saturation, the excitation coil inductance, L_{exc} and ohmic resistance, R_s become small, thereby, the capacitor voltage and discharge current become high (Musmann and Afanassiev, 2010). Therefore, the period of core saturation is a function of the magnitude of excitation coil inductance and parallel capacitor during core magnetization (David *et al.*, 2010).

The presence of capacitor, C_{pick} in the output, V_s, of the pick-up coil, L_{pick} combined with ferro-resonance excitation mode is referred to as parametric amplification (Ripka *et al*, 2010; Cao *et al.*, 2011). Tuning the fluxgate sensor output is useful because, it increases the sensitivity of the sensor, especially when the number of pick-up coil is small (Cao *et al.*, 2011). Pick-up coil output is tuned to the second harmonic of the excitation frequency in order to attenuate all other signals (Lv and Liu, 2014).

2.2.6 Fluxgate Magnetometer Core Materials

Ferromagnetic cores of the fluxgate sensors are generally made of materials with high permeability, low coercivity, low magnetostriction, and high electrical resistivity (Lv and Liu, 2014). Till today, many different materials have been used as ferromagnetic core for fluxgate sensors (David *et al.*, 2010). The fluxgate core material can be ferrite or tape wound cores, but the best results are obtained by custom winding the cores using Permalloy or amorphous material (Tumanski, 2011). Ferrite material is easy to manufacture when compared to those well performing materials such as permalloy and amorphous materials (Ripka, 2001; Wu *et al.*, 2012). However, ferrites have low sensitivity performance and are rarely used in the production of fluxgate sensor (Zorlu, 2008). Due to high permeability and low magnetostriction, permalloy in the form of a thin tape is the material traditionally used for the sensor core (Zorlu, *et al.*, 2010). Electroplated layers of ferrites (Primdahl, 1979) and FeNi based alloys (Lv and Liu, 2014) have also been used as the core material. After 1980's

amorphous magnetic materials, which are also called magnetic glasses, became popular due to their superior magnetic properties (David *et al.,* 2010). Magnetic glasses and electroplated ferromagnetic layers became widely known with the trend of miniaturizing the sensors, and producing them together with the signal conditioning electronics (He and Shiwa, 2014).

Previously, most research conducted on fluxgate sensors demonstrated that the performance of the sensor is majorly based on the sensor's ferromagnetic core (David *et al.,* 2010; Ripka *et al.,* 2010; He and Shiwa, 2014; Lv and Liu, 2014). For the best optimization of the fluxgate sensor design, the core material should be chosen carefully as the sensor performance depends on the geometric and magnetic properties of the magnetic core material, output signal processing type, the excitation frequency and temperature range requirement (David *et al.,* 2010; Lv and Liu, 2014).

2.2.7 Magnetization Behavior of Ferromagnetic Materials

Magnetization *M* is the property of magnetic materials that describes the additional magnetic flux density residing in the material (Ando *et al.,* 2012). Figure 2.14 shows the hysteresis loop, which demonstrates the relationship between the magnetic flux density *B* and the magnetic field strength *H* (magnetization, *B*-*H*) and also provides information about the magnetic properties of a material (Platil & Ripka, 2012; Purnama *et al,* 2012; Matsuoka *et al,* 2013).

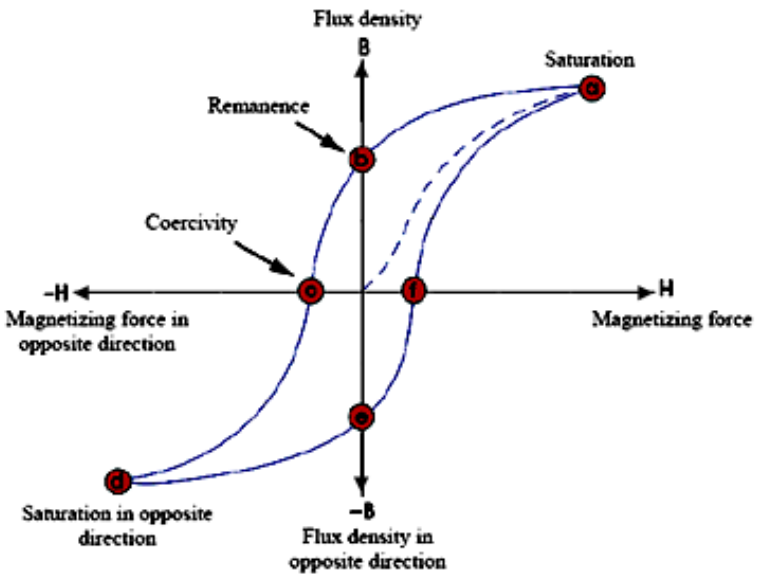

Figure 2.14: Magnetization (*B*-*H*) Curve of a Ferromagnetic Material (Calister, 1985).

As shown in Figure 2.14, the loop is generated by measuring the magnetic flux *B* of a ferromagnetic material while the magnetizing force *H* is varied. A ferromagnetic material that has never been previously magnetized or has been thoroughly demagnetized will follow the dashed line as *H* is increased (Nielson *et al.,* 2010). When a magnetic field is imposed on the material, domains that are nearly aligned with the field grow at the expense of unaligned domains (Wang *et al.,* 2013). Initially the domains grow with difficulty and relatively large increase in the field is required to produce even a little magnetization. As the field increases in strength, favorably oriented domains grow more easily (Suitella *et al,* 2011). Eventually, at point "a" almost all of the magnetic domains are aligned and an additional increase in the magnetizing force will produce very little increase in magnetic flux which signifies that the material has reached its point of magnetic saturation (Tumanski, 2011). The level of saturation of ferromagnetic materials depends on the magnetic permeability and the magnitude of the excitation current (Suitella *et al.,* 2011).

Hysteresis behavior may be explained by the motion of domains walls (Musmann & Afanassiev, 2010; Tumanski, 2011; Suitella *et al*, 2011). Upon reversal of the field direction, when *H* is reduced back down to zero, the upper section of the curve is followed from

saturation (from point “a” to point “b”). At point “b”, some magnetic flux remains in the material even though the magnetizing force is zero. This is referred to as the point of retentivity on the graph and indicates the remanence or level of residual magnetism in the material. As the magnetizing force is reversed, the properties follow the curve to point “c”, where the flux has been reduced to zero. This is called the point of coercivity on the curve. The reversed magnetizing force has flipped enough of the domains so that the net flux within the material is zero. The force required to remove the residual magnetism from the material, is called the coercive force or coercivity of the material (Ando *et al.*, 2010).

As the magnetizing force is increased in the negative direction, the material will again become magnetically saturated but in the opposite direction at point “d”. Reducing *H* to zero brings the curve to point “e”. It will have a level of residual magnetism equal to that achieved in the other direction. Increasing *H* back in the positive direction will return *B* to zero. The curve does not pass through the origin of the graph because some force is required to remove the residual magnetism. The curve will take a different path from point “f” back to the saturation point where it will complete the loop.

2.2.8 Soft and Hard Magnetic Materials

Ferromagnetic materials are categorized according to the properties of their *B*-*H* curves. Figure 2.15 shows the comparison of the *B*-*H* curves of the soft and hard ferromagnetic materials. Hysteresis loss occurs when energy is lost as a result of heat dissipation during the domain wall movement process (Zorlu, 2008). Hysteresis loss *W* per cycle is expressed (Ripka, 2001) as:

$$W = \int H \,.\, dB \tag{2.21}$$

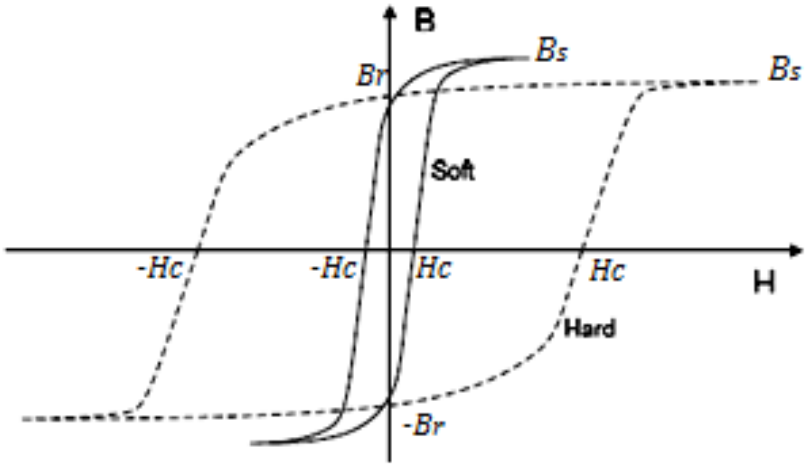

Figure 2.15: B-H Curves of the Soft and Hard Magnetic Materials (Zorlu, 2008).

Table 2.2 shows the magnetic properties of soft and hard magnetic materials. Permanent magnets are made from hard magnetic materials such as steel, cobalt steel, and carbon steel (Goldman, 1999).

Table 2.2: Comparison of Magnetic Properties between Soft and Hard Magnetic Materials.

Magnetic Property	**Soft Magnetic Material**	**Hard Magnetic Material**
Hysteresis loop, *W*	Narrow area	Large area
Remanence, B_r	High	High
Coercivity, H_c	Low	High
Saturation flux density, B_s	High	Good

As shown in Figure 2.15, soft magnetic materials are ferromagnetic materials with tall, narrow *B-H* curve, and smaller loop area, and usually have smaller hysteresis losses (Zorlu, 2008). Small amount of energy is required to move the domain walls of soft ferromagnetic materials (Ripka, 2001). On the other hand, hard magnetic materials, especially permanent magnets are ferromagnetic materials with wider *B-H* loops, higher residual magnetization, and coercive field values (Zorlu, 2008). Soft magnetic materials usually have coercive field range between 10 to 100 A/m, while the coercive field of some of the hard magnetic materials can be in the order of tens of kA/m (Zorlu, 2008).

2.2.9 Demagnetization of Magnetic Material

Demagnetization factor is usually related to the aspect ratio of core diameter to core length (Nourmohammadi *et al.,* 2015). A smaller core diameter and long magnetic core having a smaller aspect ratio can considerably reduce demagnetization effect and hence increased the performance of sensor in terms of voltage sensitivity and reduce the field noise and power consumption (Janosek *et al.*, 2014). Apart from the use of a high-permeability core, irrespective of the technology used, it is also essential to optimize the dimensional configurations of the coils and the magnetic core for sensitivity enhancement, field noise, and power reduction with respect to demagnetization effects (Todaro *et al.*, 2012; Lu and Huang, 2015). Figure 2.16 shows the ferromagnetic material with the surface magnetic charges gathered at the edges of the material when exposed to the external magnetic field H_{ext}.

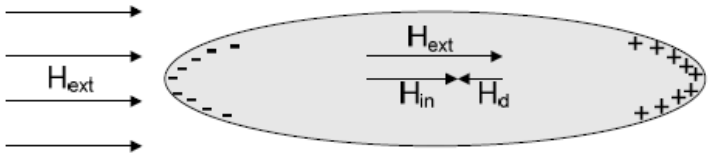

Figure 2.16: Ferromagnetic Material under External Magnetic Field (Zorlu, 2008).

A demagnetizing field H_d, opposing the external magnetic field H_{ext}, is induced in the core material due to surface magnetic charges at the edges of the material, and the internal magnetic field H_{in} in the ferromagnetic material can be written (Ripka, 2001; Kubik and Ripka, 2007; Todaro *et al.*, 2012; Lu *et al.*, 2014) as:

$$H_{in} = H_{ext} + H_d \tag{2.22}$$

This can also be written (Ripka, 2001; Kubik and Ripka, 2007; Todaro *et al.*, 2012) as:

$$H_{in} = H_{ext} - DM(H_{in}) \tag{2.23}$$

where H_d is the demagnetizing field proportional to the magnetization M of the material with demagnetization factor D. Demagnetization factor, D is a dimensionless quantity between 0 and 1 (Zorlu, 2008).

The core magnetization M in the ferromagnetic material can be expressed with a linear approximation (Ripka, 2001; Zorlu, 2008; Lu *et al.,* 2014) as:

$$M(H_{in}) = (\mu_r - 1)H_{in} \tag{2.24}$$

where μ_r is the relative permeability of the material.

The resulting internal magnetic field H_{in} in the ferromagnetic material can be expressed (Lu *et al.,* 2014; Todaro *et al.,* 2012; Tumanski, 2013; Solorzano, 2013) as:

$$H_{in} = \frac{H_{ext}}{1 + D(\mu_r - 1)} \tag{2.25}$$

It can be seen from equation (2.12) that the field seen by the ferromagnetic material is reduced due to the demagnetization effect. This can be attributed to the decrease of the permeability value of the ferromagnetic material (David *et al.,* 2010). The resulting permeability value is called the apparent permeability and it is expressed (Solorzano, 2013) as:

$$\mu_{app} = \frac{\mu_r}{1 + D(\mu_r - 1)} \tag{2.26}$$

By considering the apparent permeability, the behavior of a finite sized ferromagnetic material subjected to a magnetic field can be predicted.

2.2.10 Ferrite Core Material

Ferrite is one of the most diverse magnetic materials used in industry, finding use primarily as power transformer cores, electromagnetic interference suppression cores, and signal conditioning cores in computer hardware, and telecommunications (Heynen, 2015). Soft ferrite, in particular, composed primarily of iron typically combined with Nickel and Zinc (NiZn) or Manganese and Zinc (MnZn) (Rajput, 2010; Heynen, 2015). Soft ferrites consist of Meo.Fe_2O_3 alloys, where M_e stands for a bivalent metal oxide such as nickel, manganese, copper, magnesium, zinc, cadmium blended with 48 to 60 percent of iron oxide (Rajput, 2010). Due to their high resistivity (Goldman, 1999), which reduces energy loss from eddy

currents; ferrites magnetic materials are more useful in most electronics industry (Heynen, 2015). The low cost and short lead time due to availability of the material is one of the advantages of soft ferrite (MMG, 2014). The saturation flux density of ferrites is less than 0.5 Tesla with curie temperature of 220^{o}C (MMG, 2014).

Among the commercially available ferrite materials, manganese zinc (MnZn) ferrites usually have high permeability, high curie temperature, low coercive force and the high resistivity (Bae *et al.,* 2013). The low relative magnetic permeability of ferrite in the order of 10^3 (Bae *et al.,* 2013) makes them a rare choice for fluxgate sensor development because it produces low sensitivity sensor (Ripka, 2001). However, higher electrical resistivity reduces energy losses from eddy current, when compared to those of permalloy and amorphous material (Heynen, 2015).

2.2.11 Helmholtz Coils

Helmholtz coil is a parallel pair of two similar circular coils, spaced one radius apart with coils wound in series such that current passes in same direction in each coil (Abbott, 2015). Helmholtz coils are usually employed to create magnetic fields to null the earth's magnetic field, calibrate magnetic sensors, and used for other experiments in which a controllable amount of uniform magnetic field is required (Abbott, 2015). The basic principle of Helmholtz coils is that the coils produces uniform magnetic field at the center (Abbott, 2015; Daron *et al.,* 2015). This arrangement of coil was invented by German physicist, Hermann von Helmholtz, over a century ago (Bhatt *et al,* 2010). The intensity of magnetic field is directly proportional to the number of turns and the current through the coils (Abbott, 2015). Starting with the desired dimension based on the radius/ coil separation *R* and magnetic field strength *B,* the required current I_C and the number of turn N can be traded and selected according to the following equation for field strength at the center of the Helmholtz coil (Bhatt *et al.,* 2010):

$$B = N \cdot \frac{\mu_0 . I_C}{R} \cdot \left(\frac{4}{5}\right)^{3/2} \quad (2.27)$$

where R is the radius of each turn of a coil, I_C is the coil current, and μ_0 is the permeability of air. The power supply for driving the coils must also be taken into consideration when calculating the diameter of wire to be used to ensure it can provide the current needed to generate the required magnetic field (Bhatt *et al.,* 2010). The schematic describing the configuration of Helmholtz coils is shown in Figure 2.17.

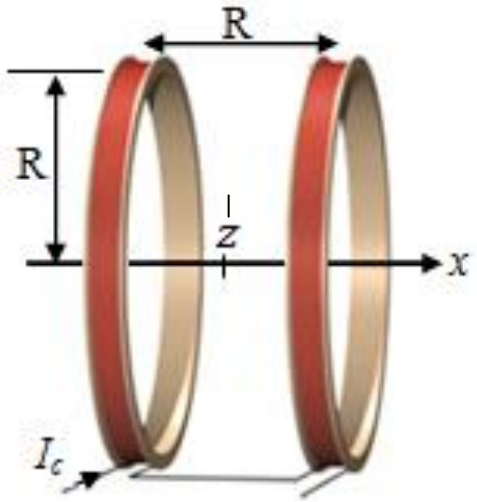

Figure 2.17: The Schematic Diagram of Helmholtz Coils (Bhatt *et al*, 2010)

Each of the individual Helmholtz coils produces uniform magnetic field parallel to the axis of the coils (Bhatt *et al*, 2010), and the two coils form a system such that a controllable amount of uniform magnetic field can be accomplished by controlling the applied current (Abbott, 2015). The uniform field within the coil accounts from the summation of fields parallel to the axis and the difference of vertical component fields (Abbott, 2015). Helmholtz coil design is simple and there are many commercially available designs for all kinds of applications. In order to examine the magnetic field sensing of a fluxgate sensor, a large area with uniform magnetic field is required (Butta *et al.,* 2010). The advantage of having a large area is that it will allow easy access of the sensor during measurement (Butta *et al.,* 2010). A laboratory

design and characterization of Helmholtz coils is a better choice when Helmholtz coil with larger areas that are available in the market are very expensive.

2.2.12 Overview of Optimization

The fluxgate magnetometer is a device for measuring weak magnetic field by using the nonlinear relationship between the magnetic flux density B and the magnetic field strength H (Lu *et al.*, 2014; Can and Topal, 2015). In order to analyze, design and optimize fluxgate magnetometer, simulations are necessary. During the simulations, the accuracy of an optimization technique for finding the optimum parameters of fluxgate magnetometer core, pick-up coil, and detection circuit elements and as well as modeling the behavior of fluxgate magnetometer are significant (Can and Topal, 2015). There have been numerous approaches to optimize the parameters and model the behavior of fluxgate magnetometer, which can be divided into two categories (Grosz and Paperno, 2012):

1. The Part-by-Part optimization approach, which ignores the underlying mathematical model equations of the core material, coils, and electronics circuit, such as magnetization and demagnetization of core magnetic material (Lu *et al.*, 2014), non-linear resonance of fluxgate excitation (Ferro-resonance), stability and sensitivity of sensor output (Parametric amplification) (Musmann and Afanassiev, 2010), and induced electromagnetic induction in the core (Tumanski, 2013),
2. Analytical optimization approach which includes mathematical modeling of fluxgate sensor behavior which can be numerically solved using software tool such as Finite Element Method (FEM). FEM tools however does not allow users to specify the design purposes and are difficult to apply to complex optimization problems such as when dealing with optimization problems involving large number of design variables and multiple objective functions.

A poor design may result when increasing the design variables and objective functions of fluxgate magnetometer, and even cause degradation to the fluxgate performance. Hence, an optimal magnetic core, pick-up coil and detection circuit elements design for the fluxgate magnetometer is desirable and this is the problem considered in this research work.

Solution of a fluxgate magnetometer core, pick-up coil, and detection circuit elements optimization problem typically involves two major parts. The first part is a systematic optimization approach which provides information about the matching behavior under various geometrical conditions of the magnetic core, pick-up coil, and detection circuit and the second is an optimization algorithm that leads to a convergence of the iterative geometry and dimension of core, pick-up, and detection circuit elements by updating the solutions. Therefore, fluxgate magnetometer parameters optimization can be categorized as variable domain problems in which the domain geometry and dimension have to be modified in each iteration to fulfill some requirements.

Among the several numerical methods used in the optimization of the fluxgate magnetometer, the most appealing one in the context of variable domain problems is the Finite Element Method (FEM) (Janosek *et al.*, 2014). The main drawback of FEM is that the mesh must be modified whenever the geometry of the problem is changed and also become complex when dealing with variable domain problems (Kazemzadeh-Parsi, 2015).

Optimization appears in many real world problems and a considerable amount of work has been done in developing efficient algorithms for solving optimization problems. Classical optimization algorithms are considerable for unconstrained optimization problems and use the gradient information which is difficult to obtain (Kazemzadeh-Parsi, 2015). In addition, the classical methods may converge to local optimum points and the gradient-free algorithms may be a desirable choice to overcome these difficulties (Kazemzadeh-Parsi, 2015).

Metaheuristic algorithms are high level heuristic algorithms and they generally perform better than heuristic algorithms (Yang and He, 2013). The two major components of metaheuristic algorithms are the selection of the best solutions and randomization (Fister *et al.,* 2014). The selection of the best solutions ensures the convergence of the solutions to the optimality, while the randomization avoids the solutions from being trapped at local optima and, at the same time increases the diversity of the solutions (Arora and Singh, 2013; Yang and He, 2013). The combined efforts of these two components usually ascertain the achievement of global optimality. Majority of these algorithms were developed as a result of the behavior of biological or physical systems in nature (Yang, 2013). The metaheuristic optimization techniques have gained popularity in recent years as a result of their ability to deal with complex optimization problems which are otherwise difficult to solve (Ali *et al.,* 2012). The most popular optimization techniques are Genetic Algorithm (GA) (Kenwright, 2014), evolutionary strategies (Back *et al.,* 1991), evolutionary programming (Fogel, 1994), Particle Swarm Optimization (PSO) (Ali *et al.,* 2012), Ant Colony Optimization (ACO) (Ke *et al.,* 2010), Bee Colony Algorithm (BCA) (Ushie *et al.,* 2015), Artificial Bee Colony (ABC) (Gao *et al.,* 2014), Firefly Optimization Algorithm (FOA) (Yang, 2010) and krill herd algorithm (Gandomi and Alavi, 2012). Apart from the bio inspired algorithms, there are nature inspired algorithms that mimic physical phenomena such as Simulated Annealing (SA) (Said *et al.,* 2014; Cruz-Chavaz *et al.,* 2015; Konak and Konak, 2015), and Harmony Search (HS) (Bao *et al.,* 2015).

FOA is a recently developed, promising, and metaheuristic optimization technique, which was originally proposed by Yang (Yang, 2010). The FOA is based on the idealized behavior of the flashing characteristics of fireflies. Based on Yang's works, the FOA is very efficient in finding the global optima with high success rates (Yang, 2010). It is also shown, using various test functions, that the FOA is superior to both PSO and GA in terms of both

efficiency and success rate (Yang, 2010; Fister *et al.*, 2013; Yang, 2013; Yang, 2014). After the first presentation of the FOA (Yang, 2010), some modifications were proposed by different researchers (Wang, *et al.*, 2012; Coelho and Mariani, 2012; Gandomi *et al.*, 2013). In order to optimize the performance of fluxgate magnetometer in this research work, the original FOA was modified to improve the performance of fluxgate magnetometer. The modification consist of adding a systematic optimization approach by simultaneously finding the geometry and dimension of the magnetic core, pick-up coil, and detection circuit elements to match the excitation and detection circuit and as well obtain the behavior of the fluxgate magnetometer with respect to the noise and sensitivity.

To evaluate the applicability of the proposed optimization technique in the performance of fluxgate magnetometer, two different fluxgate magnetometers were developed based on the Part-by-Part Optimization (PPO) technique and the results are presented.

2.2.12.1 Multi-Objective Optimization

Optimization is performed to obtain the best result under given conditions (Ushie *et al.*, 2015). The ultimate goal of optimization is either to minimize or maximize the desired objective (Grosz and Paperno, 2012). In any practical situation, the objective required is a function of certain decision variables (Yang, 2010). Several optimization algorithms have been developed for solving FMS optimization problems (Kim *et al.*, 2013; Fister *et al.*, 2014). Multi-objective optimization problem involves multiple objective functions with a possibility of conflicting each other (Santos *et al.*, 2013; Yang, 2013). The objectives and constraints are functions of x, which is a vector of design variables with dimensionality n. The aim of multi-objective optimization is to find a solution (solutions) that minimizes the objective functions and satisfies the constraints of these functions (Irina, 2014). In the case of conflicting objectives, a critical objective function that takes care of other objectives is formed by using a weighting factor for each function (Yang, 2013). Multi-objective

optimization problem can be written in the generic form mathematically as follows (Yang, 2010)

Minimize

$$f(x) = \left(f_1(x), f_2(x), \dots, f_i(x)\right) \quad (2.28)$$

subject to:

$$g_j\,(x) \leq 0 \quad (2.29)$$

And

$$l_j\,(x) = 0 \quad (2.30)$$

For

$$x = (x_1, x_2, \dots, x_n)^T \quad (2.31)$$

Where $j = 1, 2, \dots, m$.

where x is an n-dimensional vector called the design variables, f_1, f_2, …, f_i are the objective functions. $g_j(x)$ and $l_j(x)$ are the inequality and equality constraints, respectively. The inequalities can also be written as ≥ 0 and the objectives can also be formulated as maximization. n is the number of variables, and m is the number of constraints. The expressions in equation (2.28) to equation (2.31) are called a constrained optimization problem. Some optimization problems may not involve any constraints and are called unconstrained optimization problems (Yang, 2010).

2.2.13 Part-by-Part and Analytical Optimization Approaches to FMS Design

In order to optimize the performance of magnetometers, conventional approaches of finding the optimal configuration is usually employed based on designing the magnetometer part-by-part (Grosz and Paperno, 2012), which include designing the sensor core of the magnetometer first, selecting the pick-up coil geometry, and, finally develop a low noise

detection circuit. However, such part-by-part optimization design approach does not give optimal magnetometer performance (Grosz and Paperno, 2012).

Several researchers have used analytical optimization approach to design magnetometer (Coillot *et al.,* 2010; Grosz *et al.*, 2010; Grosz *et al.*, 2011) by using analytical model equations which was numerically solved to find the optimum magnetometer parameters (Coillot *et al.*, 2010; Grosz *et al.*, 2010; Grosz *et al.,* 2011; Chen *et al.,* 2011). However, analytical optimization approach is not convenient when the need to perform a large number of numerical calculations to find the optimum parameters of magnetometer arises and, thereby, does not allow easy interpretation of the results obtained (Grosz and Paperno, 2012).

2.3 Review of Similar Works

Due to their high reliability, robustness, compact size, low power consumption, high sensitivity and economy, the study and development of new variants of fluxgate sensor systems have been evolving. Reducing the size and weight of fluxgate sensors is essential in terrestrial and space technologies and in the microelectronics industry. Therefore, there is increasing demand for the possibility of reducing their size and making them compatible with microelectronics technology. Overview of the efforts made by various researchers to develop planar and wire-wound fluxgate sensors, their signal processing and systems development with these magnetic sensors was given in this section.

There are three main problems to overcome in the development of a fluxgate sensor: the reduction of the coils, the reduction of the ferromagnetic core in the device, and the reduction of the interfacing circuits (excitation and detection circuits). There are three basic approaches for the optimization of the coils. The first approach comprises of using planar coils in several layers, with the magnetic core sandwiched between them, which is referred to as Printed Circuit Board (PCB) technology. The second approach is based on the use of several fabrication steps to make spiral coils surrounding a ferromagnetic thin film that acts as a

sensing core, which is known as Micro-Electromechanical Systems (MEMS). The last approach consists of using three dimensional (3-D) coils wound round the ferromagnetic core, which is referred to as wire-wound technology.

Baschirotto *et al.* (2006) worked on "A CMOS front-end circuit for integrated fluxgate magnetic sensors" to reduce noise and enhanced the sensitivity of a fluxgate sensor. The analog front-end contains an excitation circuit, a timing circuit and a detection circuit. A 400 kHz oscillator frequency was divided to get a 100 kHz triangular wave generator and 200 kHz clock frequency. The 100 kHz frequency was used as excitation circuit to drive excitation coil while the 200 kHz frequency was used to as a reference frequency to demodulate the output of the fluxgate sensor. The schematic of the excitation electronics circuit consists of an integrator followed by a trans-conductance amplifier and a class AB amplifier stages. Second harmonic principle was used to obtain the output signal of the sensing coil. The detection circuit has a synchronous demodulation unit followed by a second order Sallen-Key low pass filter to extract the second harmonic frequency signal of the output of the fluxgate sensor. However, the main drawback of this analog front-end circuit is the complexity of the circuit and hence it would be difficult to integrate this analog front-end circuit with fluxgate system.

A double axis micro-fluxgate sensor with its analog front-end circuit has been presented in **Baschirotto *et al.* (2009)**. A 0.5μm CMOS process followed by post processing for the magnetic core was used to fabricate the micro-fluxgate sensor. A new technique called dc magnetron sputtering was used which allowed the achievement of a ferromagnetic core of good properties with a lower thickness. The excitation coil has a resistance of 123.4Ω which was excited with a 100 kHz excitation signal frequency and required 18mA of current to saturate the core. The differential peak to peak voltage was 3.5mV which was amplified by 33dB before it was processed by the detection electronics circuit. The excitation circuit uses

3.3V to generate a square wave of 100 kHz which was integrated to obtain a triangular waveform around mid supply range. Also, an operational amplifier with low-impedance class AB output stage which uses a 26V power supply provides all the current required for the micro-fluxgate sensor. A Sallen- Key filter was used to extract the second harmonic component of the output voltage which was amplified further before being digitized by a 13-bit incremental ADC. On the other hand, this analog front-end is complex and hence it would be difficult to integrate it with other fluxgate circuits. Also the power consumption for the analog front-end was around 76.3mW which was very high. In addition, the use of a decoupling stage increases the cost of the interface circuit.

A research work of **Ferri *et al.* (2009)** focused on investigating a low-voltage fluxgate magnetic sensor interface circuit with digital output for portable applications. Two different excitation circuits were proposed to generate the needed triangular voltage. The excitation circuit of 3.3V with an H-bridge and an external inductance of 380μH, changes the excitation current direction through the excitation coil, thus eliminating the use of split power supply. Also, the excitation circuit with 5V power supply has a triangular voltage generator, a voltage to current converter and an H-bridge. The detection circuit performs a synchronous demodulation to obtain the extract second harmonic signal in the output of the sensing coil. The demodulation was done at a frequency of 200 kHz with the output passed through a Sallen- Key filter that produces a dc signal proportional to the second harmonic frequency of the output voltage. The dc signal is amplified by a programmable gain amplifier (PGA) before it is digitized by a 13 bit incremental ADC. The total power consumed by the interface circuit and its area are not mentioned. The drawback of this study was its failure to address the effect of parameters optimization on the characteristics of sensor core, and more importantly the dimensions of the sensor core and the number of excitation and sensing coils which plays a crucial role in matching the excitation and detection circuits.

Sebbes *et al.* (2010) described the analytical optimization of the developed fluxgate sensor having high temperature and made of Vitroperm VP800R as the ferromagnetic rod core. The optimum length and diameter of the rod core, and the number of turns of pick-up coil required for optimizing the sensitivity of the sensor were found. The optimization approach enabled the analysis of the closed-loop sensitivity of the fluxgate magnetometer as a function of the temperature and has also produced a fluxgate sensor for operation at high temperature. The sensor showed linearity up to 50 μT, with maximum sensitivity of 130 mV/μT. The magnetic field noise was 15pT/√Hz at 100 Hz. In this study, because of the use of the closed-loop configuration, the sensitivity of the fluxgate sensor was greatly enhanced. However, the sensor exhibited an increased noise level, which was due to pick-up coil thermal resistance. One of the reasons may be due to the use of magnetic core dimension as the only variable, without considering the matching of the pick-up coil and detection circuit. The optimal performance of the excitation and detection circuits is not only determined by the dimension and geometry of the sensor core, but it also depend on the number of excitation and pick-up coils turns. Hence, optimizing the dimension of the core and number of pick-up coil turns can further minimize the thermal resistance of the pick-up coil, which could in turn reduce the noise level of the fluxgate sensor.

Lu *et al.* (2011) reported the optimization of fluxgate sensors performance based on manufacturing technique. The sensor used dual-core configured by two 3-D excitation coils formed by the wire-bonding technique and four planar pick-up coils fabricated on silicon substrate through the standard CMOS process. The ferromagnetic cores were made of amorphous 2714A provided by Metglas Ltd with low saturation magnetic flux of 10 μT. The approach was reported to allow the characterization of the sensor and found to be operated along a nearly linear V-B region around the zero point and at the second harmonic frequency. The sensor sensitivity was 11 V/T at 50 kHz excitation frequency and current of 105 mA.

The magnetic field noise was 12 nT/√Hz at 1 Hz. On the other hand, the performance of the sensor was very poor with respect to sensitivity and power consumption, which could be due to limitations on the space, number of magnetic layers, and number of excitation and pick-up coils imposed by the MEMS manufacturing technology. In addition to this, there was no report of optimization used for finding the optimal dimensions of sensor core, pick-up coil and detection circuit elements. This could eventually lead to mismatch between the sensor parameters because of the strong relationship between the sensor core, number of excitation and pick-up coils turns, and the excitation and detection circuits.

Jeng *et al.* (2012) examined the possibility of optimizing the performance of fluxgate sensor by detecting several field-sensitive harmonics. Wire-wound technology with dual rod cores was employed. They developed an analytical model and numerical simulation to optimize the voltage sensitivity and noise of a miniature fluxgate sensor by adding up the responses of four even harmonics. The sensor demonstrated a voltage noise of 27 nV/√Hz which was slightly greater than the value of 23 nV/√Hz estimated from 1.3 mV/μT sensitivity and 18 pT/√Hz noise at 1 Hz. The magnetic field noise was 200 pT/√Hz at 1 Hz. The proposed optimization method reduced the field noise of a chip-scale fluxgate sensor for which the coil inductance was too small and a tuned excitation circuit was not possible. However, it was not suitable for a tuned fluxgate sensor of which the harmonic spectrum had been concentrated to the second harmonic and the higher order harmonics became small.

Lei *et al.* (2012) reported a micro fluxgate sensor with 3-D solenoid coils acting as excitation and pick-up coils using thick photo-resist based UV lithography and electroplating. A rectangular ring-shaped ferromagnetic core was realized with iron-based nano-crystalline alloy using gluing and chemical wet etching processes. They developed an analytical model and experimental set-up to optimize the voltage sensitivity, noise and linear operation range of the sensor. The linear range exhibited by the sensor was 500 μT, with maximum sensitivity

of 583.1 V/T at 100 kHz excitation frequency with effective excitation current of 150 mA-rms. The magnetic field noise was 13.57 nT/√Hz at 1 Hz and the noise RMS level was 23 nT within a 10 mHz - 25 Hz frequency bandwidth. However, the noise of the developed micro-fluxgate sensor was far above the 10 pT/√Hz benchmark level of noise which was due to the limitations on space, number of magnetic layers, and number of coil turns.

Rovati and Cattini (2012) presented a fluxgate sensor based on planar technology, with dual crossed ferromagnetic core realized using commercially available Vitrovac 6025 (composition (Co, Fe, Mo) 73% and (Si, B) 27%). Vitrovac hysteresis loop model according to the Jiles-Atherton model was developed and a PSPICE simulation model for the electronic design of the sensor was employed to optimize the sensitivity, noise, and linear operation range of the sensor. Experimental verification showed linear behavior up to 38 μT without the additional compensation coils. The maximum sensitivity was 13.3 mV/μT at 10 kHz excitation frequency and excitation current of 600 mA. The magnetic field noise was 12.2 nT/√Hz at 1.5 Hz. However, the performance of the sensor was lower than the commercial fluxgate sensors, which was due to the effect of the presence of external ferromagnetic masses and /or stray fields.

In the work of **Karthik, (2013)**, analog front-end circuit that uses a charge pump based excitation circuit to generate the triangular excitation current was investigated. The proposed analog front-end circuit uses phase delay technique in the detection circuits. The developed analog front-end architecture consists of the excitation circuit with a charge pump which charges and discharges an external capacitor to produce a triangular voltage waveform at its output. The charge pump works on a 100 kHz clock frequency. The triangular voltage waveform generated by the charge pump is converted into a triangular current by a voltage to current converter. The detection circuit consists of a double differential preamplifier that amplifies the difference between the output of the sensing coils and a differential reference

voltage. The output of the micro-fluxgate sensor was 30 mv and was amplified before it was fed to a comparator. However, this study failed to address the effect of optimum parameters of sensor core and the number of excitation and sensing coils which is critical in matching the excitation and detection circuits.

Miles *et al.* (2013) analyzed a prototype fluxgate magnetometer sensor based on traditional 3-D wire-wound excitation and pick-up coils and ferromagnetic ring core. They employed digital feedback process to optimize the sensitivity, noise, and linear operation range while reducing the complexity, parts count, and physical size of the sensor. The sensor exhibited a linear behavior up to 65 μT, at 28.8 kHz excitation frequency. The magnetic noise was 10 pT/√Hz at 1 Hz and the RMS noise was 18 pT within a 1-400 Hz frequency bandwidth. The sensor power consumption was 1.5 W. The design of this sensor was simple due to the traditional 3D wire-wound method used in its manufacturing. The simplicity was however at the expense of larger sensor size, lower integration capability, and considerable power consumption. The level of noise achieved was due to the core diameter. The core dimension, excitation coil and pick-up coil play a significant role in matching the excitation and detection circuits.

Matsuoka *et al.* (2013) developed a prototype fluxgate sensor based on traditional 3-D coils and 20 mm diameter ferromagnetic ring core made of nickel-molybdenum permalloy. They employed delta-sigma analogue-to-digital converter consisting of analogue circuit of delta-sigma modulation to optimize the sensor. The linear range of the sensor was 60 μT at 11 kHz excitation frequency. The magnetic noise obtained from the engineering model was 7.7 – 8.9 pT/√Hz at 1 Hz and the RMS noise was 33.5 – 37.3 pT within a 100 mHz - 10 Hz frequency bandwidth. However, the sensor weight and power consumption in the order of 118 g and 2.17 W, respectively, significantly put this sensor at a disadvantage. The sensor was too bulky and system-incompatible to meet the dimensional and power requirements of a

miniature product. A large cross section of the magnetic core material used led to higher excitation current needed to saturate the ferromagnetic material which eventually increased the power consumption.

Janosek *et al.* (2014) presented a fluxgate sensor based on traditional coils with 3-D 50 mm diameter ferromagnetic ring core realized using Vitrokov 8116 (Co-Cr-Fe-B-Si) metallic glass tape. They developed an analytical model and employed a 3-D FEM simulation which accurately described the optimum number of ring core tape layers that optimized the sensitivity, noise, and linear operation range of the sensor. The sensor magnetic noise was 3.26 pT/√Hz at 1 Hz and the RMS noise was 7 pT within a 0.1-10 Hz frequency bandwidth. The noise reduction was limited by the bending stress and relatively low demagnetizing factor. The noise for a given geometry slowly decreases with the decreasing demagnetizing factor up to a given minimum from which it increases much faster.

Lu *et al.* (2014) presented the developed flip-chip fluxgate magnetometer with two 3-D excitation coils and four planar pick-up coils fabricated on a PCB substrate via lithographic methods. The Metglas 2714A ferromagnetic material (Metglas) was employed as ferromagnetic core and having a low saturation magnetic flux density of 10 μT. The optimum geometric dimensions of excitation coils were found for optimizing the sensor performance in terms of sensitivity and noise level of the sensor. The FEA modeling and simulation was carried out to analyze the magnetic flux density distribution in the magnetic cores. The approach allowed the analysis of the developed sensor for sensitivity and noise level of the sensor. A maximum sensitivity of 593 V/T was obtained when excited at 50 kHz of excitation frequency, and 600mA excitation current. The minimum magnetic field noise was 50 pT/Hz at 1Hz. However, the reported decreased sensitivity and enhanced noise level could be due to limitations on the space, number of magnetic layers, and number of excitation and pick-up coils imposed by the MEMS manufacturing technology. In addition to this, optimization of

the entire magnetometer parameters such as the sensor core, pick-up coil and detection circuit elements was performed. This led to mismatch between the sensor parameters because of the strong relationship between the sensor core, number of excitation and pick-up coils turns, and the excitation and detection circuits.

Can and Topal (2015) designed ring core fluxgate with three different diameters which were prepared by using Metglas 2714A ribbons in traditional 3D wire-wound technology. The ring cores diameters were 10 mm, 15 mm, and 20 mm (named FG10, FG15, and FG20) with saturation induction of 570 mT and a DC permeability of 10^5. The excitation coils were 90, 155, and 350 turns. The pick-up coils also were 1020, 1410, and 1900 turns, respectively. The second harmonic measurements were carried out under a calibrated coil by investigating the sensitivity and noise level which were found to be 597, 1798, and 11400 V/T, respectively. The noises were determined to be 31.7, 23.8, and 2.72 nT/√Hz at 1 Hz for FG10, FG15 and FG20, respectively. These sensors however, have larger noise values when compared the performance with other sensors having identical geometries due to the limitations of the electronics and the measurement area.

Ansari *et al.* (2015) presented the FEA-based optimization of fluxgate magnetometer performance with E-core as the ferromagnetic core. The optimum number of turns of pick-up coil and its width required to optimize the sensitivity of the sensor were found. The optimization approach enabled the analysis of the sensitivity of the fluxgate magnetometer with respect to the number of pick-up coil turns and width of the coil. The magnetic flux distribution was proved to induce voltage of 0.053 mV in the pick-up coil output with respect to the optimal number of turns. However, the design has been proved using FEA, it is yet to be validated to ascertain the effectiveness of the approach used and investigate the degree of matching of the parameters as the sensor core and detection circuit optimization was not considered along with optimization of pick-up coil. Moreover, by using FEA-based

optimization, the need to perform large number calculations to find the optimum fluxgate sensor configuration makes this approach not suitable and, does not allow easy interpretation of the results obtained.

2.4 Summary

The literature related to this research topic has been reviewed for last six years in order to find out work carried out by various researchers. The selected researchers have developed and experimented different sensors for different applications with the aim of optimizing the performance of fluxgate magnetometer using various optimization techniques. Some manufacturing restrictions (limitations on the number of magnetic layers and number of excitation and pick-up coils) were suffered by micro-fabrication (PCB and MEMS technologies) processes which made it to compromise on the performance of fluxgate sensors. In addition to the dimension and geometry of the magnetic core, the design of excitation and pick-up coils play a crucial role on the performance of a fluxgate sensor. There is need to improve the noise of the sensor, which requires optimization of the magnetic material used in the magnetic core since electrodeposited cores usually exhibit higher noise than bulk cores. Also, the number of pick-up coil used for detecting the flux changes in the magnetic core needs to be optimized since coil winding resistance causes thermal noise. Finally, there is need to optimize the detection circuit used to detect the pick-up coil output voltage since the voltage noise and detection circuit elements result in increased voltage noise of the detection circuit. The possibility of optimizing the dimension of the magnetic core, pick-up coil, and detection circuit parameters is focused in this research.

CHAPTER THREE

MATERIAL AND METHODS

3.1 Introduction

In this chapter, the detailed procedures carried out in the design and development of fluxgate sensors by using modified Firefly Optimization Algorithm (FOA) and Part-by-Part optimization (PPO) techniques are described. The chapter is divided into two parts. In the first part, the materials used for the design and development of the Fluxgate Magnetometer Sensor (FMS) are presented, while the second part includes the specific actions taken to

implement the drive electronics, sense electronics, and fluxgate magnetometer sensor are presented.

3.2 Materials

The tools and materials utilized for this research and how they were used are presented in this section.

3.2.1 Equipments Used

The material used to accomplish the aim and objectives of this research work include the followings:

1. **A Four Channel Digital Signal Oscilloscope:** (Tektronix model: TPS 2024B) to display and evaluate the magnitude of the excitation voltage waveforms, ferro-resonance voltage waveforms, and the output waveform of the pick-up coil.
2. **An LCR Meter:** (UNIT Model: UT-51) to measure both the self and mutual inductances of the excitation and pick-up coil.
3. **A Magnetic Field Strength Meter:** (Tenmars Model: TM-191) to calibrate the developed Helmholtz coils and evaluate the developed fluxgate sensors for magnetic field characterization.
4. **A Programmable DC Power Supply:** (Tektronix 0-72V, 1.2A, model: PSW 4721) used to supply the required excitation current and power the whole FMS system.
5. **A Bar Magnet:** to evaluate the developed sensors response to positive and negative orientation of the magnetic field.
6. **A Digital Multi-Meter:** (Tektronix 2050 model) to evaluate the pick-up coil output voltage corresponding to the measured external magnetic field.
7. **A Spectrum Analyzer:** (Agilent N9230B 9 kHz -3 GHz) to evaluate the amplitude of the spectral component at 10 Hz.

8. **A pair of Helmholtz Coils:** to generate uniform magnetic field and impose the external magnetic field during the characterization of the developed sensors.
9. **Analog Magnetic Compass:** to identify the magnetic poles of the earth at different locations during the characterization of the optimized FMS for earth's magnetic field measurements.
10. **A Data Acquisition Instrument:** (Dataq Model: DI-145) used for acquiring and evaluating the real-time magnetic field data from fluxgate magnetometer.
11. **A Testing Board:** to supply the excitation coils of the developed fluxgate sensors with a square wave excitation current at 5 kHz and evaluate the output voltage from the pick-up coils.
12. **WINDAQ Software:** to record waveforms directly and continuously to disk while monitoring a real time display of the waveforms on-screen and playback data acquired through DI-145 instrument.
13. **ANSYS Electromagnetic Software:** (ANSYS Version13.0) to analyze the magnetic field distribution in the ring core and the required excitation current to saturate the core.
14. **Optimization Algorithm:** Modifications were made to the Firefly optimization algorithm to address fluxgate sensor optimization problems.
15. **MATLAB Program:** (Version 7.0.4) to write program for firefly algorithm developed for design FMS and Helmholtz coils.
16. **Personal Computer**: to implement the MATLAB program written for simulating the modified FOA developed for FMS optimization design. The personal computer used is a 1.50 GHz Intel® core™ Duo CPU Windows 7 Ultimate 32-bit.
17. **Test Locations:** Since the developed FMS is a magnetic field meter, then the earth's magnetic field measurement becomes imperative. Any geographic location is an ideal

area. The magnetic field strength of Electrical and Computer Engineering, ABU Zaria; Arugungu street, Katsina road in Kaduna; and Old NEPA area, Kuje, Abuja were used to test the developed optimized FMS and obtained the measured results.

3.3 Method

In this section of the thesis, details implementations of each of the methodology as outlined in section 1.6 are presented. Chosen electronic design exploits analog control of the excitation electronics together with analog output signal processing. This approach will require analog interfaced drive electronics, sense electronics, sensor, and analog-digital converter. Component values were optimized to improve performance and to minimize currents in the fluxgate magnetometer. Then the circuit was tested on a breadboard and soldered on a prototyping board.

The main components of a fluxgate magnetometer were presented making special emphasis on the blocks that are responsible for the three stages used for derive electronics, sense electronics, and fluxgate sensor. Figure 3.1 presents the block diagram of the fluxgate magnetometer system, which is composed mainly of 9 different blocks. The drive electronics consists of square wave oscillator, two frequency divider, and current amplifier. The sense electronics include the band pass filter, synchronous detector, low pass filter, and voltage-to-current converter.

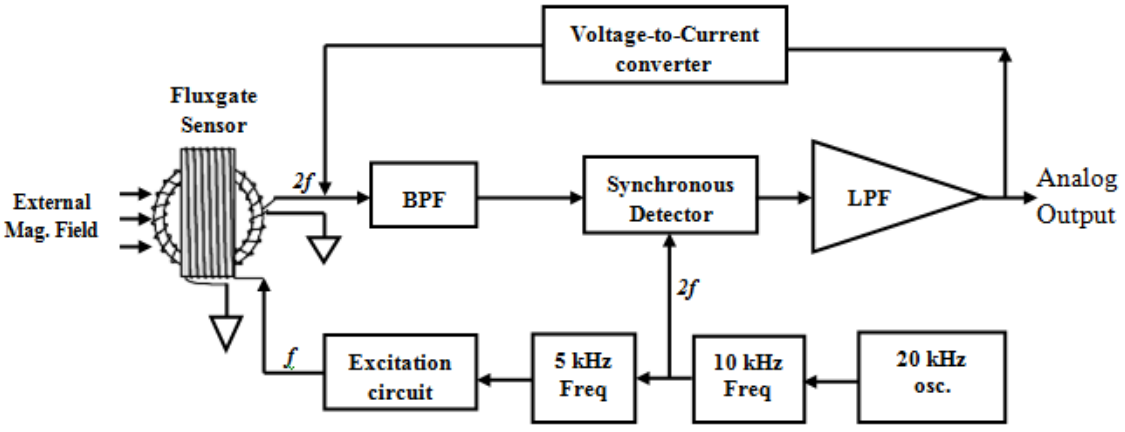

Figure 3.1: The Block Diagram of Major Components of a Fluxgate Sensor.

3.3.1 Fluxgate Magnetometer Drive Electronics Development and Simulations

The drive electronics circuit was used to drive the excitation coil of the fluxgate sensor and it consists of a drive oscillator, frequency divider, and current booster (voltage to current converter). The software that was used for the simulations is based on the NI Circuit Design Suite 11.0 from the National Instruments (NI, 2010). Several simulations were performed to find the best excitation frequency required to saturate the fluxgate magnetic core material. The first analysis step was to evaluate the optimum excitation frequency and current value that guarantees the ferromagnetic material to saturate, for a given geometrical dimension of the excitation coils. By carrying out simulations using different excitation frequencies shown in Appendix H, a peak current of 29.3mA turned out to be sufficient to drive the excitation coil with the geometrical dimensions of the magnetic cores. The screenshot of the simulation results is presented in Appendix H. After an iterative process of design optimization, the excitation frequency selected is a 5 kHz square wave. Using the NI Circuit Design Suit 11.0 for simulations, the schematic diagram shown in Figure 3.2 was obtained.

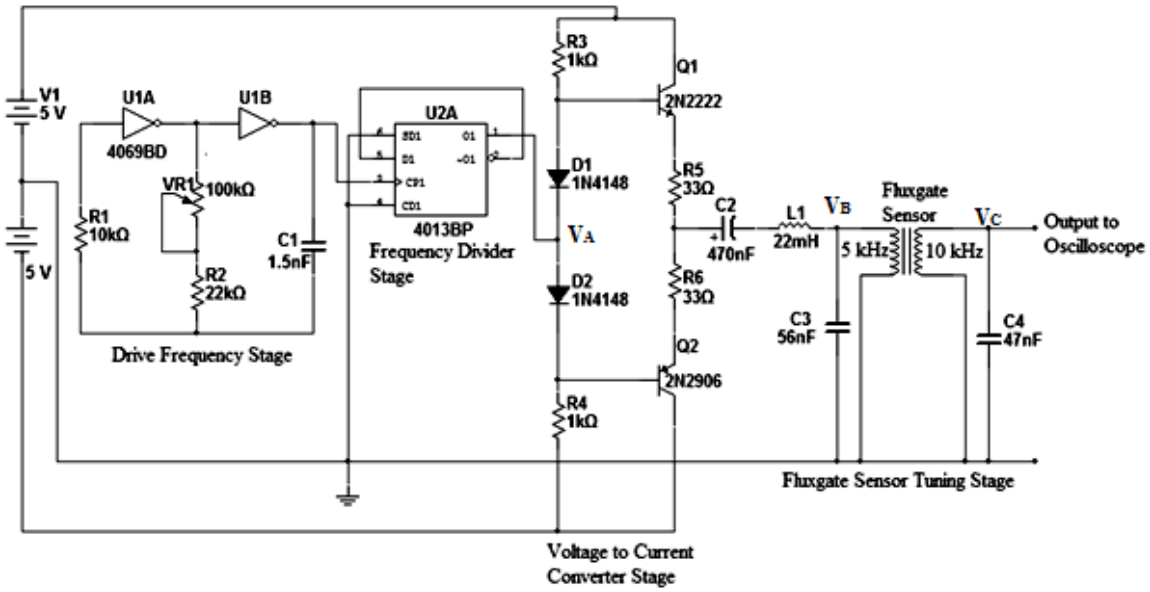

Figure 3.2: Driver Circuit of Developed Fluxgate Sensors

3.3.1.1 Square Wave Generator Circuit

As shown in Figure 3.3, in order to ensure proper clocking of the excitation and detection circuits, the whole circuit was driven by a square wave oscillator at 20 kHz frequency (see Appendix H).

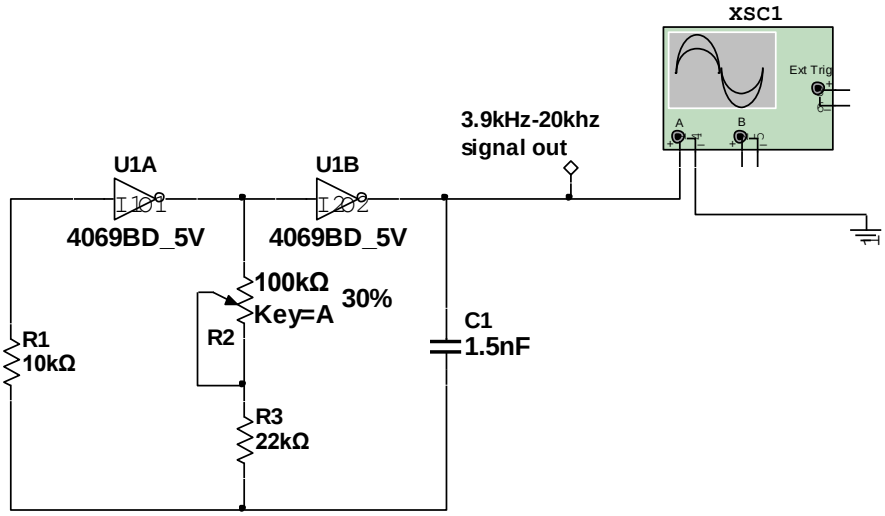

Figure 3.3: Square Wave Generator Circuit

By using a 20 kHz master clock, a duty cycle of 50% on both the 5 kHz and the 10 kHz output waveforms can be ensured. A duty cycle different from 50% could compromise the demodulation of the signals produced by the sensing coils and, hence, it has to be avoided. As shown in Figure 3.2, by using equation (2.8), the oscillator block was built around resistors R1, R2 and potentiometer VR1 with capacitor C1 and Integrated Circuit (IC), hex-inverter 4069BD (U1A & U1B). The oscillator circuit was tuned to twice the excitation frequency ($2f_{exc}$) and variable between 1 kHz and 20 kHz by means of a 100 kΩ potentiometer (VR1).

3.3.1.2 Frequency Divider Circuit

As shown in Figure 3.4, the output of this oscillator were two signals: a 5 kHz square wave signal with its complementary output, that is used to drive the excitation coil, and a 10 kHz square wave signal, used to drive the synchronous detector circuit and to realize the second harmonic demodulation needed to measure the sensor output. A frequency divider which divided the oscillator frequency by two was built using D-flip-flop 4013BP IC.

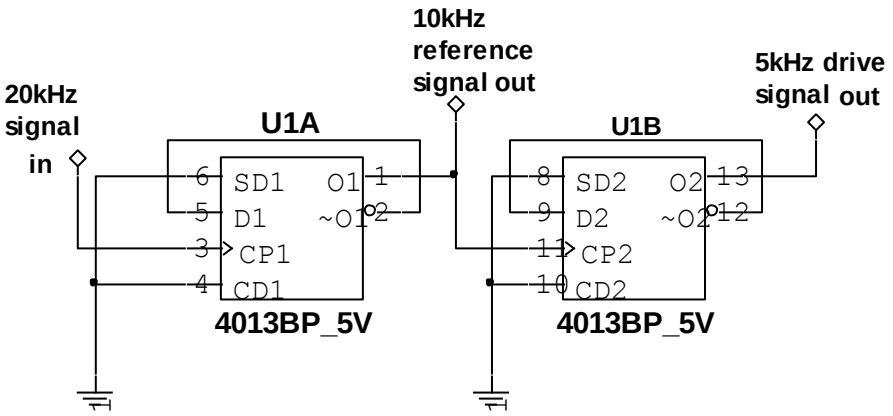

Figure 3.4: Frequency Divider Circuit

3.3.1.3 Voltage-to-Current Amplifier Circuit

The frequency divider output produce analog output voltage but the currents are weak and cannot be directly used to drive the magnetic core to saturation. The oscillator and the frequency divider can only produce a few tens of milli-amperes at most, while the sensor core requires many amperes. Hence, there is need for current amplification by using power transistors. Therefore, a complementary emitter-follower was used for efficient bipolar current amplification. Figure 3.5 shows a low-noise class-AB power amplifier used as current amplifier in this research by using NPN and PNP transistors Q1 and Q2 respectively. The two transistors Q1 and Q2 were configured as a complementary emitter-follower. The base of the two transistors was driven by the frequency divider circuit which in turn provided the excitation current needed to drive the excitation coil. Other amplifier circuits were also tried but this class-AB amplifier provided all the current required by the sensor.

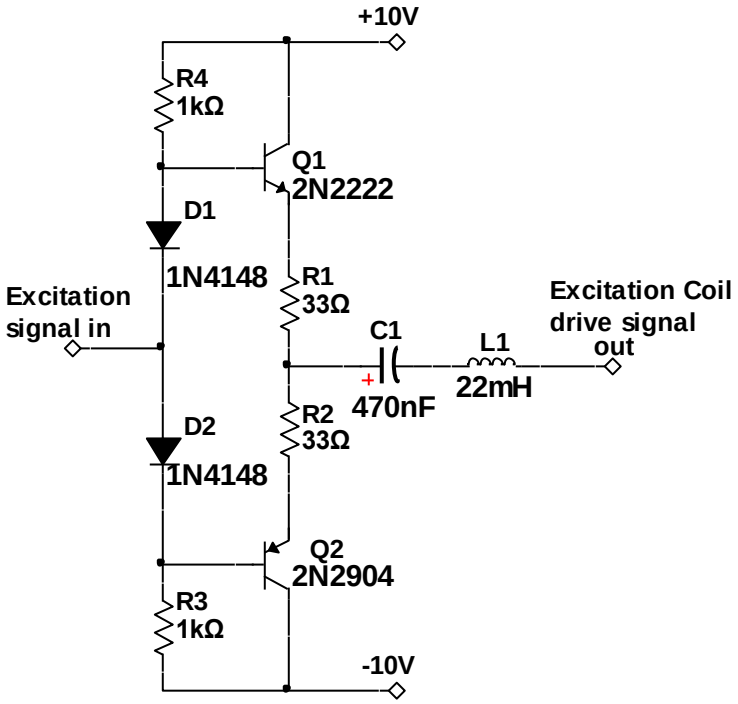

Figure 3.5: Voltage to Current Amplifier Circuit

As shown in Figure 3.5, transistors Q1 and Q2 formed a push-pull complementary amplifier. Resistor R4 and diode D1 biased the NPN transistor Q1 while D2 and R3 biased the transistor Q2. Resistors R1 and R2 set the operating current for the output of the transistors (equations in section 2.2.5.3). The two diodes serve to bias the transistors and reduce the cross-over distortion that occurs when the input waveform crosses zero. Without the diodes, the oscillator output would have to swing 1.2V to turn one transistor on and then bring the other transistor off. Capacitor C1 served to block the DC component of the current source from reaching the excitation resonant circuit. As shown in Figure 3.2, when transistor Q1 is turned on, capacitor C3 (Figure 3.2) is charged smoothly as the charging current is limited by inductor L1 (Figure 3.2). The main function of the inductor L1 is to limit the current drawn from the source for the fluxgate excitation current. This was achieved by the use of a high impedance (larger than the fluxgate sensor) inductor, which operates in the non-saturated mode over part of the excitation period. In the non-saturated state, the high impedance of the inductor limits the current flowing from the source to the excitation circuit.

In order to achieve high sensitivity and stability of the output signal of the fluxgate sensor, the excitation and pick-up coil tuning (ferro-resonance and parametric amplification modes described in section 2.2.5.6) was employed. The excitation coil was tuned to the frequency of excitation (5 kHz) with the aid of Capacitor C3 connected in parallel with excitation coil. C3 also served to increase the saturation current for the sensor coil without additional power consumption. The capacitor C4 (pickup tuning) served to increase the pickup coil output voltage and also to tune the output frequency of the pickup coil to twice the excitation frequency ($2f_{exc}$).

3.3.2 Fluxgate Magnetometer Sense Electronics

Fluxgate signal demodulation is usually accomplished with a phase sensitive detector, typically a CMOS analogue switch, which follows the operational amplifier. The information on the external magnetic field is extracted by a synchronous demodulation.

3.3.2.1 Synchronization Switch Circuit

Figure 3.6 shows the main section of the synchronization switch which was built around a PNP transistor (2N2906) and CD4066 quad analog switch low off-set, and resistors 1kΩ and 2.2 kΩ for R1 and R2 (see section 2.2.5.5 for equations) respectively. Other methods of fluxgate signal synchronization were also tried but the complexity and cost of the circuit put them at disadvantage. The CD4066 was chosen as a switch because of its low charge injection which makes it avoid further offset problems.

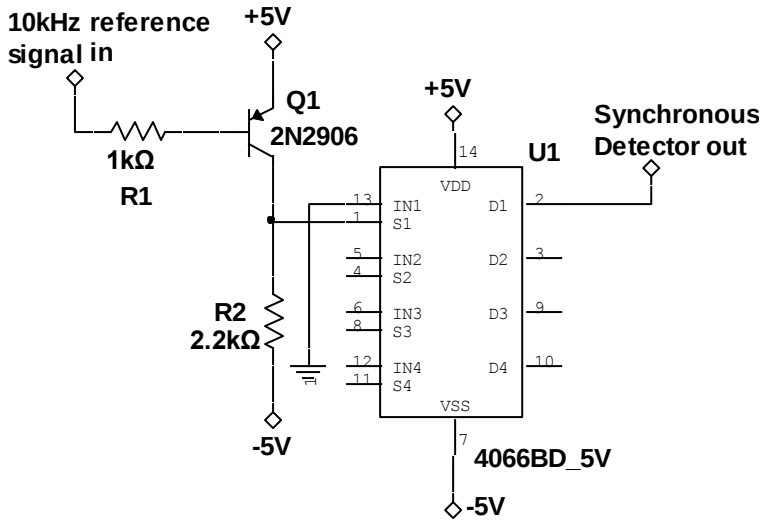

Figure 3.6: Sysnchronous Detector Circuit.

Since the analog switch (CD4066P) operates in the range of ±5 supply voltage, the reference signal (applied to the input of the transistor) needs to be translated. It should swing in the same range as the supply voltage. When the input signal at the base of the transistor is zero, the emitter voltage is more positive than the base voltage. This causes the output of the transistor at the collector to reach the maximum positive supply voltage. When base voltage from the reference reaches +5 volts it causes the output voltage of the transistor to reach its maximum negative supply voltage. The output of the transistor is being fed to the control pin (pin 1) of the analog switch. This switch will be turned on and off at the rate of the reference frequency (10 kHz). The output of the switch was connected to the input of the amplifier as shown in Figure 3.7. Depending on the phase relation between the analytical signal and reference signal, the modulated signal can be either totally recovered or discriminated. When the signal and the reference are in phase (0 degrees or 180 degrees), a strong DC term (positive for 0 degrees, negative for 180 degrees) is produced, which is proportional to the strength of the input signal. But when the reference and signal are out of phase (90 or 270 degrees), a zero DC term is produced completely rejecting the input signal. This circuit was used in order to reduce the bulky nature and cost of a commercial lock-in-amplifier with no

signal or performance degradation. The circuit is able to extract low level signals from high levels of noise. Its small size makes it easy to incorporate as a signal processor in fluxgate sensor systems.

3.3.2.2 Pick-up Coil Output Voltage Amplification Circuit

The pick-up coil of the fluxgate sensor detects the signal induced by the flux collapse (saturation) and flux recovery (de-saturation) of the core magnetizing current. This small induced voltage output signal of the pick-up coil was detected and it was compensated by amplifying and filtering the signal. The second harmonic component of the induced voltage across the pick-up coil was conditioned by using the electronics circuit built for the sensor. Figure 3.7 shows the circuit diagram of the amplification circuit.

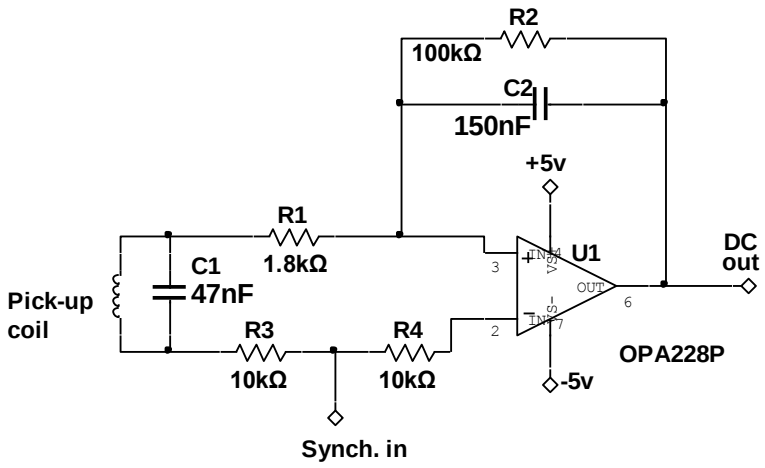

Figure 3.7: FMS Detection and Filter Circuit

As shown in figure 3.6, when the switch is open, the analytical signal passes through the (R1, R2) 1.8KΩ and 100KΩ resistors (see equations in section 2.2.5.4). When the switch is closed, the analytical signal reaches the output of OPA228P op-amp through the (R3, R4) 10KΩ and (R1, R2) 1.8KΩ and 100KΩ resistors path. The analytical signal will be recovered or demodulated as it comes out of the OPA228P which acts as a synchronous rectifier or demodulator. The output voltage from the pick-up coil is small compared to the reference voltage of the Analog to Digital Converter (ADC). A low noise operational amplifier

(OPA228) from Texas Instruments was used to design electronic circuit based on modified FOA results. This operational amplifier was used due to its ability to perfectly suit the system and its response time is much smaller than the sampling period of the ADC. The frequency of the voltage produced by the pick-up coil is the second harmonic of the excitation frequency. As shown in Figure 3.7, at very low frequencies (within the cut-off frequency or frequency response of the amplifier), the capacitor C2 was an open circuit and the gain of the signal conditioning circuit was high, which made it acted as an amplifier. Likewise low frequency occurs when no current goes through the capacitor C2, so the voltage across the resistor R1 was near zero.

3.3.2.3 Low Pass Filter

In order to reduce noise from external sources, the input signal to the ADC was filtered. Since any components of the signal from the pick-up coil at frequencies above the 10 kHz second harmonics frequency will only add noise to the wanted signal, these are not desired. To remove these unwanted signals, the amplifier was also configured as a low-pass Butterworth filter. A simple first order multiple-feedback Butterworth active Low Pass Filter (LPF) was used to remove the high-frequency components from the pick-up coil signal and produced a DC output voltage proportional to the applied external magnetic field. The main advantage with Butterworth filters is that it is linear in the pass band region (has no ripple). As shown in Figure 3.7, the signal conditioning circuit is a general form for first-order (one reactive element) low-pass filters. At high frequencies, capacitor C2 acts as a short circuit, so the gain of the amplifier goes to zero. The frequency was considered to be high when the large majority of current goes through the capacitor C2 and the magnitude of the capacitor C2 impedance is much less than that of feedback resistor R2. Since resistor R1 now has little effect on the signal conditioning circuit, the signal conditioning circuit acted as an integrator. The filter cut-off frequency of 10 Hz was used, because, the FMS was expected to be capable

of measuring the DC magnetic field and low frequency AC magnetic field below 10 Hz frequencies.

3.3.3 Analog to Digital Conversion of Fluxgate Sensor Output Signal

The output voltage of the modified FOA fluxgate sensor was converted to magnetic field by using 8051 microcontroller. The Liquid Crystal Display (LCD) was used to display numerical value of magnetic field by use of ADC. All the data processing is in digital form, so it is essential to use ADC. ADC 0804 IC (Integrated Circuit) was used. The range of input voltage was 0-5V. In this research, the input voltage was a DC (Direct Current) so as to get steady output on the LCD. If AC (Alternating Current) voltage is used as input to the ADC, it will display running numbers continuously due to the alternating nature of the AC voltage. The block diagram of the developed model FOA fluxgate magnetometer is shown in Figure 3.8.

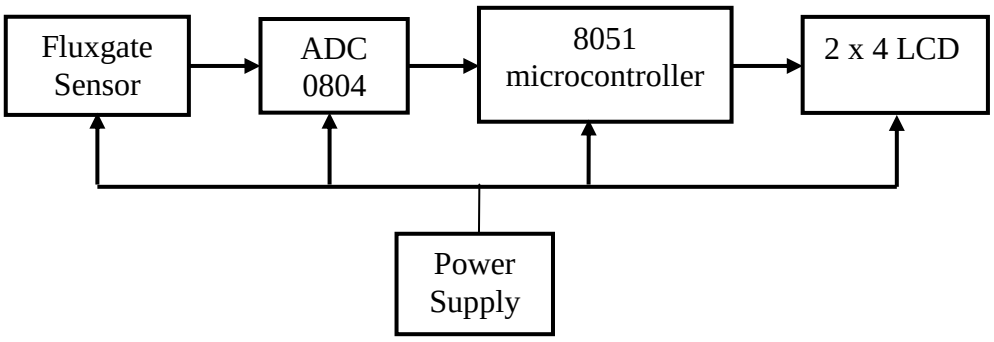

Figure 3.8: Block Diagram of Fluxgate Magnetometer Model

The magnetic field changes are detected by the fluxgate magnetometer. The analog output of the developed fluxgate magnetometer is digitized using Analog-to-Digital Converter (ADC) ADC0804. The digital output of ADC is simultaneously displayed on Liquid Crystal Display (LCD). The analog circuit of the developed modified FOA fluxgate sensor is shown in Appendix H1. The output voltage increases when fluxgate sensor is positioned along the sensitive axis (Figure 3.1). This sensor senses the changes in magnetic field and the analog output voltage of the fluxgate sensor is directly proportional to the external magnetic field strength being measured. This output is drawn through detection circuit (Figure 3.7) and is

given to ADC 0804. The digital stage implemented for the fluxgate sensor developed in this research is presented in Appendix H2.

The conversion of fluxgate sensor analog output to digital was achieved using ADC0804. It is required to convert the analog output of the fluxgate sensor (probe) to digital form for further processing. The conversion from analog data to digital data was achieved using ADC0804, which is a single channel ADC with 8-bit resolution. ADC0804 incorporates successive approximation method for conversion of analog data into its digital form (Texas Instruments, 2015). The microcontroller used in this research work is AT89C51. It is the heart of the developed fluxgate magnetometer which received the data from the fluxgate sensor through the detector circuit (Figure 3.7). The fluxgate sensor gives the output corresponding to changes in external magnetic field being measured. The purpose of the microcontroller is to process these data and display the processed data on LCD (Appendix H2). The AT89C51 is a low power, high performance CMOS 8-bit microcontroller with 8K bytes of flash memory, 256 bytes of RAM, 32 I/O lines, Watch dog timer, 2 data pointers, Two 16-bit timers/counters and clock circuitry. The LCD is the display unit at the user end. It will indicate the magnitude of the external magnetic field in micro Tesla (μT) values. The fluxgate sensor data (external magnetic field strength) received through ADC (Figure 3.8) is processed in the microcontroller and is fed to the LCD for display.

As shown in the circuit of Appendix H2, reference voltage input $V_{ref}/2$ pin (pin9) of the ADC0804 is left opened, which means that the input voltage can span between 0 to 5V and the step size will be 5/256 = 19.53mV (see Appendix H). The equation for the digital output of ADC0804 is D_{out} = Vin/Step size (see Appendix H). In this circuit, for a maximum input voltage of 4.8V, the digital output will be 4.8/19.53mV = 245 (see Appendix H) and so the binary equivalent of 245 is 11110101. Digital output of the ADC0804 was interfaced to port 1 (P1.0 to P1.7) of the microcontroller. Control signals for the ADC were INTR, CS, WR,

and RD (see Appendix H) were connected to the P3.4, P3.5, P3.6 and P3.7 pins of the AT89C51 microcontroller respectively. Liquid Crystal Display (LCD) (see Appendix H) was interfaced to port 2 of the AT89C51 microcontroller. Digital input of the LCD was interfaced to port 2 (P2.0 to P2.7) of the microcontroller. Control signals for the LCD were RS, RW, and EN (see Appendix H) were connected to the P3.0, P3.1, and P3.2 pins of the AT89C51 microcontroller respectively.

3.3.4 Power Supply

To provide a stable voltage to the excitation circuit, a voltage regulator circuit was used to maintain a stable supply voltage to excitation circuit. The power supply was used to provide all the voltages necessary for driving the various components along with reference voltages. This adds up to the regulated supply voltages of +5 V, ±10 V, and ground.

3.3.5 Fluxgate magnetometer Sensor

In this section, the results of the analytical model equations based on the PPO technique and modified FOA design of the FMS and the Helmholtz coils modeled in this research were verified experimentally. Due to the complex MEMS and PCB technologies manufacturing process, traditional wire-wound technology was used for FMS because the manufacturing process was relatively simple and production costs are low. Therefore, in order to carry out the experiments to validate the PPO and modified FOA design models of both the FMS and the Helmholtz coils, the FMS were assembled with excitation and pick-up coils based on the traditional wire-wound technology. The ring core used in the FMS was a commercially available MnZn ferrite, easy to get and cheap. The original size of ferrite ring core was not suitable for the core of FMS so the core was grounded (using grinding machine) to the required dimensions obtained from the analytical and modified FOA design results.

The dimension of the sensor core and number of excitation coil turns play an important role in matching the sensor excitation circuit of FMS, and, thereby reducing the excitation current

(Zorlu *et al.*, 2010; Lei *et al.*, 2011). The magnetic core material needs to be deeply saturated to avoid perming effect (Ripka, 2010). The excitation coil is a closed winding geometry shown in Figure 3.9, wound with the coil evenly distributed circumferentially on the ring core.

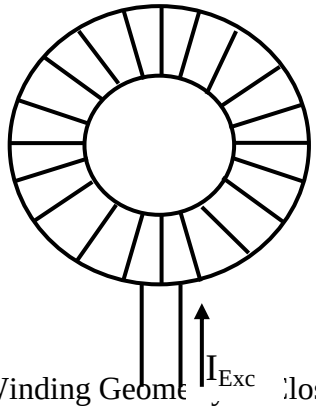

Figure 3.9: The Ring Coil Winding Geome[illegible]losed Winding Configuration.

The ring core used in this research was a commercially available MnZn ferrite (MMG, 2014). Manganese zinc ferrite was chosen as the core material because of its high resistivity which reduces eddy current in the core, low saturation flux density, and high relative magnetic permeability (datasheet is shown in **Appendix A**). Details of the core geometric dimensions and magnetic properties are shown in Table 3.1.

Table 3.1: Geometric and Magnetic Properties of MnZn Ferrite Ring Core (MMG, 2014).

Quantity	**Original core size**
Internal radius, r_1 (m)	0.004
Outer radius, r_2 (m)	0.009
Height, h (m)	0.004
Saturation flux density, B_{sat} (T)	0.38

Magnetic field strength, *H* (A/m)	796
Initial permeability	10000
Operation frequency, *f* (kHz)	10
Resistivity, ρ (Ω-m)	1
Density (g/m^3)	4900

The geometric dimensions of the original size of the MnZn ferrite ring core are shown in Figure 3.10. Radius, r_i is the internal radius of the magnetic core, radius r_o is the outer radius of the magnetic core, and height *h* is the magnetic core height.

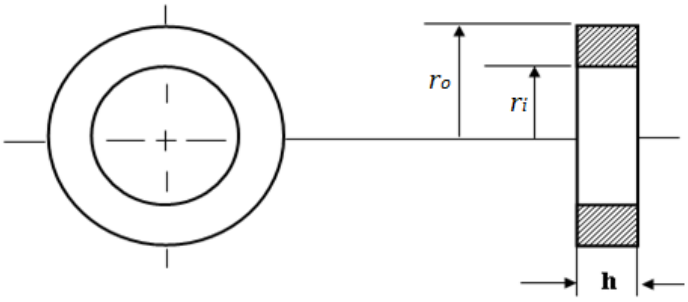

Figure 3.10: MnZn Ferrite Ring Core Geometric Dimensions.

The effective cross section area A_{eff} of the core material was calculated (Snelling, 1998) as:

$$A_{eff} = \frac{h \ln^2\left(\frac{r_o}{r_i}\right)}{\left(\frac{1}{r_i} - \frac{1}{r_o}\right)} \ (m^2) \qquad (3.1)$$

The effective magnetic path length l_{eff} was calculated as (Snelling, 1998):

$$l_{eff} = \frac{2\pi \ln\left(\frac{r_o}{r_i}\right)}{\left(\frac{1}{r_i} - \frac{1}{r_o}\right)} \ (m) \qquad (3.2)$$

where, where r_i is the internal radius of the core, r_o is the outer radius of the core and *h* is the height of the core.

When a high excitation current is applied to an excitation coil, the excitation magnetic field is produced; then, the curve of the B-H path causes the relative magnetic permeability to change

during the cycle (Platil and Ripka, 2012). The apparent permeability, μ_a, generally at specific flux densities and temperatures is calculated (Tumanski, 2013) as:

$$\mu_a = \frac{1}{\mu_0} \cdot \frac{B_{sat}}{H_{sat}} \tag{3.3}$$

where B_{sat} is the peak flux density in Tesla and H_{sat} is the peak magnetic field strength in A/m.

Therefore, with respect to the magnetic properties presented in Table 3.1,

$$\mu_a = \frac{1}{1.2568 \times 10^{-6}} \cdot \frac{0.38}{796}$$

Thus, the apparent permeability of the MnZn ferrite core is

$$\mu_a = 379.84$$

When a current runs through a wire, the wire gets hot because of Joule-heating. Joule-heating is generated when an electric current passes through a conductor (Kim *et al.*, 2011). To prevent the insulation of the wire from melting, a peak excitation current value must be found (Kim *et al.*, 2011). By taking demagnetization factor and temperature increase of the wire into account, the wire diameter of 0.361mm American Wire Gauge (AWG 27) with maximum current carrying capacity of 288 mA (PowerStream, 2013) was chosen as the excitation coil. The inner diameter of the ring was used to calculate the number of excitation coil turns because the wire turns used to be denser at the inner diameter than the outside diameter of a ring core. Therefore, the number of excitation coil turns N_{exc} is calculated as:

$$\mathrm{N_{exc}} = \frac{2\pi \mathrm{r_i}}{\mathrm{d_w}} \tag{3.4}$$

where, r_i is the inner radius of the magnetic core and d_w is the wire diameter.

$$\mathrm{N_{exc}} = \frac{2 \times 3.142 \times 0.004}{0.000361} \text{ turns}$$

$$\mathrm{N_{exc}} = 69 \text{ turns}$$

The excitation current value sets a limit to the magnetic field generated inside the magnetic core. Thus, the magnitude of the excitation current applied to the coil was calculated (Tumanski, 2013) as:

$$I_{exc} = \frac{\mathrm{H_{sat}} \cdot \mathrm{l_e}}{\mathrm{N_{exc}}} \tag{3.5}$$

Where N_{exc} is the number of turns of the excitation coil, I_{exc} is the excitation current needed to magnetize the core, H_{sat} is the magnetic field strength, and l_e is the effective magnetic path length the magnetic core.

By using equation (3.2) and considering the geometric dimensions given in Table 3.1, the effective magnetic path length, l_e = 0.0328 m for the MnZn ferrite core. The effective magnetic path length (equation (3.2)) was used to calculate the effective excitation current because the magnetic field is expected to be distributed across the core cross section.

Therefore, from equation (3.5),

$$I_{exc} = \frac{379.84 \times 0.03282}{69} \quad (A)$$

$$I_{exc} = 180.67\ mA$$

The excitation coil could still be driving at excitation current higher than the calculated value, because the calculated current is still within the 288mA range recommended by the manufacturer.

3.3.6 Magnetic Field Model of Fluxgate Magnetometer

This section examines the development of the model of magnetic field distribution in FMS core using the ANSYS finite element analysis package. The equations governing the Finite Element Method (FEM) and the basic structure of ANSYS program are described.

3.3.6.1 Finite Element Method

In this section, we present the specific procedure to compute the magnetic field distribution in a ferrite ring core. In this research, the FEM was used to find the magnetic fields distribution

in the magnetic core of the proposed FMS using three-dimensional (3D) magnetostatic analysis. Magnetostatic analysis is governed by the curl and divergence formula of Maxwell's equations (Hayt and Buck, 2006; Sadiku, 2010; Biswas and Banerjee, 2014):

$$\nabla \times \mathbf{H} = \mathbf{J} \tag{3.6}$$

$$\nabla . \mathbf{B} = 0 \tag{3.7}$$

Where the bold letters are the vector quantities, $(\nabla \times)$ is the curl operator, $(\nabla .)$ is the divergence operator, $\boldsymbol{H}$, and $\boldsymbol{J}$ are the vectors of the magnetic field strength (Amperes per meter), and the current density (Amperes per square meter). $\boldsymbol{B}$ is the vector of the magnetic flux density (Teslas or webers per square meter).

The magnetic flux density *B* expressed as the gradient of a scalar quantity V_m is written as (Hayt and Buck, 2006; Sadiku, 2010):

$$\mathbf{B} = -\nabla \mathrm{V_m} \tag{3.8}$$

Where V_m represents the scalar magnetic potential, $-\nabla V_m$ is the negative gradient of the scalar magnetic potential. Equation (3.8) implies that the negative gradient scalar magnetic potential equals the magnetic flux density. By principle, the curl of the gradient of any scalar is identically zero. In regions of space where current is zero, the current density *J* is zero (Hayt and Buck, 2006; Sadiku, 2010; Biswas and Banerjee, 2014):

$$\nabla \times \mathbf{B} = 0 \tag{3.9}$$

The divergence of the magnetic flux density *B* is zero and can be expressed as (Hayt and Buck, 2006; Sadiku, 2010):

$$\nabla . \boldsymbol{B} = 0 \tag{3.10}$$

By substituting equation (3.8) into equation (3.10), the divergence of the gradient of the scalar field is also zero (Hayt and Buck, 2006; Sadiku, 2010):

$$-\nabla . \nabla \mathrm{V_m} = 0 \tag{3.11}$$

or

$$\nabla^2 V_m = 0 \quad (\mathbf{J} = 0) \tag{3.12}$$

Equation (3.12) is useful to calculate the magnetic field in magneto static cases (Hayt and Buck, 2006). These equations represent the behavior of the entire system, the boundary conditions are imposed, and the solution is generated (Sadiku, 2010).

3.3.6.2 ANSYS Program Structure

ANSYS package was operated in the graphical user interface (GUI method) mode in which a program file is read into the ANSYS processor and the output results are written to an output file (ANSYS, 2011). This method is in contrast to using the command file approach to enter and analyze the model (Biswas and Banerjee, 2014). The GUI method is simpler to perform analysis as the GUI has been developed (ANSYS, 2014). This makes the software user friendly as compared to command file approach, which is a little bit difficult (ANSYS, 2014). Although, the command file approach requires minimum file space and the entire analysis can be described in a small text file (ANSYS, 2014). Therefore, in this research, a GUI method in ANSYS was used to generate and analyze the magnetic field distribution. The flowchart for the implementation of the magnetic field modeling and simulation in this research based on the ANSYS processing stages is illustrated in Figure 3.11.

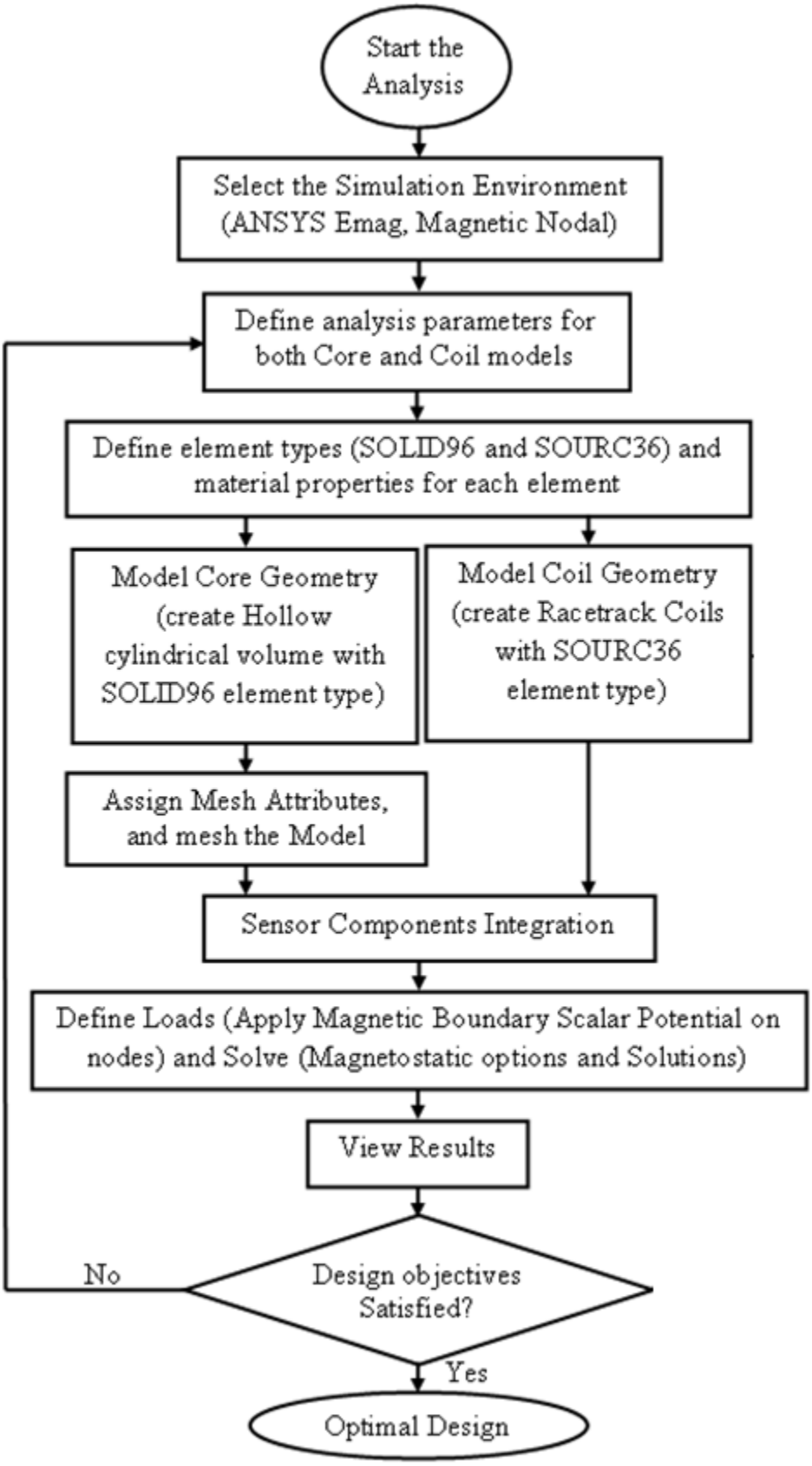

Figure 3.11: ANSYS Finite Element Analysis Flowchart for the Magnetic Field Modeling

The ANSYS environment is divided into three subsections such as preprocessing stage, solution stage, and post-processing stage:

1. The preprocessor (/PREP7) stage is where the model of the magnetic system was developed. In this stage, general modeling parameters were defined such as:
    a. Define the Physical Environment

        In order to ensure availability of the elements needed for performing 3-D static analysis in ANSYS environment, the Magnetic-Nodal was specified from the list of the magnetic analysis types. The SOLID96 element was employed to model the magnetic core material while the SOURCE36 element was used to represent the current-conducting regions (details provided in Appendix B). This is to ensure that the source field created by SOURCE36 elements closely matched the boundary conditions on the meshed domain, the source elements were placed so that the resulting saturating field fulfilled the boundary conditions for the total field.

        Each material such as air, permeable materials, and current-conducting regions has certain required material properties. This is why data for various materials with their magnetic properties are embedded in the ANSYS material's library. In the model used in this research, the material properties (see Table 3.1) were used as the new material models. The material usually saturates at approximately 380 mT (MMG, 2014). The material properties for MnZn ferrite are presented in Appendix A. The SOURC36 element was chosen for the coil windings. The material properties for the air surrounding the core and coil were chosen as a constant with relative permeability of 1.

    b. Build the Core and Racetrack Coil Models and Mesh the Core

        In order to construct the three-dimensional (3-D) model, volume was chosen for the 3-D drawing of the ring core. In a 3-D scalar magnetostatic analysis, current

sources were not modeled as an integral part of the sensor excitation core and coil geometry, because the SOURCE36 elements are not true finite elements and are in a two-dimensional 2-D analysis (ANSYS, 2014). Therefore, a dummy finite element, SOURCE36 was used to represent the shape and location of current sources (ANSYS, 2014). The magnitude of current applied to the coil was specified as element real constant (see Appendix B). Plate 3.1 shows the model of the ring core without coil windings.

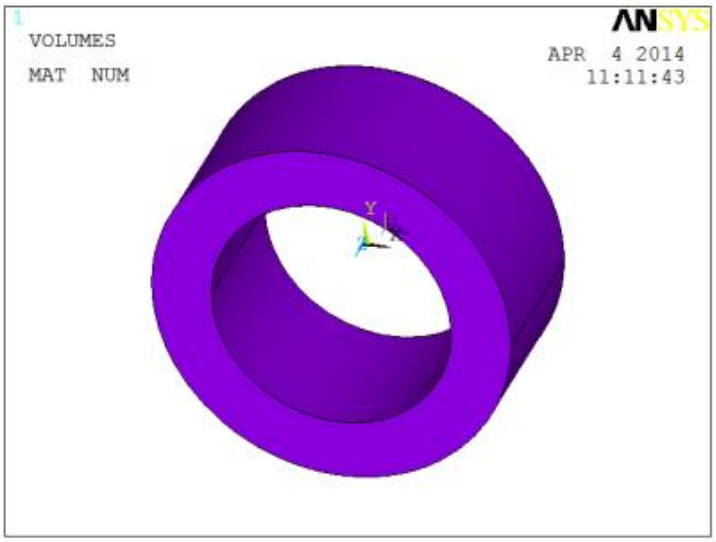

Plate 3.1: Fluxgate Sensor Magnetic Core Model with SOLID96 Element.

To generate the mesh, suitable dimensions of the elements were chosen while the adaptive mesh refinement was utilized. The adaptive refinement of the mesh consists of making a finer mesh at the spatial points that are more irregular, such as corners, regions with irregular borders. The attributes were then assigned to each component in the model. Attributes are the element types and options, element coordinates, and material properties. The area representing the magnetic core consists of approximately 3,216 nodes forming over 14,896 elements were obtained from the ANSYS program. Plate 3.2(a) shows the meshed model of the fluxgate sensor core with coil windings modeled around the ring core volume as shown in Plate 3.2(b).

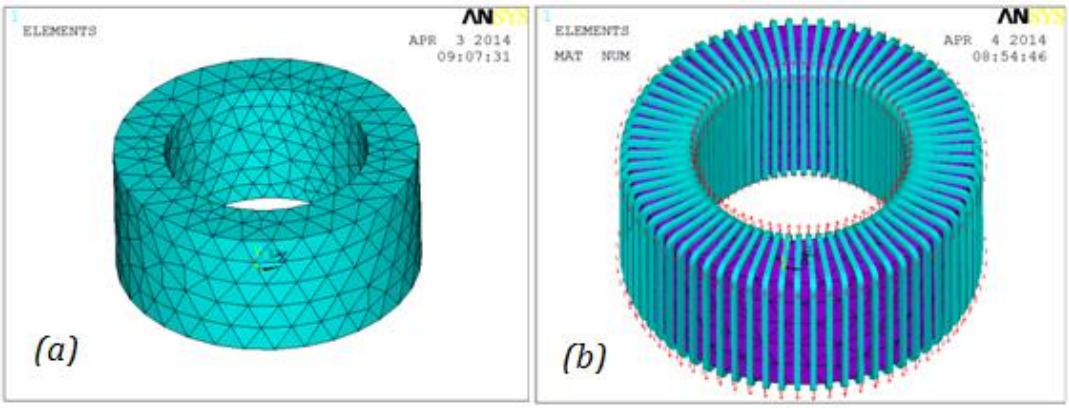

Plate 3.2: Meshing of the Fluxgate Sensor Core Model

c. Magnetic Core Model Excitation

In this section, boundary conditions were specified such that no flux escapes and the magnetic flux travel parallel to the boundary lines set by the geometry of the magnetic core. This was carried out by using magnetic scalar potential (MAG) in the ANSYS to specify flux-normal (ANSYS, 2014). Excitation current was also applied through the SOURC36 element by invoking the RACE macro because the RACE macro allows the ANSYS user to define a racetrack current source in the working plane coordinate system (ANSYS, 2011). The current flows in a counterclockwise direction with respect to the working plane.

2. The solution processor (/SOLU) is the stage at which the finite element solutions were generated. As shown in Plate 3.3, the magnetic analysis was solved and the solution was obtained. The 3-D static scalar magnetic analysis in the fluxgate magnetic core was solved using Generalized Scalar Potential (GSP) as the model include excitation coil and magnetic material with closed magnetic circuit (see Appendix B).

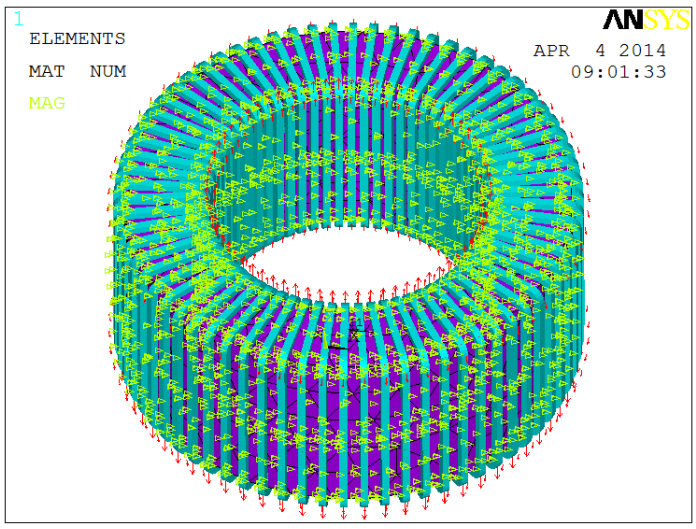

Plate 3.3: Magnetic Ring Core, Excitation Coil, and Specified Scalar Potential.

This was in contrast to the Reduced Scalar Potential (RSP) which is recommended for model with only coil or magnetic material and Difference Scalar Potential (DSP) method which is meant for only the model with open magnetic circuit such as rod core but with excitation coil. The GSP method in ANSYS required three load steps solution sequence:

a. The first load step calculated the approximate solution for only the magnetic core material.

b. The second load step found the solution for only the free space (air) and

c. The last load step calculated the final solution.

Therefore, in the solution processor, the analysis type and options were defined, loads were applied, and ensure that at least one node in the magnetic core region was assigned a scalar potential value of zero. The ANSYS electromagnetic analysis solution was then performed and the convergence norms were computed with corresponding convergence criteria for each equilibrium iteration. ANSYS considered a solution to be converged whenever specified convergence criteria were met.

3. In the postprocessor stage, the outputs were generated using /POST1 for static magnetic field. One of the most important steps in the magnetic field analysis is to

view the results of an analysis so as to understand the effects of the applied loads on the design. In ANSYS, POST1 general processor is used to review the results for magnetostatic analysis while POST26 is used to review the results for transient state analysis. Using the post-processor in this work, the contours of the magnetic field distribution were displayed and obtained.

3.3.7 Fluxgate Sensor Design

In this section, optimization of the entire fluxgate magnetometer was carried out based on the analytical model that included the sensor core, pick-up coil, and detection circuit. The analytical model was numerically solved using modified Firefly Optimization Algorithm (FOA) to simultaneously find the optimum FMS configuration subject to large set of parameters such as, sensor core, pick-up coil, and the noise of the detection circuit. The optimization routines based on modified FOA for selecting optimum design for FMS and Helmholtz coils, optimization results and experimental verification were discussed. Also, in order to check the effectiveness of the proposed modified FOA technique in this research, two different FMS were designed based on Part-by-Part Optimization (PPO) technique. The fluxgate magnetometer core was designed to obtain the optimum sensor core dimensions, geometry of the pick-up coil was then selected, and, a low noise detection circuit was finally developed based on FOA results.

3.3.7.1 Part-by-Part Optimization Design of Fluxgate magnetometer

In order to optimize the performance of fluxgate magnetometers, Part-by-Part Optimization (PPO) technique of finding the optimal dimensions of the sensors core was employed by designing the magnetometer part-by-part. The core of the fluxgate magnetometer was first designed analytically to obtain the optimum geometric dimensions of the core and pick-up coil, distribution of the pick-up coil over the sensor core was then selected, and, finally developed a low noise detection circuit.

The original size of the MnZn ferrite ring core was not suitable for the core of FMS because it had been demonstrated from the results of both the analytical calculations and the FEA of the magnetic flux density distribution (see section 3.3.2.3) that this ring core requires very high excitation current and will consume large power. The excitation current reduction method employed in this research work was by reducing the core material structure (Zorlu *et al.,* 2010). In order to compare the results of the proposed modified FOA technique and the part-by-part optimization technique (see section 2.2.13), and to investigate the effect of demagnetization (see section 2.2.9) of the ring core, two different ring core geometric dimensions were obtained. The details of their geometric dimensions and magnetic properties are presented in Table 3.2. The core was grinded and polished to the required size by using grinding machine. Structural view of the magnetic cores obtained from the modification of the original ring core is depicted in Figure 3.12.

Table 3.2: Geometric Dimensions of different Ring Cores.

	Values	
Quantity	**Core A**	**Core B**
Internal radius, r_1 (mm)	4	4
Outer radius, r_2 (mm)	7	5
Height, h (mm)	2	3

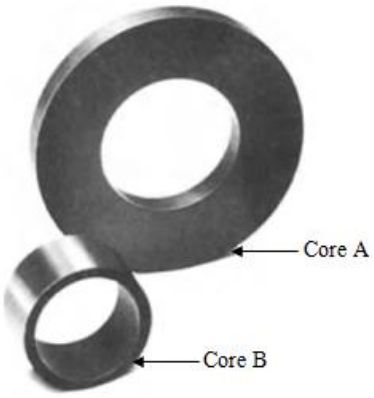

Figure 3.12: Structural view of the Magnetic Cores obtained.

The number of turns of pick-up coil used for the signal detection determines the sensitivity of the sensor (Lu and Huang, 2015). However, thermal noise of the sensor increases because of increasing resistance of the pick-up coil caused by increase in the number of pick-up coil turns (He and Shiwa, 2014). Another factor that affects the sensitivity is the placement of the coil. Coils wound around the ring core should be placed around the middle of the core, and planar sensing coils should be placed around the edges of the core (Zorlu, 2008).

The number of turns of pick-up coil with respect to the geometric dimensions of the two magnetic cores realized (presented in Table 3.3) was calculated as (Tumanski, 2013):

$$N_s = \frac{2.r_o\,.h_c}{d_w^2} \tag{3.13}$$

Where r_o is the core outside diameter, h_c is the core height, and d_w is the wire diameter including insulation.

To prevent the insulation of the wire from melting, a peak excitation current value must be found (Kim *et al.,* 2011). By taking demagnetization factor and temperature increase of the wire into account, the wire diameter of 0.226mm (AWG 31) with maximum current carrying capacity of 113 mA (PowerStream, 2013) was chosen as the excitation coil. Therefore, by using equation (3.13), sensor A pick-up coil winding turns were found to be:

$$N_s = \frac{2 \times 0.007 \times 0.002}{(0.226 \times 10^{-3})^2}\ turns$$

$$N_s = 548\ turns$$

While sensor B pick-up coil winding turns were found to be:

$$N_s = \frac{2 \times 0.005 \times 0.003}{(0.226 \times 10^{-3})^2}\ turns$$

$$N_s = 587\ turns$$

The amplitude of the second harmonic voltage V_{2f} induced in the sensor pick-up coil with respect to the geometric dimensions of the core and the applied magnetic field was found (Tumanski, 2011; Tumanski, 2013; Miles *et al.*, 2013) by:

$$V_{2f} = 2.\pi.f_{exc}.N_s.\mu_0.\mu_a.A_c.H_{ext} \quad (3.14)$$

Where f_{exc} is the excitation frequency (Hz), N_s is the number of turns of the pick-up coil, μ_0 is the permeability of air, μ_a is the apparent permeability of the core material, A_c is the cross-section area of the magnetic cores, and H_{ext} is the applied external magnetic field in Oested.

Equation (3.14) represents the output voltage of the pick-up coil and shows that the output voltage of the pick-up coil is proportional to the excitation frequency, number of turns of pick-up coil, apparent permeability of the core, cross sectional area of the magnetic core, and the applied external magnetic field.

The voltage sensitivity S_{sen} of the sensors was calculated by using the relation (Tumanski, 2013):

$$S_{sen} = \frac{\text{change in output}}{\text{change in input}}$$

That is,

$$S_{sen} = \frac{dV_{2f}}{dH_{ext}} \quad (3.15)$$

where V_{2f} is the second harmonic voltage of the excitation signal, and H_{ext} is the external magnetic field. $V_s = \omega_o n A \mu_o \mu_e H_{ext}$

The detection circuit model of FMS pick-up coil circuit is shown in Figure 3.13 while the sources of noise in a FMS element are illustrated in Figure 3.14.

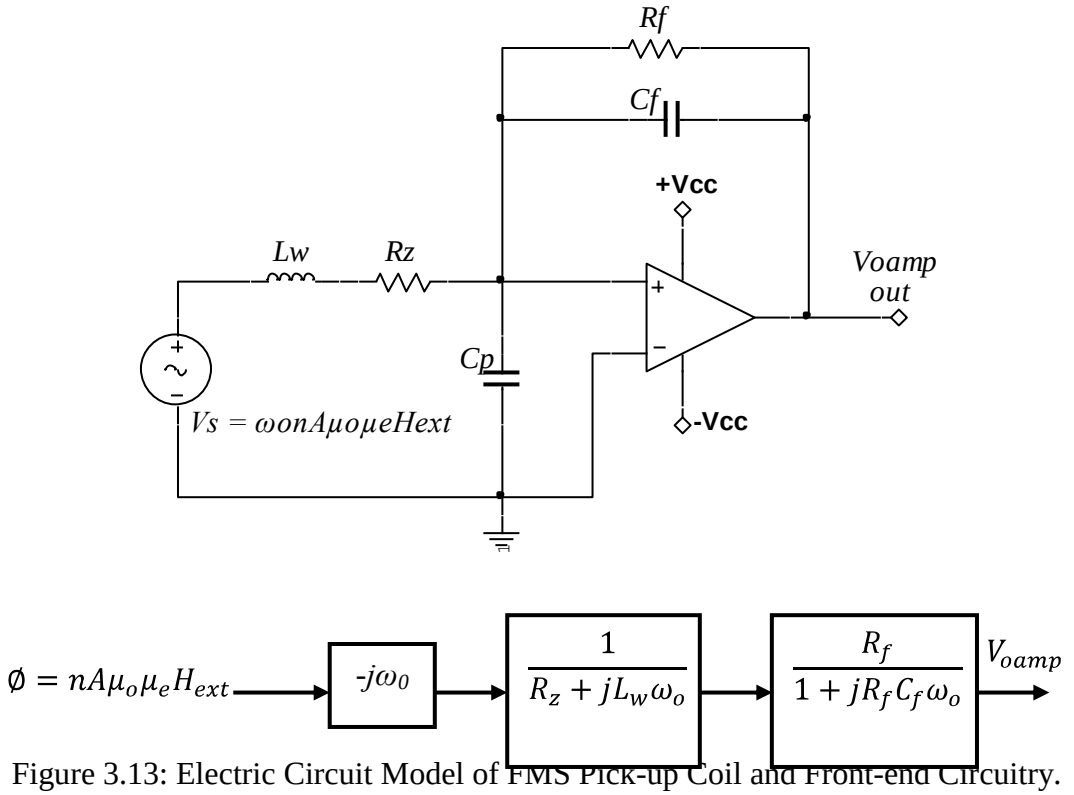

Figure 3.13: Electric Circuit Model of FMS Pick-up Coil and Front-end Circuitry.

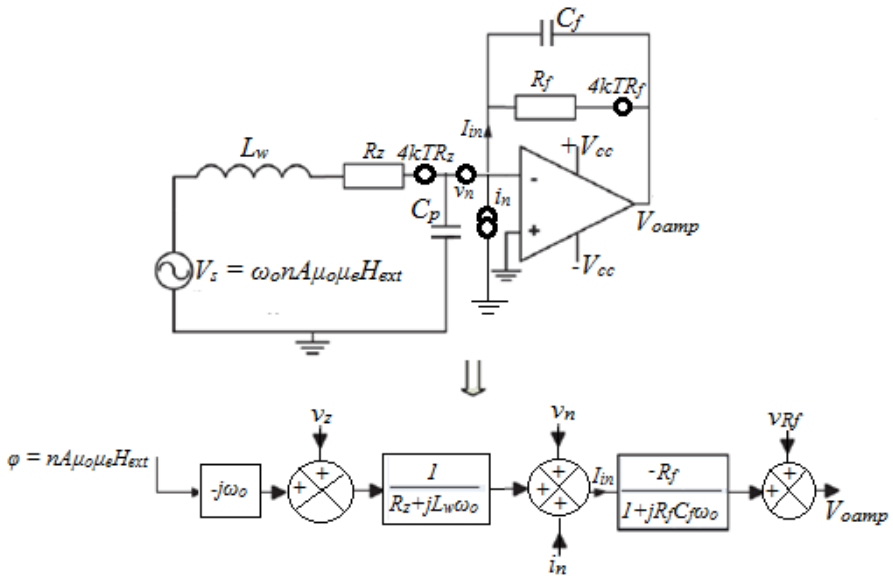

Figure 3.14: Noise Sources in Equivalent Circuit of Pick-up Coil Connected to an Amplifier.

In order to calculate the performance of the designed FMS associated with the detection circuit, the frequency response of FMS detection amplifier was computed as (Han *et al.*, 2012; Chen *et al.*, 2015):

$$V_{oamp} = \frac{R_f}{R_z} \cdot \frac{V_{2f}}{1 + \left(\frac{L_w + R_f C_f}{R_z}\right) j\omega - \frac{R_f}{(R_z)} . L_w C_f \omega^2} \quad (3.16)$$

The total sensitivity S_{tot} of the FMS was expressed as:

$$S_{tot} = \frac{R_f}{R_z} \cdot \frac{S_{sen}}{1 + \left(\frac{L_w + R_f C_f}{R_z}\right) j\omega - \frac{R_f}{(R_z)} . L_w C_f \omega^2} \quad (3.17)$$

Where, $R_z = R_w + R_g$, R_w is the pick-up coil winding resistance, L_w is the pick-up coil inductance, C_f is the amplifier feedback capacitor, R_f is the amplifier feedback resistor.

The spectral density of the total noise of the FMS and the amplifier (shown in Figure 3.8) referred to the coil input was found as (Chen *et al.*, 2015):

$$V_{tot} = v_{rw} + v_{rg} + v_{amp} + i_{amp} + v_{rf} \quad (3.18)$$

Where v_{tot} is the spectral density of the total sensor noise, v_{rw} is the spectral density of the pick-up coil thermal noise, v_{amp} is the spectral density of the amplifier voltage noise, i_{amp} is the spectral density of the amplifier current noise, v_{rf} is the spectral density of the amplifier feedback resistor thermal noise and v_{rg} is the spectral density of the amplifier gain resistor thermal noise.

Therefore, the spectral density of the pick-up coil thermal noise (Chen *et al.*, 2015)

$$v_{rw} = 4kT_0R_w \cdot \frac{1}{R_w^2 + (L_w\omega)^2} \cdot \frac{R_f^2}{1 + \left(R_w C_f \omega\right)^2} \quad (3.19)$$

Where k is the Boltzmann constant, T_0 is the absolute temperature in kelvin, R_w is the pick-up coil winding resistance, L_w is the pick-up coil inductance, C_f is the amplifier feedback capacitor, R_f is the amplifier feedback resistor.

Resistance R_w of the pick-up coil was (Chen *et al.*, 2015):

$$R_w = \frac{4.\rho.n.l_m}{\pi.d_w^2} \quad (3.20)$$

Where ρ is the resistivity of the wire, l_m is the total length of the sensor pick-up coil.

Height T_w of pick-up coil layers was:

$$T_w = d_w + (n_{Tw} - 1)\frac{\sqrt{3}}{2}d_w \quad (3.22)$$

Where n_{Tw} is the number of turns required to make up coil height.

Coil axial length b_w was expressed as:

$$b_w = d_w + (n_{bw} - 1)d_w \quad (3.21)$$

Where n_{bw} is the number of turns required to make up coil axial length.

Total length l_m of pick-up coil winding was calculated by using:

$$l_m = 2d_o + h + 2T_w + 4t_b \quad (3.23)$$

Where h is the core height and t_b is the pick-up coil bobbin thickness.

The spectral density of the amplifier voltage noise was:

$$v_{amp} = \frac{v_n^2}{R_w^2 + (L_w\omega)^2} \cdot \frac{R_f^2}{1 + \left(R_w C_f \omega\right)^2} \quad (3.24)$$

Where v_n is the voltage noise of the amplifier.

The spectral density of the amplifier current noise was found by equation (3.25) as:

$$v_{iamp} = i_n^2 \cdot \frac{R_f^2}{1 + \left(R_w C_f \omega\right)^2} \quad (3.25)$$

Where i_n is the current noise of the amplifier.

The spectral density of the amplifier feedback resistor thermal noise (Coillot *et al.*, 2010; Chen *et al.*, 2015; Motchenbacher and Connelly, 1993)

$$v_{rf} = 4kT_0R_f \quad (3.26)$$

The spectral density of the amplifier gain resistor thermal noise was:

$$v_{rg} = 4kT_0R_{rg} \quad (3.27)$$

Where R_{rg} is the amplifier gain resistor.

The FMS noise is defined as $H_n(f)$ for which the induced voltage of equation (3.16) equals the spectral density of the total noise of equation (3.18) and is expressed (Richard and Kenneth, 1989) as:

$$H_n(f) = \frac{\sqrt{v_{tot}}}{S_{tot}} \tag{3.28}$$

Where H_n is the equivalent magnetic noise, S_{tot} is the total FMS sensitivity.

Equation (3.28) represents the equivalent magnetic field noise of the whole sensor system after processing the output signal of the pick-up coil. Equation (3.15) through equation (3.28) shows that the equivalent magnetic field noise H_n is dependence on the dimension and geometric parameters of the sensor core, pick-up coil, and detection circuit. The dimension and geometric parameters of the sensor materials include the variables such as core outside diameter, core inside diameter, core height, coil bobbin thickness, amplifier gain resistor, amplifier feedback resistor and capacitor.

3.3.7.2 FOA Design of Fluxgate Magnetometer and Helmholtz Coils

In section 3.3.6.1 above, PPO approach of optimizing the fluxgate magnetometer was discussed. However, such part-by-part optimization design approach does not usually produce optimal magnetometer performance (Grosz and Paperno, 2012).

Optimization of the entire fluxgate magnetometer was carried out based on analytical model that included the sensor core dimension, the pick-up coil winding geometry and dimensions, and the noise of the detection circuit. Analytical model was numerically solved by using Firefly Optimization Algorithm (FOA) to simultaneously finding the optimum dimensions and geometry of the sensor core, pick-up coil, and detection circuit elements subject to a set of parameters such as, core thickness, core and coil aspect ratio, pick-up coil volume, output voltage of the detection circuit as the optimization constraints.

The modified FOA was written in MATLAB program to perform the optimization. The section provides an overview of the techniques employed by MATLAB to determine the optimum design. Then, the modified FOA written to interact with MATLAB to optimize the fluxgate magnetometer was explored. Some of the problems encountered in creating this function were examined, and the engineering choices made are discussed. An examination of the bounds selected for the optimization variables is given. Finally, the optimization was performed to select the best possible dimensions and geometry of sensor core, pick-up coil, and detection circuit elements for fluxgate magnetometer performance with respect to voltage sensitivity and noise level, and the results of the optimization are presented and discussed.

The FMS problem involves large number of design variables. Most of these variables have influence either on the objective function (sensor size, pick-up coil, and detections circuit) or on the specific constraints (geometric dimensions). The goal of the optimization in this research is to simultaneously optimize the variables of a pick-up coil, magnetic core and the detection circuit that minimize the magnetic field noise and enhances the voltage sensitivity.

The algorithm starts by placing the fireflies in random locations. The location of a firefly corresponds to the values of the parameters (geometry and dimensions of the FMS magnetic core, pick-up coil, and detection circuit) for the objective function (reducing the core size, reducing the noise level, and enhancing the voltage sensitivity of the sensor) to be solved. Then from each firefly's newly acquired position, the objective function is evaluated, and the firefly's light intensity is set as the inverse evaluation. The inverse is used since the goal is to minimize the objective function. Thus a lower function evaluation will result in a higher light intensity.

In order to ease the problem of high dimensionality, ten design variables were identified and are presented in Table 3.3. The geometry constraints and operating limits are shown in Table 3.4.

Table 3.3: Fluxgate Sensor Design Variables and Ranges

Variables	**Range**	**Unit**
Core outside diameter	10 – 20	mm
Core inside diameter	8 – 18	mm
Core height	1 – 4	mm
Number of Layers of Pick-up coil	5 – 150	-
Pick-up Coil bobbin thickness	1 – 10	mm
Pick-up coil axial length turns	5 – 150	-
Amplifier Feedback resistor	1 – 270	kΩ
Pick-up coil inductance	4 – 10	mH
Amplifier feedback capacitor	100 – 180	nF
Amplifier input resistor	1 – 5	kΩ

Table 3.4: Fluxgate Sensor Design Constraints

Variables	**Range**	**Unit**
Core thickness	≤ 3.0	mm
Pick-up wire diameter	≤ 0.361	mm
Sensor winding turns	≤ 2000	-
Core aspect (diameter to height) ratio	≤ 10	-
Coil aspect (length to height) ratio	≤ 20	-
Amplifier output voltage	≤ 5.0	-

These design variables were represented as:

$$X = [x_1, x_2, \ldots x_{10}] = \begin{bmatrix} Core\ outside\ diameter \\ Core\ inside\ diameter \\ Core\ height \\ Sequential\ winding\ layers\ of\ pickup\ coil \\ Pick-up\ coil\ bobbin\ thickness \\ Sequential\ axial\ winding\ of\ pickup\ coil \\ Amplifier\ feedback\ resistor \\ Pick-up\ coil\ inductance \\ Amplifier\ feedback\ capacitor \\ Amplifier\ input\ resistor \end{bmatrix}^T \quad (3.29)$$

While the geometry constraints and operating limits were represented as:

$$g(x) \leq 0 \Leftrightarrow \left\{ \begin{array}{c} \text{core thickness} \leq 0.003 \\ \text{pickup coil winding turns } \leq 2000 \\ \text{core aspect ratio} \leq 10 \\ \text{coil aspect ratio } \leq 20 \\ \text{pick} - \text{up wire diameter} \leq 0.361 \\ \text{Amplifier output voltage } \leq 5.0 \end{array} \right\} \tag{3.30}$$

The optimization design of FMS problem was formulated by defining the minimum equivalent magnetic noise as the objective function as:

$$Minimize\ H_n(x) = \frac{\sqrt{v_{tot}}}{S_{tot}} \tag{3.31}$$

The goal of the optimization of Helmholtz coils in this section was to find the optimal number of coils turns and suitable coil geometry of the Helmholtz coils that minimize the driving current coil current and magnetic field of the Helmholtz coils. The algorithm starts by placing the fireflies in random locations. The location of a firefly corresponds to the values of the parameters (number of turns and geometry Helmholtz coils) for the objective function (Coil current and magnetic field) to be solved. Five design variables were identified and are presented in Table 3.5. The geometry constraints and operating limits are shown in Table 3.6.

Table 3.5: Helmholtz Coils Design Variables and Ranges

Variables	**Range**	**Unit**
Coil width turns	10 – 50	-
Coil height turns	5 – 50	-
Wire diameter	0.135 – 1.0	mm
Coil radius	0.1 – 0.25	m
Coil current	10 – 250	mA

Table 3.6: Helmholtz Coils Design Constraints

Constraints	**Range**	**Unit**
Total winding turns	≤ 2500	-
Magnetic field	≤ 500	μT

The design variables were written as:

$$X = [x_1, x_2, \dots x_5] = \begin{bmatrix} \text{Coil width turns} \\ \text{Coil height turns} \\ \text{Wire diameter} \\ \text{Coil radius} \\ \text{Coil current} \end{bmatrix}^T \tag{3.32}$$

The geometric constraints and operating limits were represented as:

$$g(x) \leq 0 \Leftrightarrow \begin{Bmatrix} \text{Total winding turns} \\ \text{Total magnetic field} \end{Bmatrix} \tag{3.33}$$

The optimization design problem of the Helmholtz coils was formulated by defining the magnetic field inside the Helmholtz coils as the objective function:

$$Minimize\ B(z) = \frac{\mu_0 . I_c . R^2}{2} . \begin{pmatrix} \left(\left(z + \frac{R}{2}\right)^2 + R^2\right)^{-\frac{3}{2}} \\ + \left(\left(z - \frac{R}{2}\right)^2 + R^2\right)^{-3/2} \end{pmatrix} \tag{3.34}$$

The multiple objectives in this research using FOA were implemented based on the following steps:

1. Initialize the number of fireflies, *n*, biggest attraction β_0, absorption coefficient of light intensity γ, step size factor α, and maximum number of iterations or generations t_{max}.
2. Initialize the positions of fireflies randomly, namely initializing design variables of the FMS parameters (magnetic core, pick-up coil, and detection circuit), the values of objective function (noise level) of fireflies are set as their maximum brightness of fluorescence I_0.

3. Calculate relative brightness and attractiveness of fireflies, which belong to the population. The direction of movement depends on the relative brightness of fireflies. Here (Yang, 2013):

$$I = I_0 \times e^{-\gamma r i j} \tag{3.35}$$

$$\beta = \beta_0 \times e^{-\gamma r i j} \tag{3.36}$$

where I_0 is the maximum fluorescence brightness of the firefly, namely the fluorescence brightness itself (r = 0), which depends on the value of the objective function. β_0 is the maximum attractiveness, namely the attractiveness of the light source (r = 0). γ is the absorption coefficient of the light intensity. The fluorescence will gradually weaken according to the increasing distance and the absorption of media. The absorption coefficient of light intensity is set to reflect this feature. r_{ij} is the spatial distance between firefly i and j.

4. Update the spatial positions of fireflies. Random perturbations are injected to the firefly with the best position. The updated equation is:

$$x_i = x_i + \beta \times (x_j - x_i) + \alpha \times (rand - 0.5) \tag{3.37}$$

where x_i, x_j represent the spatial positions of firefly i and j, respectively. α is the step size factor. *rand* is random factor distributed uniformly in [0,1].

5. Recalculate the brightness of fireflies according to the updated positions.
6. Return to Step 3 until the search precision is met or the maximum number of generations is achieved.

When the modified FOA was first executed for the fluxgate magnetometer, the maximum output voltage of the amplifier obtained was smaller than expected (see Table E4). This can be explained by examining the outside diameter obtained for the sensor core. This core dimension would be good for minimum volume design, the choice was to increase the pick-up coil winding turns, since this would increase the sensor sensitivity for a given number of

pick-up coil turns. However, as the coil turns increases, two effects were considered. First, for larger coil turns, the weight of sensor increases. Second, the resistance of larger pick-up coil is larger, so complex detection circuit is required to overcome the thermal noise caused by the larger winding resistance. So, the optimization routine found a balance between the sensor core dimensions by running a FOA sensitivity analysis (Appendix F).

3.3.8 Fluxgate Sensors Fabrication

Based on the optimum values of the dimensions and geometric parameters obtained from the analytical calculations for PPO and modified FOA design, three FMS prototypes were fabricated and studied. Parameters and the values of the two analytical models and the modified FOA model are contained in Table 3.7.

Table 3.7: Optimum values of modified FOA and PPO Model Sensors

Parameters	**Modified FOA Sensor**	**PPO Sensor A**	**PPO Sensor B**	**Unit**
Core outside diameter	12.00	14.00	10.00	mm
Core inside diameter	8.00	8.00	8.00	mm
Core height	2.00	2.00	3.00	mm
Number of Pick-up coil turns	646	548	587	-
Pick-up Coil bobbin thickness	5.00	-	-	mm
Amplifier Feedback resistor	100.00	100.00	100.00	kΩ
Amplifier feedback capacitor	150.0	150.00	150.00	nF
Amplifier input resistor	1.80	1.80	1.80	kΩ

The sensors were of different thickness made from MnZn ferrite. These thicknesses were 2 mm, 3 mm and 1 mm for FOA sensors and PPO sensors A and B, respectively.

3.3.9 Helmholtz Coils Construction

Helmholtz coils were designed and simulated using modified FOA and Matlab software. In this research, the primary objective of the Helmholtz coils designed was to provide uniform magnetic field in the test area for characterizing the FMS obtained from experiments. The coil was driven by DC source. A low frequency Helmholtz coil driver was used to generate the required magnetic field. Since the magnetic field density is proportional to electrical current, to generate high magnetic field, high current is needed. However, at high frequency the Helmholtz coils impedance is also high, which will require high voltage to drive the desired current. For a given driver voltage amplitude, the coil current is inversely proportional to the coil impedance. Therefore the two opposing factors that affect the magnetic field are current and frequency.

Each of the Helmholtz coils was wound with 22 turns coil width and 25 turns coil height as obtained from modified FOA design results. Each coil had a diameter of 12.88 cm with 550 turns each of copper wire. The copper wire with 0.449 mm diameter was wound on each coil bobbin. When winding the coils, care was taken to ensure that the windings were in order by exerting pressure on the wire as the winding proceeded, but at the same time ensure that the pressure exerted was not too large as the wire might break, which might be risk after winding 500 turns.

A major problem that was encountered after winding the coil was that the coil forms (bobbin around which the coil was wound) were deformed due to the pressure produced by the tight windings. The form had its original width at the bottom, but as more and more layers of windings were added, the width of the form was expanding. Since the windings were almost finished, there was nothing to do about it. However, for future windings of coils of this kind,

the lessons learned from this research was to ensure that the coil forms are made strong enough to resist the pressure of all the windings. Plate 3.4 shows the final Helmholtz coil structure with test bed at the center.

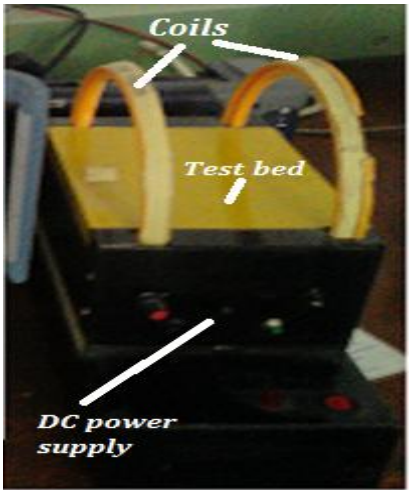

Plate 3.4: Complete Helmholtz Coils with Test Bed.

After having finished the fabrication of the Helmholtz coils, there was need to characterize the coils to ascertain that the coils work the way the modified FOA predicted. Therefore, the magnetic fields inside the Helmholtz coils were measured as a function of distance x along the axis of symmetry of the Helmholtz coils (see Figure 2.13). Furthermore, the magnetic field across the midway point between coils was measured as a function of the current through the coils. The objectives of these measurements were to study and verify the equations (equation (2.14) and equation (3.34)) for the magnetic field of a pair of Helmholtz coils, and also to learn about the rationale for using Helmholtz coils.

In order to measure the magnetic field as a function of distance x along the axis of symmetry of the Helmholtz coils and when the current through the coils was varied, magnetic field strength meter (Tenmars, model TM-191 portable) was used to measure the DC magnetic field in the coils. Figure 3.15 shows the block diagram of the apparatus and setup for Helmholtz coils magnetic fields measurements. The actual implementation of the setup is shown in Plate 3.5.

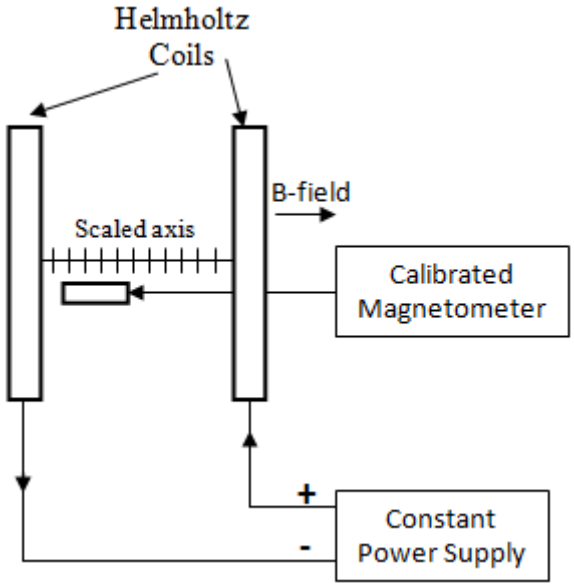

Figure 3.15: Block Diagram of Experimental Setup for Characterizing the Helmholtz Coils.

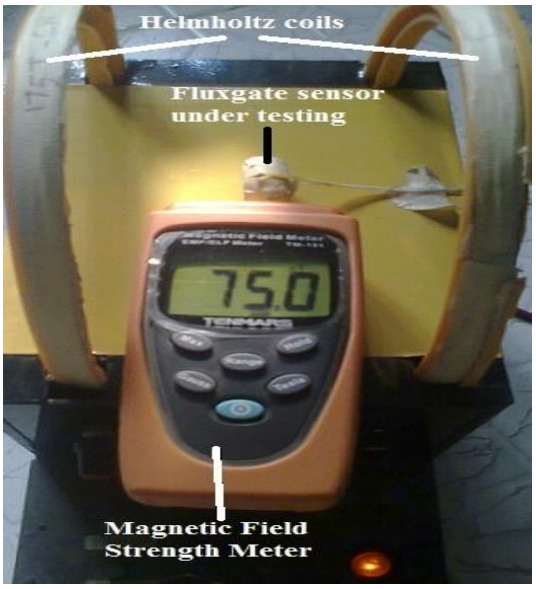

Plate 3.5: Actual Implemented Test-Bed (Helmholtz Coils) for Characterizing the FMS.

As shown in Figure 3.14, during the measurements, a constant current of 100 mA (obtained from optimization results) was passed through the coils and read the value of the magnetic field (Plate 3.5) on a calibrated magnetic field meter (Tenmars, model TM-191 portable) for each 3 mm. The flux density was measured along the horizontal axis (see Figure 2.13) of the coils. The measured magnetic field was in the range of 180 μT with 8 μT resolution.

3.4 Summary

In this chapter, three fluxgate magnetometers were designed and developed based on part-by-part and modified FOA techniques. A core and coil materials were selected with optimal sizing analysis by considering several parameters such as permeability, aspect ratio of the ferromagnetic core and that of the coil, demagnetization factors, coil diameter, and number of coil turns. Following the PPO and modified FOA results analysis, three fluxgate magnetometers were developed along with the detection circuit and the Helmholtz coils for evaluating the developed sensors.

CHAPTER FOUR

RESULTS AND DISCUSSIONS

4.1 Introduction

This chapter presents the results of the magnetic field distribution inside the magnetic core, which was obtained by using ANSYS electromagnetic software. This is followed by the experimental measurements carried out on the developed sensors (with/without the sense electronic circuits) by using the magnetic field of the Helmholtz coils. The result will then be compared to existing fluxgate sensors.

4.2 FEA Simulation Results

The Finite Element Analysis (FEA) results showed that 70 turns of excitation coil requires 165 mA excitation current for the given geometric dimensions (see Table 3.1) of the core. However, the analytical calculations of the excitation coil turns and the predicted saturation magnetic flux density by FEA were in good agreement (by 1.43% and 5.56%, respectively), except the excitation current difference of 9.5%. This difference showed the strong relationship between the magnetic flux density, number of excitation coil turns, and the

excitation current. In addition, the dependence of the magnetic flux density on the excitation current was significant in this case. Table 4.1 shows the comparison between the results of analytical calculations and the FEA simulations of the excitation coil turns and excitation current obtained.

Table 4.1: Comparison of Results obtained from Analytical Model and Simulations.

Physical Variable	**Analytical Model**	**FEA**	**Difference (%)**
Flux density, B_s (T)	0.38	0.36	5.56
Number of excitation winding turns, N_e	69	70	1.43
Excitation current, I_e (mA)	180.67	165	9.50

It has been demonstrated in this research that FEM provides sufficient accuracy in the computation of the magnetic field characteristics. On the other hand, these results showed that the sensor will consume large power because of the dimension of the ring core and the required excitation current for saturation. Furthermore, ANSYS software, like all other FEA software, does not allow the users to express the optimization purposes in details by formulating the objective functions, which is the requirement for the fluxgate optimization problems in this research.

Once the solution was found, the postprocessor (/POST1) was utilized to examine the results. Plate 4.1 illustrates the magnetic flux density distribution inside the excitation coil as found from the ANSYS analysis for ring core geometry. The relative magnetic permeability of the magnetic core was 10,000 and the permeability of air and the volumes occupied by windings was 1. The number of excitation coils and current predicted by the ANSYS were 70 turns and 165 mA, respectively in contrast to the 69 turns and 180.67 mA obtained from analytical modeling (see section 3.3.4). The simulation result showed the magnetic flux density around each turn of wire linked the fields produced in the adjacent turns when current passed through the excitation coil.

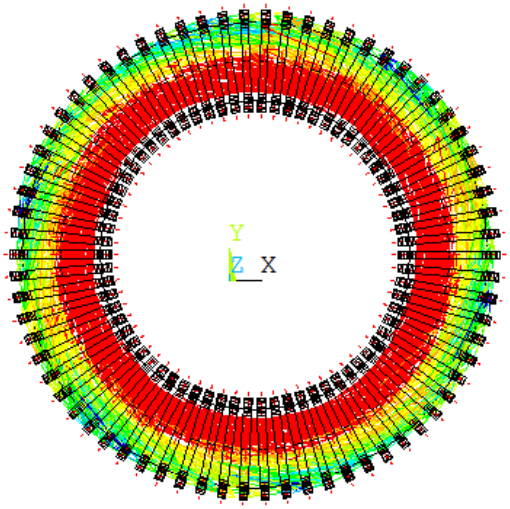

Plate 4.1: Magnetic Flux Distribution Pattern in Ring Core.

It was seen that the inner side of the ring core diameter was very close to saturation, whereas the outer side of the ring core diameter was still not saturated. By increasing the current, fully saturated core was obtained. The combined effect is that the magnetic field lines formed closed paths which have neither beginning nor an end as the coil was uniformly wound. As shown in Plate 4.1, the red flux lines indicate the maximum magnetic flux density in the core volume. It was observed that the magnetic field values decreased from the maximum (plotted in red flux lines or contour region) value to the minimum value (plotted in deep blue flux lines or contour region). The magnetic flux density values inside the core are presented in Plate 4.2 with windings not shown and Plate 4.3, with windings shown, while the magnetic flux density direction is shown in Plate 4.4.

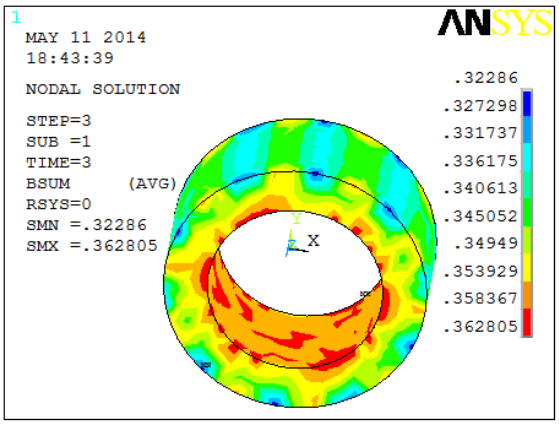

Plate 4.2: Distribution of Magnetic Flux Density values (Windings not Shown).

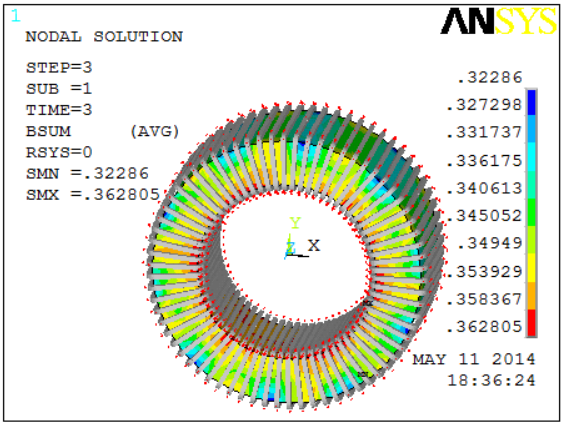

Plate 4.3: Distribution of Magnetic Flux Density values (Windings Shown).

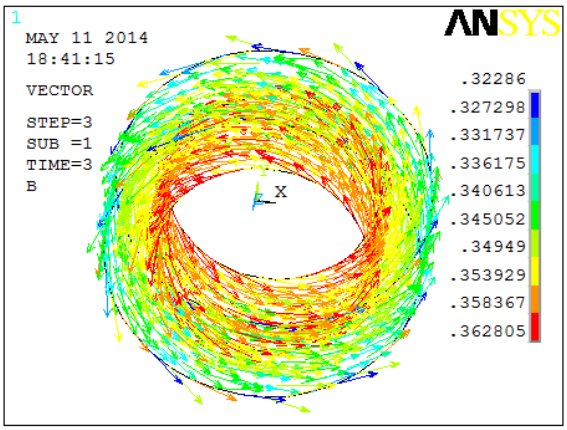

Plate 4.4: Distribution of Magnetic Flux Density Vector

As shown in Plate 4.3, the arrows around the windings specify the direction of the excitation current in the windings. The greatest values of the magnetic flux density (B = 0.3628 T) were obtained at the inner region of the fluxgate sensor ring core. As seen in Plate 4.4, the value of the magnetic flux density was seen to be decreasing towards the core outside diameter. Therefore, as shown in Plate 4.1, it is shown that the magnetic flux density in the interior of core along the ring core cross-section relatively decreased as the ring core diameter was increased from internal diameter to the outside diameter. The detailed GUI steps and its translation into command program listing are shown in Appendix D1.

4.3 Fluxgate Sensor Optimization Results

Due to the modified Firefly Optimization Algorithm (FOA) and Part-by-Part Optimization (PPO) design techniques employed, a number of combinations of parameters were obtained

for FMS designs. However, each of these parameters obtained from optimization design approach had resulted in FMS with different output voltage and noise level. The optimization results provided the parameters for a Helmholtz coils and fluxgate magnetometer such that the voltage sensitivity of the fluxgate magnetometer was maximized and the magnetic field noise level minimized subject to specified desired output voltage of the fluxgate magnetometer. This section examines the results of the optimization routine by finding the dimension and geometry of Helmholtz coils, sensor core, pick-up coil, and detection circuit elements that best satisfied the previously developed objective function (see section 3.3.6.2) for the fluxgate magnetometer and Helmholtz coils. Both PPO design and FOA design approaches were examined and discussion of the results is provided.

The FOA was written in Matlab environment and the results were obtained by running the developed program (see Appendix D) on a 1.50 GHz Intel® core™ Duo CPU Windows 7 Ultimate 32-bit personal computer.

The optimization of FMS using part-by-part optimization approach was first carried out by analytical design of FMS core dimension. The optimization of the *entire* fluxgate magnetometer was then run to simultaneously find the sensor core, pick-up coil, and detection circuit elements, and then the Helmholtz coils with minimum dimensions and geometry that would satisfy the desired design constraints (see section 3.3.6.2) for the fluxgate magnetometer and Helmholtz coils. Data for both the FMS and Helmholtz coils primary design variables when displayed on the screen to show their iterative process as well as the plots for the oscillatory trend in the iterative process was observed which was caused by the randomization parameter of the modified FOA are presented in Appendix E and F. The resulting fluxgate magnetometer parameters obtained from PPO design approach and modified FOA runs are shown in Table 4.2.

Table 4.2: Comparison of Results obtained from modified FOA and Analytical Calculations.

Parameters	**Modified FOA Sensor**	**PPO Sensor A**	**PPO Sensor B**	**Unit**
Core outside diameter	0.012	0.014	0.010	m
Core inside diameter	0.008	0.008	0.008	m
Core height	0.002	0.002	0.003	m
Pick-up coil wire diameter	0.1926	0.226	0.226	mm
Number of Pick-up coil turns	646	548	587	-
Pick-up Coil bobbin thickness	0.005	-	-	m
Amplifier Feedback resistor	100.005	-	-	kΩ
Amplifier feedback capacitor	150.00	-	-	nF
Amplifier input resistor	1.80	-	-	kΩ
Magnetic path length ($\times 10^{-2}$)	3.058	3.282	2.804	m
Core size ($\times 10^{-6}$)	3.946	5.846	2.988	m^2
Voltage sensitivity	1.28	0.428	0.364	mV/μT
Noise level at 1 Hz	3.465 pT	103.58 nT	121.59 nT	/√Hz

As seen in Table 4.2, the optimum core dimension, pick-up coil, and detection circuit elements obtained from modified FOA design predicted the lowest noise level and highest voltage sensitivity of the sensor.

The voltage sensitivities for the fluxgate sensors with different ring core diameters and cross-section areas obtained from modified FOA and PPO design approaches were calculated using equation (3.14) and compared. Table 4.3 shows the voltage responses of the three fluxgate sensors having 12 mm core diameter for modified FOA design, and 14 mm and 10 mm core diameters for PPO design A and B, respectively under different external magnetic fields range. The magnetic field range used was based on the magnetic field range of the available

calibrated magnetometer (0 μT to 200 μT). The obtained results verified the decrease in the sensitivity due to decreasing volume of the pick-up coil caused by decreasing sensor core dimension. However, for each sensor, it was observed that the output voltage was increasing as the external magnetic field was increasing. This was due to increasing magnetization field in the core caused by increase in external magnetic field, which further increased the voltage induced in the pick-up coil.

Table 4.3: Output Voltages for different Sensors obtained from Analytical Calculations.

External Magnetic Field (μT)	**Modified FOA Sensor (mV)**	**PPO Sensor A (mV)**	**PPO Sensor B (mv)**
5	1.91	2.40	1.32
15	5.72	7.21	3.95
25	9.54	12.01	6.58
35	13.35	16.82	9.21
45	17.17	21.62	11.84
55	20.98	26.43	14.47
65	24.80	31.23	17.10
75	28.61	36.04	19.73
85	32.43	40.84	22.36
95	36.24	45.65	24.99
105	40.06	50.45	27.62
115	43.87	55.26	30.25
125	47.69	60.07	32.89
135	51.50	64.87	35.52
145	55.32	69.68	38.15
155	59.13	74.48	40.78
165	62.95	79.29	43.41
175	66.76	84.09	46.04
185	70.58	88.90	48.67
195	74.39	93.70	51.30
205	78.21	98.51	53.93

From Table 4.3, it was observed that the voltage sensitivity decreased as the core dimension decreased. In addition, the voltage sensitivity level of each sensor was limited by the magnetic flux induced in the core which was as a result of the core size.

Figure 4.1 shows the calculated fluxgate output voltage (realized from the results of the Table 4.3) as a function of the external magnetic field (range from 0 μT to 200 μT). The results

show that the sensors response described the magnetic characteristics of the sensor core. By using equation (3.15), the sensitivity of modified FOA-based sensor was 381.50 V/T while PPO sensors A and B showed voltage sensitivities of 480.55 and 263.05 V/T, respectively under the same excitation frequency of 5 kHz.

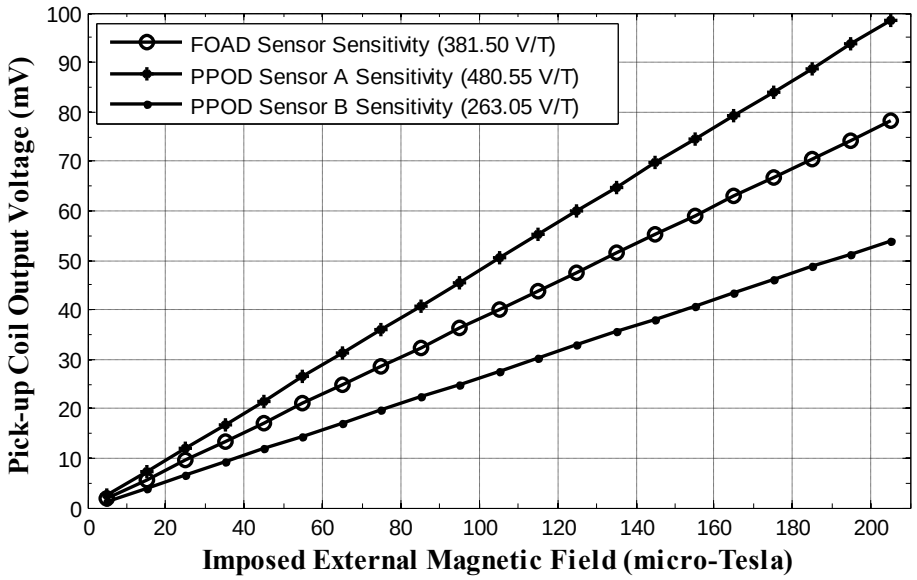

Figure 4.1: Calculated Output Voltages of different FMS Pick-up Coils.

Although, modified FOA-based sensor has highest number of pick-up coil turns which could enable it detect the induced magnetic flux in the core more than the PPO sensors, however, its sensitivity was limited by core dimension which has reduced the magnetic flux induction capability. Moreover, highest sensitivity seen with PPO sensor A was attributed to the increased magnetic flux in the core due to higher sensor core dimension, while the poor magnetic quality of PPO sensor B significantly reduced its performance due to reduced core size.

The sensors were designed to withstand up to 99 mA current. Copper wire having 0.411 mm was wound as the excitation coil on each sensor with 49 turns. The completed ring cores with excitation coils wound circumferentially were put inside a pick-up coil bobbin, which were constructed to hold the pick-up coil as shown in Plate 4.5(a). Finally, the pick-up coil with

646, 548, and 587 turns was wound diametrically on the core with copper wire having 0.2 mm and 0.226 mm, for the modified FOA-based sensor, and PPOD sensors A and B, respectively. The completed sensors assembly is shown in Plate 4.5(b).

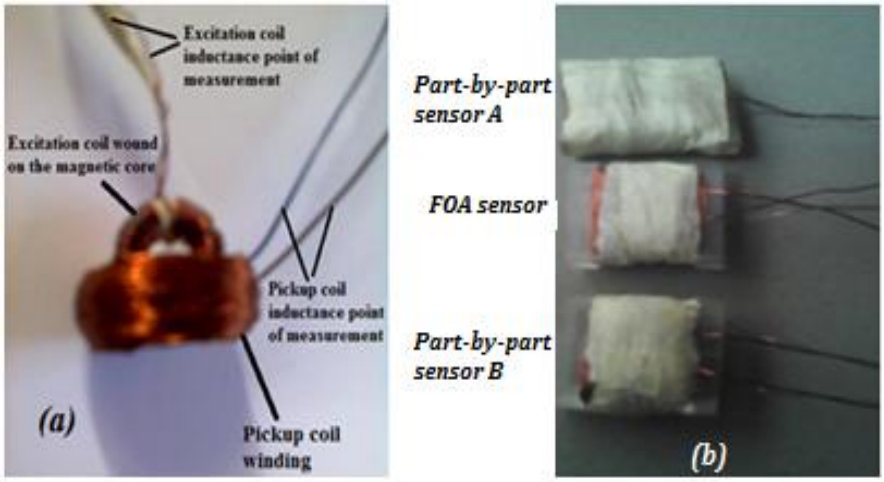

Plate 4.5: (a) Sensor Assembly; (b) Complete Package of FMS Prototypes.

The completed fluxgate sensor prototype is shown in Plate 4.6.

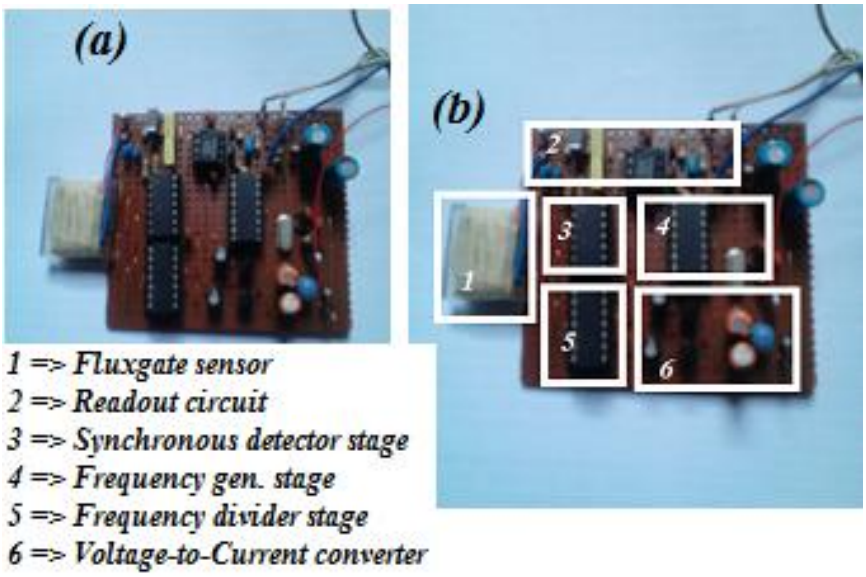

Plate 4.6: Complete Fluxgate Sensor System

As shown in Plate 4.6, the final dimension of the fluxgate sensor was 0.023 m × 0.02 m × 0.01 m, the dimension of the fluxgate sensor together with the printed circuit board was 0.085 m × 0.063 m × 0.01 m, while the whole system package was 0.093 m × 0.071 m × 0.022 m.

4.4 Helmholtz Coils Optimization Results

Table 4.4 shows the results for the Helmholtz coils design variables (see Table E2 of Appendix E). In the Helmholtz coils, the wire size was decreasing and the coil radius was also decreasing in an effort to optimize the magnetic field of Helmholtz coils. Consequently, there was not a significant increase in the dimensions and geometry of the coils between the runs.

Table 4.4: FOA Results for the Helmholtz Coils Simulations.

	Input variables					**Output variable**
Helmholtz Coils	**Coil width turns**	**Coil height turns**	**Wire diameter (mm)**	**Coil radius (mm)**	**Coil current (mA)**	**Magnetic field (μT)**
FOA Design	22	25	0.449	12.88	100	332

The primary difference between the Helmholtz coils and fluxgate magnetometer is that the Helmholtz coils uses a pair of similar coils to generate uniform magnetic field which was used to evaluate the performance of the sensor (see section 2.2.11) while the fluxgate magnetometer is used to detect the magnetic field created by the Helmholtz coils.

With the coil parameters obtained from modified FOA designs of the Helmholtz coils, Matlab programs (presented in Appendix D4) were written to obtain the magnetic field plot arising from the contributions of the designed coils as shown in Figure 4.2.

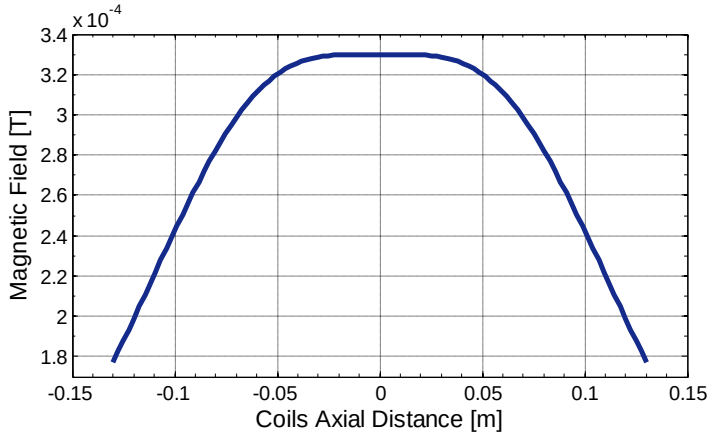

Figure 4.2: Axial Magnetic Field against Distance for Helmholtz Coils FOA Design.

It can be concluded that the magnetic field is very homogeneous as long as the shape of the coils is approximately a square. Therefore, any deviation from the optimum coil configuration would cause the graph to be in different form.

The measured magnetic fields of the Helmholtz coils for 100 mA (obtained from FOA optimization results) of DC current through the coils were presented in Table G1 of Appendix G. The values of the measured magnetic field plotted as a function of axial distance is shown in Figure 4.3.

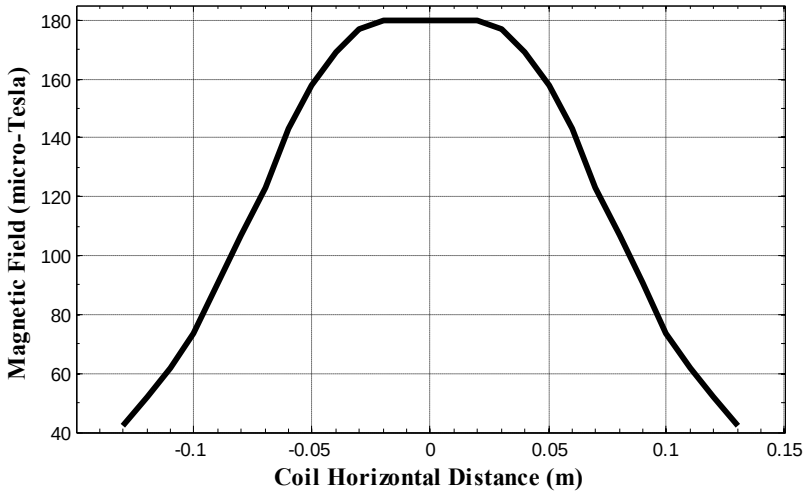

Figure 4.3: Measured Magnetic Field of Helmholtz Coils.

As seen in Figure 4.3, the measured magnetic flux density was far from the simulated value because of the limited range of the calibrated magnetometer employed (0 μT to 200 μT). The measured flux density along the axis of the coil was symmetric about the center. This showed that the coils were aligned perfectly and the magnetic flux density from the individual coils was symmetric.

To investigate the dependence of magnetic field at the center point (where the magnetic field was peak) of Helmholtz coils on the applied driving current, a calibrated magnetometer was placed at the centre point (where the magnetic field was peak) of the coils. A measurement of

the magnetic field was made for each 2 mA in the range of 100 mA (see Table G1 of Appendix G). The measurements and calculated values were plotted as shown in Figure 4.4.

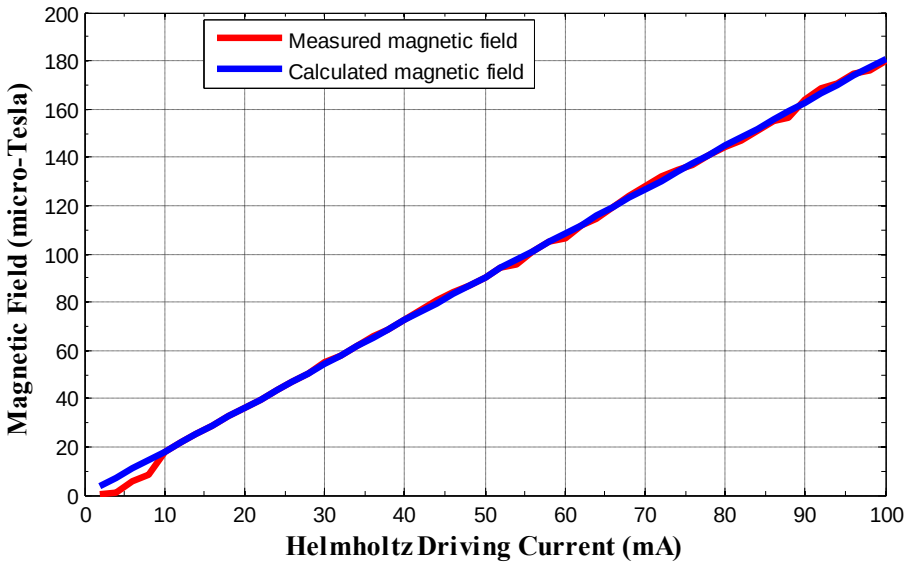

Figure 4.4: The Magnetic Field in the Center Point of Coils as a Function of Current.

The figure showed that the measurements agreed with the calculations. However, it was observed that the magnetic field measurements were not consistent at the current below 10 mA which resulted in the magnetic field not also consistent below 10 μT. Generally, the inconsistencies in the measurements could be due to the interference of the earth's magnetic field or the presence of other magnetic field sources such as phones, laptops, buckle from a belt, and other. The presence of magnetic interference could cause increase or decrease of the magnetic field of a sensor and even the Helmholtz coils. Decrease in the magnetic field signifies interference from negative magnetic field while increase in magnetic field signifies positive magnetic interference. Also, the calibrated magnetometer used had a measurement accuracy of ±3 % and it was as well not sensitive to very low magnetic field. In addition, it was suspected that another reason for the drift of the measurements in comparison to the calculated values was the heat, which was produced in the Helmholtz coils material when current was run through the coils.

4.5 Performance of Fluxgate Sensors Based on Objective Three

The third objective of this research work is to develop an interface electronic circuits that can reduce the noise and increase the sensitivity of the entire fluxgate sensor system and characterize the FMS in terms of voltage sensitivity and noise level. Therefore, the performance testing of the developed sensors are as follows:

1. Explore the performance of the excitation circuit,
2. Evaluate the pick-up coil without the detection circuit,
3. Assess the entire sensors with detection circuit.
4. Examine the optimized sensor sensitivity response with respect to earth's magnetic field intensity and directions.

4.5.1 Performance Responses of the Fluxgate Excitation Electronic Circuit

Figure 4.5 shows the block diagram of the performance testing of the FMS carried out by using a Helmholtz coils to provide uniform magnetic field. As seen in the diagram, the sensor was placed within the uniform magnetic field with its axis aligned with the field axis of the Helmholtz coils. The tests of the sensors were done by passing excitation current through the excitation coil. The sensors pick-up coil output signal was connected to an oscilloscope (section 3.2).

4.5.1.1 Details of Electronic Testing Board and Experimental Set-up

The completed ferrite ring core with excitation coil was put in a pick-up coil bobbin, which was specially constructed to hold the pick-up coil. The pick-up coil has 646 turns of 0.1926 mm diameter enameled copper wire. The block diagram of the fluxgate magnetometer electronic testing board is shown in Figure 4.5. It consists of a 5 kHz driving oscillator, frequency divider, current booster, fluxgate sensor, synchronization circuit, and detection amplifier circuit. In order to magnetically saturate the ferrite core, a square wave current had been applied to generate adequate magneto-motive force (*mmf*) for driving the sensor core. A square wave signal of frequency *f* generated by the drive oscillator (CD4069) is divided by a

frequency divider (CD4013). The function of the IC (C4013) is to produce a drive frequency and a reference frequency for the sensor excitation and signal processing respectively. The square wave signal is boosted by using Class AB push-pull complementary amplifier that has low second harmonic distortion.

The excitation drive circuit is a lossy inductor whose inductance is a nonlinear function of the drive current (Primdahl, 1979). In order to resolve this problem, the excitation coil was tuned to the excitation frequency by a parallel. This was to enable matching of the excitation coil and the excitation circuit. The tuning will balance the fluxgate sensor drive inductance making the load more resistive (Ripka, 2001). This can improve the power transfer factor of the drive circuit and sensor. Furthermore, the pick-up coil inductance is a non-linear function of the permeability of the ferrite core. The pick-up coil output was filtered using an band-pass filter operating at second harmonic $2f$ resonance frequency to eliminate the odd and higher even harmonics signals detected by the pick-up coil. As the synchronous detector is phase sensitive, it is therefore called a Phase-Sensitive Detector (PSD). Since the output of the fluxgate sensor is amplitude modulated by the measured field, the function of PSD is to demodulate the pick-up coil output signal back to DC or near zero frequency. To remove the higher frequencies resulted from the multiplication process in the PSD, a low pass filter at the output of the PSD is necessary. A buffer amplifier with high input impedance and ultra low noise configurations has been constructed using an ultra-low noise op-amp (OPA 228P) has been added to strengthen the output signal and attenuated the higher frequency signals.

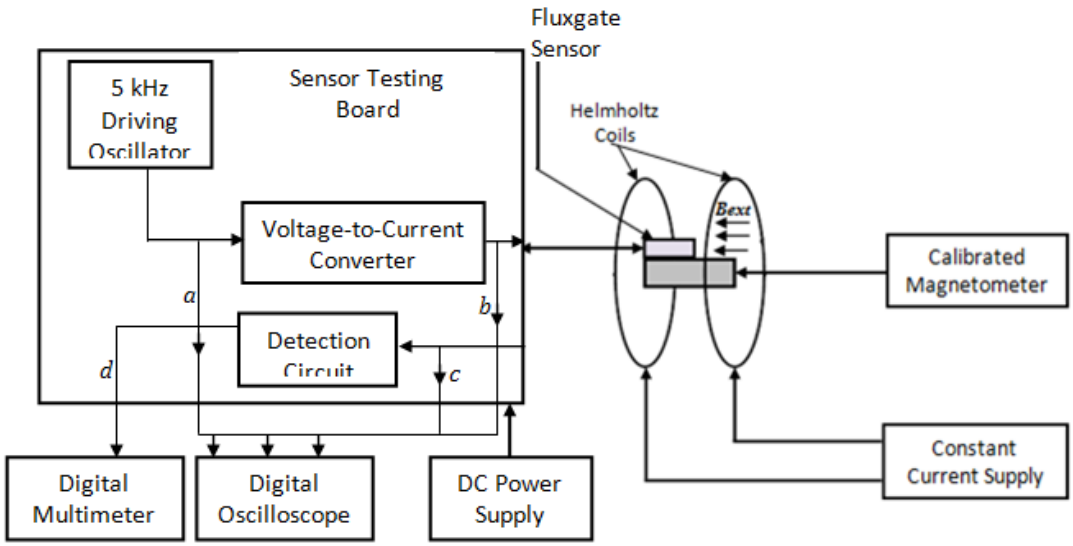

Figure 4.5: Block Diagram of the Experimental Setup for the Sensor Characterization.

The actual experimental setup is shown in Plate 4.7 with Tektronix (0-72V, 1.2A) Programmable DC Power Supply (model: PSW 4721) used to power the sensor through the testing board with the calculated excitation current of 99 mA for the sensors.

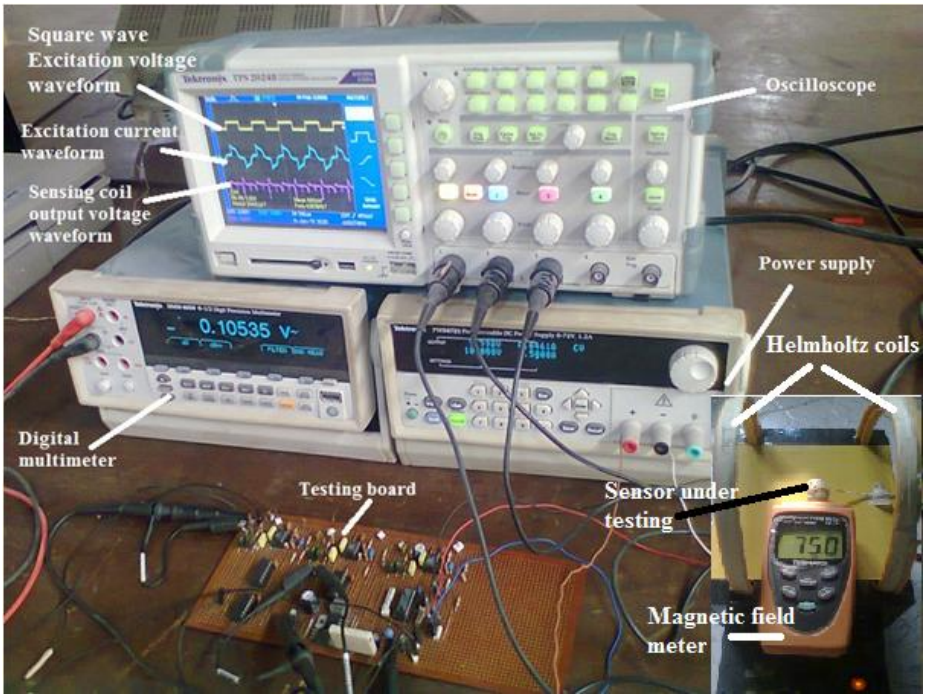

Plate 4.7: Actual Experimental Setup for the Characterization of the Fluxgate Sensors.

The excitation and pickup coil signal waveforms were examined by connecting the Tektronix Four Channel Digital Signal Oscilloscope (model: TPS 2024B) to the sensor excitation stage

(at points a, b, and c shown in Figure 4.5) on the testing board. FEM simulation showed that the excitation current was 165 mA with the original ring core (see Table 4.1), but was lowered to an excitation current of 33.94 mA, 49.50 mA, and 42.43 mA, for PPO sensors A and B, and modified FOA-based sensor, respectively due to the reduction in the ring core size, which has greatly reduced the demagnetizing effect of the sensor, thereby the saturation magnetization current and the power consumption. The amplitude and frequency of the excitation current are two major electrical parameters governing the sensor's sensitivity and field noise. Therefore, the sensitivity of the developed fluxgate sensors as a function of the excitation current at various excitation frequencies were investigated and the results showed that the excitation frequency of 5 kHz produced the optimal performance of the fluxgate sensors, because the sensors exhibited maximum peak voltage and minimum excitation current at this frequency. It was observed that the perming decreases with the excitation current due to better saturation of the magnetic core.

4.5.1.2 Time Dependent Response

Plate 4.8 shows the FMS output voltage waveforms when 5 kHz excitation frequency voltage square wave was applied to the excitation coil wound around the ring core (shown in Plate 3.5(a)) without any external magnetic field. The sensors outputs showed properties similar to those of typical fluxgate sensors (see Figure 2.6) with reference to the excitation waveform shown in Plate 4.8(a) tested at point 'a' as shown in Figure 4.5.

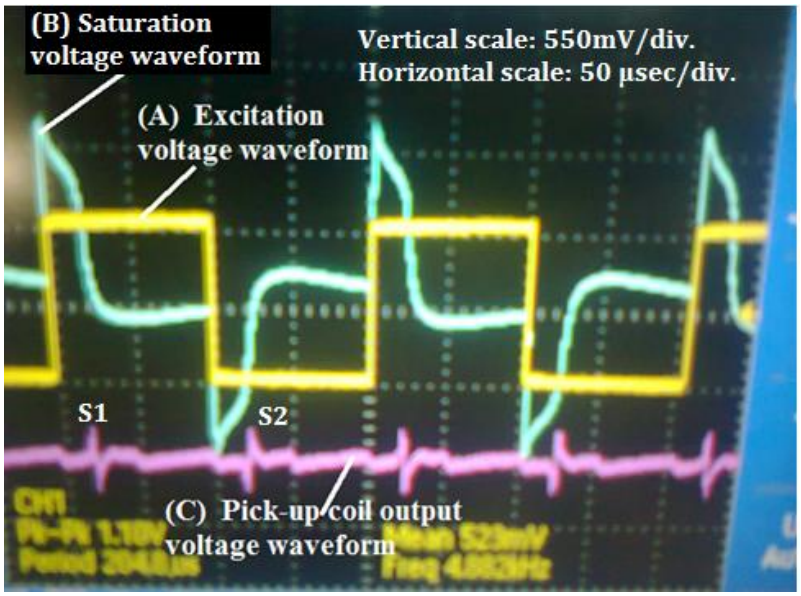

Plate 4.8: Oscilloscope Output Waveforms for the Fluxgate Sensor Excitation Circuit.

Plate 4.8(b) shows the ferro-resonance (see section 2.2.5.6) excitation voltage (2.2 V peak to peak) in the excitation coil (tested at point 'b' as shown in Figure 4.5), when applied a current of 99 mA from the power supply. This induced voltage also represented the time variation of the magnetic flux in the ferromagnetic core material inside the pick-up coil. The non-square (deformed square shape) peaked behavior of ferro-resonance excitation voltage waveform was due to saturation of the ferromagnetic material. As a result, this ferro-resonance voltage signal had a strong component at the second harmonic of the excitation frequency because of its capability to attenuate all other unwanted harmonic signals.

Plate 4.8(c) represents the induced pick-up coil voltage (440 mV peak to peak) signal (tested at point 'c' in Figure 4.5) in the absence of external magnetic field. Ideally, the pick-up coil output signal supposed to be zero when the opposing fluxes in both sections of the ferromagnetic ring core material placed inside the pick-up coil mutually cancelled each other. However, small geometrical asymmetries observed in the output voltage of the pick-up coil as shown in Plate 4.8(c). This was attributed to the irregularity in the winding of the coils and magnetic hysteresis effects, which could be due to the presence of the remnant magnetic field generated by the unsaturated parts of the magnetic core or the influence of the earth's

magnetic field and other sources of magnetic interference within the laboratory during the experimental measurements.

Plate 4.9 shows the FMS responses to external magnetic field due to a bar magnet (scaled to 50µs per division on the horizontal axis and 550 mV per division on the vertical axis). These responses reflected both the influences from the applied field of a bar magnet and the remnant magnetic field (Plate 4.8(c)). It was observed that when positive external magnetic field (North-pole of a bar magnet) was applied to the sensor, the amplitude of the pick-up coil output signal was increased and the values of magnetic field signature, S1 was higher than S2 (Plate 4.9(a)).

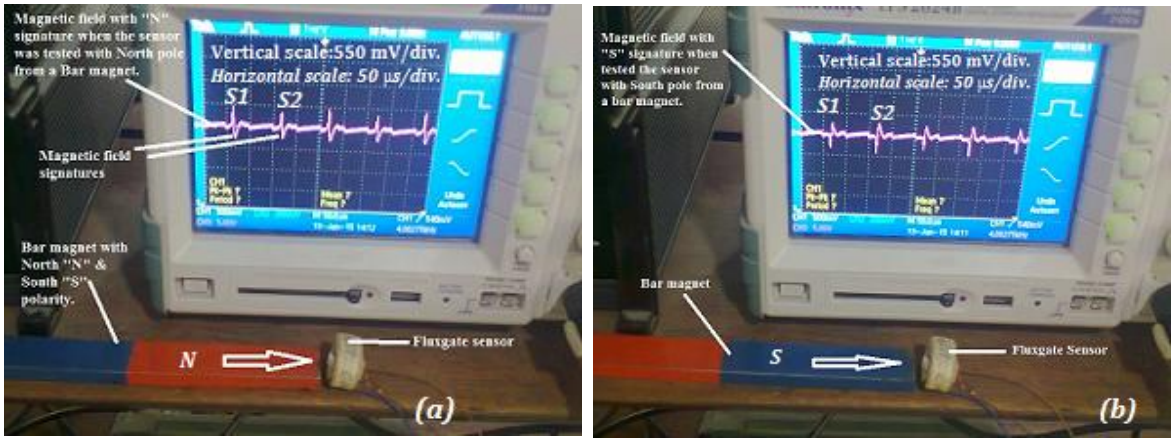

Plate 4.9: Magnetic Field Sensing from a Bar Magnet.

The values of the positive and negative peaks were also different. The values of the positive peaks in S1 and S2 were 550 mV and 330 mV, respectively, while the value of the negative peaks in both S1 and S2 was 275 mV (Plate 4.9(a)). When negative external magnetic field (South-pole of a bar magnet) was applied to the sensor (Plate 4.9(b)), the amplitude of the pick-up coil output signal was also increased, but in the opposite direction and the values of magnetic field signature, S1 was smaller than S2 (Plate 4.9(b)). The values of the positive and negative peaks were different too. The value of the positive peaks in both S1 and S2 was 275 mV (Plate 4.9(a)), while the values of negative peaks in S1 and S2 were 330 mV and 550 mV, respectively. These observations could be due to the simultaneous decreased

permeability of the hysteresis loop in both reverse and forward magnetization curves (Section 2.2.7).

4.5.1.3 Response of Pick-up Coil without Detection Circuit

The tuned second harmonic output voltage responses of the developed FOA and PPO fluxgate sensors as a function of the applied external magnetic field were verified. As seen in Plate 4.7, Tektronix Digital Multimeter (2050 model) (with root mean square (rms) range selected) was connected to the pick-up coil output terminal (point 'c' shown in Figure 4.5) of the prototype sensors to measure the peak output voltages of the sensors corresponding to the external magnetic field supplied from the Helmholtz coil. Magnetic field strength meter (calibrated magnetometer) was used to evaluate the magnitude of the magnetic field supplied from the Helmholtz coil to the fluxgate sensors. This was done by placing the magnetic field strength meter (sensor) perpendicular to the magnetic field of the Helmholtz coil (Plate 3.5). The measurements of the output response to field variations were made with 15 μT as the minimum magnetic field and 75 μT with step of 10 μT. The 15 μT resolution of these measurements was limited by output capability of the Helmholtz coils at the minimum driving current. It was noticed that the minimum driving current for the Helmholtz coils was 8 mA. Below this minimum driving current (8 mA), the Helmholtz coils operation became unstable resulting in the fluctuations of the output magnetic field of the calibrated magnetometer used. In addition, the 75 μT maximum magnetic field of these measurements was limited by the induced excitation field (±67.99 μT, ±50.67 μT, and ±86.50 for modified FOA, and PPO sensors A and B, respectively) inside the sensor core. This was obtained from equation (3.5), and these calculations validated the principle of fluxgate magnetometer. The smaller the sensitivity the higher the magnetic field ranges of sensor. It was noticed that the magnetic field linearity of these sensors was increasing as the core dimension was decreasing. This was due to the increasing nature of the excitation current as the core dimension

decreases which in turn increases the linearity of the sensor. Table 4.5 presents the tuned second harmonic output voltage obtained from the experimental measurements (Plate 4.7) of the pick-up coil output voltage.

Table 4.5: Pick-up Coil Output Voltages of different Sensors obtained from Measurements.

External Magnetic Field (μT)	PPO Sensor A (mV)	PPO Sensor B (mV)	Modified FOA Sensor (mV)
15	9.42	5.12	18.10
25	15.45	8.54	29.32
35	21.23	10.43	38.89
45	27.49	14.23	51.34
55	33.37	17.44	63.23
65	39.18	22.48	74.33
75	46.32	26.32	86.45

This data shows that the modified FOA simulation routine provided an accurate geometric dimension of the sensor core and the pick-up coil. During the experimental data measurements, it was observed that the sensitivity increased as the core dimension decreased up to an optimum dimension of the core at which the voltage sensitivity began to decrease.

The plot shown on Figure 4.6 (obtained from Table 4.5) shows the response of the pick-up coils of the developed sensors when tuned to second harmonic of the excitation frequency under the imposed external magnetic field from Helmholtz coils.

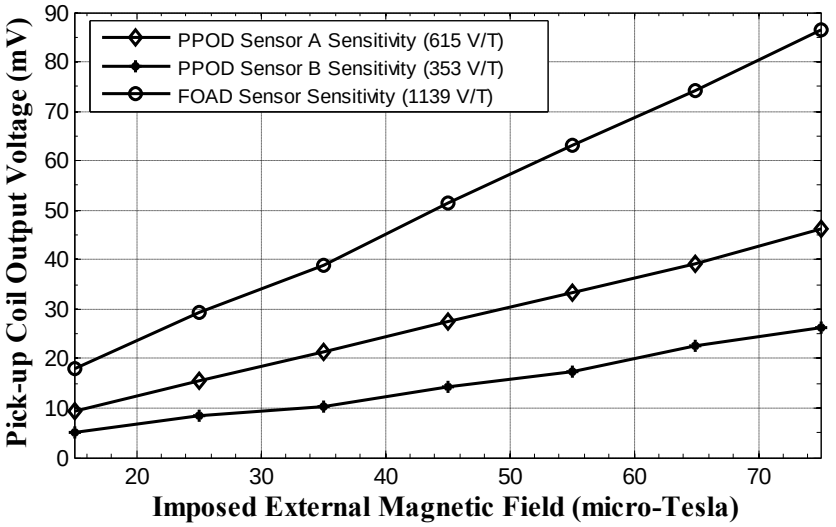

Figure 4.6: Fluxgate Parallel Tuned Output Plotted against External Magnetic Field.

Equation (3.15) was used to evaluate the sensitivity of the sensors for the applied external magnetic field. The FMS exhibited voltage sensitivity of 615V/T, 353V/T and 1139V/T at 75μT external magnetic field range and 5 kHz excitation frequency for PPO sensors A and B, and FOA sensor, respectively. Output voltages obtained from PPO and modified FOA sensors were compared with the corresponding values obtained from the experimental results are presented in Table 4.6.

Table 4.6: Comparison of the Calculated and the Experimental Output Voltage Results.

External Magnetic Field (μT)	PPOD Sensor A (mV)		FOAD Sensor (mV)		PPOD Sensor B (mV)	
	Calc.	Meas.	Calc.	Meas.	Calc.	Meas.
15	6.41	9.42	5.12	18.10	5.46	5.12
25	10.70	15.45	8.54	29.32	9.11	8.54
35	14.97	21.23	11.96	38.89	12.75	10.43
45	19.24	27.49	15.37	51.34	16.39	14.23
55	23.52	33.37	18.79	63.23	20.03	17.44
65	27.79	39.18	22.21	74.33	23.68	22.48
75	32.07	46.32	25.62	86.45	27.32	26.32

These results were in contrast to the calculated values of sensitivity of 480.55V/T, 263.05V/T, and 381.50V/T at 200 μT obtained from PPO sensors A and B, and the FOA sensor, respectively. This was attributed to the effect of tuning the output of pick-up coil (see

section 2.2.5.1), which has increased the pick-up coil output voltage significantly (by 45.84%, 35.69%, and 71.90% for PPO sensors A and B, and FOA sensor, respectively) when compared to the output voltage sensitivity (333.10V/T, 227.02V/T, and 320.02V/T for PPO sensors A and B, and modified FOA sensor, respectively) of the untuned pick-up coil.

4.5.1.4 Responses of the Sensors Pick-up Coils with Detection Circuit

The signal conditioning circuit (detection circuit) was connected to the output of the pick-up coil (point 'd' shown in Figure 4.5) while the PPO and modified FOA sensors were tested in orders to evaluate their responses in terms of noise and sensitivity to the magnetic field. The possibility of using them like a compass was also verified. This was considered essential to evaluate the operation feasibility of the miniature sensors. The experiments were carried out with a pair of Helmholtz coils which generated the required variable homogeneous magnetic field of 0 μT – 200 μT. The testing of the developed sensors had been performed in a magnetically free environment and a Helmholtz coil was used to provide uniform test field. The FMS was then placed in the uniform magnetic field with the sensor axis aligned with the field axis of the Helmholtz coil. The amplified sensors pick-up coil second harmonic output voltage was then connected to a Tektronix DMM 2050 (6½ Digital Precision Multimeter) to validate the modified FOA design and PPO design approaches. The measurements of noise voltage spectrum density at 1 Hz were performed using the set-up shown in Figure 4.7. The actual experimental set-up of the FMS is presented in Plate 4.10.

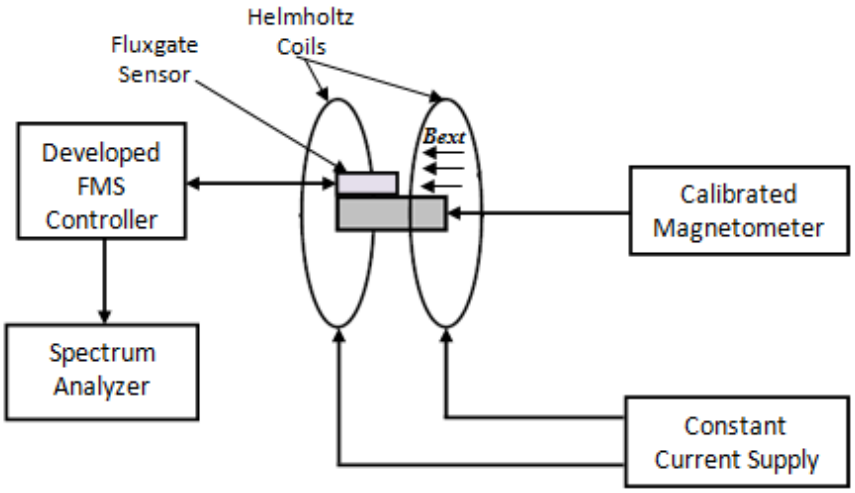

Figure 4.7: Block Diagram of the Experimental Set-up for the FMS Noise Analysis

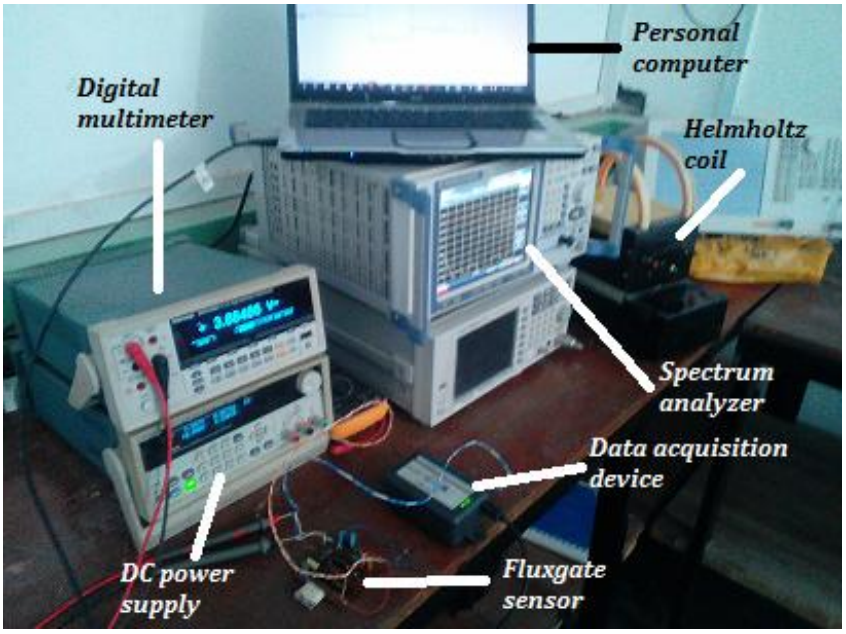

Plate 4.10: Actual Experimental Setup for the Noise Analysis of the FMS.

As shown in Figure 4.7, a 75 μT peak magnetic field from Helmholtz coil was applied to the sensor, and the output voltage was measured using spectrum analyzer. In order to determine the sensitivity of the developed sensors, the measured voltage was then divided (equation (3.15)) by the maximum magnetic field strength of 75 μT. The external magnetic field from the Helmholtz coil was shut down and the voltage noise spectral density was measured from the output of the sensor. The voltage noise spectral density was divided by the sensitivity to

give the magnetic noise spectral in unit of T/√Hz (equation (3.28)). This measurement range was used because the Helmholtz coils output field was not stable at magnetic field below 15 μT, resulting from minimum driving current of the Helmholtz coils, while the maximum sensitivity (75 μT) was limited by the output capability of the excitation field in the sensor core. The magnetic field range of a sensor is limited by the excitation field range in the sensor core (Lu and Huang, 2015).

Figure 4.8 is the curve (obtained from the measured output voltage of the developed sensors) showing the comparison between the measured output voltage responses of the PPO design sensors (PPODS) A and B, and modified FOA design sensor (FOADS) under the imposed external magnetic field range of 75 μT from the Helmholtz coils at 5 kHz excitation frequency.

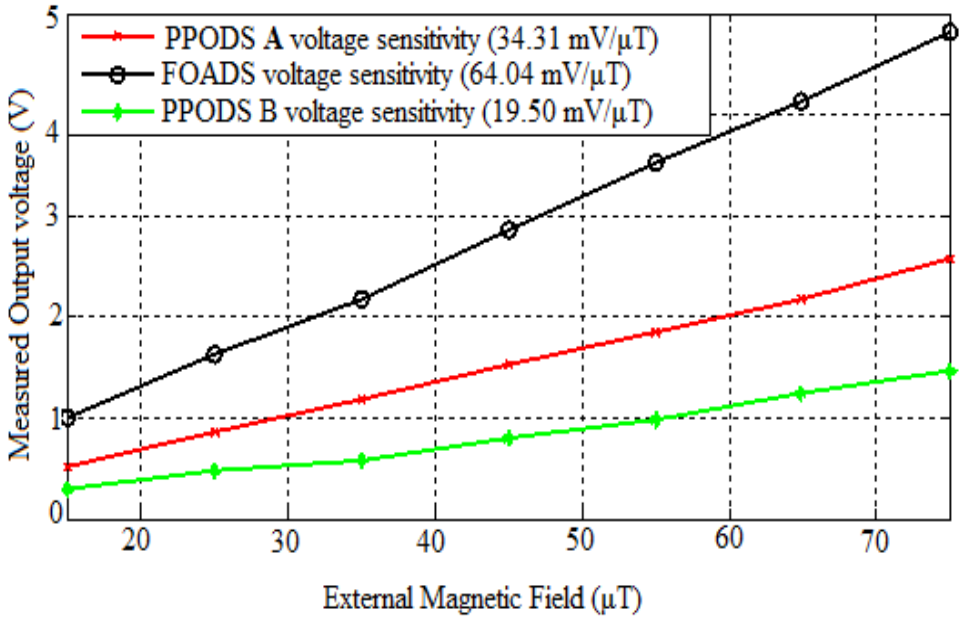

Figure 4.8: Output Voltage of different Fluxgate Magnetometer Sensors

Figure 4.8 can be explained by using aspect ratio of the sensor magnetic core. The effect of aspect ratio of the ferromagnetic core was observed in the responses of the fabricated FMS. Aspect ratio of ferromagnetic core is the ratio of ring core diameter to core height. The

voltage sensitivity as a function of aspect ratio of ferromagnetic core of each sensor is illustrated in Figure 4.9.

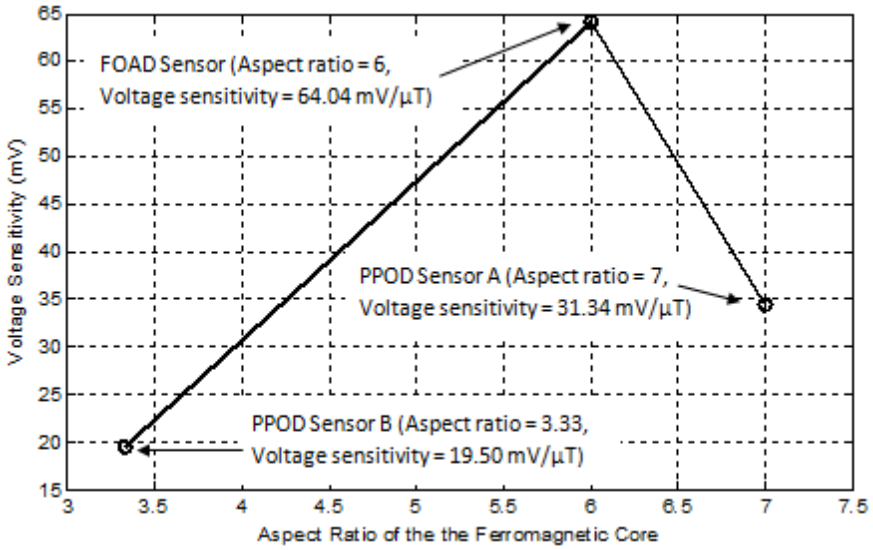

Figure 4.9: Voltage Sensitivity vs. Aspect Ratio of different FMS Core.

The voltage sensitivity of the sensors was achieved by analyzing the sensor's second harmonic signals with respect to different ring core outside diameter of the developed FMS (*i.e.*, 12 mm, 14 mm, and 10 mm for modified FOA sensor and PPO sensors A and B, respectively) under the same excitation frequency of 5 kHz. It was evident that the sensor with ferromagnetic core having optimum aspect ratio (decreased demagnetization effect) exhibited significant increase of the pick-up coil voltage sensitivity. For instance, the field sensitivity, by using 10 mm of ring core outside diameter and 5 kHz of excitation frequency, arrived at the maximum value of 19.50mV/μT at 49.50mA of current amplitude, while the field sensitivity of the optimial sensor with 12 mm ring core outside diameter and 5 kHz of excitation frequency, increased to a maximum value of 64.04 mV/μT at 42.43 mA of current amplitude, and finally made a descent to 31.34 mV/μT at 33.94 mA of the current limit. These measurement results hence verified the sensitivity characteristics of the developed FMS.

The external magnetic field from the Helmholtz coils was shut down and the voltage noise of the sensors was measured. The field noise spectral density of the studied fluxgate sensors was obtained from DI-145 (see Appendix G3) FFT analyzer. The measurements of the voltage noise spectral densities were found to be 422.85nV/√Hz, 1.41μV/√Hz, and 316.16nV/√Hz for PPOD sensors (PPODS) A and B, and modified FOAD sensor (FOADS), respectively at 5 kHz excitation frequency. The field noise spectral density (equation (3.28)) of the FMS is the ratio of the voltage noise spectral density to its corresponding voltage sensitivity. The results indicated that by increasing the voltage sensitivity, the field noise of the sensor is reduced. Figure 4.10 shows the noise spectrum of these sensors.

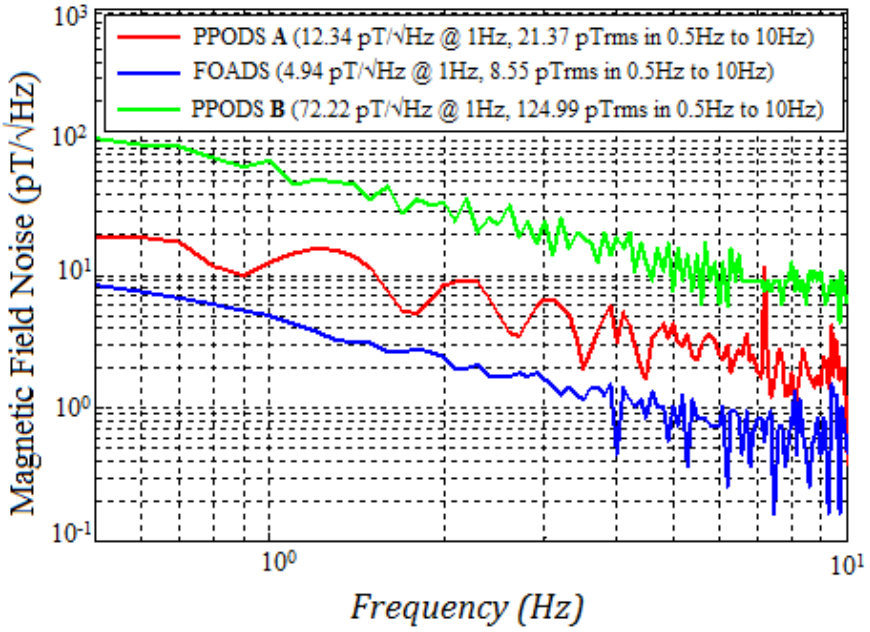

Figure 4.10: Magnetic Field Noise Spectral Density of Developed FMS.

Within the low frequency range (0.5 – 10 Hz), the RMS noise was 21.37 pT, 124.99 pT, and 8.55 pT for PPO sensors A, and B, and modified FOA sensor, respectively. Comparing the minimum field noise of 3.465pT/√Hz predicted by modified FOA simulation, there was good agreement between the measured field noise and the FOA simulated field noise, which shows the effectiveness of modified FOA technique for optimization design of fluxgate

magnetometer. The magnetic field noise of the sensors examined with respect to different aspect ratio of the sensor core is illustrated in Figure 4.11.

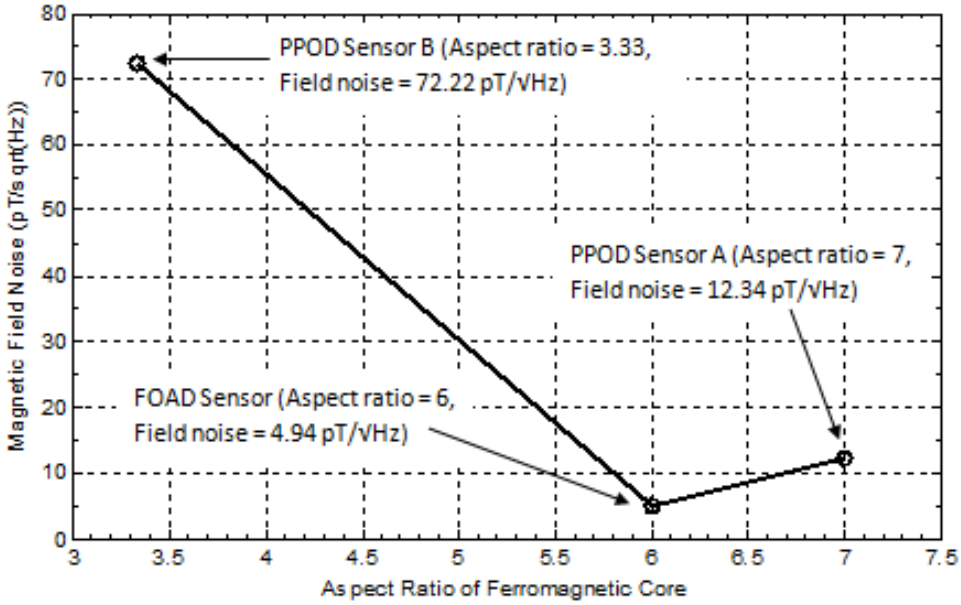

Figure 4.11: Magnetic Field Noise vs. Aspect Ratio of Different FMS Core.

As shown in Figure 4.11, the voltage noise spectral density of the sensors developed using PPO and modified FOA was achieved by examined the sensor's magnetic field noise with respect to different ring core outside diameter of the FMS (*i.e.*, 12 mm, 14 mm, and 10 mm for modified FOA sensor and PPO sensors A and B, respectively) under the same excitation frequency of 5 kHz. It was evident that the sensor with ferromagnetic core having optimum aspect ratio decreased demagnetization effect and provided significant decrease of the field noise. For instance, the field noise of the PPO sensor B using 10 mm of ring core outside diameter and 5 kHz of excitation frequency was 72.22pT/√Hz at 1Hz with 49.50mA of peak excitation current, while the field noise of FOA sensor with 12 mm ring core outside diameter and 5 kHz of excitation frequency decreased to an optimum value of 4.94 pT/√Hz at 1Hz with 42.43 mA of peak excitation current, and finally for sensor having 14 mm ring core outside diameter, the field noise ascended to 12.34 pT/√Hz at 1Hz with 33.94 mA of the

current limit and 5 kHz of excitation frequency. These measurement results hence verified the magnetic field noise characteristics of the developed FMS.

4.5.2 Sensing the Magnitude and Direction of Earth's Magnetic Field

To further explore the performances of the developed modified FOA sensor in this research, the optimized sensor was exposed to earth's magnetic field by turning the sensor 360^0 on the horizontal plane. It was observed that 4.8V was produced from its output when the sensor pointed towards North pole with corresponding magnetic field of 49.44 μT (49440 nT) and 0.2V when pointed towards South pole which indicated -49.44 μT (-49440 nT). Since earth's magnetic field ranges from 30 μT to 50 μT (Lu and Huang, 2015), the developed modified FOA sensor was therefore considered capable for electronic compasses or other advanced applications. By using equation (3.15), the sensitivity of the modified FOA sensor resulted in 4.8 V/49440 nT (97.09 mV/μT). The multiplying factor was obtained as:

$$C_{factor} = \frac{Mag_{val}}{V_{tot}} \tag{4.1}$$

Where V_{tot} is the total output voltage of the sensor, Mag_{val} is the corresponding earth's magnetic field intensity, F. Therefore,

$$C_{factor} = \frac{49440.00}{4.80} \ nT/V$$

$$Scale\ factor = 10300.00 \quad nT/V$$

The output of the optimized sensor was clamped to the mean of 2.5V (for 0 nT) so that if no magnetic field is present, the output voltage will be 2.5V. Setting this criterion was due to bi-directional nature of the magnetic field, so 2.5V to 4.8V was allocated for positive field (towards North pole) and 0.2V to 2.5V was for negative field (towards South pole). The magnetic field corresponding to the output voltage is shown in Table 4.7.

Table 4.7: Magnetic Field corresponding to Output Voltage

Geomagnetic Components	Output Voltages (V)	Corresponding Magnetic field values (nT)
North	4.8	49440
East/West	2.5	0
South	0.2	-49440

The possibility of using the optimized sensor for measuring the earth's magnetic field was demonstrated by employing the sensor to measure the magnetic field at different geomagnetic locations (such as Electrical and Computer Engineering (ECE) Department, ABU Zaria; Arugungu street, Katsina road in Kaduna, and Old NEPA area of Kuje, Abuja). These few different geomagnetic locations were selected for evaluation purpose, and since the earth's magnetic field exist everywhere (Ali *et al.,* 2012). The magnetic field corresponding to the output voltages measured at the selected geomagnetic locations were calculated and compared with the total magnetic field strength obtained from the International Geomagnetic Reference Field (IGRF). The earth's total magnetic field for a given region is constant (Siddharth *et al.,* 2011) and its value can be obtained from the International Geomagnetic Reference Field (IGRF) model which is available from several websites (e.g. noaa.ngdc.gov, magnetic-declination.com, solarham.com). This has becomes a basis for magnetic field sensor calibration (Siddharth *et al.,* 2011). The magnetic field of the Earth's consists of the three components, the vertical component (called Z-component) of the magnetic field and the two horizontal components (called X and Y-components). The output voltages measured at different geomagnetic locations (Electrical and Computer Engineering Department, ABU Zaria; Arugungu street, Katsina road in Kaduna; and Old NEPA area of Kuje, Abuja) are presented in Table 4.8.

Table 4.8: Output Voltages obtained from Optimal Sensor at different Locations.

Earth's Magnetic Field Components	Measured Voltages (V)		
	ECE Dept, ABU, Zaria	Arugungu area, Katsina road, Kaduna	Old NEPA area, Kuje, Abuja
X-Component	3.305	3.282	3.240
Y-Component	0.02	0.021	0.026
Z-Component	0.126	0.172	0.371

As shown in Table 4.8, the value of the magnetic field corresponding to the measured voltages for each magnetic field component was obtained as:

$$Mag_{val} = C_{factor} \times V_{meas} \quad (4.2)$$

Where Mag_{val} is the corresponding magnetic field value, C_{factor} is the scale factor, and V_{meas} is the voltage obtained from optimized FMS output during field measurements.

All the output voltages obtained from the optimized FMS during magnetic field measurements were multiplied by the scale factor to obtain the magnetic field corresponding to the measured output voltages.

By employing equation (4.2), the corresponding earth's magnetic field component in Zaria as measured at the ECE Department, ABU, Zaria was calculated as:

$$Mag_{zaria(X)} = 10300.00 \times 3.305\ nT$$

$$Mag_{zaria(X)} = 34041.5\ nT$$

$$Mag_{zaria(Y)} = 10300.00 \times 0.02\ nT$$

$$Mag_{zaria(Y)} = 206.00\ nT$$

$$Mag_{zaria(Z)} = 10300.00 \times 0.126\ nT$$

$$Mag_{zaria(Z)} = 1297.80\ nT$$

Therefore, the total magnetic field intensity, F was obtained by using:

$$F = \sqrt{X^2 + Y^2 + Z^2} \quad (4.3)$$

Where X is the Northward magnetic field component, Y is the Eastward magnetic field component, and Z is the downward magnetic field component.

By employing equation (4.3), the corresponding total earth's magnetic field intensity, F, in Zaria (ECE Department, ABU, Zaria) was calculated as:

$$F_{zaria} = \sqrt{34041.50^2 + 206.00^2 + 1297.80^2} \ nT$$

$$F_{zaria} = 34066.85\ nT$$

Also, by employing equation (4.2), the corresponding earth's magnetic field component in Kaduna (Arugungu area, Katsina road, Kaduna) was calculated as:

$$Mag_{kaduna(X)} = 10300.00 \times 3.282\ nT$$

$$Mag_{kaduna(X)} = 33804.60\ nT$$

$$Mag_{kaduna(Y)} = 10300.00 \times 0.021\ nT$$

$$Mag_{kaduna(Y)} = 216.30\ nT$$

$$Mag_{kaduna(Z)} = 10300.00 \times 0.172\ nT$$

$$Mag_{kaduna(Z)} = 1771.60\ nT$$

By employing equation (4.3), the corresponding total earth's magnetic field intensity, F, in Kaduna (Arugungu area, Katsina road, Kaduna) was calculated as:

$$F_{kaduna} = \sqrt{33804.60^2 + 216.30^2 + 1771.60^2} \ nT$$

$$F_{kaduna} = 33851.68\ nT$$

Finally, by using equation (4.2), the corresponding earth's magnetic field component in Abuja (Old NEPA area, Kuje, Abuja) was calculated as:

$$Mag_{abuja(X)} = 10300.00 \times 3.240\ nT$$

$$Mag_{abuja(X)} = 33372.00\ nT$$

$$Mag_{abuja(Y)} = 10300.00 \times 0.026\ nT$$

$$Mag_{abuja(Y)} = 267.80\ nT$$

$$Mag_{abuja(Z)} = 10300.00 \times 0.371\ nT$$

$$Mag_{abuja(Z)} = 3821.30\ nT$$

By employing equation (4.3), the corresponding total earth's magnetic field intensity, F, in Abuja (Old NEPA area, Kuje, Abuja) was calculated as:

$$F_{abuja} = \sqrt{33372.00^2 + 267.80^2 + 3821.30)^2} \ \ nT$$

$$F_{abuja} = 33591.14\, nT$$

The corresponding calculated earth's magnetic field components at the three geomagnetic locations are presented in Table 4.9.

Table 4.9: Magnetic Field values obtained from Optimized Sensor at different Locations.

Earth's Magnetic Field Components	**Magnetic Field Values (nT)**		
	ECE Dept, ABU, Zaria	**Arugungu area, Katsina road, Kaduna**	**Old NEPA area, Kuje, Abuja**
X-Component	34041.50	33804.60	33372.00
Y-Component	206.00	216.30	267.80
Z-Component	1297.80	1771.60	3821.30

Therefore, the comparison of the IGRF standard total magnetic field intensity values with the total magnetic field intensity values obtained at the three geomagnetic locations (Zaria, Kaduna, and Abuja) by using the optimized sensor is presented in Table 4.10.

Table 4.10: Comparison of the Magnetic Fields obtained from IGRF and Optimized Sensor.

	Total Magnetic Field Intensity Values		
	ECE Dept, ABU, Zaria	**Arugungu area, Katsina road, Kaduna**	**Old NEPA area, Kuje, Abuja**
OFM Total Magnetic Field Intensity, F	34066.85	33851.68	33591.14
IGRF Standard Mag. Field intensity, F	34067.50	33852.70	33592.90
Measurement accuracy (%)	99.99	99.99	99.99

The results presented in Table 4.10 shows that the optimized fluxgate sensor realized was able to detect the earth's magnetic field, therefore validating the proposed Firefly optimization design of FMS and the systematic optimization approach for finding the

dimension and geometry of the sensor core, pick-up coil, and detection circuit simultaneously. The measurement accuracy (%) of the magnetic field was obtained using:

$$\%\ accuracy = \frac{M_{meas}}{M_{ref}} \times 100\% \tag{4.4}$$

where M_{ref} is the IGRF magnetic field standard values and M_{meas} is the total magnetic field values obtained from the measurement of magnetic field at different locations (Electrical and Computer Engineering (ECE) Department, ABU Zaria; Arugungu street, Katsina road in Kaduna; and Old NEPA area of Kuje, Abuja) using the developed optimized sensor. Therefore, the measurement accuracy for Zaria was obtained as:

$$\%\ accuracy = \frac{34066.85}{34067.50} \times 100\%$$

Measurements accuracy for Zaria $= 99.998\%$

Also, the measurement accuracy for Kaduna was obtained as:

$$\%\ accuracy = \frac{33851.68}{33852.70} \times 100\%$$

Hence, Measurements accuracy for Kaduna $= 99.996\%$

Finally, the measurement accuracy for Abuja was calculated as:

$$\%\ accuracy = \frac{33591.14}{33592.90} \times 100\%$$

Therefore, measurements accuracy for Abuja $= 99.994\%$

The measurement accuracy, 99.99%, for Zaria, Kaduna, and Abuja, respectively underlines the possibility to use the developed optimized sensor for earth's magnetic field exploration and even like a compass. However, the errors seen in the corresponding magnetic field obtained from the developed optimized sensor was attributed to heading error, which was due to a change in the orientation of the magnetometer during magnetic field measurements. In addition, dead zone effect was also observed, which was due to the angular region of magnetometer orientation in which the magnetometer produces poor or no measurements.

To verify DC or low frequency (~1 Hz) characteristics of the developed modified FMS, the sensor was further employed as an electronic compass to detect geomagnetic fields in the ETAP laboratory of Ahmadu Bello University, Zaria, Kaduna by carrying out an in-plane measurement, as demonstrated in the block diagram of experimental set-up of Figure 4.12 and the actual experimental set-up of Plate 4.11.

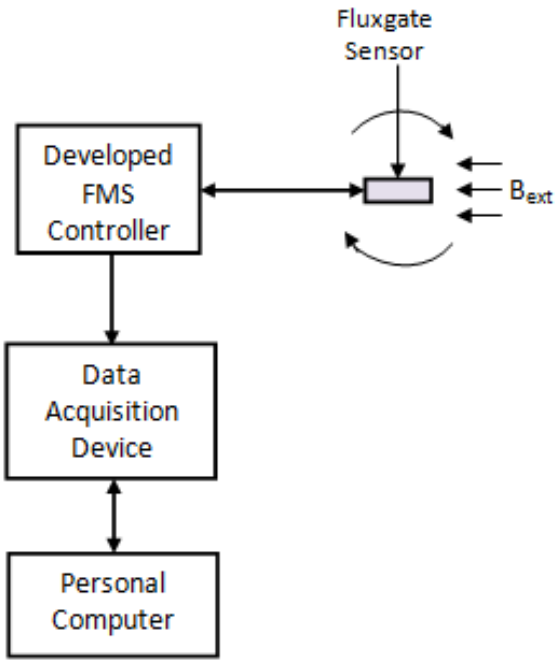

Figure 4.12: Block Diagram of Experimental Set-up for Earth's Magnetic Field Recording

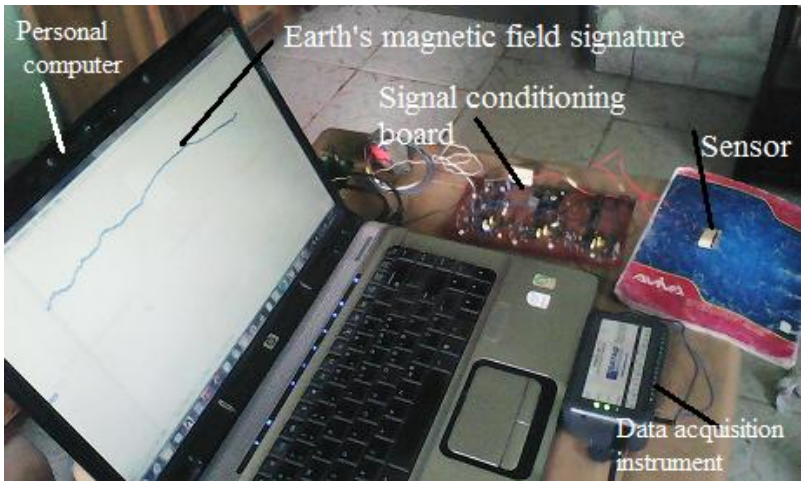

Plate 4.11: FMS Test Setup

As shown in Figure 4.12, the amplified signal from the FMS controller was fed into the Data acquisition (Dataq) instrument shown in Appendix G3. Data acquisition instrument is a portable data recording module that communicates through personal computer's universal serial bus port (Dataq, 2012). Dataq DI-145 was employed in this work, which featured four different channel inputs located on a single sixteen-position screw terminal block for easy connection and operation. DI-145 utilized the functionality of WINDAQ recording and playback software to explore all the features encased in these small inexpensive instruments (Dataq, 2012). Power was derived from the interface port so no external power was required. All software required to record and playback waveforms was included with the purchase of any DI-145 data acquisition starter kit via download. WINDAQ software is an invaluable resource to record and analyze data (Dataq, 2012) and is available for free from Dataq website (www.dataq.com).

Figure 4.13 shows the magnetic field plot while rotating the FMS in a horizontal plane (360^{o}) (Figure 4.12), the signal generated by the optimized FMS was sampled by the data acquisition instrument (shown in Appendix G4) for 80 seconds at 10 sec/div. in the horizontal axis and 200 nT/div. in the vertical axis.

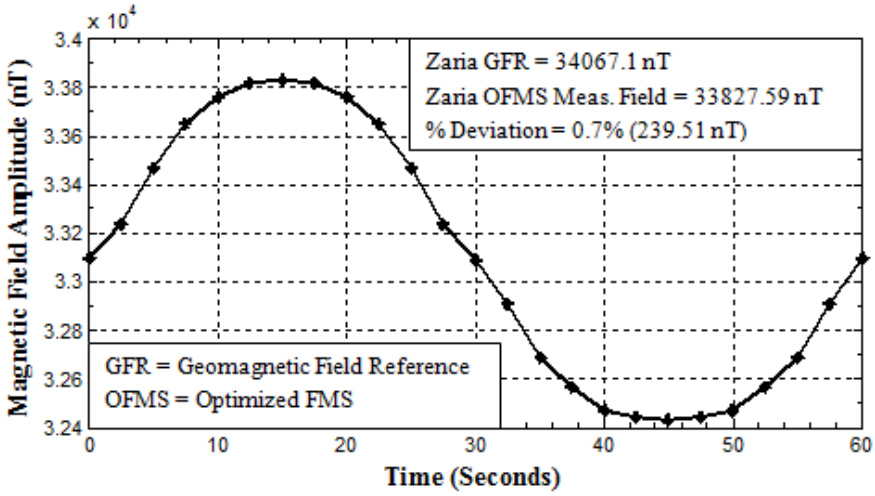

Figure 4.13: Measured Earth's Magnetic Field Strength at ETAP Lab. ABU Zaria.

As can be seen, the measured magnitude and direction of the earth's magnetic fields corresponding to the azimuth angle were consistent and reveal an accurate angle difference of 90° between in-plane axes. Therefore, the results provided in this research work verified the promising characteristics of the developed traditional wire-wound FMS based on the innovative firefly optimization algorithm design of a fluxgate magnetometer.

4.6 Performance of the Optimized FMS Based on Objective Five

The comparison of the voltage sensitivity, field noise, power consumption, and the sensor core diameter of the developed FMS based on modified FOA was compared with those developed through PPO. The proposed optimal design was examined by making a comparison between the conventional method using part-by-part optimization (PPO) approach and optimal sensor shown in Table 4.11. The percentage (%) increase in sensitivity with respect to PPO sensor A was obtained using:

$$\%\ improvement = \frac{V_{FOA} - V_{PPOA}}{V_{PPOA}} \times 100\% \tag{4.5}$$

where V_{FOA} is the voltage sensitivity obtained from optimal sensor, and V_{PPOA} is the voltage sensitivity obtained from PPO sensor A.

Table 4.11: Experimental Measurements obtained from modified FOA and PPO Sensors.

Variable Comparison	**Modified FOA Sensor**	**PPO Sensor A**	**PPO Sensor B**	**Unit**
Core outside diameter	12.00	14.00	10.00	mm
Core inside diameter	8.00	8.00	8.00	mm
Core height	2.00	2.00	3.00	mm
Number of Pick-up coil turns	646	548	587	-
Pick-up Coil bobbin thickness	5.00	2.00	1.00	mm
Amplifier Feedback resistor	100.00	100.00	100.00	kΩ
Amplifier feedback capacitor	150.00	150.00	150.00	nF
Amplifier input resistor	1.80	1.80	1.80	kΩ
Performance Comparison	**Modified FOA Sensor**	**PPO Sensor A**	**PPO Sensor B**	**Unit**
Magnetic path length ($\times 10^{-2}$)	3.058	3.282	2.804	m

Core size ($\times 10^{-6}$)	3.946	5.846	2.988	m^2
Voltage sensitivity	64.04	34.31	19.50	mV/μT
Noise level at 1 Hz	4.94	12.34	72.22	pT/√Hz

As seen in Table 4.11, the field sensitivity of sensor with 10 mm ring core outside diameter was 19.50mV/μT, while the field sensitivity of optimal sensor with 12 mm ring core outside diameter increased to a maximum value of 64.04mV/μT, and finally made a descent to 31.34mV/μT when the ring core outside diameter was 14 mm.

Despite the decrease in optimal sensor dimension from 14 mm to 12 mm with respect to PPO sensor A, the improvement in the sensitivity of optimal sensor over PPO sensor A was:

$$\% \, S_{PPOA} = \frac{64.04 - 34.31}{34.31} \times 100\%$$

Hence, the improvement in the sensitivity of optimal sensor over PPO sensor A was 86.65%.

Also, the percentage (%) increase in magnetic field noise with respect to PPO sensors A and B, N_{PPO} was obtained using:

$$\% \, N_{inc} = \frac{N_{PPO} - N_{FOA}}{N_{PPO}} \times 100\% \qquad (4.6)$$

Therefore, decrease in optimal sensor dimension from 14 mm to 12 mm with respect to PPO sensor A decreased the noise level of PPO sensor A by:

$$\% \, N_{inc} = \frac{12.34 - 4.94}{12.34} \times 100\%$$

Hence, the sensor noise level decreased by 59.97% with optimum FMS dimension.

However, the optimal sensitivity decreased when the core was further reduced from 12 mm optimum dimension to 10 mm. This was calculated as:

$$\% \, S_{PPOB} = \frac{V_{FOA} - V_{PPOB}}{V_{FOA}} \times 100\% \qquad (4.7)$$

where V_{FOA} is the voltage sensitivity obtained from optimized sensor, and V_{PPOB} is the voltage sensitivity obtained from the PPO sensor B.

By using equation (4.7), the percentage (%) decrease in sensitivity with respect to PPO sensor B, was calculated as:

$$\%\, S_{PPOA} = \frac{64.04 - 19.50}{64.04} \times 100\%$$

Hence, the sensitivity of the optimum sensor decreased by 69.55%.

Using equation (4.6), the percentage (%) increase in magnetic field noise with respect to PPO sensors B, was:

$$\%\, N_{inc} = \frac{72.22 - 4.94}{72.22} \times 100\%$$

Therefore, the reduction in noise level achieved from optimal FMS with respect to PPO sensors B was 93.16%, which was remarkable improvement for the developed optimized FMS.

The improvements achieved with modified FOA designed sensor over the PPO sensors, with respect to sensitivity and noise was attributed to mismatch problem on the part of PPO sensors and the effect of the aspect ratio of the sensor magnetic core. The mismatch was as a result of the same optimized detection circuit (Table 4.11) used for characterizing the three sensors. The dimensions of sensor core, number of excitation and pick-up coils determine the matching of the excitation and detection circuits. However, it was evident that the sensor with ferromagnetic core having optimum aspect ratio decreased demagnetization effect and contributed significant increase of the pick-up coil voltage for sensitivity. With respect to sensitivity, the sensitivity of a FMS increases with an increase in aspect ratio, and for an optimum value of the aspect ratio, the sensitivity is maximum. Beyond this optimal value, increasing the aspect ratio will decrease the sensitivity. On the other hand, the noise of a FMS decreases with an increase in aspect ratio, and for an optimum value of the aspect ratio, the noise is minimum. Beyond this optimal value, if the aspect ratio increases, the noise will increase.

In order to illustrate the improvement in the performance of the modified FOA sensor proposed and developed in this research work, the voltage sensitivity, magnetic field noise, power consumption, and sensor core diameter were benchmarked against two different existing FMS such as Matsuoka *et al.*, (2013), and Can and Topal, (2015) as presented in Table 4.12 and the chart illustrating this differences is shown in Figure 4.13.

Table 4.12: Comparison of the Current Work and some Existing Fluxgate Sensors

Reference	**Diameter (mm)**	**Noise (pT/√Hz at 1 Hz)**	**Max. B (±μT)**	**Power consumption (W)**	**Sensitivity (mV/μT)**	**Core Material**
Matsuoka *et al.*, (2013)	20	7.7 – 8.9	60	2.17	Unspecified	Ni-Mo permalloy
Can & Topal, (2015)	20	2720	30	Unspecified	11.40	Metglas 2714A
FOAD Sensor	12	4.94	49.44	0.446	64.04	MnZn Ferrite

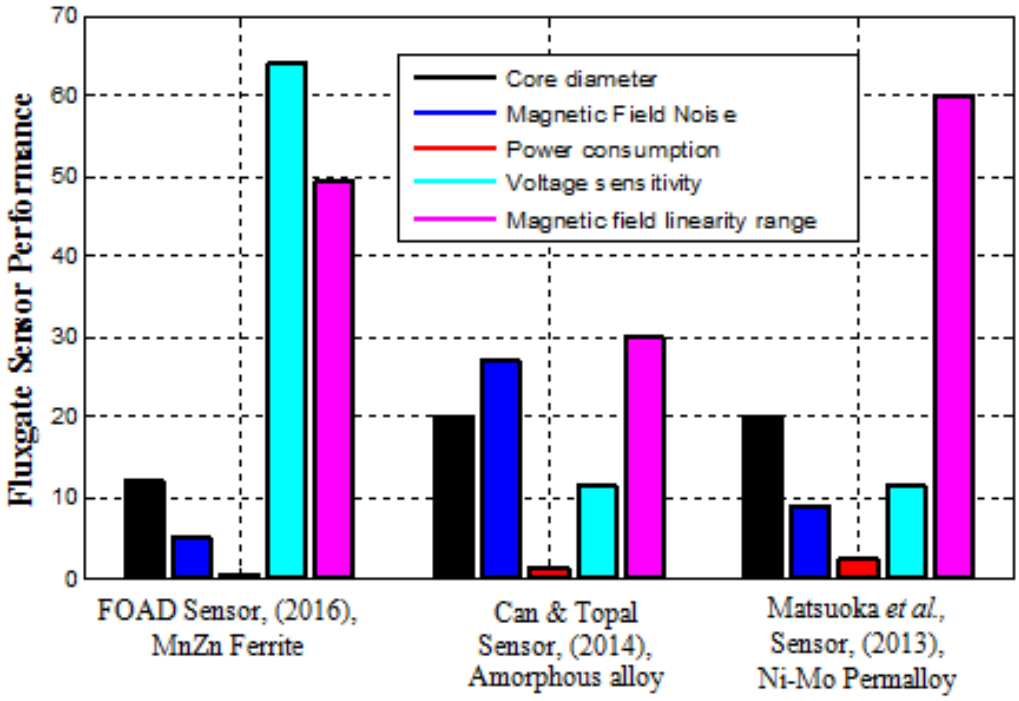

Figure 4.14: Comparison between the modified FOA Sensor and some Existing FMS.

Contrasting the three FMS results presented in Table 4.11 using the chart shown in Figure 4.14, the developed FMS in this research exhibited the following characteristics:

1) Smaller sensor core size (diameter) compared to the optimum core diameter suggested in the solutions reported in Matsuoka *et al.*, (2013), and Can and Topal, (2015).
2) A lower noise with respect to the solutions reported in Matsuoka *et al.*, (2013), and Can and Topal, (2015), due to optimum aspect ratio of ferromagnetic core obtained from modified FOA design.
3) Lower power consumption with respect to Matsuoka *et al.*, (2013) due to reduced core dimension which has resulted to demagnetization effect of the core, thereby reduced the excitation current and hence the power consumption.
4) Higher voltage sensitivity than the sensors reported in Can and Topal, (2015). The optimum dimension and geometry of sensor core, pick-up coil, and detection circuit significantly enhanced the voltage sensitivity by a factor of 5.6 due to the matching of the excitation and detection circuits which was aided by the ferro-resonance mode excitation and parametric amplification mode of detection employed in this research.
5) A much simpler realization of the ferromagnetic core with respect to Can and Topal, (2015) due to the reduction of the complexity of a FMS realized with modified FOA design without sacrificing precision or size of the sensor.

Therefore, considering the improvement achieved in the performance of fluxgate sensor using FOA and the systematic optimization approach used for finding the optimum dimensions of the sensor magnetic core, pick-up coil, and detection circuit simultaneously, the developed FMS achieved the overall objectives of this research work because of its reduced noise, power consumption, enhanced sensitivity, lower cost, and efficient fabrication.

4.7 Summary

The results obtained from the experimental measurements of steps 6, 7, and 8 have been presented and discussed. Despite the decrease in optimal sensor dimension from 14 mm to 12 mm with respect to PPO sensor A, the improvement in the sensitivity of optimized sensor over PPO sensor A was 86.65%, while the optimal sensor sensitivity degraded by 69.55% when the core was reduced from 12 mm to 10 mm. In addition, the reduction in noise level achieved from optimal sensor with respect to PPO sensors A and B was 59.97% and 93.16%, respectively, which was remarkable improvement for the modified FOA sensor. The improvements achieved with modified FOA designed sensor over the PPO sensors, with respect to sensitivity and noise could be attributed to mismatch problem on the part of PPO sensors and the effect of the aspect ratio of the sensor magnetic core. The mismatch was as a result of the same optimized detection circuit (see Table 4.11) used for characterizing the three sensors. The results showed the possibility of modified FOA for fluxgate magnetometer design problems.

Therefore, considering the improvement achieved in the performance of the optimized FMS using FOA and systematic optimization approach for simultaneously finding the optimum dimension and geometry of the magnetic core, pick-up coil, and detection circuit elements, the developed FMS achieved the overall aim of this research work because it reduced the noise by 50.6%, power consumption by 76.89%, and core diameter by 40% when compared with some existing FMS (see Table 4.12).

CHAPTER FIVE

CONCLUSION, LIMITATIONS AND RECOMMENDATION

5.1 Conclusions

In this research activity, a miniature fluxgate magnetometer with magnetic ring core in a square cross section of 2 mm was realized. The sensor was wire-wound based on traditional technology process.

The signal conditioning of the developed modified FOA fluxgate sensor was done by external electronics circuits. A square wave excitation current produced by a frequency oscillator circuit was fed to the excitation coil. The Helmholtz coils produced the external magnetic field to be measured. The second harmonic frequency of the induced voltage across the pick-up coil was measured with detection electronic circuit synchronized with the reference frequency from the square wave oscillator.

The results achieved from the experimental measurements by using the sense electronics circuit built for the purpose demonstrated that the sensitivity of FMS increased by 86.65% while the magnetic field noise decreased by 59.97% with an increase in aspect ratio and for an optimum value of aspect ratio. Also, the sensitivity was maximum while the field noise was minimum. Beyond this optimal value, an increase in the aspect ratio decreased the sensitivity by 69.55% and increased the magnetic field noise by 93.16% as computed from Table 4.11. It was observed that there was a strong relationship between the dimensions and geometry of FMS parameters with its sensitivity and noise. It was also noticed that the dimension of the sensor core, excitation, and pick-up coils turns were critical in matching excitation and detection circuits.

The introduction of the combined Firefly Optimization Algorithm (FOA) and the systematic optimization approach to FMS design problem in this research, by simultaneously finding the optimum dimensions and geometry of the sensor core, pick-up coil, and detection circuit, significantly improved the matching of the excitation and detection circuits. However, the poor performance results observed with PPO sensors A and B represented in Table 4.7 were

the evidence of the incompatibility of the degrading optimized detection circuit used for these sensors.

The developed optimized sensor for earth's magnetic field exploration showed good sensitivity of 97.09 mV/μT and linearity in the range of about ±49.44 μT. The power consumption of the sensor was 131 mW, the sensor electronics consumed 315 mW, while the whole sensor system consumed 446 mW. However, the optimized sensor high power consumption limits its possible application in portable system, but its performance is still better than the traditional technology-based solutions presented in literature whose values are higher as shown in Table 4.12.

Hence, good sensitivity and low power consumption, as well as the possibility of detecting magnetic field along two perpendicular directions make the developed FOA-based sensor suitable for portable compass application.

5.2 Limitations of the Research

Relevant limitations experienced during the course of this research work are as follows:

a. Non availability of the magnetic shield to protect the tested sensors from environmental and earth's magnetic field interference, which slightly affected the experimental measurements during Helmholtz coils characterizations.
b. Non availability of very low resolution spectrum analyzer for noise analysis which led to the adoption of the available Fast Fourier Transform (FFT) available on dataq instrument obtained from National Instruments.

5.3 Recommendations for Further Works

In addition to the results obtained in this research, there are some points that could be further improved, which included but not limited to the following:

1. Measurement of the perming and sensitivity stability with the variation of the temperature.
2. Evaluation of the possibility to improve the magnetic field properties of the Helmholtz coils.

REFERENCES

Abbott, J. J. (2015). Parametric design of tri-axial nested Helmholtz coils. *Review of Scientific Instruments, 86*/1-10.

Adewole A.P.; Otubamowo, K.; Egunjobi, T.O. and Kien, M. N. (2012). A comparative study of simulated annealing and genetic algorithm for solving the travelling salesman problem. *International Journal of Applied Information Systems (IJAIS)*, 4(4).

Ali, A.S.; Siddharth, S.; Syed, Z. and El-Sheimy, N. (2012). Swarm optimization-based magnetometer calibration for personal handheld devices. *Sensors*, *12*/12455-12472.

Alicke, F. (2015). *Low-Power Signal Conditioning for a Pressure Sensor*. Texas Instruments, Texas.

Andò, B.; Baglio, S.; Bulsara, A.; and Malfa, S. (2010). RTD Fluxgate Behavioral Model for Circuit Simulation. *In Proceedings of European Conference on Sensors, Actuators and Microsystems* (Eurosensors XXIV), Linz, Austria, *5-8*/1288–1291.

Andò, B.; Baglio, S.; Bulsara, A.R.; and Malfa, S. (2012). Adaptive modeling of hysteretic magnetometers. *IEEE Transactions on Instrumentation and Measurements*, *61*/1361–1367.

ANSYS (2011). *Low-Frequency Electromagnetic Analysis Guide*, ANSYS, Inc.

ANSYS (2014). *Low-Frequency Electromagnetic Analysis Guide*, ANSYS, Inc.

Ansari, M.T M. H.; Sulaiman, N, and Jusoh, A. Z. (2015). Analysis of geometrical features of e-shaped core μ-coil fluxgate magnetometer. *ARPN Journal of Engineering and Applied Sciences*, *10(18)*/8417-8420.

Anuradha, G.; Devi, D.L. and Babu, M.S.P (2014). ANTRANK: An ant colony algorithm for ranking web pages. *International Journal of Emerging Trends & Technology in Computer Science (IJETTCS), 3(2)*/208-212.

Arora, S. and Singh, S. (2013). The firefly optimization algorithm convergence analysis and parameter selection. *International Journal of Computer Applications (0975 – 8887) 69(3)*/48-52.

Aylaj, B. and Belkasmi, M. (2014). New simulated annealing algorithm for computing the minimum distance of linear block codes. *Advances in Computational Research*, *6(1)*/153-158.

Back, T., Hoffmeister, F. & Schwefel, H. (1991). A survey of evolution strategies. *Proceedings of the Fourth International Conference on Genetic Algorithms and their Applications*, San Mateo, CA, /2-9.

Bao, X.; Liu, S.; Zhang, N. and Dong, M. (2015). Combinatorial test generation using improved harmony search algorithm. *International Journal of Hybrid Information Technology*, *8(9)*/121-130.

Bae, S.; Hong, Y.K.; Lee, J.; Park, J.; Jalli, J.; Abo, G.S.; Kwon, H.M. and Jayasooriya, C.K.K. (2013). Pulsed ferrite magnetic field generator for through-the-earth communication systems for disaster situation in mines. *Journal of Magnetics*, *18(1)*/43-49.

Bajeh, A. O. and Abolarinwa, K. O. (2011). Optimization: A comparative study of genetic and tabu search algorithms. *International Journal of Computer Applications (IJCA)*, 31(5).

Bai, Q. (2010). Analysis of particle swarm optimization algorithm. *Journal of Computer Information Science*, *3*/180–184.

Baschirotto, A.; Borghetti, F.; Dallago, E.; Malcovati, P.; Marchesi, M.; Venchi, G. (2006). A CMOS front-end circuit for integrated fluxgate magnetic sensors. *Circuits and Systems, 2006. ISCAS 2006. Proceedings. 2006 IEEE International Symposium*, 4/4406.

Baschirotto, A.; Dallago, E.; Ferragina, V.; Ferri, M.; Grassi, M.; Malcovati, P.; Marchesi, M.; Melissano, E.; Morelli, M.; Rossini, A.; Ruzza, S.; Siciliano, P.; Venchi, G.

(2007). A CMOS 2D Micro-Fluxgate Earth Magnetic Field Sensor with Digital Output. *Solid-State Circuits Conference, 2007. ISSCC 2007. Digest of Technical Papers. IEEE International*, /390,610.

Baschirotto, A.; Dallago, E.; Malcovati, P.; Marchesi, M.; Melissano, E.; Morelli, M.; Siciliano, P.; Venchi, G. (2009). An Integrated Micro-Fluxgate Magnetic Sensor With Front-End Circuitry, *Instrumentation and Measurement, IEEE Transactions*, 58(9)/3269-3275.

Baschirotto, A.; Dallago, E.; Ferri, M.; Malcovati, P.; Rossini, A. and Venchi, G. (2010). A 2D micro-fluxgate earth magnetic field measurement system with fully automated acquisition setup, *Measurement*, *43*(1)/46-53.

Baumjohann, W. *et al.* (2010). Magnetic field investigation of Mercury's magnetosphere and the inner heliosphere by MMO/MGF, *Planet Space Science*, *58(2)*/279–286.

Benkhoff, J.; Casteren, J.V.; Hayakawa, H.; Fujimoto, M.; Laakso, H.; Novara, M.; Ferri, P.; Middleton, H.R. and Ziethe, R. (2010). BepiColombo-Comprehensive exploration of Mercury: Mission overview and science goals, *Planet Space Science*, *58(1)*/2–20.

Bhatt, V.; Rautela, R.S.; Sharma1, P.; Tiwari, D.C. and Khushu, S. (2010). Design and development of Helmholtz coil for hyperpolarized MRI. *Proceedings of the COMSOL Conference*, 1-6.

Biswasa, P.K. and Banerjee, S. (2014). Design and ANSYS software based simulation of U-I yype actuator and rail used in electromagnetic levitation system. *International Journal of Applied Science and Engineering*. *12(3)*/225-239.

Boriskin, A.V. and Sauleau, R. (2012). Hybrid Genetic Algorithm for Fast Electromagnetic Synthesis. In Dr. Olympia Roeva (Ed.), *Real-World Applications of Genetic Algorithms*. Shanghai: InTech.

Butta, M.; Ripka, P.; Infante, G.; Badini-Confalonieri G.A., and Vázquez, M. (2010). Magnetic microwires with field induced helical anisotropy for coil-less fluxgate. *IEEE Transactions on Magnetics, 46(7)*/2562-2565.

Butta, M. (2012). *Orthogonal Fluxgates*, *Magnetic Sensors - Principles and Applications*, Dr Kevin Kuang (Ed.). Shanghai: InTech.

Calister, W.D. (1985). *Materials Science and Engineering*, (3rd Ed.), New York: Wiley.

Can, H. & Topal, U. (2015). Design of ring core fluxgate magnetometer as attitude control sensor for low and high orbit satellites. *Journal of Superconductivity and Novel Magnetism. 28*/1093-1096.

Cao, D.; Liu, S.; and Jiang, C. (2011). Maximum energy transfer conditions in parametric amplification of current-output fluxgate sensors. *Sensors and Actuators A Physical*, *173/*136–140.

Chen, Z.; Zhou, S. and Jiang, A. (2011). Miniaturization design on magnetic induction sensors. In *Proceedings for International Conference on Electronic, Mechanical Engineering Information Technology*, 4626–4629.

Chen, C.; Liu, F.; Lin, J. and Wang, Y. (2015). Investigation and optimization of the performance of an air-coil sensor with a differential structure suited to helicopter TEM exploration. *Sensors*, *25*/23325-23340.

Coelho, L. D. S. & Mariani, V. C. (2012). Firefly algorithm approach based on chaotic Tinkerbell map applied to multivariable PID controller tuning. *Computers & Mathematics with Applications*, *64*(8)/2371-2382.

Coillot, C.; Moutoussamy, J.; Lebourgeois, R.; Ruocco, S. and Chanteur, G. (2010). Principle and performance of a dual-band search coil magnetometer: A new instrument to investigate fluctuating magnetic fields in space. *IEEE Sensors Journal*, *10(2)*/255–260.

Coillot, C.; Moutoussamy, J.; Chanteur, G.; Robert, P. and Alves, F. (2013). On-board hybrid magnetometer of NASA CHARM-II rocket: principle, design and performances. *Journal of Sensors and Sensors System, 2*/137–145.

Crevecoeur, G.; Sergeant, P.; Dupré, L. and Walle, R.V. (2010). A two-level genetic algorithm for electromagnetic optimization. *IEEE Transactions on Magnetics, 46(7)*/2585-2595.

Cruz-Chavez, M.A.; Martinez-Rangel, M.G. and Cruz-Rosales, M.H. (2015). Accelerated simulated annealing algorithm applied to the flexible job shop scheduling problem. *International Transactions in Operational Research, 00*/1–19.

Cui, Z. J. (2013). Design of a novel excitation circuit for low perming error fluxgate. *Advanced Materials Research, 748*/859-863.

Daron, B.B.; Jonathan, E. and Madsen, M.J. (2015). Magnetic field mapping. *Wabash Journal of Physics (WJP), 4*(3)/1-13.

Dataq (2012). Multimedia fast guide to Windaq Software. *Windaq Acquisition Waveform Recording Software by DATAQ Instruments, Inc.* Available online at http://www.dataq.com/product/software. retrieved on 30th January, 2012.

David, C.; Marina, D.-M.; Lucas, P.; Claudio, A. (2010). Small fluxgate magnetometers: Development and future trends in Spain. *Sensors*, *10*/1859–1870.

Dian, P.R.; Siti, M.S.; Siti, S.Y. (2011). Particle swarm optimization: Technique, system and challenges. *International Journal of Applied Computation.14*/19–27.

Evans, K. (2006). Fluxgate magnetometer explained. *Invasens,* http://www.invasens.co.uk/FluxgateExplained.PDF Accessed 10 November 2009.

Eyal, W. and Eugene, P. (2011). Noise investigation of the orthogonal fluxgate employing alternating direct current bias. *Journal of Applied Physics*. *109/*1063.

Fairchild Semiconductor (2002). CD4049 Hex Inverting Buffer Manual. Fairchild Semiconductor Corporation.

Ferri, M.; Surano, A.; Rossini, A.; Malcovati, P.; Dallago, E.; Baschirotto, A. (2009). Low-voltage fluxgate magnetic current sensor interface circuit with digital output for portable applications. *Sensors, 2009 IEEE*, /79-82.

Fister, I., Fister Jr., I., Yang, X. S. & Brest, J. (2013). A comprehensive review of firefly algorithms. *Swarm and Evolutionary Computation*, *13*(1)/34-46.

Fister, I.; Yang, X.S.; Fister, D. and Fister, I. J. (2014). Firefly Algorithm: A Brief Review of the Expanding Literature. *Studies in Computational Intelligence 516*/347-360.

Fogel, L. (1994). *Evolutionary programming in perspective: The top-down view*. Computational Intelligence: Imitating Life, edited by Zurada. J.M., Marks, Jr., R., and Robinson, C., IEEE Press, Piscataway, NJ, USA.

Frydrych, P.; Szewczyk, R. and Salach, J. (2014). Magnetic fluxgate sensor characteristics modeling using extended preisach model. *Proceedings of the 15th Czech and Slovak Conference on Magnetism*, Kosice, Slovakia. *126*(1)/18-19.

Gandomi, A. H. & Alavi, A. H. (2012). Krill herd: A new bio-inspired optimization algorithm. *Communications in Nonlinear Science and Numerical Simulation*, *17*/4831-4845.

Gandomi, A. H., Yang, X. S., Talatahari, S. & Alavi, A. H. (2013). Firefly algorithm with chaos. *Communications in Nonlinear Science and Numerical Simulation*, *18*(1)/89-98.

Gao, X.; Zhao, Y. and Wang, H. (2013). An algorithm for elimination of redundant sensors in RFID network based on the degree of overlap, *IJACT, 5(1)*/158-167.

Gao, W.; Zhao, B.; Zhou, G.T.; Wang, Q.Y. and Yu, C.Y. (2014). Improved artificial bee colony algorithm based gravity matching navigation method. *Sensors, 14*/12968-12989.

Gholizadeh, S. and Barati, H. (2012). A comprative study of three metaheuristics for optimum design of trusses. *International Journal of Optimization in Civil Engineering*, *3/*423-441.

Goldman, A. (1999). *Handbook of Modern Ferromagnetic Materials*. The Kluwer International Series in Engineering and Computer Science. New York: Springer Science LLC.

Gordon, D.I. and Brown, R.E. (1972). Recent advances in fluxgate magnetometry. *IEEE Transactions on Magnetics*, *8/*76–82.

Grosz, A. and Paperno, E. (2012). Analytical optimization of low frequency search coil magnetometers. *IEEE Sensors Journal*, *12(8)*/2719-2723.

Grosz, A.; Paperno, E.; Amrusi, S. and Liverts, E. (2010). Integration of the electronics and batteries inside the hollow core of a search coil. *Journal of Applied Physics*, *107(9)*/704–706.

Grosz, A.; Paperno, E.; Amrusi, S. and Zadov, B. (2011). A three-axial search coil magnetometer optimized for small size, low power, and low frequencies. *IEEE Sensors Journal*, *11(4)*/1088–1094.

Han, F.; Harada, S. and Sasada, I. (2012). Fluxgate and Search Coil Hybrid: A Low-Noise Wide-Band Magnetometer. *IEEE Transactions on Magnetics*, *48(11)*/3700-3703.

Hayt, W.H. and Buck, J.A. (2006). *Engineering Electromagnetic*s. The McGraw-Hill Publishing Company Limited.

He and Shiwa, (2014). A magnetic sensor with amorphous wire. *Sensors. 14*/10644 – 10649.

Hsieh, C.H; Dai, C.L. and Yang, M.Z. (2013). Fabrication and characterization of CMOS-MEMS magnetic microsensors. *Sensors*, *13*/14728-14739.

Heynen (2015). Kaschke Ferrite News. Available online at http://heynen.com/kaschke-ferrite-news.htm. Retrieved 25-12-2015.

http://magnetic-declination.com. Retrieved 05-03-2016.

Huang, W.S. and Lu, C.C. (2010). A novel 3D CMOS micro-fluxgate magnetic sensor for low magnetic field detection. *IEEE Sensors 2010 Conference*, 1791-1794.

Huang, W.S. Lu, C.C. and Jeng, J.T. (2010). Harmonic frequency characterizations of a CMOS micro fluxgate sensor for low magnetic field detection, In *Proceedings on Eurosensors XXIV*, Linz, Austria, *5*/993–996.

Indrasari, W.; Djamal, M.; Srigutomo, W. and Ramli (2012). A magnetic distance sensor with high sensitivity based on double secondary coil of fluxgate. *IOSR Journal of Applied Physics (IOSR-JAP), 2(5)/*29-35.

Irina, B. (2014). Multi-objective Algorithms for Coupled Optimization of Mechanical and Electromagnetic Systems, *Dissertations.* Paper 492.

Janosek, M.; Vyhnánek, J.; Zikmund, A.; Butvin, P. and Butvinová, B. (2014). Effects of core dimensions and manufacturing procedure on fluxgate noise. *Proceedings of the 15th Czech and Slovak Conference on Magnetism*, Košice, Slovakia, *126(1)*/104-105.

Jeng, J.T; Chen, J.H. and Lu, C.C. (2012). Enhancement in sensitivity using multiple harmonics for miniature fluxgates. *IEEE Transactions on Magnetics*, *48(11)*/3696-3699.

Karthik, P. (2013). A CMOS Analog Front-End Circuit for Micro-Fluxgate Sensors. A M.Sc. Thesis (Unpublished). Arizonal State University.

Kazemzadeh-Parsi, M. J. (2015). Optimal shape design for heat conduction using smoothed fixed grid finite element method and modified firefly algorithm. *Iranian Journal of Science and Technology*, *39*(2)/367-387.

Ke, L.; Feng, Z.; Ren, Z. and Wei, X. (2010). An ant colony optimization approach for the multidimensional knapsack problem. *Journal of Heuristics*, *16(1)*/65–83.

Kenwright, B. (2014). Epigenetics and genetic algorithms for inverse kinematics. *Experimental Algorithms, 9(4)*/1-13.

Kim, Y. H.; Kim, Y.; Yang, C. S. and Shin, K. H. (2013). Optimization of operation frequency of orthogonal fluxgate sensor fabricated with Co based amorphous wire. *Journal of Magnetics, 18(2)*/159-162.

Kim, S. J.; Moon, B. Y.; Chang, Y. K. and Oh, H. S. (2011). Design of a low-cost 2-axes fluxgate magnetometer for small satellite applications. *Journal of Astronomical Space Science, 22(1)*/35-46.

Kiran, M.S. and Babalik, A. (2014). Improved artificial bee colony algorithm for continuous optimization problems. *Journal of Computer and Communications, 2*/108-116.

Kirchhoff, M. R. and Büttgenbach, S. (2010). MEMS fluxgate magnetometer for parallel robot application. *Microsystems Technology, 16*/787–790.

Konak, S.K. and Konak, A. (2015). A simulated annealing algorithm with a dynamic temperature schedule for the cyclic facility layout problem. *14th INFORMS Computing Society Conference*, Richmond, Virginia, 200-211.

Korepanov, V. and Marusenkov, A. (2012). Flux-gate magnetometers design peculiarities. *Survey Geophysics, 33*/1059-1079.

Kubik, J. and Ripka, P. (2007). Racetrack fluxgate sensor core demagnetization factor. *Sensors and Actuators A, 143*/237-244.

Kugelstadt, T. (2001). *Active Filter Design Techniques In: Op Amps for Everyone*. Texas Instruments Incorporated. Dallas, Texas.

Kumar, S.; Sharma, V.K and Kumari, R. (2014). Randomized memetic artificial bee colony algorithm. *International Journal of Emerging Trends & Technology in Computer Science (IJETTCS), 3(1)*/52-62.

Larsen, C. A. (2012). *Signal Conditioning Circuitry Design for Instrumentation Systems*. Sandia National Laboratories, Califonia.

Lee, S.H.; Yi, H.C.; Han, K. and Kim, J.H. (2015). Genetic algorithm-based design optimization of electromagnetic valve actuators in combustion engines. *Energies, 8*/13222-13230.

Leepattarapongpan, C.; Phetchakul, T.; Penpondee, N.; Pengpad, P.; Srihapat, A.; Jeamsaksiri, W.; Chaowicharat, E.; Hruanun, C. and Poyai, A. (2014). A merged magnetotransistor for 3-axis magnetic field measurement based on carrier recombination–deflection effect. *Microelectronics Journal, 45*/565–573.

Lei, C.; Chen, L.; Lei, J.; Yang, X.H. and Zhou, Y. (2011). Low power integrated fluxgate sensor with a spiral magnetic core, *Microsystems Technology, 17(12)*/1697-1702.

Lei, J.; Chong, L. and Yong, Z. (2012a). Micro fluxgate sensor using solenoid coils fabricated by MEMS technology. *Measurement Science Review, 12(6)*/286-289.

Lei, J.; Chong, L. and Yong, Z. (2012b). Fabrication and characterization of a new MEMS fluxgate sensor with nanocrystalline magnetic core, *Measurement, 45*/535–540.

Li, C. and Ren, W. (2014). Application of angle and fluxgate sensor algorithm in design the smart sensor system. *Journal of Chemical and Pharmaceutical Research, 6(6)*/760-767.

Lu, C.; Huang, W.; Liu, Y. and Jeng, J. (2011). Design, fabrication, and characterization of a 3-D CMOS fluxgate magnetometer. *IEEE Transactions on Magnetics, 47(10)*/3752-3755.

Lu, C.; Liu, Y.; Jhao, F. and Jeng, J. (2012). Responsivity and noise of a wire-bonded CMOS micro-fluxgate sensor. *Sensors and Actuators A, 179/*39– 43.

Lu, C.C.; Huang, J. Chiu, P.K.; Chiu, S.L. and Jeng, J.T. (2014). High-sensitivity low-noise miniature fluxgate magnetometers using a flip chip conceptual design. *Sensors, 14/*13815-13829.

Lu, C. C. and Huang, J. (2015). A 3-Axis miniature magnetic sensor based on a planar fluxgate magnetometer with an orthogonal fluxguide. *Sensors, 15*/14727-14744.

Lv, H. and Liu, S. (2013). Research on MEMS technology of micro fluxgate sensor. *International Journal of Digital Content Technology and its Applications (JDCTA), 7(6)*/1159-1167.

Lv, H. and Liu, S. (2014). Design and fabrication of low power consumption micro fluxgate sensor. *Sensors and Transducers, 182(11)*/22-27.

Mann, I. R., Rae, I. J., Ozeke, L. G., Miles, D. M., and Yau, A. W. (2011). Plasma and Radiation *In Molniya Orbit (PRIMO) Science Objective and User's Needs Definition Document, Technical report*, Universities of Alberta, Edmonton, Canada.

Marshall, S.V. (1967). An analytical model for the fluxgate magnetometer. *IEEE Transactions on Magnetics*, *3*/459–463.

Matandirontya, E.; Van Zy, R.R.; Gouws, D.J. & Saunderson, E. F. (2013). Evaluation of a commercial-off-the-shelf fluxgate magnetometer for cubesat space magnetometry. *Journal of Small Satellites. 2(*1)/133-146.

Matsuoka, A.; Shinohara, M.; Tanaka, Y.M.; Fujimoto, A. and Iguchi, K. (2013). Development of fluxgate magnetometers and applications to the space science missions. *An Introduction to Space Instrumentation*, Edited by K. Oyama & C. Z. Cheng, 217–225.

Miguel, L.F.F.; Lopez, R.H. and Miguel, L.F.F. (2013). Multimodal size, shape, and topology optimization of truss structures using the firefly algorithm. *Advanced Engineering Software, 56/*23–37.

Miles, D.M.; Bennest, J.R.; Mann, I.R. and Millling, D.K. (2013). A radiation hardened digital fluxgate magnetometer for space applications. *Geoscience Instrumentation Methodology Data System, 2*/213–224.

MMG (2014). Soft Ferrite Materials and Components for Power, Signal and EMC Applicationss. Available online at www://adamsmagnetic.com. Retrieved 25-03-2014.

Musmann G. & Afanassiev Y. (2010). *Fluxgate Magnetometers for Space Research*. Books on Demand GmbH, Norderstedt.

Motchenbacher, C.D. and Connelly, J.A. (1993). *Low-Noise Electronic System Design*. New York: John Wiley & Sons.

Narod, B.B. (2014). The origin of noise and magnetic hysteresis in crystalline permalloy ring-core fluxgate sensors. *Geoscience Instrumentation Methodology Data System, 3/* 201–210.

Nielsen, O. V., Afanassiev, Y., and Fornaçon, K. H. (2010). Magnetic Materials for Sensors, In Musmann, G. (Ed.), *Fluxgate Magnetometers for Space Research*. Books on Demand, Nordersted.

NOAA (2016). *NGDC Mobile Declination Calculator*. Available online at http://ngdc.noaa.gov/geomag-web/calculators/mobileDeclination. Retrieved 05-03-2016.

Nourmohammadi, A.; Asteraki, M.H.; Feiz, S.M.H.; Habibi, M. (2015). A generalized study of coil-core-aspect ratio optimization for noise reduction and SNR enhancement in search coil magnetometers at low frequencies. *IEEE Sensors Journal*. *15(11)*/6454-6459.

Pathak, N. N.; Basu, B. and Mahanti, G.K. (2011). Combination of inverse fast fourier transform and modified particle swarm optimization for synthesis of thinned mutually coupled linear array of parallel half-wave length dipole antennas. *Progress In Electromagnetics Research M, 16*/105-115.

Platil, A. and Ripka, P. (2012). Fluxgate sensor and real operating–mode *B-H* curve. *Journal of Electrical Engineering, 63(7)*/118-121.

Powerstream (2013). Wire Guage and Current Limits Including Skin Depth and strength. Available online at www.powerstream.com/wire_size.htm. Retrieved 01-02-2013.

Primdahl, F. (1970). The fluxgate mechanism. Part 1: The gating curves of parallel and orthogonal fluxgates, *IEEE Transactions on Magnetics*, *6*/376–383.

Primdahl, F. (1979). The fluxgate magnetometer. *Journal of Physics E: Science and Instrumentation, 12*/241–253.

Purnama, B.; Suharyana, & Sutomo, A.D. (2012). Sensitive magnetic field sensor based on compensated double pick-p coil. *The Journal for Technology and Science, 23(1)*/21-24.

Rajput, R.K. (2010). *Magnetic Materials: Material Science and Engineering* (Rev. Ed). Daryaganj Delhi: Katson Books.

Richard, B. and Kenneth, J. (1989). *Sensors - A Comprehensive Survey.* In Gopel, W. Hesse, J. and Zemel, J.N. (Eds.). Hanau, FRG: Vacuumschmelze GmbH.

Ripka, P. (Ed), (2001). *Magnetic sensors and magnetometers*. Artech House, Boston, MA.

Ripka, P. and Janosek, M. (2010). Advances in magnetic field sensors, *IEEE Sensors Journal*, *10*/1108–1116.

Ripka, P. (2010). Advances in magnetic sensors. *17th Symposium IMEKO TC 4, 3rd Symposium IMEKO TC 19 and 15th IWADC Workshop Instrumentation for the ICT Era*, 9-19.

Ripka, P.; Butta, M.; Jie, F. and Li, X. (2010). Sensitivity and noise of wire-core transverse fluxgate. *IEEE Transactions on Magnetics, 46*/654–657.

Rovati, L. and Cattini, S. (2012). Zero-field readout electronics for planar fluxgate sensors without compensation coil. *IEEE Transactions on Magnetics*, 1-8.

Sadiku, M. N. O. (2010). *Elements of Electromagnetic*. OXFORD University press.

Said, G.N.A.; Mahmoud, A.M.; Horbaty, S.M. (2014). A comparative study of meta-heuristic algorithms for solving quadratic assignment problems. *(IJACSA) International Journal of Advanced Computer Science and Applications, 5(1)/*1-6.

Santos, C, L.; Bora, L.C.; Schauenburg, F. and Alotto, P. (2013). A multi-objective firefly approach using beta probability distribution for electromagnetic optimization problems. *IEEE Transactions on Magnetics, 49(5)/*2085.

Sebbes, P.; Ludwig, F. & Schilling, M. (2010). Fluxgate magnetometer for temperatures up to 180°C. *Journal of Electrical Engineering, 61(7)*/21-23.

Snelling, E.C. (1998). *Soft Ferrites: Properties and Applications*. (2nd Ed). London, U.K.: Butterworth.

SolarHam (2015). Magnetometer data. *SolarHam by Amateur Radio Station VE3EN*. Available online at http://www.solarham.net/magnetogram.htm. retrieved on 23rd December, 2015.

Solorzano, E.F. (2013). A fluxgate magnetometer and an EMIS algorithm to study Europa's subsurface. *Objective Europa*, 1-9.

Souar, Y. and Mouffok, O. (2014). Using genetic algorithms in integer programming for decision support. *Academic Journal of Interdisciplinary Studies, 3(6)*/11-16.

Suitella, D.Y. and Windarto, D.M.T (2011). High precision fluxgate current sensor. 1-6.

Sun, J. and Kosel, J. (2013). Extraordinary magneto-resistance in semiconductor/metal hybrids: A review, *Materials, 6*/500-516

Texas Instrument Inc. (2014). *Differential Signal Conditioning Circuit for Current and Voltage Measurement Using Fluxgate Sensors.* Texas Instruments Inc.

Todaro, M. T.; Sileo, L. and Vittorio, M. D. (2012). Magnetic field sensors based on micro-electromechanical systems (MEMS) technology. In Kevin Kuang (Ed.), *Magnetic Sensors - Principles and Applications*. Europe: InTech.

Trishchenko, A. P. and Garand, L. (2012). Observing polar regions from space: advantages of a satellite system on a highly elliptical orbit versus a constellation of low Earth polar orbiters, Can. *Journal of Remote Sensing, 38*/12–24.

Tseng J.Z; Wu C.C. and Dai C.L. (2014). Modeling and manufacturing of a micro-machined magnetic sensor using the CMOS process without any post-process. *Sensors, 14/*6722–6733.

Tumanski, S. (2011). *Handbook of Magnetic Measurements* (Rev. Ed). NY: CRC press.

Tumanski, S. (2013). Modern magnetic field sensors: A Review. *Przegląd Elektrotechniczny, 89/*1-12.

Ushie, O.J.; Abbod, M. and Ashigwuike, E.C. (2015). Naturally based optimisation algorithm for analogue electronic circuits: GA, PSO, ABC, BFO, and Firefly a Case Study. *Journal of Automation and Systems Engineering, 9(3)*/173-184.

Vandenbosch, G.A.E. and Vasylchenko, A. (2011). A Practical Guide to 3D Electromagnetic Software Tools. In Prof. Nasimuddin Nasimuddin (Ed.), *Microstrip Antennas*. Shanghai: Intech.

Velasco, Q. G.; Román, L. M.; Conesa, R. A. and Jeréz, F. (2011). Design of a low-consumption fluxgate transducer for high-current measurement applications. *IEEE Sensors Journal*, 11(2)/280-287.

Waheed, O.T. and Rehman, A. (2011). Design and development of a fluxgate magnetometer for small satellites in low earth orbit. *Journal of Space Technology*, 1(1)/78-82.

Wang, G., Guo, L., Duan, H., Liu, L. & Wang, H. (2012). A modified firefly algorithm for UCAV path planning. *International Journal of Hybrid Information Technology, 5*(3)/123-144.

Wang, Y.; Wu, S.; Zhou, Z.; Cheng, D.; Pang, N. and Wan, Y. (2013). Research on the dynamic hysteresis loop model of the residence times difference (RTD)-fluxgate. *Sensors, 13*/11539-11552.

Wang, X.; Gao, X.Z. and Zenger, K. (2015). An introduction to harmony search optimization method. *Springer Briefs in Computational Intelligence, 88/*46.

Weiss, E.; Paperno, E. and Plotkin, A. (2010). Orthogonal fluxgate employing discontinuous excitation. *Journal of Applied Physics*, 107(9)/717.

Weiss, E. and Paperno, E. (2011). Noise investigation of the orthogonal fluxgate employing alternating direct current bias. *Journal of Applied Physics*, 109/529.

Wu, S.; Chen, S.; Ouyang, J.; Zuo, C.; Yu, L. & Yang, X. (2012). Fabrication of MEMS-based micro-fluxgate sensor with runway-shaped Co-based amorphous alloy core. *Conference on Journal of Physics, 263*/1-6.

Yang, X.S. (2010). *Engineering Optimization: An Introduction with Metaheuristic Applications.* Hoboken, New Jersey: John Wiley and Sons, Inc.

Yousif, S.M.E. (2011). *Data Analysis*. MAGDAS School, Redeemer's University, Mowe, Ogun State, Nigeria.

Yang, X.S. (2012). Efficiency analysis of swarm intelligence and randomization techniques. *Journal of Computating and Theoretical Nanoscience, 9(2)*/189–198.

Yang, X.S. (2013). Multi-objectives firefly algorithm for continuous optimization. *Engineering Computation, 29*/175–184.

Yang, X.S. and He, X. (2013). Firefly Algorithm: Recent Advances and Applications. *International Journal of Swarm Intelligence, 1(1)*/36–50.

Yang, X. S. (2014). Cuckoo search and firefly algorithm: Theory and applications. *Studies in Computational Intelligence, 516*, Springer.

Yazdani, D. and Meybodi, M.R. (2010). AFSA-LA: A New Model for Optimization. *Proceedings of the 15th Annual CSI Computer Conference (CSICC'10).*

Zhang, Y.; Steiger, M.; Hibbs, A.D.; Grimm, R.E. and Sprott, T.A. (2010). Dual-mode, fluxgate-induction sensor for UXO detection and discrimination, *Journal of Environmental Engineering and Geophysics. 15(2)*/51–64.

Zorlu, O. (2008). Orthogonal fluxgate type magnetic micro-sensors with wide linear opretation range. PhD Thesis, Middle East Technical University, Ankara.

Zorlu, O.; Kejik, P. and Teppan, W. (2010). A closed core micro-fluxgate sensor with cascaded planar FeNi rings. *Sensors and Actuators A, 162*/241–247.

APPENDIX A

Figure A1: Data Sheet of Manganese Zinc Ferrite F39 Ring core (MMG-Neosid, 1998)

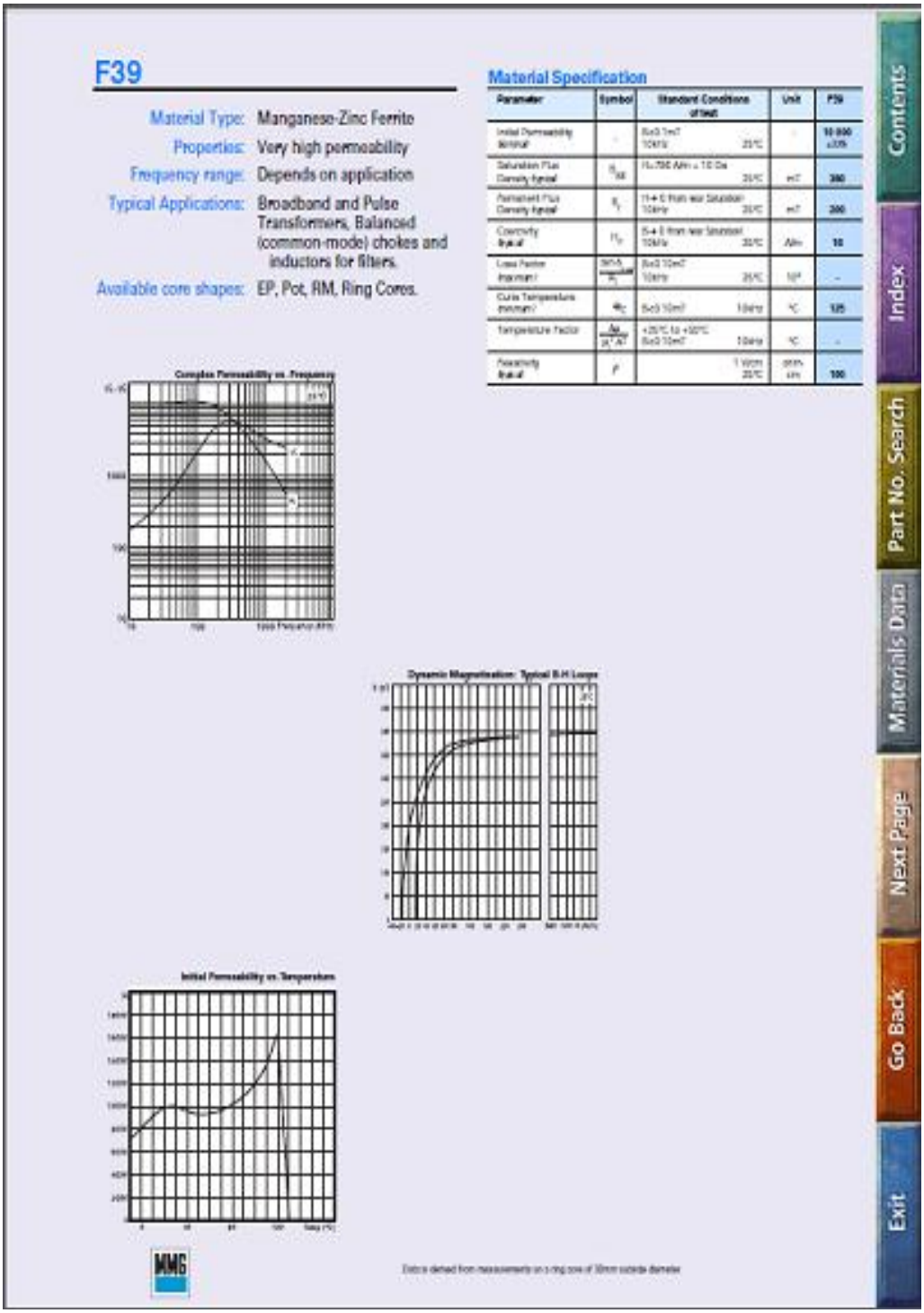

APPENDIX B

B.1 Development of Magnetostatic Model

The development of the model was carried out using 3-D static scalar magnetic analysis (3-D scalar potential analysis). In ANSYS, element SOLID96 is specifically designed for magnetic applications (ANSYS, 2011). SOLID96 element type is a 3-D eight nodes brick shape element with single degree of freedom. The only degree of freedom is the magnetic scalar potential (ANSYS, 2014). The scalar potential formulation involves three different analysis methods: Reduced Scalar Potential (RSP), Difference Scalar Potential (DSP), and Generalized Scalar Potential (GSP) (ANSYS, 2014). The type of problem being analyzed determines which method is best to use: RSP is used when the model contains no iron regions, or if it has iron regions but does not have current sources. Numerical cancellation errors may produce an inaccurate solution if RSP method is used when the model has both iron regions and current sources (ANSYS, 2009). The DSP method is used for models which contains iron region that does not provide a closed iron loop to magnetic flux and the current source that produces the magnetic flux, while a GSP method is used for models which contain iron region that provides a closed loop to magnetic flux and the current source which produces the magnetic flux (ANSYS, 2009). This is why SOLID96 element and GSP method are considered for the magnetic analysis in this research work.

SOLID96 element has the 3D magnetic field modeling capability. When this element is used in this research work to model the fluxgate structures in ANSYS, the areas occupied by current leads (coils) are not included in the finite element model (ANSYS, 2011). The geometry, node locations and the coordinate system for this element are shown in Figure B.1. The element is defined by eight nodes and the material properties. A tetrahedral-shaped element may be formed by defining the same node numbers for nodes M, N, O, and P; and nodes K and L (ANSYS, 2014). The element has nonlinear magnetic capability for modeling B-H curves or permanent magnet demagnetization curves (Saeed, 2003). A wedge-shaped element and a pyramid-shaped element may also be formed as shown in Figure B.1.

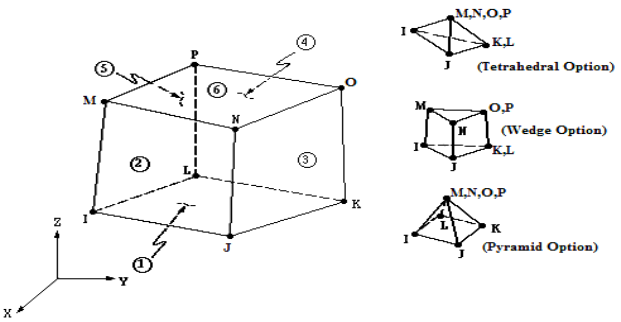

Figure B.1: SOLID96 3-D Element Geometry (Saeed, 2003; ANSYS, 2011)

In this model work, SOURC36 is another finite element type used to model the coils region for the sensor model. In ANSYS 3-D scalar potential analysis, current sources are not modeled as an integral part of the geometry. SOURC36 finite element is rather used to represent the shape and location of the current sources (ANSYS, 2014). SOURC36 elements type are special finite element type which are used for non-magnetic space modeling. It is possible to define coils, bars or arcs at any location in the model (ANSYS, 2011). The amount of current and other current-source data are specified as element real constants. The entire current source has to be modeled even if the rest of the model uses half-symmetry or quarter-symmetry (Saeed, 2003; ANSYS, 2011). The geometry and the coordinate system for this element are shown in Figure B.2.

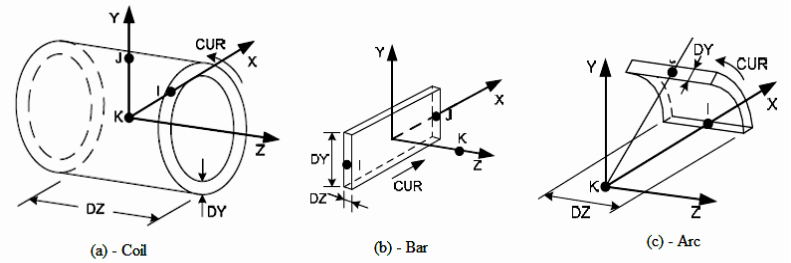

Figure B.2: Geometry of Current Source Element SOURC36 (ANSYS, 2014)

B.2 ANSYS Software Simulation

ANSYS is one of the most common FE computer packages. It was released for the first time in 1971. ANSYS is a comprehensive general-purpose FE computer program that contains

over 100,000 lines of code. ANSYS has been the leading FEA program for well over the last two decades. The current version of ANSYS includes computational structural dynamics, finite element solvers (FE), finite volume solvers for fluid dynamics (CFD), mesh-free particle solvers for high velocity, large deformation and fragmentation problems (SPH), and multi-solver coupling for multi-physics solutions including coupling between FE, CFD and SPH methods (Saeed, 2003).

ANSYS Multiphysics is a powerful interactive environment for modeling and solving all kinds of scientific and engineering problems based on partial differential equations (PDEs). To solve the PDEs, ANSYS Multiphysics uses the proven finite element method (FEM). The software runs the finite element analysis together with adaptive meshing and error control using a variety of numerical solvers. The user can perform a various types of analysis including stationary and time dependent analysis, linear and nonlinear analysis, eigen frequency and modal analysis. The ANSYS program uses Maxwell's equations as the basis for magnetic field analysis. The primary unknowns (degrees of freedom) that the finite element solution calculates are either magnetic potential or flux. Other magnetic field quantities are derived from these degrees of freedom, depending on the option chosen.

APPENDIX C

Magnetic Field Model of the Helmholtz Coils

In order to obtain these magnetic field values, Helmholtz coil design was optimize. The maximum driving current along with the very high magnetic field required large number of

number of turns in the Helmholtz coils windings. The magnetic field produced along the axis of a single circular coil was expressed as:

$$B(z) = \frac{\mu_0 . I_H}{2} . \frac{R^2}{(x^2 + R^2)^{3/2}} \qquad (C1)$$

where *z* is the distance from the centre to the axial field point, *R* is the radius of each turn of a coil, I_H is the coil current, and μ_0 is the permeability of air.

The magnetic field is a vector, which as magnitude and the direction of the magnetic field. But for axial points, the direction is always, due to the rotational symmetry of the coil, along the axis. Therefore the field may be stated by just a scalar value, the value along the axis.

The magnetic field for two coils placed in distance *R* apart (as shown in Figure 3.15), both carrying current I_H, with z = 0 at the midpoint of the coils was expressed as:

$$B_1(z) = \frac{\mu_0 I_H}{2} . \frac{R^2}{\left(\left(z + \frac{R}{2}\right)^2 + R^2\right)^{3/2}} \qquad (C2)$$

$$B_2(z) = \frac{\mu_0 I_H}{2} . \frac{R^2}{\left(\left(z - \frac{R}{2}\right)^2 + R^2\right)^{3/2}} \qquad (C3)$$

The resulting magnetic field from the two coils was obtained using the principle of superposition:

$$B(z) = \frac{\mu_0 . I_H . R^2}{2} . \left(\left(\left(z + \frac{R}{2}\right)^2 + R^2\right)^{-3/2} + \left(\left(z - \frac{R}{2}\right)^2 + R^2\right)^{-3/2}\right) \qquad (C4)$$

Equation (C1) together with equation (C4) can be used to compare the form of the magnetic field of a single coil with the field of the Helmholtz coils, respectively.

APPENDIX D

Computer Programs

In this section the main calculation routines and their input/output parameters are presented. Programming of the modeling and simulation of the magnetic field distribution in fluxgate sensor was performed using ANSYS (version 14.0) and the implementation of Firefly Optimization Algorithm (FOA) for Fluxgate Magnetometer Sensor (FMS) and Helmholtz coils were writing in MATLAB (version 7.0.4 with service pack 2).

Appendix D1: ANSYS Program for the Implementation of the Modeling and Simulation of the Magnetic Field Distribution in Fluxgate Sensor.

```
//batch list
```

```
//prep7
//title, 3-D Static Magnetic Analysis Problem - Tetrahedral
//com,
! define problem analysis parameters
! Ferromagnetic core:
ri = 6                          ! Internal radius of the core
ro = 9                          ! Outer radius of the core
hf = 8                          ! Height of the core
! Coil:
xc = 0.0018                     ! x-location of vertical leg of the coil
yc = 0.00425                    ! y- location of the horizontal leg of the coil
rad = 0.0005                    ! radius of curvature
n=70                            ! number of coil turns
i=0.01895               ! total excitation current
dy = 0.000315                   ! in-plane thickness
dz = 0.000315                   ! out-of-plane thickness
cname = coil1                   ! component name
!
!define element type
!
et,1,SOLID96                    ! define SOLID96 as element type
et,2,SOURC36            ! define SOURC36 as element type
!
!define material properties for coil and Ferrite
!
mp,murx,1,1                     ! permeability of coil
tb,bh,2,,20             ! permeability of ferrite (B – H curve)
tbpt,,20,.15
,,40,.274
,,60,.320
,,80,.348
,,100,.360
,,140,.374
,,180,.380
,,220,.386
,,680,.392
,,720,.394
,,400,.4
```

```
!
!create toroidal core volume
!
/pnum,volu
cylinder,0,0,ri,ro,hf     ! model dimensions (millimeters)
!
!set volume attributes
!
vsel,s,volu,,1                    ! select core volume
vatt,2,1,1                !assign attributes to toroidal core volume
!
!mesh the model
!
allsel,all                ! select everything
smrtsize,3                ! set smart size meshing level 3 (fine)
mshape,1,3d                       ! using tets
mshkey,0                  ! free volume mesh
vmesh,all                 ! mesh all solid volumes
!
!scale the model to meters
!
allsel,all                ! select everything
vlscale,all,,,.001,.001,.001,,0,1     ! scale models to MKS (meters)
!
!create the coils
!
local,12,0,7.5,0,4,0,270,,                    ! rotated local Cartesian system
wpcsys,12
race,xc,yc,rad,n*i,dy,dz,'coil1'     ! create racetrack coil
wpcsys,81
race,xc,yc,rad,n*i,dy,dz,'coil70'   ! create racetrack coil
/eshape,1
eplot                                                 ! plot element
save
finish
!
!apply boundary conditions
!
```

```
/solu
d,all,mag,0                          ! set potentials to zero (flux-parallel)
!
!solve
!
allsel,all                           ! select everything
magsolv,4,,,,,1                              ! solve magnetic field (GSP)
save
finish
!
!summarize toroidal coil magnetic field results
!
/post1
/com,
plnsol,h,sum                                 ! plot field strength magnitude
/com
plnsol,b,sum                                 ! plot flux density magnitude
/com
plvect,h,,,vect,elem,on              ! plot field strength as vector
/com
plvect,b,,,vect,elem,on              ! plot flux density as vector
save
finish
```

Appendix D2; Matlab Program Implemented for FMS Design Problems using Firefly Optimization Algorithm.

```
function minFGS
clc;
clear;
global v_amp i_amp GAMMA_w GAMMA_c S_amp S_sen R_w
global K0 T0 d_w A_c n_w rho f mu0
para = [50 20 0.9 1 0.7];
format long;
disp('Solving Firefly optimization problem for FMS...');
Lb = [0.01 0.008 0.001 5 0.001 5 1000 0.004 100e-9 1000];
Ub = [0.02 0.018 0.004 150 0.01 150 270000 0.01 180e-9 5000];
```

```
 % Initial random guess
u0 = Lb+(Ub-Lb).*rand(size(Lb));
 [u,fval,NumEval] = ffa_minFGS(@cost,@constraint,u0,Lb,Ub,para);
% Display results
optimum_sensor_dimensions = variables
optimum_equiv_mag_Field_noise = objective
total_number_of_function_evaluations = NumMaxEval
% Objective function
 function z = objfun(x)
d_w = 0.135e-3;
f = 5000;
mu0 = 1.2568e-6;
He = 0.75;
K0 = 1.38e-23;
T0 = 298;
GAMMA_c = 4.9e6;
GAMMA_w = 8.9e6;
b_w = d_w+(x(6)-1)*d_w;
T_w = d_w+(x(4)-1)*sqrt(3)/2*d_w;
l_m = 2*(x(1)+x(3)+2*T_w+4*x(5));
n_w = (b_w*T_w)/d_w^2;  %Number of pick up winding turns.
V_n = sqrt(4*K0*T0*R_w); %Noise voltage
A_c = 0.25*pi*(x(1)^2-x(2)^2);
A_w = x(1)*x(3)+2*x(1)*x(5)+2*x(3)*x(5)+4*x(5)^2;
S_sen = V_s/75e-6;
f0 = 1/(2*pi*x(7)*x(9));
z = 2*pi*f*mu0*mue*He*A_w*n_w;
 end
% Constrained optimization using penalty methods
function [g,geq] = constraint(x)
W_c = GAMMA_c*A_c*x(3); %Core weight.
W_w = GAMMA_w*0.25*pi*d_w^2*n_w*l_m;
V_s = 2*pi*f*mu0*mue*He*A_w*n_w;
f0 = 1/(2*pi*x(7)*x(9));
g(1) = 0.002-(x(1)-x(2));
g(2) = (x(1)-x(2))-0.003;
g(3) = (x(4)/x(6))-1;
g(4) = (n_w/2000)-1;
```

```
g(5) = (b_w/x(1))-1;
geq = [];
end
% Start Firefly Optimization Algorithm
function [nbest,fbest,NumMaxEval]= ffa_minFGS(fhandle,nonhandle,u0, Lb, Ub, para)
if nargin<6,
   para = [20 10 0.25 1.2 1];
end
if nargin<5,
   Ub = [];
end
if nargin<4,
   Lb = [];
end
if nargin<3,
   disp('Usuage: FA_minFGS(@cost, @constraint,u0,Lb,Ub,para)');
end
n = para(1);
MaxGeneration = para(2);
alpha = para(3);
betamin = para(4);
gamma = para(5);
NumMaxEval = n*MaxGeneration;
if length(Lb) ~= length(Ub),
   disp('Simple bounds/limits are improper!');
   return
end
% Calcualte dimension
d = length(u0);
% Initial values of an array
zn = ones(n,1)*10^100;
% generating the initial locations of n fireflies
[ns,Lightn] = init_ffa(n,d,Lb,Ub,u0);
for k = 1:MaxGeneration,    % start iterations
alpha = alpha_new(alpha,MaxGeneration);

% Evaluate new solutions (for all n fireflies)
for i = 1:n,
```

```
   zn(i) = Fun(fhandle,nonhandle,ns(i,:));
   Lightn(i) = zn(i);
end
% Ranking fireflies by their light intensity/objectives
[Lightn,Index] = sort(zn);
ns_tmp = ns;
for i = 1:n,
 ns(i,:) = ns_tmp(Index(i),:);
end
%% Find the current best
nso = ns;
Lighto = Lightn;
nbest = ns(1,:);
Lightbest = Lightn(1);
% Output the results to screen
fbest = Lightbest;
str = strcat('Optimum Noise : =',num2str(fbest), '  Optimum Dim: =',num2str(nbest));
str = strcat(str,' iter =');
str = strcat(str,num2str(k));
disp(str);
% Move all fireflies to the better locations
[ns] = ffa_move(n,d,ns,Lightn,nso,Lighto,nbest, Lightbest,alpha,betamin,gamma,Lb,Ub);
end
end
% The initial locations of n fireflies
function [ns,Lightn] = init_ffa(n,d,Lb,Ub,u0)
  if length(Lb) > 0,
   for i = 1:n,
   ns(i,:) = Lb+(Ub-Lb).*rand(1,d);
   end
else
   % generate solutions around the random guess
   for i = 1:n,
   ns(i,:) = u0+randn(1,d);
   end
end
% initial value before function evaluations
Lightn = ones(n,1)*10^100;
```

```
end
% Move all fireflies toward brighter ones
function [ns] = ffa_move(n,d,ns,Lightn,nso,Lighto, Lightbest,alpha,betamin,gamma,Lb,Ub)
% Scaling of the system
scale = abs(Ub-Lb);
% Updating fireflies
for i = 1:n,
% The attractiveness parameter
   for j = 1:n,
      r = sqrt(sum((ns(i,:)-ns(j,:)).^2));
     % Update moves
   if Lightn(i) > Lighto(j), % Brighter and more attractive
      beta0 = 1;
      beta = (beta0-betamin)*exp(-gamma*r.^2)+betamin;
      tmpf = alpha.*(rand(1,d)-0.5).*scale;
      ns(i,:)=ns(i,:).*(1-beta)+nso(j,:).*beta+tmpf;
   end
  end % end for j
end % end for i
% Check if the updated solutions/locations are within limits
[ns] = findlimits(n,ns,Lb,Ub);
end
% Apply nonlinear constraints by the penalty method
z = z+getnonlinear(nonhandle,u);
end
function Z = getnonlinear(nonhandle,u)
Z = 0;
lam = 10^15;
lameq = 10^15;
% Get nonlinear constraints
[g,geq] = nonhandle(u);
% Apply inequality constraints as a penalty function
for k = 1:length(g),
   Z = Z + lam*g(k)^2*getH(g(k));
end
% Apply equality constraints
for k = 1:length(geq),
  Z = Z+lameq*geq(k)^2*geteqH(geq(k));
```

```
end
end
% Test if inequalities hold
function H = getH(g)
        if g <= 0,
           H = 0;
        else
           H = 1;
        end
end
% Test if equalities hold
function H = geteqH(g)
        if g == 0,
           H = 0;
        else
           H = 1;
        end
        end
end
```

Appendix D3: Matlab Program Implementation for Helmholtz Coils using FOA.

```
function mincon_Helmholtz_Sim_1
para = [50 20 0.5 1 1];
% Simple bounds/limits
disp('Solving Firefly optimization problem for Helmholtz coils...');
Lb = [10 5 0.135 0.1 0.1];
Ub = [50 50 1.0 0.25 0.25];
% Initial random guess
u0 = Lb+(Ub-Lb).*rand(size(Lb));
[u,fval,NumEval] = ffa_mincon(@cost,@constraint,u0,Lb,Ub,para);
% Display results
bestsolution = u
bestojb = fval
total_number_of_function_evaluations = NumEval
% Cost or Objective function
 function B_h = cost(x)
  %global w;
mu_0 = 1.2568e-6;
```

```
rho_m = 8960;

rho_r = 1.6e-8;

c = 385;

T = 2.78e-2;

z = 0;

b_w = x(3)+(x(1)-1)*x(3);

T_w = x(3)+(x(2)-1)*sqrt(3)/2*x(3);

n_w = (b_w*T_w)/x(3)^2; %Number of pick up winding turns.

B_h = (mu_0*n_w*x(5)*x(4)^2)/2*(((z+x(4)/2)^2+x(4)^2)^(-3/2)+((z-x(4)/2)^2+x(4)^2)^(-3/2));

% Constrained optimization using penalty methods by changing f to F=f+ \sum %lam_j*g^2_j*H_j(g_j)

% where H(g)=0 if g<=0 (true), =1 if g is false

 end

function [g,geq] = constraint(x)

b_w = x(3)+(x(1)-1)*x(3);

T_w = x(3)+(x(2)-1)*(sqrt(3)/2*x(3));

g(1) = b_w-T_w;

geq = [];

end

% Start FA

function [nbest,fbest,NumEval]= ffa_mincon(fhandle,nonhandle,u0, Lb, Ub, para)

% Check input parameters (otherwise set as default values)

if nargin<6,

   para = [20 50 0.25 0.2 1];

end

if nargin<5,

   Ub = [];

end

if nargin<4,

   Lb = [];

end

if nargin<3,

   disp('Usuage: FA_mincon(@cost, @constraint,u0,Lb,Ub,para)');

end

% n = number of fireflies

% MaxGeneration = number of pseudo time steps

n = para(1);

MaxGeneration = para(2);

alpha = para(3);
```

```
betamin = para(4);
gamma = para(5);
% Total number of function evaluations
NumEval = n*MaxGeneration;
% Check if the upper bound & lower bound are the same size
if length(Lb) ~= length(Ub),
   disp('Simple bounds/limits are improper!');
   return
end
% Calcualte dimension
d = length(u0);

% Initial values of an array
zn = ones(n,1)*10^100;
% ----------generating the initial locations of n fireflies
[ns,Lightn] = init_ffa(n,d,Lb,Ub,u0);
% Iterations or pseudo time marching
for k = 1:MaxGeneration,    %%%%% start iterations
% This line of reducing alpha is optional
 alpha = alpha_new(alpha,MaxGeneration);
% Evaluate new solutions (for all n fireflies)
for i = 1:n,
   zn(i) = Fun(fhandle,nonhandle,ns(i,:));
   Lightn(i) = zn(i);
end
% Ranking fireflies by their light intensity/objectives
[Lightn,Index] = sort(zn);
ns_tmp = ns; %This line displays the array of the variable used.
for i = 1:n,
 ns(i,:) = ns_tmp(Index(i),:);
end
%
%% Find the current best
nso = ns;
Lighto = Lightn;
nbest = ns(1,:);
Lightbest = Lightn(1);
% Output the results to screen
```

```
fbest = Lightbest;
str = strcat('Best u: =',num2str(nbest),'  Bestobj: =',num2str(fbest));
str = strcat(str,' iter =');
str = strcat(str,num2str(k));
disp(str);
% Move all fireflies to the better locations
[ns] = ffa_move(n,d,ns,Lightn,nso,Lighto,nbest,Lightbest,alpha,betamin,gamma,Lb,Ub);
end   %%%%% end of iterations
end
function [ns,Lightn] = init_ffa(n,d,Lb,Ub,u0)
  % if there are bounds/limits,
if length(Lb) > 0,
   for i = 1:n,
   ns(i,:) = Lb+(Ub-Lb).*rand(1,d);
   end
else
   % generate solutions around the random guess
   for i = 1:n,
   ns(i,:) = u0+randn(1,d);
   end
end
% initial value before function evaluations
Lightn = ones(n,1)*10^100;
end
% Move all fireflies toward brighter ones
function [ns] = ffa_move(n,d,ns,Lightn,nso,Lighto,nbest,Lightbest,alpha,betamin,gamma,Lb,Ub)
% Scaling of the system
scale = abs(Ub-Lb);
% Updating fireflies
for i = 1:n,
% The attractiveness parameter beta=exp(-gamma*r)
    for j = 1:n,
        r = sqrt(sum((ns(i,:)-ns(j,:)).^2));
      % Update moves
    if Lightn(i) > Lighto(j), % Brighter and more attractive
       beta0 = 1;
       beta = (beta0-betamin)*exp(-gamma*r.^2)+betamin;
       tmpf = alpha.*(rand(1,d)-0.5).*scale;
```

```
      ns(i,:)=ns(i,:).*(1-beta)+nso(j,:).*beta+tmpf;
    end
  end % end for j

end % end for i
% Check if the updated solutions/locations are within limits
[ns] = findlimits(n,ns,Lb,Ub);
end
function alpha = alpha_new(alpha,NGen)
delta = 1-(10^(-4)/0.9)^(1/NGen);
alpha = (1-delta)*alpha;
end
function [ns] = findlimits(n,ns,Lb,Ub)
for i = 1:n,
    % Apply the lower bound
  ns_tmp = ns(i,:);
  I = ns_tmp < Lb;
  ns_tmp(I) = Lb(I);

  % Apply the upper bounds
  J = ns_tmp > Ub;
  ns_tmp(J) = Ub(J);

  % Update this new move
  ns(i,:) = ns_tmp;
end
end
% d-dimensional objective function
function z = Fun(fhandle,nonhandle,u)
% Objective
z = fhandle(u);
% Apply nonlinear constraints by the penalty method
% Z = f+sum_k=1^N lam_k g_k^2 *H(g_k) where lam_k >> 1
z = z+getnonlinear(nonhandle,u);
end
function Z = getnonlinear(nonhandle,u)
Z = 0;
% Penalty constant >> 1
```

```
lam = 10^15;
lameq = 10^15;
% Get nonlinear constraints
[g,geq] = nonhandle(u);
% Apply inequality constraints as a penalty function
for k = 1:length(g),
   Z = Z+ lam*g(k)^2*getH(g(k));
end
% Apply equality constraints (when geq=[], length->0)
for k = 1:length(geq),
  Z = Z+lameq*geq(k)^2*geteqH(geq(k));
end
end
% Test if inequalities hold
% H(g) which is something like an index function
function H = getH(g)
if g <= 0,
   H = 0;
else
   H = 1;
end
end
% Test if equalities hold
function H = geteqH(g)
if g == 0,
   H = 0;
else
   H = 1;
end
end
%% ==== End of Firefly Algorithm implementation ======
end
```

Appendix D4: Matlab Program Implementation for Plotting the Graph of Magnetic field of Helmholtz coils.

```
d_w = 0.449e-3;
%Current running through the wire
I_c = 0.1;
```

```
%Radius of the coils (distance from the centre to the beginning of the first
%winding)
R_i = 0.13;
%Width of each of the coils
a = 22*d_w;
%Height of each of the coils
b = d_w+23*sqrt(3)/2*d_w;
%Permeability of the vacuum
mu_0 = 4*pi*10^(-7);
%Number of windings in the width (in the first layer)
N_k = a/d_w;
%Number of windings in the height
N_j = (b-d_w)/(sqrt(3)/2*d_w)+1;
total_number_of_windings = N_j*(N_k-1/2)+1/2*rem(N_j,2)
%x position of the first winding
z1 = R_i+d_w/2;
%z position of the first winding
x1 =0.134/2+d_w/2;
%Initializes a parameter used later
c_start = 1;
%Sets the z values for which the B_field is calculated for
for x = linspace(-0.15,0.15,100)
%Initialize s parameters used later
B1_start = 0;
B2_start = 0;
%Loop that runs through all the layers with the number of N_j wires in them.
%It sums up each of these wire's contribution to the magnetic field .
for k = 1:N_k
   for j = 1:2:N_j
   z_j = z1+(j-1)*sqrt(3)/2*d_w;
   x_k = x1+(k-1)*d_w;
   B2 = B1_start+(mu_0*I_c*z_j^2)/2*(((z_j)^2+(x-x_k)^2)^(-3/2)...
      +((z_j)^2+(x+x_k)^2)^(-3/2));
   B1_start = B1;
   end
end
%Loop that runs through all the layers with the number of N_j-1 wires in them.
%It sums up each of these wire's contribution to the magnetic field .
```

```
for k = 1:N_k-1
   for j = 2:2:N_j
   z_j = z1+(j-1)*sqrt(3)/2*d_w;
   x_k = x1+d_w/2+(k-1)*d_w;
   B2 = B2_start+(mu_0*I_c*z_j^2)/2*(((z_j)^2+(x-x_k)^2)^(-3/2)...
      +((z_j)^2+(x+x_k)^2)^(-3/2));
   B2_start = B2;
   end
end
c = c_start;
%Adds the contributions from the layers with N j wires and N j?1 wires .
%This g i v e s the t o t a l magnetic f i e l d of the Helmholtz c o i l s as a function
%of the distance along the x?a x i s.
   B(c) = B1 + B2;
   c_start = c+1;
end
%Plots B as a function of x (the distance from the centre of the coil to the middle of the windings). %The average radius is also the distance
between the two coils.
close all
x = linspace(-0.15/0.115,0.15/0.115,100);
plot(x,B)
grid on
xlabel('x/R_{avg}')
ylabel('B[T]')
```

Appendix D5: C Program for converting the analog output of modified FOA fluxgate sensor to digital using 8051 microcontroller.

```
#include <REGX51.H>
#include "lcd.h"
#define adc_port P1            //ADC Port
#define rd P3_7                //Read signal P3.7
#define wr P3_6                //Write signal P3.6
#define cs P3_5                //Chip Select P3.5
#define intr P3_4              //INTR signal P3.4
void conv();                   //Start of conversion function
void read();                   //Read ADC function
unsigned int adc_avg,adc;
void main(){
char i;
LCD_INI();
while(1){                                   //Forever loop
adc_avg = 0;
for(i=0;i<10;i++){
```

```
conv();                 //Start conversion
read();                 //Read ADC
adc_avg += adc;
}
adc_avg = adc_avg/10;
wrt_cmd(0x80);
wrt_string("V(DC): ");
adc = adc_avg * 10300;
hex2lcd((unsigned char)(adc/1000));
wrt_data('.');
adc = adc%1000;
hex2lcd((unsigned char)(adc/10));
wrt_data('V');
}
}
void conv(){
cs = 0;                          //Make CS low
wr = 0;                          //Make WR low
wr = 1;                          //Make WR high
cs = 1;                          //Make CS high
while(intr);        //Wait for INTR to go low
}
void read(){
cs = 0;                          //Make CS low
rd = 0;                          //Make RD low
adc = adc_port; //Read ADC port
rd = 1;                          //Make RD high
cs = 1;                          //Make CS high
}
```

APPENDIX E

Table E.1: Trend of the Iterative Optimization Process for FGS Design Problem Using Firefly Algorithm Technique

	Input Variables										Output Variables
No. of Iterations	**Core Outside Diam. (mm)**	**Core Inside Diam. (mm)**	**Core Height (mm)**	**Pick-up Coil winding layers**	**Bobbin Thickness (mm)**	**Pick-up coil Axial winding turns**	**Amp. Feedback Res. (kΩ)**	**Pick-up coil Ind. (mH)**	**Amp. Feedback Cap. (nF)**	**Amp. Input Res. (kΩ)**	**EMFN (pT/√Hz)**
1	10.7614	8.44206	3.45298	14.8670	3.97123	34.8675	73.45	5.688	160.67	1.12	5.4562
2	10.7614	8.44206	3.45298	14.8670	3.97123	34.8675	73.45	5.688	160.67	1.12	5.4562
3	10.6818	8.13623	1.39983	23.1396	4.90201	29.0247	100.00	6.545	180.00	1.73	4.6168
4	11.1050	8.17299	1.38509	23.6820	5.00000	30.6652	99.01	6.277	172.55	2.06	4.3863
5	11.1050	8.17299	1.38509	23.6820	5.00000	30.6652	99.01	6.277	172.55	2.06	4.3863
6	11.1050	8.17299	1.38509	23.6820	5.00000	30.6652	99.01	6.277	172.55	2.06	4.3863
7	11.1050	8.17299	1.38509	23.6820	5.00000	30.6652	99.01	6.277	172.55	2.06	4.3863
8	11.1050	8.17299	1.38509	23.6820	5.00000	30.6652	99.01	6.277	172.55	2.06	4.3863
9	11.1155	8.17651	1.37826	24.0419	4.98269	30.7853	96.86	6.269	172.14	2.05	4.3139
10	11.1364	8.16474	1.37538	23.8903	5.00000	31.0604	97.84	6.263	173.28	2.07	4.3013
11	11.1364	8.16474	1.37538	23.8903	5.00000	31.0604	97.84	6.263	173.28	2.07	4.3013
12	11.1364	8.16474	1.37538	23.8903	5.00000	31.0604	97.84	6.263	173.28	2.07	4.3013
13	11.1461	8.17245	1.36468	24.1189	4.99722	30.7465	96.25	6.296	172.95	2.06	4.2964
14	11.1426	8.17209	1.36468	24.1189	4.99722	30.7592	96.31	6.295	173.00	2.05	4.2938
15	11.1426	8.17209	1.36468	24.1189	4.99722	30.7592	96.31	6.295	173.00	2.05	4.2938
16	11.1440	8.17211	1.36797	24.1008	4.99895	30.7664	96.35	6.296	173.03	2.05	4.2899
17	11.1440	8.17211	1.36797	24.1008	4.99895	30.7664	96.35	6.296	173.03	2.05	4.2899
18	11.1440	8.17211	1.36797	24.1008	4.99895	30.7664	96.35	6.296	173.03	2.05	4.2899
19	11.1440	8.17211	1.36797	24.1008	4.99895	30.7664	96.35	6.296	173.03	2.05	4.2899
20	11.1440	8.17211	1.36797	24.1008	4.99895	30.7664	96.35	6.296	173.03	2.05	4.2899

Table E.2: Trend of the Iterative Optimization Process for Helmholtz Design Problem Using Firefly Algorithm Technique

No. of Iterations	Coil width turns		Coil height turns		Wire diameter (mm)		Coil radius (mm)		Coil driving current (mA)		Magnetic field values (μT)	
	Coil 1	Coil 2	Coil 1	Coil 2	Coil 1	Coil 2	Coil 1	Coil 2	Coil 1	Coil 2	Coil 1	Coil 2
1	20	11	25	18	0.267	0.140	124.40	93.19	117.98	113.42	369.56	200.24
2	20	11	24	18	0.333	0.140	129.67	93.19	121.47	113.42	352.28	197.53
3	22	10	25	19	0.445	0.135	125.78	91.86	100.00	115.10	333.53	197.53
4	22	10	25	19	0.453	0.135	128.76	91.86	100.00	115.10	333.24	191.33
5	22	11	25	19	0.453	0.158	128.76	93.16	100.00	114.83	333.24	191.33
6	22	11	25	18	0.453	0.158	128.76	93.16	100.00	114.83	333.24	190.29
7	22	11	25	18	0.453	0.158	128.76	93.44	100.00	115.86	333.24	190.29
8	22	11	25	18	0.453	0.158	128.76	93.44	100.00	115.86	333.24	190.29
9	22	11	25	18	0.449	0.158	128.77	93.44	100.10	115.86	331.96	190.29
10	22	11	25	18	0.449	0.158	128.77	93.44	100.10	115.86	331.96	190.29
11	22	11	25	18	0.449	0.158	128.77	93.40	100.10	115.79	331.96	190.22
12	22	11	25	18	0.449	0.158	128.77	93.40	100.10	115.79	331.96	190.22
13	22	11	25	18	0.449	0.158	128.77	93.40	100.19	115.79	331.92	190.22
14	22	11	25	18	0.449	0.158	128.74	93.40	100.16	115.77	331.84	190.07
15	22	11	25	18	0.449	0.158	128.75	93.40	100.14	115.77	331.70	190.07
16	22	11	25	18	0.449	0.158	128.75	93.40	100.14	115.77	331.70	190.07
17	22	11	25	18	0.449	0.158	128.76	93.40	100.14	115.77	331.68	190.07
18	22	11	25	18	0.449	0.158	128.76	93.40	100.14	115.77	331.68	190.07
19	22	11	25	18	0.449	0.158	128.76	93.40	100.14	115.77	331.68	190.06
20	22	11	25	18	0.449	0.158	128.76	93.40	100.14	115.77	331.68	190.06

Table E.3: Screen Shot of the Trend of the Iterative Process for Helmholtz Design Problem Using Firefly Algorithm Technique

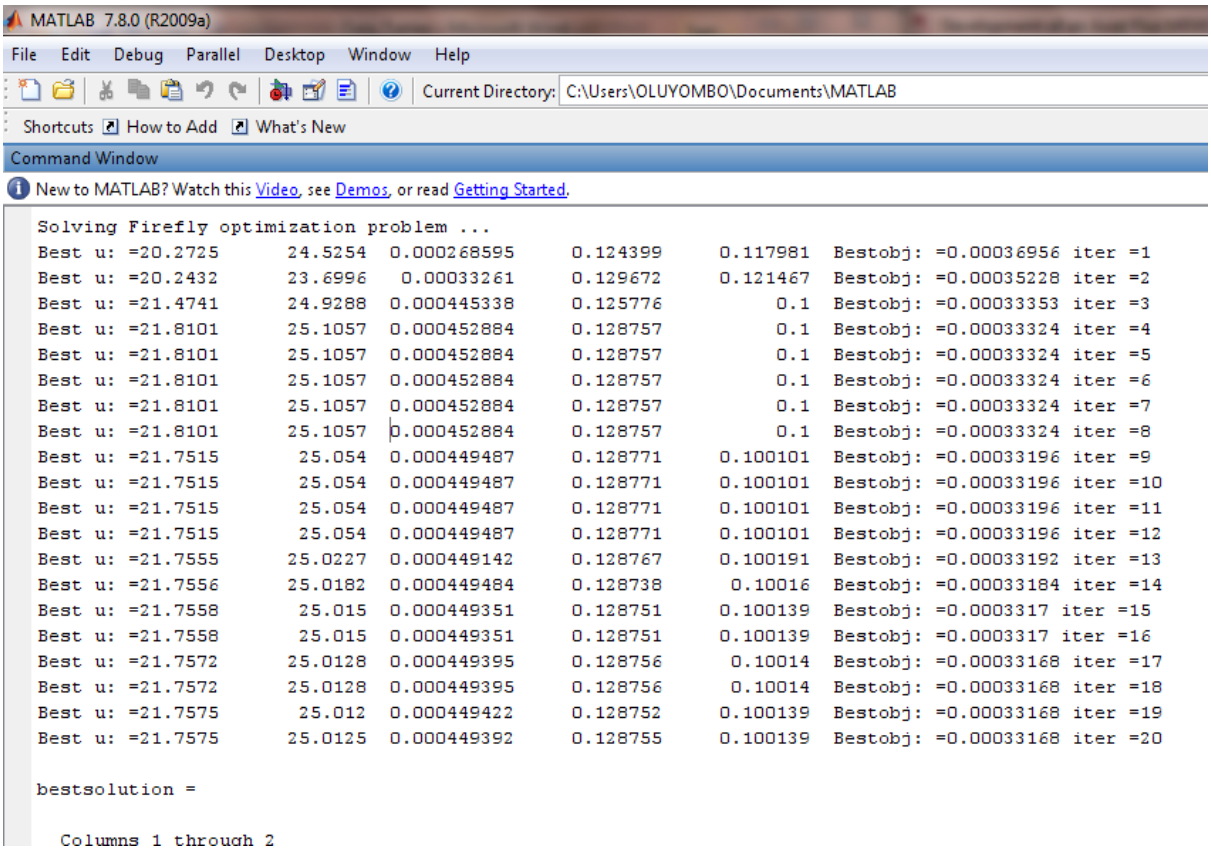

Table E.4: Firefly Optimization Algorithm Design Results

The predicted optimal design is checked by performing FOA sensitivity analysis and making a comparison between the optimized FMS parameters and the parameters obtained from FOA sensitivity analysis.

Variables Comparison	FOA	FOA Sensitivity Analysis	Unit
Core outside diameter	11.144	12.22	mm
Core inside diameter	8.172	8.0	mm
Core height	1.368	1.95	mm
Number of Layers of Pick-up coil	24	24	-
Pick-up Coil bobbin thickness	4.999	5.18	mm
Pick-up coil axial length turns	31	31	-
Amplifier Feedback resistor	96.35	105.35	kΩ
Pick-up coil inductance	6.296	6.296	mH
Amplifier feedback capacitor	173.03	173.03	nF
Amplifier gain resistor	2.05	1.75	kΩ
Sensor winding turns	646	646	-

Appendix E2: FMS Design Variables History

The history of primary design variables when displayed on the screen shows their trend. Oscillatory trend in the iterative process was observed which is caused by the randomization parameter of the firefly algorithm. Figures E.1 shows the variation of design variables as the iterations progress.

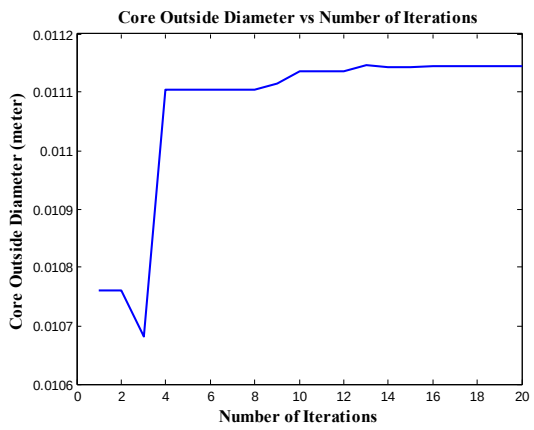

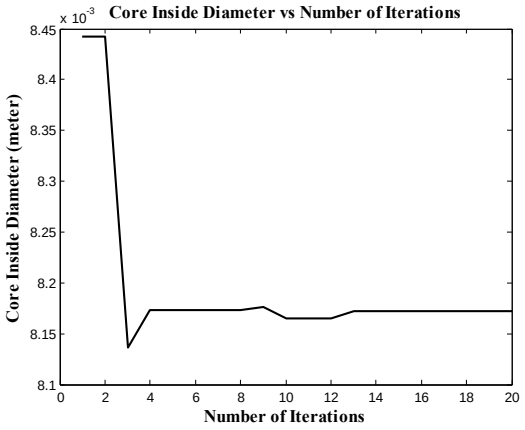

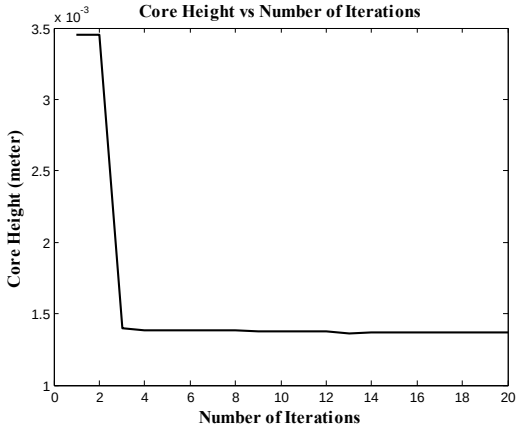
Core Height vs Number of Iterations
x 10^-3
Core Height (meter)
Number of Iterations

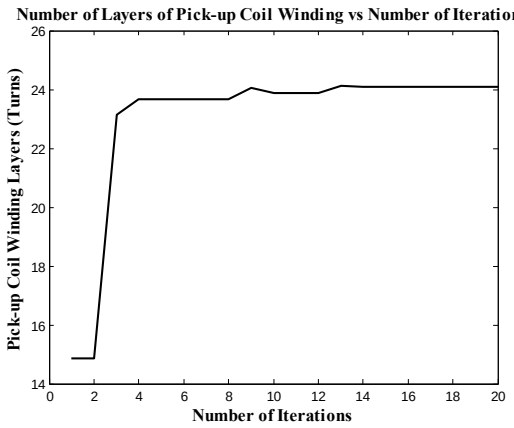
Number of Layers of Pick-up Coil Winding vs Number of Iterations
Pick-up Coil Winding Layers (Turns)
Number of Iterations

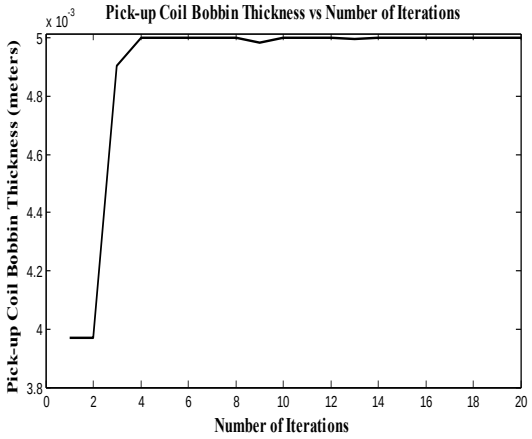
Pick-up Coil Bobbin Thickness vs Number of Iterations
x 10^-3
Pick-up Coil Bobbin Thickness (meters)
Number of Iterations

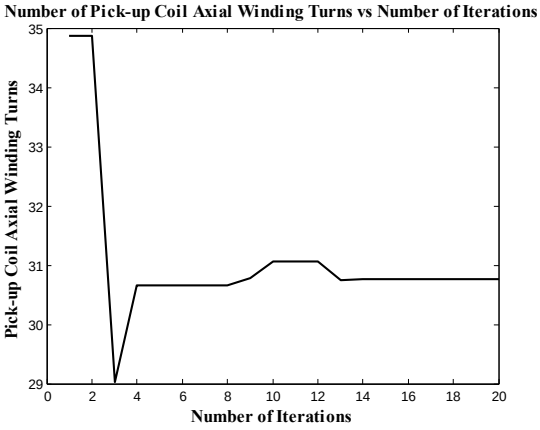
Number of Pick-up Coil Axial Winding Turns vs Number of Iterations
Pick-up Coil Axial Winding Turns
Number of Iterations

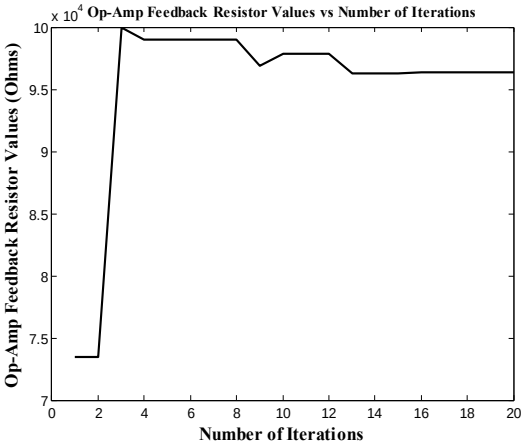
x 10^4 Op-Amp Feedback Resistor Values vs Number of Iterations
Op-Amp Feedback Resistor Values (Ohms)
Number of Iterations

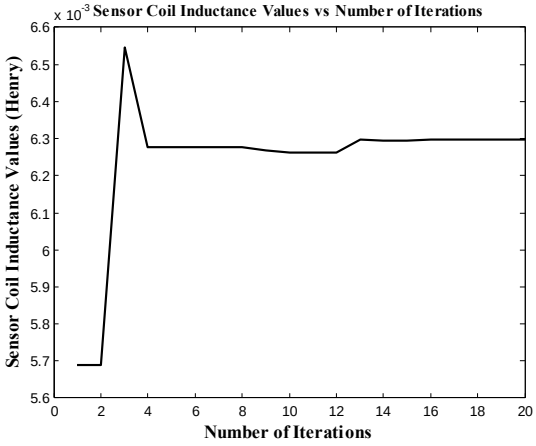
x 10^-3 Sensor Coil Inductance Values vs Number of Iterations
Sensor Coil Inductance Values (Henry)
Number of Iterations

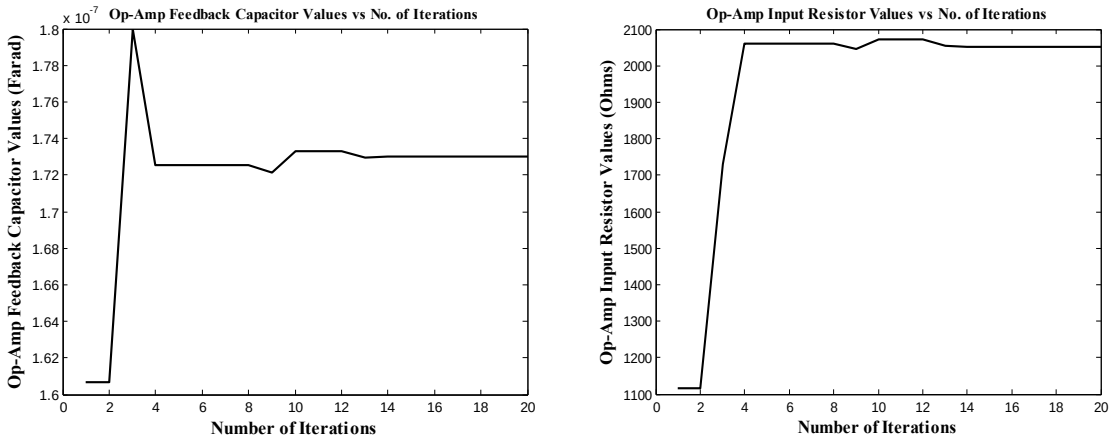

Figure E.1: History of Amplifier Feedback Capacitor for FMS Design Problem

If a design variable is not changing as shown in the design variables, such variable can be fixed for a few iterations and optimize only the remaining ones. Based on this fact, the sensitivity analysis is carried out to investigate FMS sensitivity to design variables. The proposed firefly optimization algorithm (FOA) method is used to obtain the optimal design of the fluxgate sensor core dimensions as 11.144 mm × 8.172 mm × 1.368 mm.

APPENDIX F1

Table F.1: Optimum Magnetic Field Noise and Voltage Sensitivity obtained with respect to Variation of Core Outside Diameter

Input Variables											Output Variables	
S/N	**COD (mm)**	**CID (mm)**	**Core Height (mm)**	**Pick-up Coil winding layers**	**Bobbin Thickness (mm)**	**Pick-up coil winding turns**	**Amp. Feedback Res. (Ω)**	**Pick-up coil Ind. (mH)**	**Amp. Feedback Cap. (nF)**	**Amp. Input Res. (kΩ)**	**Sensor Output Voltage (V)**	**EMFN (pT/√Hz)**
1	10.00	8.17211	1.36797	24.1008	4.99895	30.7664	96.35	6.296	173.03	2.05	3.6783	4.5353
2	11.00	8.17211	1.36797	24.1008	4.99895	30.7664	96.35	6.296	173.03	2.05	3.8623	4.3193
3	12.00	8.17211	1.36797	24.1008	4.99895	30.7664	96.35	6.296	173.03	2.05	4.0462	4.1229
4	13.00	8.17211	1.36797	24.1008	4.99895	30.7664	96.35	6.296	173.03	2.05	4.2302	3.9437
5	14.00	8.17211	1.36797	24.1008	4.99895	30.7664	96.35	6.296	173.03	2.05	4.4141	3.7793

Table F.2: Optimum Magnetic Field Noise and Voltage Sensitivity obtained with respect to Variation of Core Inside Diameter

Input Variables											Output Variables	
S/N	**COD (mm)**	**CID (mm)**	**Core Height (mm)**	**Pick-up Coil winding layers**	**Bobbin Thickness (mm)**	**Pick-up coil winding turns**	**Amp. Feedback Res. (Ω)**	**Pick-up coil Ind. (mH)**	**Amp. Feedback Cap. (nF)**	**Amp. Input Res. (kΩ)**	**Sensor Output Voltage (V)**	**EMFN (pT/√Hz)**
1	11.1440	7.500	1.36797	24.1008	4.99895	30.7664	96.35	6.296	173.03	2.05	3.8888	4.2899
2	11.1440	8.000	1.36797	24.1008	4.99895	30.7664	96.35	6.296	173.03	2.05	3.8888	4.2899
3	11.1440	8.500	1.36797	24.1008	4.99895	30.7664	96.35	6.296	173.03	2.05	3.8888	4.2899
4	11.1440	9.000	1.36797	24.1008	4.99895	30.7664	96.35	6.296	173.03	2.05	3.8888	4.2899
5	11.1440	9.500	1.36797	24.1008	4.99895	30.7664	96.35	6.296	173.03	2.05	3.8888	4.2899

Table F.3: Optimum Magnetic Field Noise and Voltage Sensitivity obtained with respect to Variation of Core Height

Input Variables	Output Variables

S/N	COD (mm)	CID (mm)	Core Height (mm)	Pick-up Coil winding layers	Bobbin Thickness (mm)	Pick-up coil winding turns	Amp. Feedback Res. (Ω)	Pick-up coil Ind. (mH)	Amp. Feedback Cap. (nF)	Amp. Input Res. (kΩ)	Sensor Output Voltage (V)	EMFN (pT/√Hz)
1	11.1440	8.17211	1.000	24.1008	4.99895	30.7664	96.35	6.296	173.03	2.05	3.7629	4.4334
2	11.1440	8.17211	1.500	24.1008	4.99895	30.7664	96.35	6.296	173.03	2.05	3.9340	4.2406
3	11.1440	8.17211	2.000	24.1008	4.99895	30.7664	96.35	6.296	173.03	2.05	4.1050	4.0639
4	11.1440	8.17211	2.500	24.1008	4.99895	30.7664	96.35	6.296	173.03	2.05	4.2761	3.9013
5	11.1440	8.17211	3.000	24.1008	4.99895	30.7664	96.35	6.296	173.03	2.05	4.4472	3.7512
6	11.1440	8.17211	3.500	24.1008	4.99895	30.7664	96.35	6.296	173.03	2.05	4.6182	3.6123
7	11.1440	8.17211	4.000	24.1008	4.99895	30.7664	96.35	6.296	173.03	2.05	4.7893	3.4832

Table F.4: Optimum Magnetic Field Noise and Voltage Sensitivity obtained with respect to Variation of Pick-up Coil Winding Turns

	Input Variables										Output Variables	
S/N	COD (mm)	CID (mm)	Core Height (mm)	Pick-up Coil winding layers	Bobbin Thickness (mm)	Pick-up coil winding turns	Amp. Feedback Res. (Ω)	Pick-up coil Ind. (mH)	Amp. Feedback Cap. (nF)	Amp. Input Res. (kΩ)	Sensor Output Voltage (V)	EMFN (pT/√Hz)
1	11.1440	8.17211	1.3679	5.00	4.99895	149.00	96.35	6.296	173.03	2.05	4.0023	4.1682
2	11.1440	8.17211	1.3679	9.00	4.99895	83.00	96.35	6.296	173.03	2.05	3.9596	4.2132
3	11.1440	8.17211	1.3679	15.00	4.99895	50.00	96.35	6.296	173.03	2.05	3.9486	4.2249
4	11.1440	8.17211	1.3679	18.00	4.99895	41.00	96.35	6.296	173.03	2.05	3.8788	4.3009
5	11.1440	8.17211	1.3679	25.00	4.99895	30.00	96.35	6.296	173.03	2.05	3.9325	4.2422
6	11.1440	8.17211	1.3679	27.00	4.99895	28.00	96.35	6.296	173.03	2.05	3.9621	4.2105
7	11.1440	8.17211	1.3679	35.00	4.99895	21.00	96.35	6.296	173.03	2.05	3.8471	4.3364
8	11.1440	8.17211	1.3679	149.00	4.99895	5.00	96.35	6.296	173.03	2.05	3.8863	4.2927

Table F.5: Optimum Magnetic Field Noise and Voltage Sensitivity obtained with respect to Variation of Pick-up Coil Bobbin

	Input Variables										Output Variables	
S/N	COD (mm)	CID (mm)	Core Height	Pick-up Coil	Bobbin Thickness	Pick-up coil	Amp. Feedback	Pick-up coil Ind.	Amp. Feedback	Amp. Input	Sensor Output	EMFN (pT/√Hz)

			(mm)	winding layers	(mm)	winding turns	Res. (Ω)	(mH)	Cap. (nF)	Res. (kΩ)	Voltage (V)	
1	11.1440	8.17211	1.3679	24.1008	1.000	30.7664	96.35	6.296	173.03	2.05	0.7164	23.2860
2	11.1440	8.17211	1.3679	24.1008	2.000	30.7664	96.35	6.296	173.03	2.05	1.3156	12.6806
3	11.1440	8.17211	1.3679	24.1008	3.000	30.7664	96.35	6.296	173.03	2.05	2.0442	8.1608
4	11.1440	8.17211	1.3679	24.1008	4.000	30.7664	96.35	6.296	173.03	2.05	2.9023	5.7479
5	11.1440	8.17211	1.3679	24.1008	5.000	30.7664	96.35	6.296	173.03	2.05	3.8899	4.2887
6	11.1440	8.17211	1.3679	24.1008	6.000	30.7664	96.35	6.296	173.03	2.05	5.0069	3.3319

Table F.6: Optimum Magnetic Field Noise and Voltage Sensitivity obtained with respect to Variation of Amplifier Feedback Resistor

Input Variables											Output Variables	
S/N	COD (mm)	CID (mm)	Core Height (mm)	Pick-up Coil winding layers	Bobbin Thickness (mm)	Pick-up coil winding turns	Amp. Feedback Res. (kΩ)	Pick-up coil Ind. (mH)	Amp. Feedback Cap. (nF)	Amp. Input Res. (kΩ)	Sensor Output Voltage (V)	EMFN (pT/√Hz)
1	11.1440	8.17211	1.3679	24.1008	4.99895	30.7664	180.00	6.296	173.03	2.05	7.2646	4.2582
2	11.1440	8.17211	1.3679	24.1008	4.99895	30.7664	150.00	6.296	173.03	2.05	6.0539	4.2655
3	11.1440	8.17211	1.3679	24.1008	4.99895	30.7664	120.00	6.296	173.03	2.05	4.8433	4.2765
4	11.1440	8.17211	1.3679	24.1008	4.99895	30.7664	100.00	6.296	173.03	2.05	4.0362	4.2874
5	11.1440	8.17211	1.3679	24.1008	4.99895	30.7664	82.00	6.296	173.03	2.05	3.2291	4.3037
6	11.1440	8.17211	1.3679	24.1008	4.99895	30.7664	68.00	6.296	173.03	2.05	2.8255	4.3154

Table F.7: Optimum Magnetic Field Noise and Voltage Sensitivity obtained with respect to Variation of Amplifier Feedback Capacitor

Input Variables											Output Variables	
S/N	COD (mm)	CID (mm)	Core Height (mm)	Pick-up Coil winding layers	Bobbin Thickness (mm)	Pick-up coil winding turns	Amp. Feedback Res. (kΩ)	Pick-up coil Ind. (mH)	Amp. Feedback Cap. (nF)	Amp. Input Res. (kΩ)	Sensor Output Voltage (V)	EMFN (pT/√Hz)

1	11.1440	8.17211	1.3679	24.1008	4.99895	30.7664	96.35	6.296	220.00	2.05	3.8886	4.2900
2	11.1440	8.17211	1.3679	24.1008	4.99895	30.7664	96.35	6.296	180.00	2.05	3.8888	4.2899
3	11.1440	8.17211	1.3679	24.1008	4.99895	30.7664	96.35	6.296	150.00	2.05	3.8889	4.2898
4	11.1440	8.17211	1.3679	24.1008	4.99895	30.7664	96.35	6.296	120.00	2.05	3.8891	4.2895
5	11.1440	8.17211	1.3679	24.1008	4.99895	30.7664	96.35	6.296	100.00	2.05	3.8893	4.2893
6	11.1440	8.17211	1.3679	24.1008	4.99895	30.7664	96.35	6.296	82.00	2.05	3.8896	4.2890

Table F.8: Optimum Magnetic Field Noise and Voltage Sensitivity obtained with respect to Variation of Amplifier Gain Resistor

	Input Variables										**Output Variables**	
S/N	**COD (mm)**	**CID (mm)**	**Core Height (mm)**	**Pick-up Coil winding layers**	**Bobbin Thickness (mm)**	**Pick-up coil winding turns**	**Amp. Feedback Res. (kΩ)**	**Pick-up coil Ind. (mH)**	**Amp. Feedback Cap. (nF)**	**Amp. Input Res. (kΩ)**	**Sensor Output Voltage (V)**	**EMFN (pT/√Hz)**
1	11.1440	8.17211	1.3679	24.1008	4.99895	30.7664	96.35	6.296	173.03	1.50	5.3183	3.7786
2	11.1440	8.17211	1.3679	24.1008	4.99895	30.7664	96.35	6.296	173.03	1.80	3.7785	4.0629
3	11.1440	8.17211	1.3679	24.1008	4.99895	30.7664	96.35	6.296	173.03	2.20	3.6258	4.4201
4	11.1440	8.17211	1.3679	24.1008	4.99895	30.7664	96.35	6.296	173.03	2.70	2.9543	4.8392
5	11.1440	8.17211	1.3679	24.1008	4.99895	30.7664	96.35	6.296	173.03	3.30	2.4171	5.3113

Appendix F2 Firefly Optimization Sensitivity Analysis Plots

The following plots illustrate the FOA sensitivity analysis performed to investigate the effects of changing the values of the optimum design variables that lead to an optimal value of noise and sensitivity of the fluxgate magnetometer sensor.

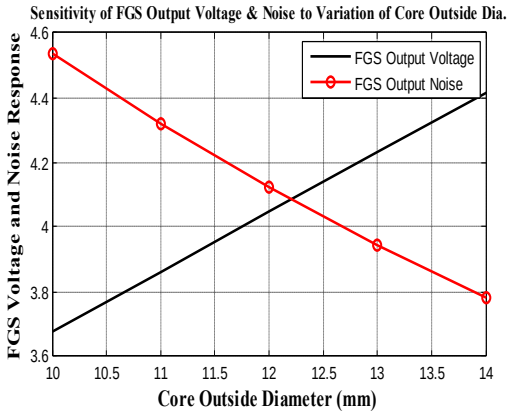

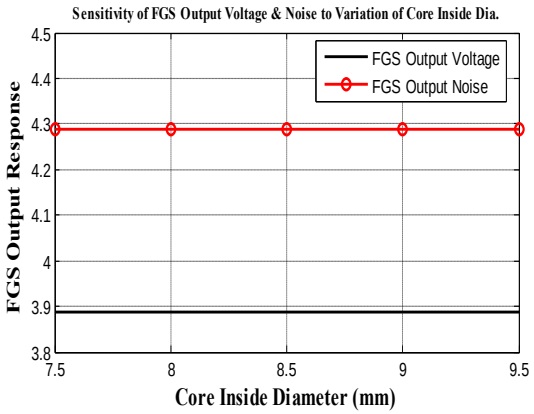

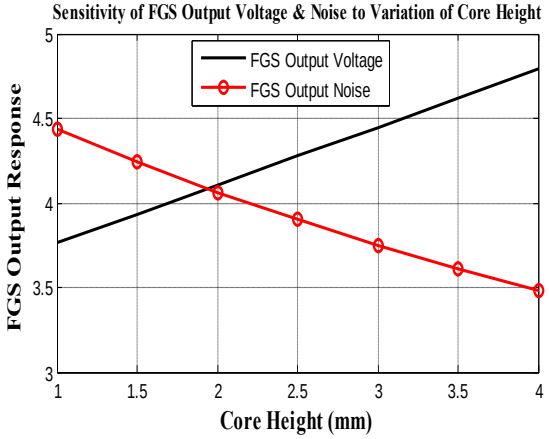

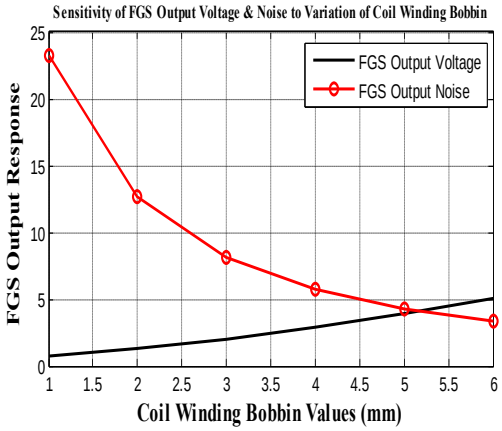

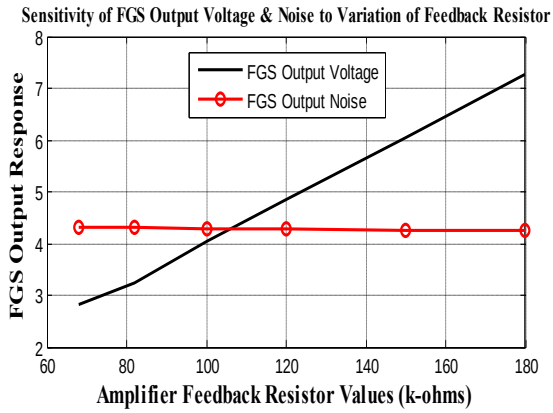

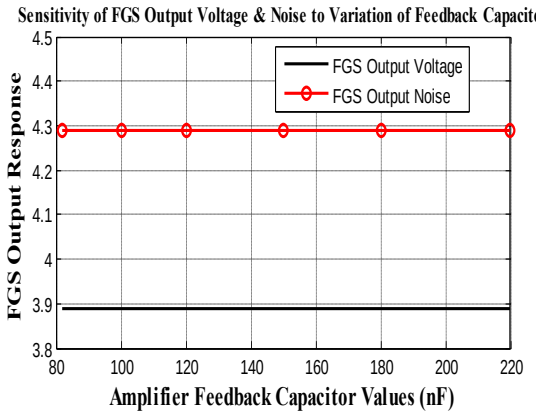

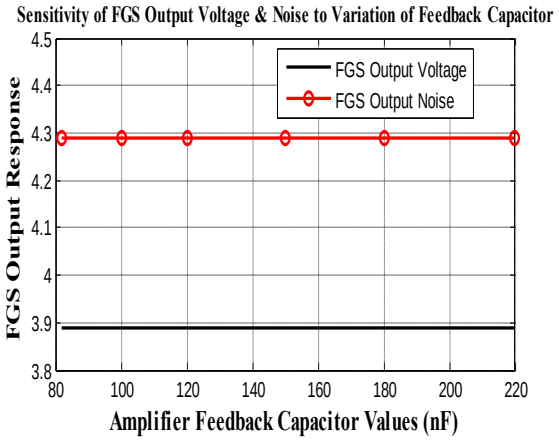

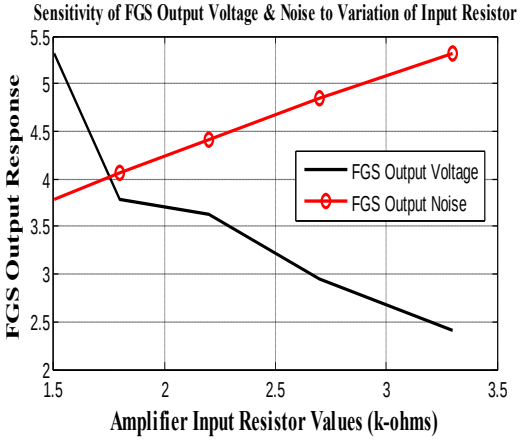

APPENDIX G

Table G.1: Measurements and Calculated Magnetic Field of Helmholtz Coils

Driving current (mA)	Calculated magnetic field	Measured magnetic field
2	3.62	0.42
4	7.24	1.24
6	10.85	6.05

8	14.47	8.14
10	18.09	18.09
12	21.71	21.71
14	25.32	25.32
16	28.94	28.94
18	32.56	32.56
20	36.18	36.18
22	39.80	39.80
24	43.41	43.39
26	47.03	47.20
28	50.65	50.22
30	54.27	54.97
32	57.89	57.88
34	61.50	61.56
36	65.12	65.72
38	68.74	68.57
40	72.36	72.66
42	75.97	76.71
44	79.59	80.91
46	83.21	84.21
48	86.83	87.03
50	90.45	90.45
52	94.06	94.06
54	97.68	95.68
56	101.30	101.30
58	104.92	104.92
60	108.54	106.54
62	112.15	112.15
64	115.77	114.27
66	119.39	118.99
68	123.01	124.16
70	126.62	127.98
72	130.24	131.77
74	133.86	134.60
76	137.48	136.64
78	141.10	140.56
80	144.71	143.97
82	148.33	147.29
84	151.95	150.97
86	155.57	154.91
88	159.19	156.39
90	162.80	163.72
92	166.42	168.38
94	170.04	170.34
96	173.66	174.55
98	177.27	176.23
100	180.89	179.90

Table G.2: FMS Output Voltages at Different Angles of Evaluation in the Magnetic Field.

Angle (degree)	PPOD Sensor A		FOAD Sensor		PPOD Sensor B	
	Measured values	Calculated values	Measured values	Calculated values	Measured values	Calculated values
0	0.03	0.00	0.08	0.00	0.02	0.00
15	0.49	0.58	0.89	0.88	0.39	0.32
30	1.09	1.13	1.76	1.70	0.78	0.62
45	1.53	1.59	2.32	2.40	0.98	0.87
60	1.98	1.95	2.92	2.94	1.00	1.07
75	2.19	2.17	3.30	3.27	1.21	1.19
90	2.25	2.25	3.39	3.39	1.23	1.23
105	2.15	2.17	3.31	3.27	1.20	1.19
120	1.97	1.95	2.91	2.94	1.01	1.07
135	1.55	1.59	2.34	2.40	0.97	0.87
150	1.08	1.13	1.75	1.70	0.76	0.62
165	0.61	0.58	0.91	0.88	0.43	0.32
180	0.01	0.00	0.06	0.00	0.01	0.00
195	-0.35	-0.58	-0.80	-0.88	-0.36	0.32
210	-1.03	-1.13	-1.76	-1.70	-0.50	0.62
225	-1.52	-1.59	-2.35	-2.40	-0.84	0.87
240	-1.85	-1.95	-2.91	-2.94	-0.98	1.07
255	-2.12	-2.17	-3.23	-3.27	-1.03	1.19
270	-2.20	-2.25	-3.35	-3.39	-1.12	1.23
285	-2.10	-2.17	-3.22	-3.27	-1.05	1.19
300	-1.97	-1.95	-2.92	-2.94	-1.00	1.07
315	-1.55	-1.59	-2.38	-2.40	-0.86	0.87
330	-1.12	-1.13	-1.85	-1.70	-0.52	0.62
345	-0.51	-0.58	-1.00	-0.88	-0.38	0.32
360	0.02	0.00	0.08	0.00	0.02	0.00

Figure G.3 Data Acquisition Instrument Controls, Indicators, and Connections

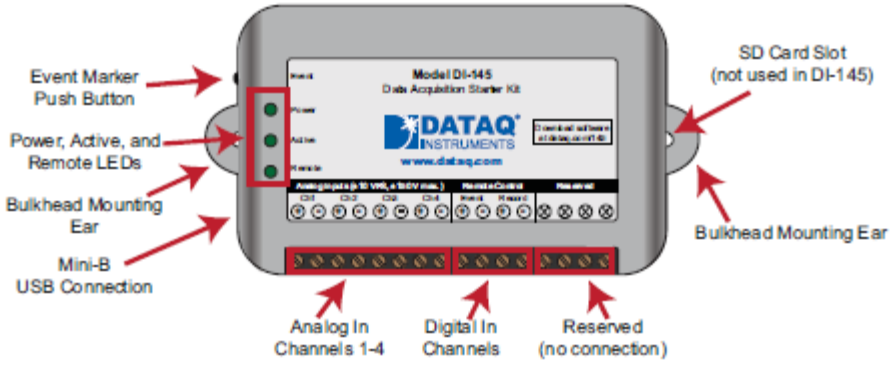

***Please note:** The SD card slot is not used in the DI-145. Allowing foreign materials to enter the device through the SD card slot may result in damage to the instrument.*

Mini-B USB Connection

Use the supplied USB cable to connect and power the instrument through your computer's USB port.

Connecting Input Signals

All input signal connections are made to the 16-port screw terminals. Each terminal is labeled directly on the instrument case.

DI-145 Signal Connections

Refer to the following for screw terminal port identification.

Ch#: Analog channels 1-4 (±10VFS, ±150V transient Max.)

Remote Control Event: Digital Input bit 0—Remote Event Marker

Remote Control Record: Digital Input bit 1—Remote Start/Stop

Reserved NC: No connection—reserved.

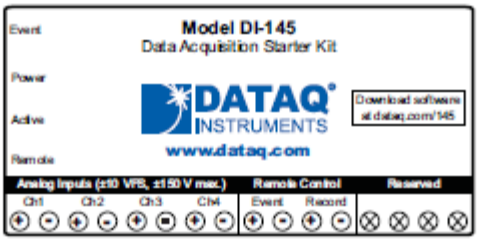

Use the following diagram to connect Analog Input Channel 1.

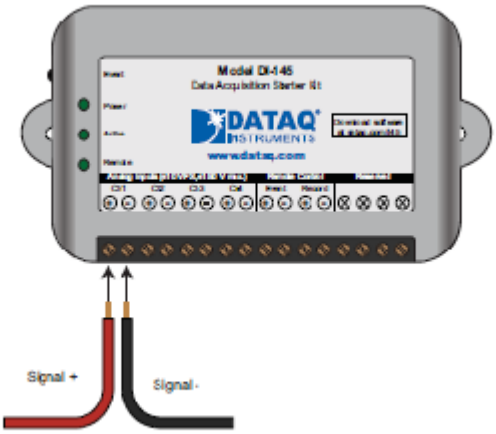

Connecting Signal Leads

To connect signal leads to the DI-145:

1. Insert the stripped end of a signal lead into the desired terminal directly under the screw.
2. Tighten the pressure flap by rotating the screw clockwise with a small screwdriver. Make sure that the pressure flap tightens only against the signal wire and not the wire insulation. Do not over-tighten.
3. Tug gently on the signal lead to ensure that it is firmly secured.

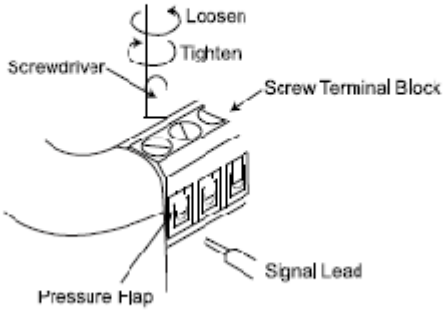

When an input signal is connected and WINDAQ Acquisition software is run, WINDAQ's real time display immediately reveals the input waveform on your computer's monitor.

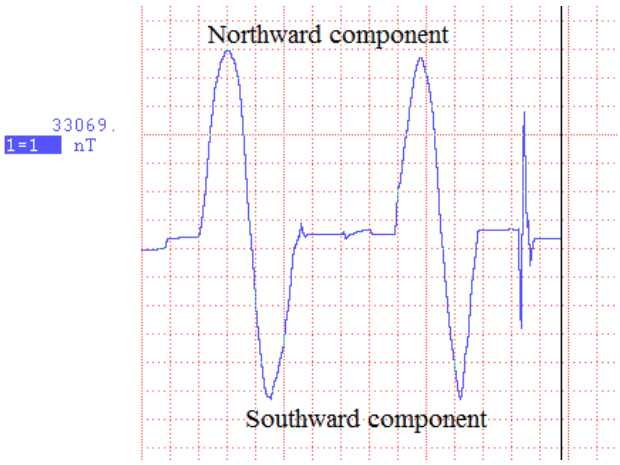

Figure G.4: Snapshot of the Northward and Southward Component of the Earth's Magnetic Field.

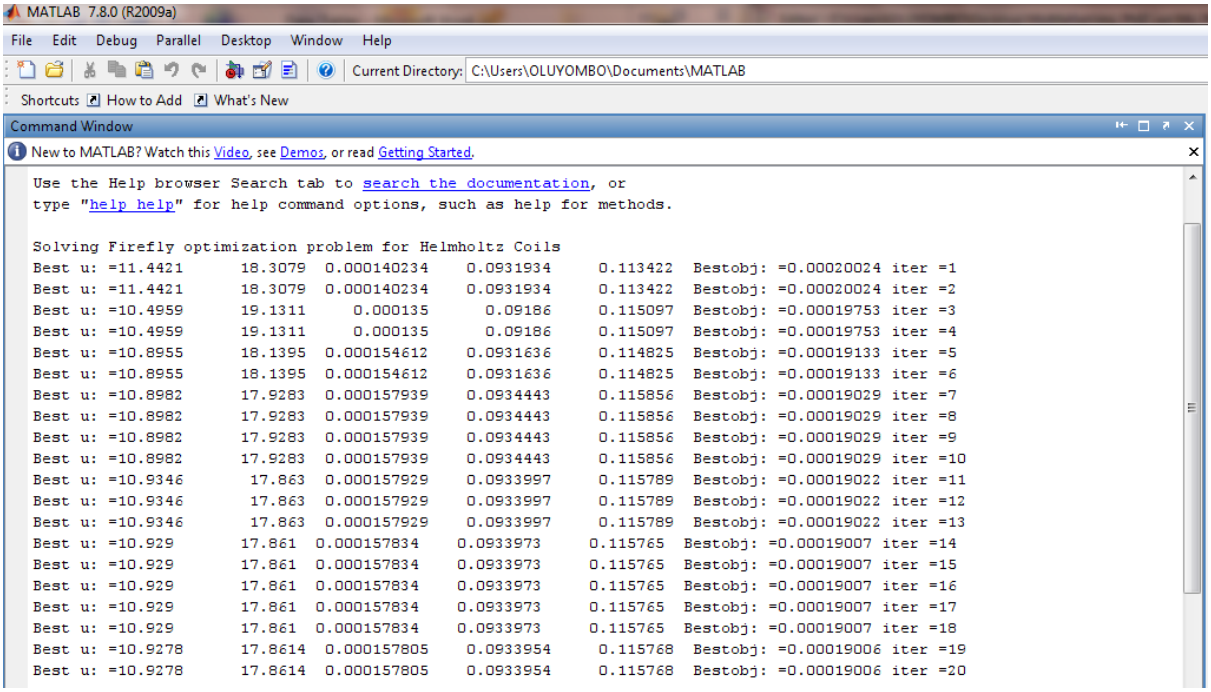
MATLAB 7.8.0 (R2009a)
File Edit Debug Parallel Desktop Window Help
Current Directory: C:\Users\OLUYOMBO\Documents\MATLAB
Shortcuts How to Add What's New
Command Window
New to MATLAB? Watch this Video, see Demos, or read Getting Started.
Use the Help browser Search tab to search the documentation, or
type "help help" for help command options, such as help for methods.
Solving Firefly optimization problem for Helmholtz Coils
Best u: =11.4421 18.3079 0.000140234 0.0931934 0.113422 Bestobj: =0.00020024 iter =1
Best u: =11.4421 18.3079 0.000140234 0.0931934 0.113422 Bestobj: =0.00020024 iter =2
Best u: =10.4959 19.1311 0.000135 0.09186 0.115097 Bestobj: =0.00019753 iter =3
Best u: =10.4959 19.1311 0.000135 0.09186 0.115097 Bestobj: =0.00019753 iter =4
Best u: =10.8955 18.1395 0.000154612 0.0931636 0.114825 Bestobj: =0.00019133 iter =5
Best u: =10.8955 18.1395 0.000154612 0.0931636 0.114825 Bestobj: =0.00019133 iter =6
Best u: =10.8982 17.9283 0.000157939 0.0934443 0.115856 Bestobj: =0.00019029 iter =7
Best u: =10.8982 17.9283 0.000157939 0.0934443 0.115856 Bestobj: =0.00019029 iter =8
Best u: =10.8982 17.9283 0.000157939 0.0934443 0.115856 Bestobj: =0.00019029 iter =9
Best u: =10.8982 17.9283 0.000157939 0.0934443 0.115856 Bestobj: =0.00019029 iter =10
Best u: =10.9346 17.863 0.000157929 0.0933997 0.115789 Bestobj: =0.00019022 iter =11
Best u: =10.9346 17.863 0.000157929 0.0933997 0.115789 Bestobj: =0.00019022 iter =12
Best u: =10.9346 17.863 0.000157929 0.0933997 0.115789 Bestobj: =0.00019022 iter =13
Best u: =10.929 17.861 0.000157834 0.0933973 0.115765 Bestobj: =0.00019007 iter =14
Best u: =10.929 17.861 0.000157834 0.0933973 0.115765 Bestobj: =0.00019007 iter =15
Best u: =10.929 17.861 0.000157834 0.0933973 0.115765 Bestobj: =0.00019007 iter =16
Best u: =10.929 17.861 0.000157834 0.0933973 0.115765 Bestobj: =0.00019007 iter =17
Best u: =10.929 17.861 0.000157834 0.0933973 0.115765 Bestobj: =0.00019007 iter =18
Best u: =10.9278 17.8614 0.000157805 0.0933954 0.115768 Bestobj: =0.00019006 iter =19
Best u: =10.9278 17.8614 0.000157805 0.0933954 0.115768 Bestobj: =0.00019006 iter =20

APPENDIX H

Electronics Circuits Simulation Results

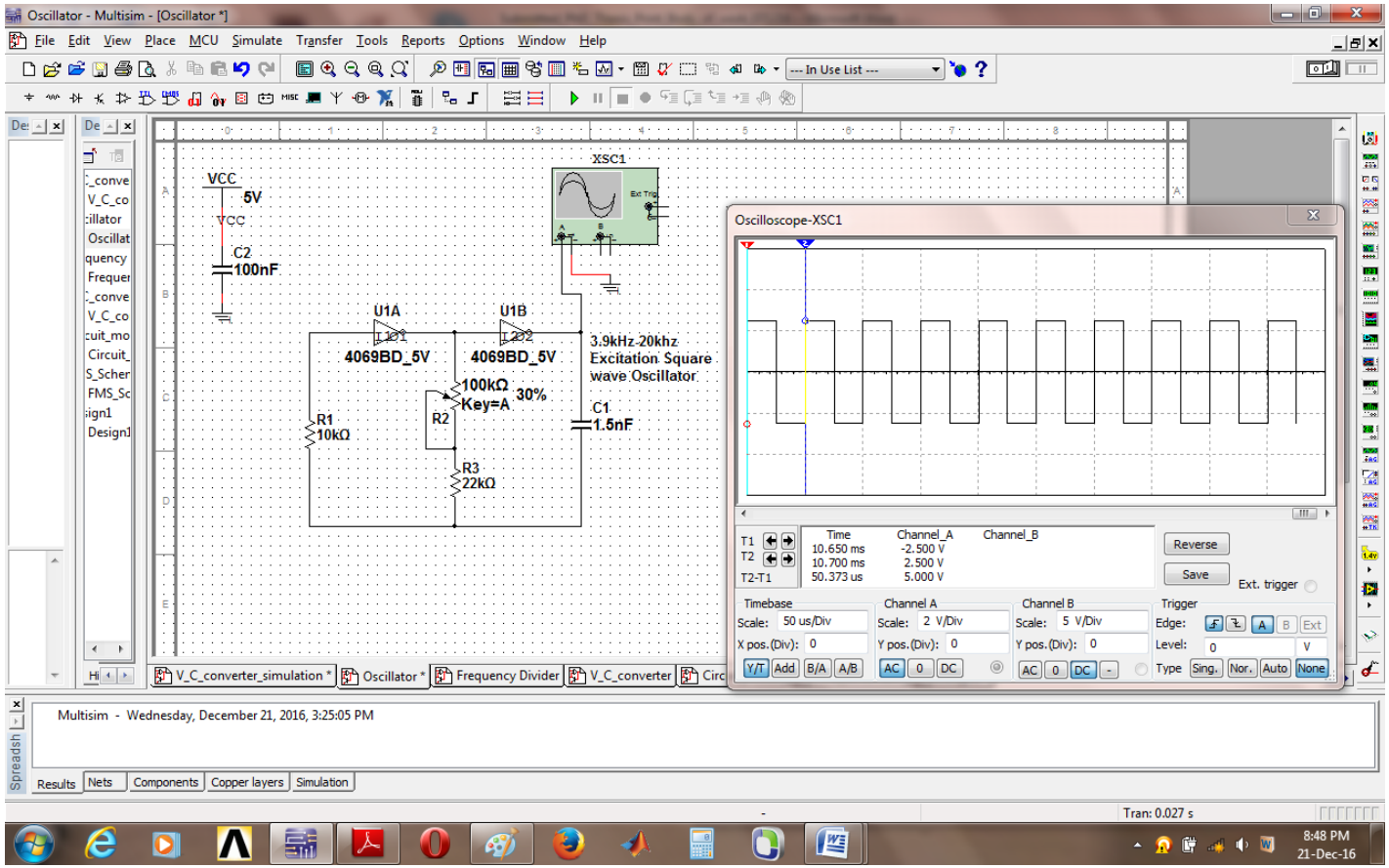

Figure H1: The Screenshot of the Excitation Square Wave Generator Simulation Result

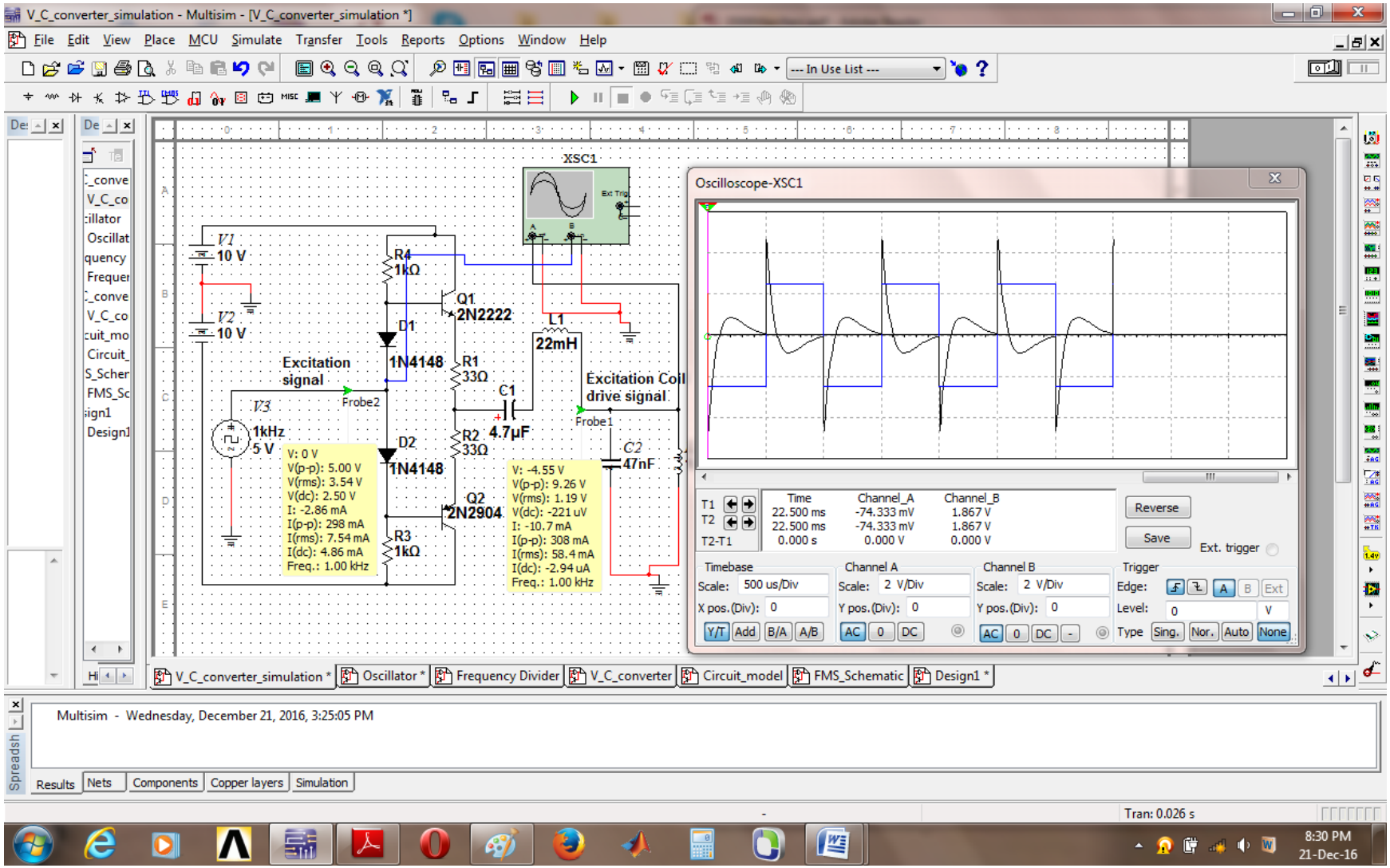

Figure H2: The Screenshot of the Voltage to Current converter Simulation Result at 1 kHz Excitation Frequency

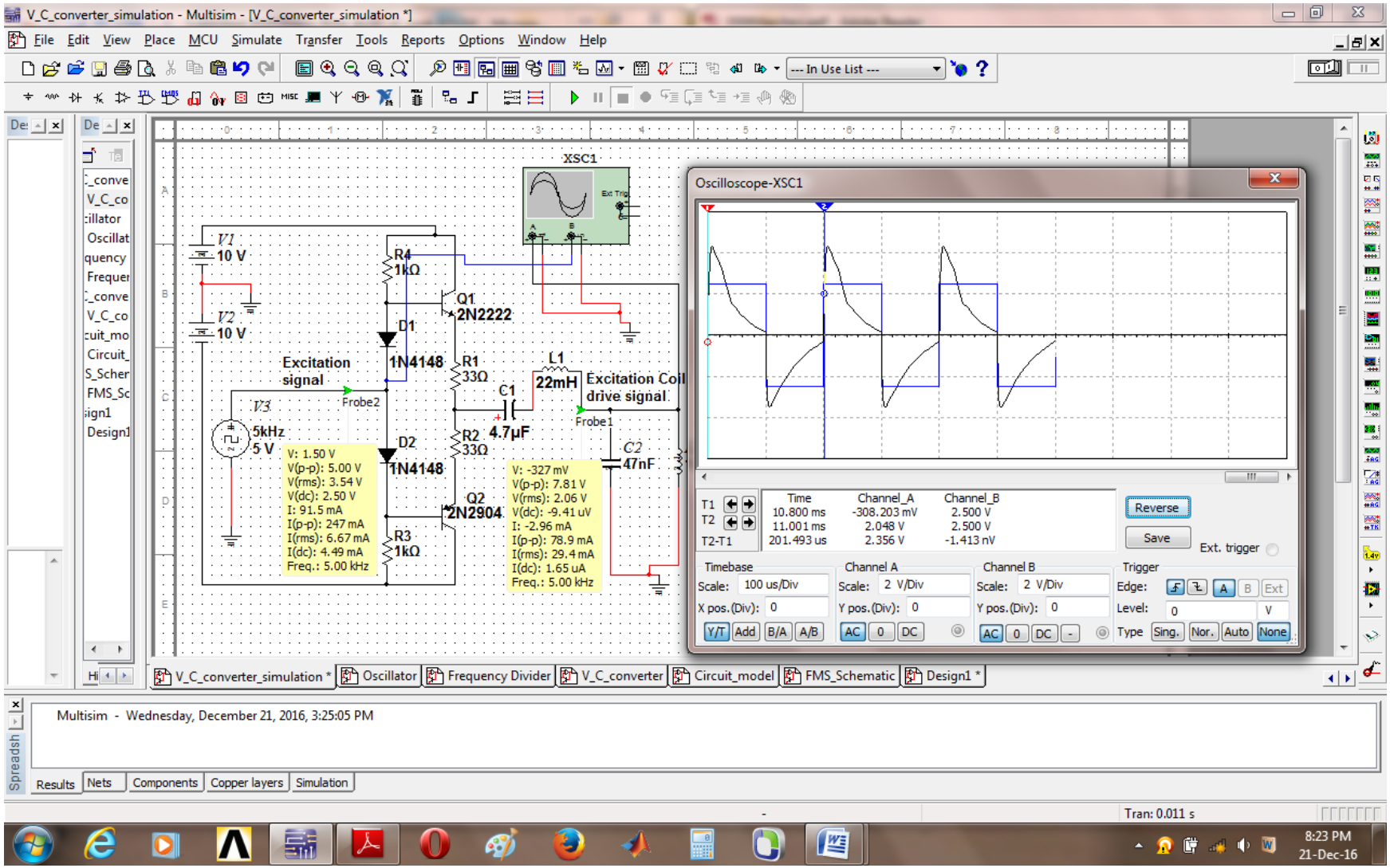

Figure H3: The Screenshot of the Voltage to Current converter Simulation Result at 5 kHz Excitation Frequency

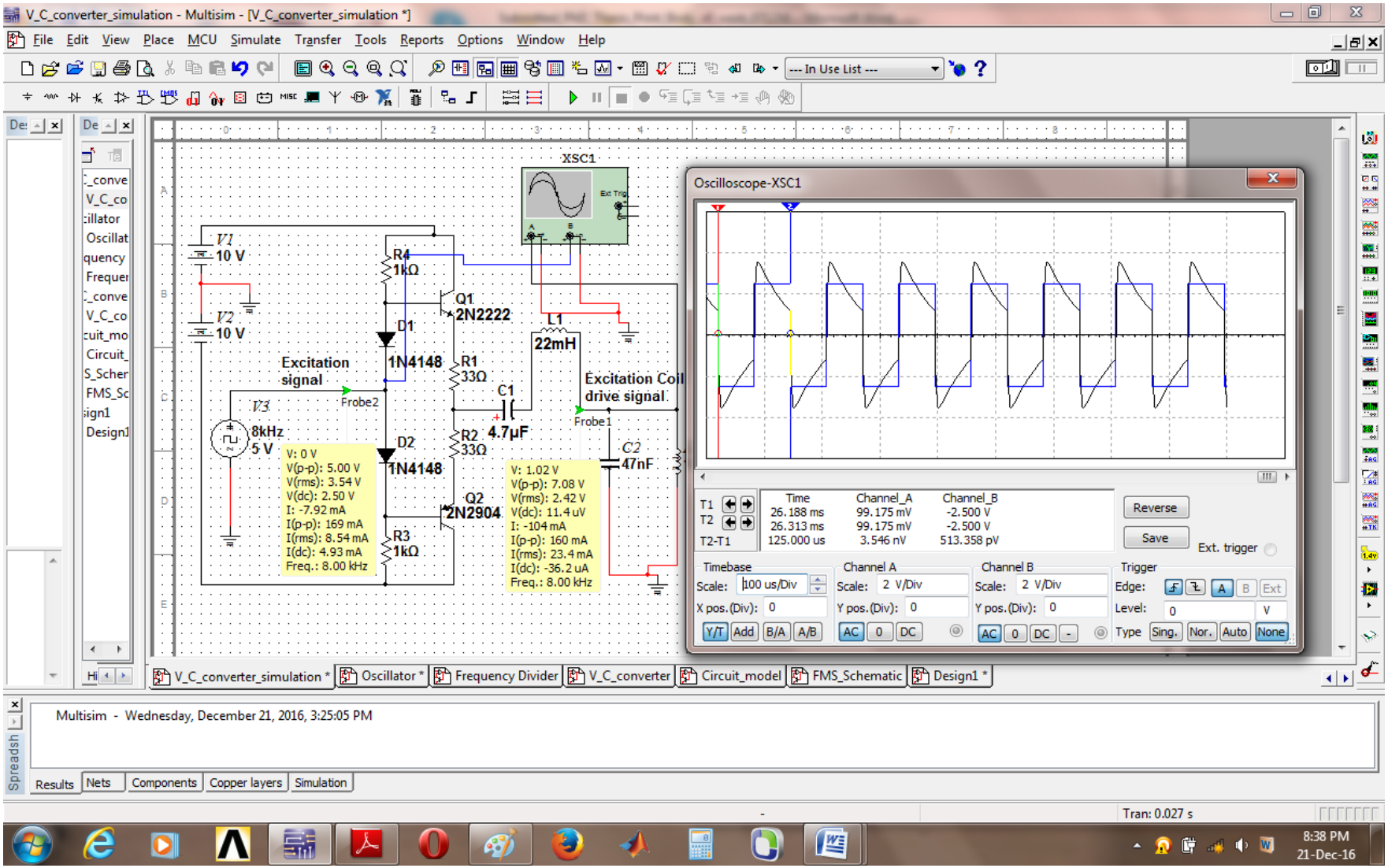

Figure H4: The Screenshot of the Voltage to Current converter Simulation Result at 8 kHz Excitation Frequency

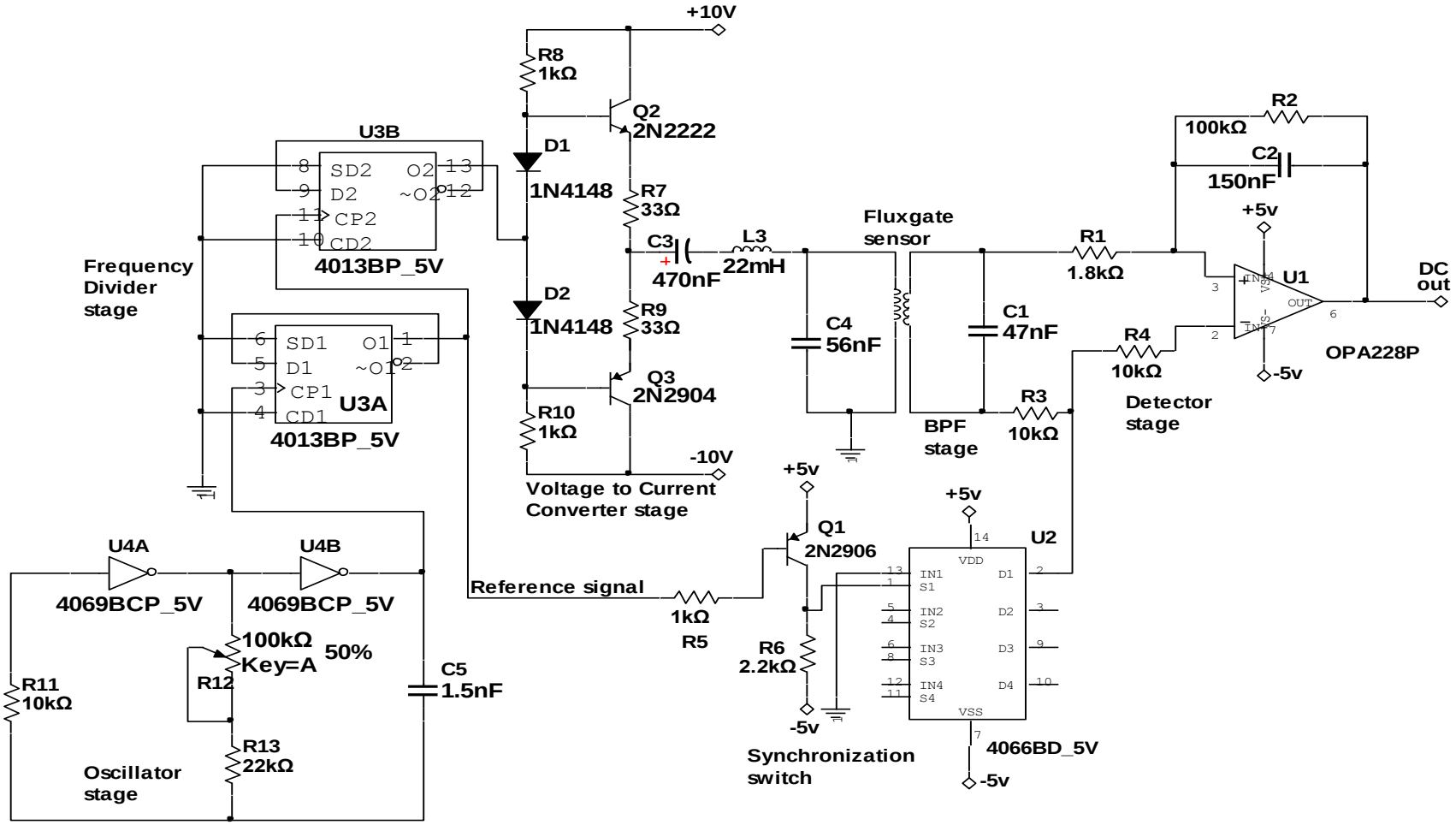

Figure H5: Full Schematic Diagram of the Developed Analog Fluxgate Magnetometer

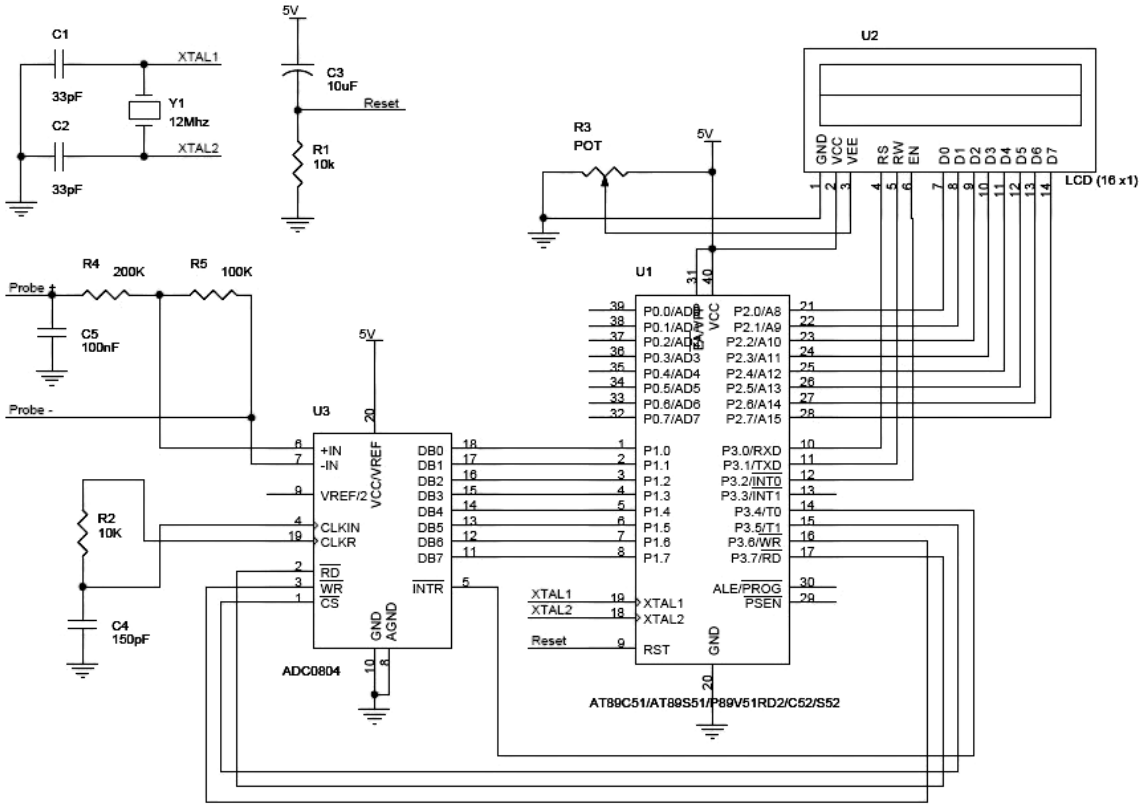

Figure H6: Digital Stage of Magnetic Field Meter using 8051 Microcontroller

Appendix H3. Analog to Digital Converter

Analog to Digital Converter (ADC) ADC0804 is an 8-bit analog to digital converter which uses successive approximation method to convert analog values to digital (Texas Instruments, 2015). ADC0804 is a single channel ADC which can take only one analog data as input. The step size of ADC0804 is varied by varying the reference voltage at pin 9 (Texas Instruments, 2015). It uses an internal clock, the frequency of which is given by (Texas Instruments, 2015):

$$f = \frac{1}{1.1RC} \qquad (H3.1)$$

where R (timing resistor) and C (timing capacitor) are 10KΩ and 150pF respectively.

Failure to connect the reference pin will lead to Vcc (supplied input voltage) is used as the default reference voltage (Texas Instruments, 2015). The pin configuration of ADC0804 is shown in Figure H7. The pin functions are presented in Table.

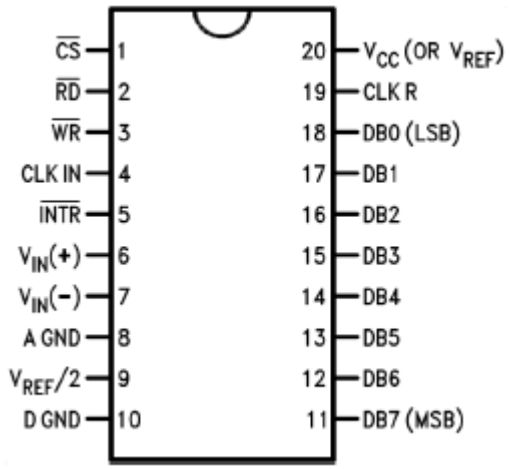

Figure H7: ADC0804 Pin Configuration (Texas Instruments, 2015)

Table H3.1: ADC0804 Pin Functions (Texas Instruments, 2015)

PIN		Input/output	Pin Description
Number	**Name**		
1	CS	Input	Chip Select
2	RD	Input	Read
3	WR	Input	Write
4	CLK IN	Input	External clock
5	INTR	Output	Interrupt
6	Vin (+)	Input	Analog input (+)
7	Vin (-)	Input	Analog input (-)
8	A Grnd	Input	Analog ground
9	$V_{ref}/2$	Input	Reference voltage
10	D Grnd	Input	Digital ground
11	DB7	Output	Data bit 7
12	DB6	Output	Data bit 6
13	DB5	Output	Data bit 5
14	DB4	Output	Data bit 4
15	DB3	Output	Data bit 3
16	DB2	Output	Data bit 2
17	DB1	Output	Data bit 1
18	DB0(LSB)	Output	Data bit 0
19	CLK R	Input	RC timing resistor
20	Vcc(or V_{ref})	Input	+5V supply voltage

The step size D at 5V is calculated as (Texas Instruments, 2015):

$$D = \frac{V_{in}}{2^n} \qquad (H3.2)$$

Where n is the resolution of the ADC. The resolution for analog to digital converter ADC0804 is eight (8).

Pin 9 of the ADC0804 is $V_{ref}/2$. In this research, this pin (pin 9) was left opened so that the input voltage can span between 0 to 5V. Therefore, at 5V, the step size is:

$$D = \frac{5}{2^8}$$

$$D = 19.53mV$$

This means for every 19.53mV rise in input voltage, the output is incremented by 1 value when the step size is at 5V. The conversion time of this IC depends on clock source.

The digital output was calculated as (Texas Instruments, 2015):

$$D_{out} = \frac{V_{in}}{D} \qquad (H3.3)$$

Where D_{out} is the digital output of the ADC, V_{in} is the analog input connected to the ADC, and D is the step size.

Since the maximum output voltage of the fabricated modified FOA sensor varies from 0 to 4.8V. Therefore, output digital data from the ADC0804 is,

$$D_{out} = \frac{4.8}{0.01953}$$

Hence, the maximum ADC0804 digital output is,

$$D_{out} = 245$$

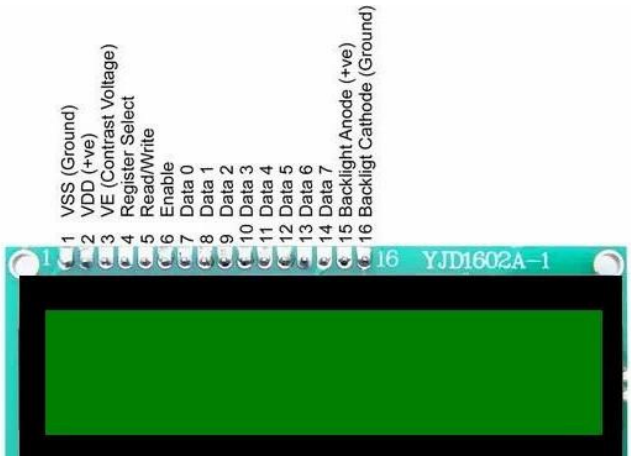

Figure H8: Pin Description of 2x16 LCD Display